Laser Site-Selective Spectroscopy of Rare-Earth Ions in Crystals of the Fluorite Structure.

A THESIS
SUBMITTED IN PARTIAL FULFILMENT
OF THE REQUIREMENTS FOR THE DEGREE
OF
DOCTOR OF PHILOSOPHY IN PHYSICS
IN THE
UNIVERSITY OF CANTERBURY

BY

Steven P. Jamison

University of Canterbury
1998

Abstract

Site-selective laser spectroscopy, Zeeman infrared and optical absorption have been employed to investigate trivalent dysprosium centers in rare-earth doped alkaline-earth fluoride crystals. These studies have characterised the two dominant centers in SrF_2:Dy^{3+}, which are determined to be the fluorine compensated C_{4v} and C_{3v} centers analogous to those observed in other SrF_2:RE^{3+} systems. The C_{3v} center is shown to correspond to the J-center of SrF_2:Er^{3+}, rather than the B-center reported for SrF_2:Ho^{3+}. In CaF_2:Dy^{3+} three single Dy^{3+} ion centers have been characterised, corresponding to the C_{4v} , C_{3v} and cubic centers. Cluster centers involving more than one Dy^{3+} ion are also present in CaF_2:0.05%Dy^{3+}, and such centers undergo efficient non-radiative cross-relaxation. This cross-relaxation eliminates the possibility of a direct investigation of the laser spectroscopy of these cluster centers, leading to the consideration of double doped systems. The laser spectroscopy of CaF_2:Dy^{3+}:Eu^{3+} reveals a cluster center with efficient $Dy^{3+}\rightarrow Eu^{3+}$ energy transfer. Through a correlation of the Eu^{3+} fluorescence with previous studies of CaF_2:Eu^{3+} this center has been determined to be a heterogeneous R-center dimer. The double doped CaF_2:Dy^{3+}:Gd^{3+} system has enabled the Dy^{3+} R-center fluorescence to be investigated. The polarised fluorescence of the C_{4v} centers in CaF_2:Dy^{3+} and SrF_2:Dy^{3+} has been analysed in terms of both electric dipole and magnetic dipole transition moments, from which it is shown that magnetic dipole processes are significant for Dy^{3+} fluorescence.

The temperature dependence of fluorescence polarisation in praseodymium and europium doped CaF_2 and SrF_2 has been employed to investigate ionic motion in the C_{4v} centers. These experiments have enabled the barrier energies for interstitial reorientation to be determined in a site-selective manner. An anomalous temperature dependence of the polarisation anisotropy is observed in the Pr^{3+} C_{4v} centers, and has been shown to be a consequence of energy transfer between the C_{4v} centers.

Acknowledgements

Many thanks go to Dr. Roger Reeves for his guidance and advice throughout the course of this research, and to Dr. Glynn Jones for the numerous discussions that have often clarified aspects of the work.

The technical support staff of this department have provided invaluable assistance with the ongoing task of keeping a lab running, and special thanks must go to Wayne Smith and Ron Culley of the mechanical workshop, and to Ross Ritchie and Geoff Graham who provided a major upgrade of the computer acquisition system during the period of this work along with frequent repairs to various pieces of electronic hardware. Thanks also to Tom Walker and Bob Flygenring who provided the cryogenic helium and nitrogen.

The crystal-field calculations presented in this thesis employed the *f-shell empirical* programs of Dr. Mike Reid, who is thanked for providing these programs and for many helpful discussions on the theoretical aspects of the trivalent lanthanides.

The Department of Physics and Astronomy is gratefully acknowledged for providing a Teaching Assistantship which enabled me to undertake this period of study.

I would like to thank fellow laser spectroscopy students Dr. Nick Strickland, Dr. Jon Wells and Tim Dean for the many discussions that enlivened and enriched the laser spectroscopy group.

A very special thank you must go to Melanie for her patient and loving support which has served as a constant source of encouragement throughout these many years of study.

Contents

Chapter 1

Introduction.

This thesis reports on laser site-selective, Zeeman infrared and optical absorption spectroscopy of CaF_2:Dy^{3+} and SrF_2:Dy^{3+}. A site-selective study of ionic motion associated with Pr^{3+} and Eu^{3+} centers in rare-earth doped CaF_2 and SrF_2 is also presented.

The laser site-selective investigation of CaF_2:Er^{3+} by Tallant and Wright [98] began a period of extensive research into the spectroscopy and defect chemistry of rare-earth doped CaF_2 and SrF_2. While there have now been laser site-selective studies of almost all the lanthanide ions in these hosts, trivalent dysprosium stands out for having received relatively little attention. There have been no site-selective spectroscopic investigations of the CaF_2:Dy^{3+} and SrF_2:Dy^{3+} systems, while the earlier non-site-selective studies have not provided an adequate description of these systems. That Dy^{3+} has not received more attention can be largely attributed to the experimental difficulties associated with the required blue laser excitation, and the complexities of the spectroscopy.

The primary objective of the spectroscopic investigations of CaF_2:Dy^{3+} and SrF_2:Dy^{3+} that are presented here is to establish the rare-earth centers occurring in these hosts, and to provide the energy level structure of these centers.

The rare-earth centers in CaF_2 are known to undergo preferential clustering at low dopant concentrations, where simple dimers and trimers occur for CaF_2:Sm^{3+} and CaF_2:Eu^{3+} [103, 37], while more complex hexamers have been proposed for CaF_2:Er^{3+} [97, 18]. The CaF_2:Dy^{3+} system is therefore of interest in determining the clustering behaviour for the rare-earths of intermediate ionic radius. For SrF_2:RE^{3+} systems the dominant center is dependent on the particular rare-earth dopant, with a change-over in the dominant center expected to occur in SrF_2:Dy^{3+} or SrF_2:Ho^{3+} [10]. With the reported spectroscopy of SrF_2:Ho^{3+} presenting an apparently anomalous center, the situation can be clarified with an investigation into SrF_2:Dy^{3+}.

The site-selective investigation of dipole reorientation in the tetragonal rare-earth centers which is presented here represents only the second such study, and expands on the previously reported results.

1.1 The rare-earths.

The rare-earths comprise the lanthanide and actinide series of elements, which are characterised by the filling of the 4f and 5f electronic shells respectively.

This thesis involves spectroscopic investigations of the trivalent lanthanide ions incorporated into a crystalline host. The fourteen trivalent lanthanides from cerium (Ce^{3+}) through to lutetium (Lu^{3+}) all possess an electronic structure with a xenon core ($1s^2 2s^2 2p^6 3s^2 3p^6 4s^2 3d^{10} 4p^6 5s^2 4d^{10} 5p^6$) with a progressive filling of the 4f shell. The radial extent of the valence 4f electrons is less than that of the filled "core" $5s^2 5p^6$ shells, which gives rise to partial shielding of the 4f electrons from interactions with surrounding ions. The energy levels are therefore less sensitive to the environment with the consequence that the inhomogeneous broadening of the energy levels, due to variations in the local environment, is relatively small. This leads to the optical transitions of the lanthanides often possessing narrow linewidths of the order of $1\,cm^{-1}$ or less. The radial eigenfunctions of the $4f^n$ shell also possess a spatial maximum that decreases through the lanthanide series, leading to the heavier ions possessing smaller ionic radii. This feature, termed the lanthanide contraction, is clearly seen in the ionic data of Table 1.1.

The shielding of the 4f electrons from the environment leads to an energy level structure which can be described in terms of $^{2S+1}L_J$ multiplets that are largely independent of the host material. The interactions with the environment remove the degeneracy of these multiplets with crystal-field splittings of the order of $500\,cm^{-1}$. Multiplet energy level diagrams for the rare-earth ions that are the main focus of attention in this thesis, namely Pr^{3+}, Eu^{3+} and Dy^{3+}, are presented in Figure 1.1.

	Ca^{2+}	Sr^{2+}	F^-	Ce^{3+}	Pr^{3+}	Nd^{3+}	Pm^{3+}	Sm^{3+}	Eu^{3+}
Atomic No.	20	38	9	58	59	60	61	62	63
Radius (Å)	0.99	1.12	1.33	1.01	0.997	0.983	0.97	0.958	0.947
Mass	40.08	87.62	19.00	140.12	140.90	144.24	(145)	150.36	151.97

	Gd^{3+}	Tb^{3+}	Dy^{3+}	Ho^{3+}	Er^{3+}	Tm^{3+}	Yb^{3+}
Atomic No.	64	65	66	67	68	69	70
Radius(Å)	0.938	0.923	0.912	0.901	0.890	0.880	0.868
Mass	157.25	158.92	162.50	164.93	167.26	168.93	173.04

Table 1.1: The ionic radii and atomic masses of the lanthanide ions and corresponding data for the ions of the host crystals [64]. This thesis is primarily concerned with Dy^{3+}, Pr^{3+} and Eu^{3+}, although Gd^{3+} and Tb^{3+} are also considered to a lesser extent.

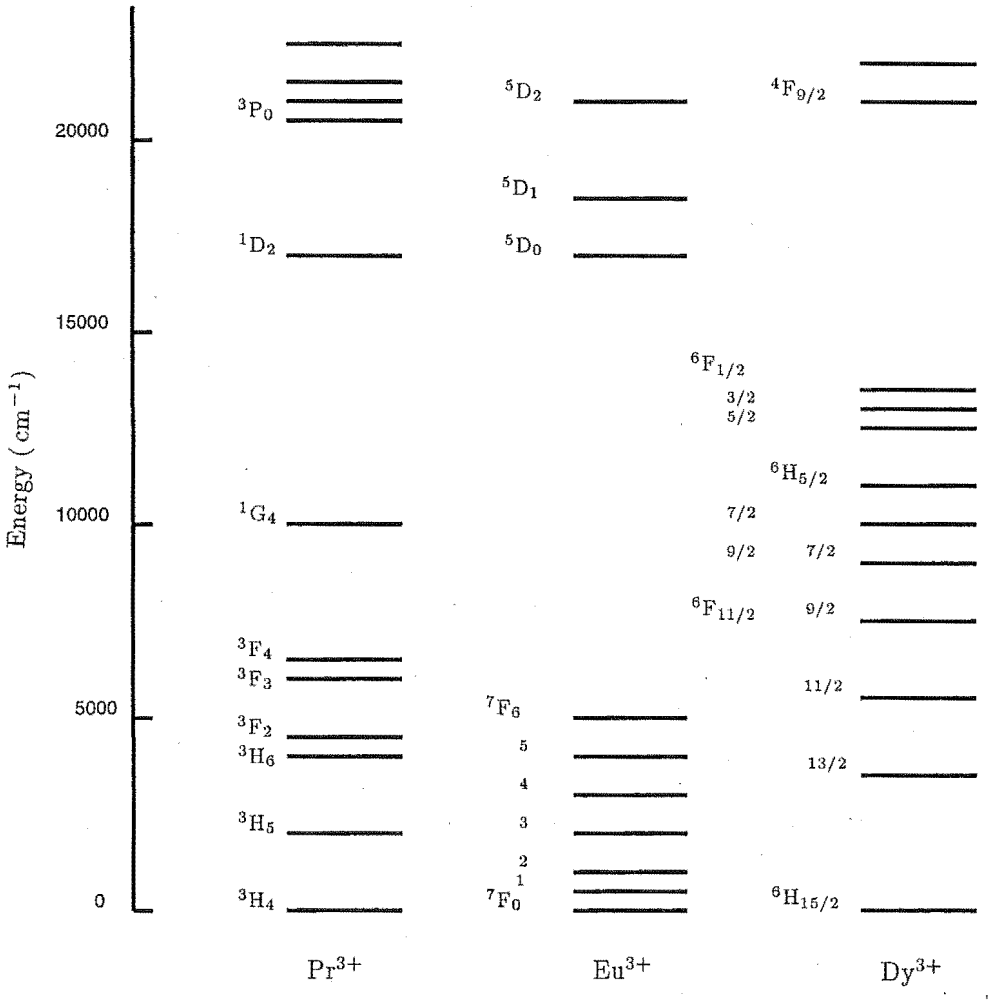

Figure 1.1: The approximate multiplet energy levels of the main rare-earths considered in this thesis.

The narrow linewidths and large number of states accessible in the optical and infrared regions make the lanthanide ions a versatile spectroscopic probe, and these ions have also proved to be of significant technological importance, with applications in areas such as high power lasers and optical communications.

1.2 The fluorite host.

The host crystals of CaF_2 and SrF_2 both possess the fluorite structure, which consists of a cubic lattice of fluorine ions with a divalent Ca^{2+} or Sr^{2+} in every second fluorine cube, as shown in Figure 1.2.

Trivalent lanthanide ions readily substitute for Ca^{2+} or Sr^{2+} when included in the melt. The different charge of the dopant ion leads to the requirement of charge compensation, and the variety of ways in which this is accomplished gives rise to a multitude of

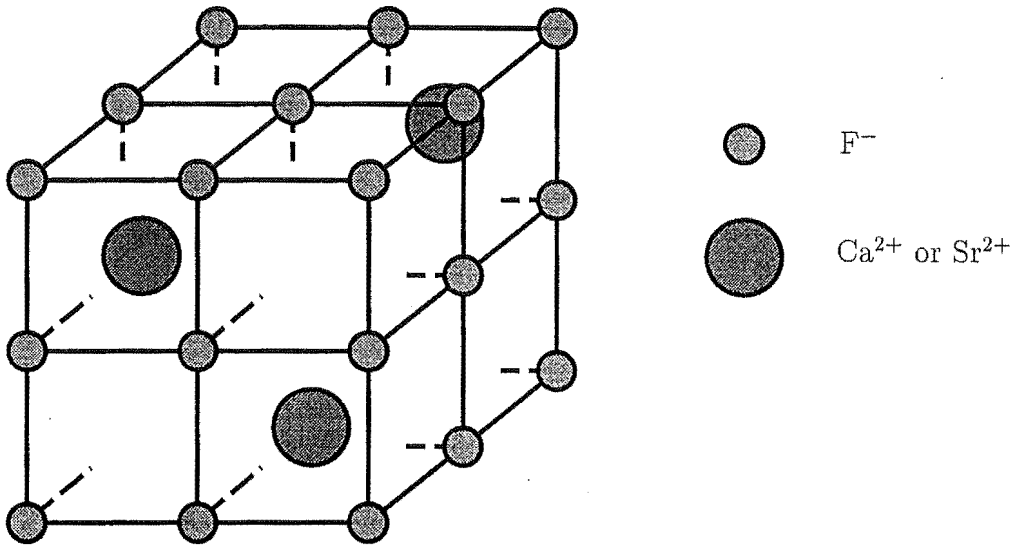

Figure 1.2: The structure of CaF_2 and SrF_2. The ionic radii of the ions are not shown to scale.

different rare-earth centers. At low rare-earth concentrations of 0.05 mol % or less, the predominant rare-earth centers in CaF_2 involve a single trivalent rare-earth ion with a charge compensating fluorine ion in an adjacent $\langle 100 \rangle$ interstitial position. The rare-earth of such a center exists in a site of tetragonal C_{4v} symmetry. The structure of the C_{4v} center is depicted in Figure 1.3. The dominant center in SrF_2:RE^{3+} is dependent on the particular rare-earth dopant. For ions from the beginning of the lanthanide series the C_{4v} symmetry center is predominant, while for smaller ions from the end of the series a trigonal C_{3v} center is formed with a charge compensating fluorine in the $\langle 111 \rangle$ interstitial position. The structure of the C_{3v} center is also shown schematically in Figure 1.3. The change over in the dominant defect center has been predicted to occur in the region of dysprosium in the lanthanide series [10, 22], and this is supported by the spectroscopy presented in this thesis.

A trigonal center is also known to occur in CaF_2:RE^{3+}, particularly for the heavier lanthanides. However the spectroscopy of these centers suggests a structure other than that of the SrF_2:RE^{3+} C_{3v} centers [62].

Because of the cubic structure of the host lattice, the interstitial charge compensation of the C_{4v} and C_{3v} centers can occur with different orientations within the crystal while maintaining a structurally equivalent rare-earth environment. For this reason, the absorption spectra of the rare-earth doped crystals will appear isotropic despite well defined symmetry axes for the particular sites. However, under certain circumstances the fluorescence from these centers will be polarised and hence non-isotropic. In this thesis the reorientation of interstitial fluorine ions has been investigated through consideration of the fluorescence polarisation.

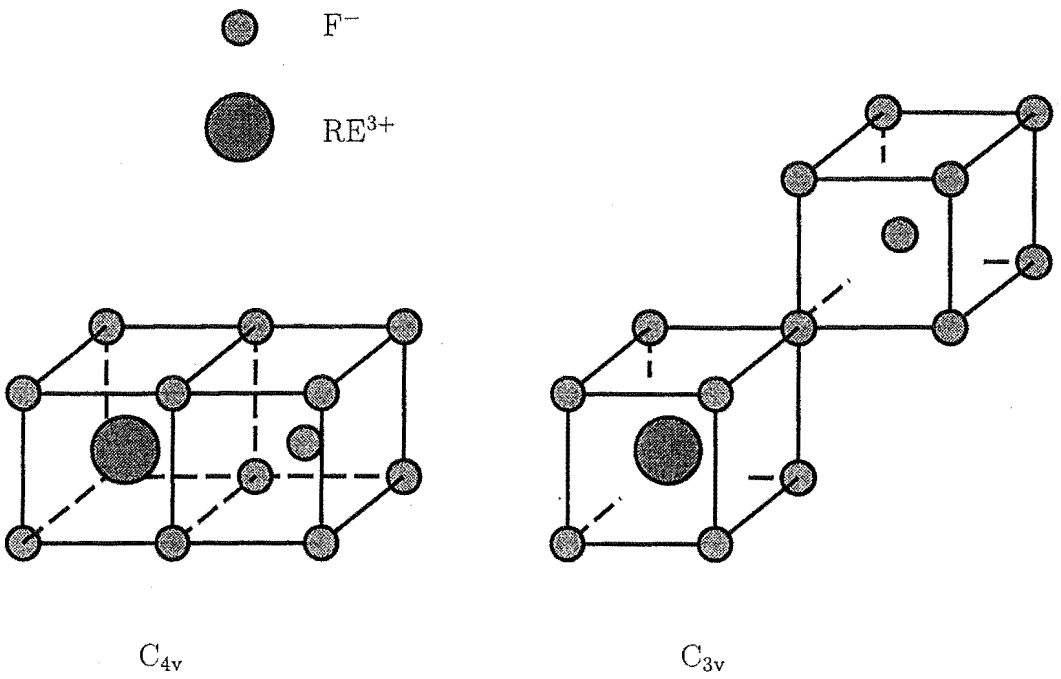

Figure 1.3: The structure of the C_{4v} centers in SrF_2:RE^{3+} and CaF_2:RE^{3+}, and the structure of the C_{3v} center in SrF_2:RE^{3+}. The ionic radii of the ions are not shown to scale.

Another rare-earth center that is known to occur is the cubic center, which consists solely of the trivalent dopant substituting for Ca^{2+} or Sr^{2+}, and with the charge compensation provided non-locally. Because of the centro-symmetric environment present in such a center the majority of the lanthanide optical transitions are forbidden. However, with the sensitivity available with laser selective techniques the optical spectroscopy of these centers can be investigated, although the transitions are often weak. Small distortions from the cubic symmetry, for example those caused by the remote charge compensation, are often invoked to explain the observation of the cubic center transitions.

At dopant concentrations greater than $\approx 0.05\% RE^{3+}$ in CaF_2, the rare-earth ions are known to undergo preferential clustering, with the formation of multi-rare-earth centers. The nature of this clustering changes through the lanthanide series, with simple dimers and trimers present at the beginning of the lanthanide series [103, 37] and more complex clusters such as hexamers proposed for the heavier ions at the end of the series [18]. CaF_2:Dy^{3+} therefore represents an intermediate system for investigations into the preferential clustering behaviour.

1.3 Thesis outline.

The work presented in this thesis covers the following areas.

- Site-selective studies of the spectroscopy of the C_{4v} and C_{3v} symmetry centers in SrF_2:Dy^{3+} and CaF_2:Dy^{3+}, including investigations of the polarised fluorescence to determine the irreducible representations associated with the energy levels of the C_{4v} centers.
- Analysis of the high symmetry centers in terms of crystal-field calculations, thereby evaluating wavefunctions for these centers.
- Zeeman infrared absorption experiments of the high symmetry centers, and analysis in terms of the crystal-field wavefunctions, thereby testing the accuracy of the crystal-field analysis.
- Experimental determination of the crystal-field co-ordinate basis, which contains an ambiguity due to the non-unique nature of the C_{3v} and C_{4v} Hamiltonians.
- An investigation into the low concentration clustering behaviour of CaF_2:Dy^{3+} and double doped CaF_2:Dy^{3+}:RE^{3+} systems.
- The spectroscopy of the CaF_2:Dy^{3+} cubic center which displays unusual vibronic transitions with very narrow linewidths, which are attributed to resonance modes. A re-evaluation of the spectroscopy of CaF_2:Sm^{3+} cubic centers in light of these vibronic transitions.
- Determination of characteristics of interstitial fluorine motion in the C_{4v} centers of CaF_2:RE^{3+} and SrF_2:RE^{3+} (RE=Pr, Eu), through a site-selective technique involving the temperature dependence of fluorescence polarisation.

Chapter two presents a brief summary of the theory that is applicable to much of the work of this thesis, such as crystal-field theory, group theory and polarisation dependent selection rules, and the Zeeman effect. Chapter three discusses experimental techniques and equipment employed in the studies reported here, including a discussion of the fluorescence polarisation behaviour for the specific experimental setup used in this thesis.

Chapter four presents the site-selective laser spectroscopy of the C_{4v} and C_{3v} centers in SrF_2:Dy^{3+}. The spectroscopy of the SrF_2:Dy^{3+} system is of interest in that the change over from a dominant C_{4v} center to a dominant C_{3v} center is expected to occur with lanthanide ions in the region of Dy^{3+}. Further, the C_{3v} center in SrF_2:Ho^{3+}

appears to differ in structure from that in SrF_2:Er^{3+} and the investigation of the Dy^{3+} trigonal center is able to clarify the anomalous nature of the center reported for Ho^{3+}. Crystal-field analyses of the C_{3v} and C_{4v} centers are presented. Zeeman infrared absorption experiments have provided a test of wavefunctions which are obtained from these crystal-field calculations. An ambiguity that exist in the coordinate basis used to describe the C_{3v} and C_{4v} centers in crystal-field calculations is addressed from the point of view of providing an experimental determination of the basis through Zeeman experiments.

Chapter five presents site-selective spectroscopy of the C_{4v} and C_{3v} centers in CaF_2:Dy^{3+}, along with crystal-field analyses of these centers. The results reported here clarify much ambiguity and disagreement that exists in the literature regarding the energy level scheme and crystal-field parameters of the C_{4v} center. The site-selective laser spectroscopy of Dy^{3+} C_{4v} centers in CaF_2 provides a completion of such studies across the lanthanide series, in that only Gd^{3+}, Yb^{3+} and Pm^{3+} have not been studied, while Ce^{3+} has been addressed through infrared absorption measurements. The CaF_2:Dy^{3+} C_{3v} center has not previously been addressed in the literature.

Chapter six reports on the spectroscopic investigation of CaF_2:Dy^{3+} and CaF_2:Dy^{3+}:RE^{3+} clustering. The preferential clustering of Dy^{3+} in CaF_2, at even moderate rare-earth concentrations of $\approx$0.05%, gives rise to centers which undergo cross-relaxation quenching of the excited states. This has led to the investigation of double doped systems, which has enabled assignment of the dominant cluster center as a R-center dimer. The spectroscopy of the CaF_2:Dy^{3+} cubic center is also reported in chapter six, along with a crystal-field analysis. The cubic center fluorescence displays interesting vibronic transitions, which possess a very narrow linewidth, and which cannot be associated with phonons present in the CaF_2 density of states. These vibronics are discussed in the context of resonance modes induced by the substitution of a Ca^{2+} ion with the much heavier rare-earth ion. The spectroscopy of the CaF_2:Sm^{3+} cubic centers is re-evaluated in light of these vibronic transitions, and it is found that similar vibronics are present in the fluorescence spectra, although they have previously been assigned as electronic transitions [103].

Chapter seven details investigations into the ionic motion of C_{4v} center interstitials in CaF_2:RE^{3+} and SrF_2:RE^{3+} where RE=Pr, Eu. The technique employed here involves observation of the fluorescence polarisation as a function of temperature, and represents only the second such investigation for the rare-earth doped fluorites. The polarisation of the emission is significantly reduced at temperatures greater than $\approx$200 K, due to the rapid reorientation of the interstitial ions between structurally equivalent interstitial positions. In contrast to more common techniques for studying the ionic motion in the

fluorites, the method employed here is intrinsically site-selective, and therefore does not possess the problems associated with assignment of the data to the particular dynamic processes involved. The barrier energies associated with the interstitial reorientation have been determined from an analysis of the fluorescence polarisation data, extending the results of Voron'ko et.al. [100]. An unexpected temperature dependence for the polarisation of the fluorescence in the Pr^{3+} centers has been determined to be due to resonant energy transfer between remote C_{4v} centers.

Chapter eight summarises the conclusions reached in the earlier chapters, and discusses possible further work that could build on these results.

Chapter 2

Theory

The theory of the f-shell energy levels and interactions has been widely discussed, with early reviews such as that of Wybourne in 1965 [105] through to the more recent review of crystal-field theory of Görller-Walrand and Binnemans in 1996 [36]. This chapter draws on these works, and others [45, 102, 51], to summarise much of the preliminary theory applicable to the work in this thesis.

2.1 The f-shell.

In determining the energy levels of the $4f^n$ shell of the trivalent lanthanide ions, the Hamiltonian can be expressed in two parts: the interactions of the free-ion, and interactions of the ion with surrounding ligands, which are usually termed the crystal-field interactions. The partially filled $4f^n$ shell possesses the property that its radial extent is less than that of other shells such as the 5s and 5p orbitals. This results in an effective shielding of the valence shell from the environment, and therefore the crystal-field interactions are usually significantly reduced in comparison to that found in, for example, the transition ions. One implication of this shielding is that the energy levels of the rare-earths are largely independent of the crystal in which they are embedded, with the crystal-field interactions significantly smaller than the spin-orbit interaction, and approximate multiplet energies are generally applicable regardless of the host.

2.1.1 The free-ion interactions.

To a first approximation the Hamiltonian of the free-ion can be expressed as a combination of the kinetic energy of the electrons, the electrostatic potential of the electrons in the field of the nucleus and of any other individual electron, and the spin-orbit interaction. Hence the Hamiltonian can be written as

$$H = \frac{-\hbar^2}{2m}\sum_i \nabla_i^2 - \sum_i \frac{Ze^2}{r_i} + \sum_{i<j}\frac{e^2}{r_{ij}} + \sum_i \zeta(r_i)\boldsymbol{l}_i \cdot \boldsymbol{s}_i \tag{2.1}$$

The subscripts refer to the i-th electron of the configuration, with r_i the nucleus-electron distance and r_{ij} the distance between the i-th and j-th electron.

Applying the central field approximation, in which the f^n electrons are considered to be moving in a spherically symmetric potential $U(r_i)$, with any distortions from other electrons of the shell considered to be small perturbations, leads to

$$H = \sum_i \left(\frac{-\hbar^2}{2m}\nabla_i^2 + U(r_i)\right) + \sum_i \left(-\frac{Ze^2}{r_i} - U(r_i)\right) + \sum_{i<j}\frac{e^2}{r_{ij}} + \sum_i \zeta(r_i)\boldsymbol{l}_i \cdot \boldsymbol{s}_i \tag{2.2}$$

The terms in the first summation separate the $4f^n$ configuration from other orbitals, while the second summation provides another uniform shift to the configuration. Therefore the first two summations can be neglected in any discussions of the energy level structure within the $4f^n$ configuration.

The remaining terms of the free-ion Hamiltonian, along with higher order corrections, can be expressed as

$$\begin{aligned} H = \; & \textstyle\sum_k F^k f_k + \sum_i \zeta(r_i)\boldsymbol{l}_i \cdot \boldsymbol{s}_i \\ & + \alpha L(L+1) + \beta G(G_2) + \gamma G(R_7) + \textstyle\sum_k M^k m_k + \sum_k P^k p_k + \sum_k T^k t_k \end{aligned} \tag{2.3}$$

It is this free-ion Hamiltonian that is used in this thesis. The $F^k f_k$ electrostatic interaction (corresponding to the e^2/r_{ij} operator) separates the configuration into "terms" that can be described by the total spin S and orbital angular momentum L. The spin-orbit interaction partially removes the degeneracy of these terms into $|L-S| \cdots L+S$ multiplets characterised by the LSJ quantum numbers, usually denoted as ${}^{2S+1}\mathrm{L}_J$. Because the spin-orbit interaction is diagonal in J but not in L and S, strictly speaking L and S are not good quantum numbers. However, because the spin-orbit interaction is usually much smaller than the electrostatic interaction and the ${}^{2S+1}\mathrm{L}_J$ multiplets are often well separated, each multiplet will tend to be dominated by contributions from particular LS terms, and hence the ${}^{2S+1}\mathrm{L}_J$ notation is still useful in describing the multiplets. The remaining terms of equation 2.3 represent additional small corrections to the Hamiltonian. The operators associated with the parameters α, β, γ take account of interactions with other configurations. The Marvin integrals M^k are associated with spin-spin and spin-other orbit interactions, while the $P^k p_k$ interaction represents two body magnetic effects, and finally the three body electrostatic interactions, applicable for ions with 3 to 11 f-shell electrons, are represented by the $T^k t_k$ terms.

2.1.2 Crystal-field interactions

The free-ion states, or multiplets, that are characterised by the above Hamiltonian correspond to a spherically symmetric environment. On embedding the ion into a crystal lattice the dominant effect is to reduce the symmetry of the potential in which the 4f electrons move. A small change in the free-ion interactions is also introduced through the nephelauxetic effect, in which the radial extent of the wavefunctions increases on introduction to the crystal. This expansion of the free-ion wavefunction results in a small change of the free-ion parameters. The non-spherical potential introduced by the the ligands surrounding the lanthanide ion can be expanded as a linear combination of the spherical harmonics

$$H = \sum_{k,q} B_q^k C_q^k \qquad \text{where} \qquad C_q^k \equiv \sqrt{\frac{4\pi}{2k+1}} Y_{k,q} \tag{2.4}$$

The B_q^k of equation 2.4 represent the radial part of the interaction, and are usually treated as parameters to be determined from experiment. The angular part is usually expressed in terms of the Racah spherical tensors C_q^k defined in equation 2.4, where the $Y_{k,q}$ are standard spherical harmonics. The advantage of using the C_q^k operators with their different normalisation from the spherical harmonics, lies in their properties as tensors.

Expressing the crystal-field interactions in terms of radial and angular parts enables constraints on the Hamiltonian to be derived based solely on the point symmetry of the lanthanide ion environment. The symmetry of the environment provides well defined relationships between various B_q^k parameters, such that the Hamiltonian is invariant with respect to symmetry operations of the environment.

Görller-Walrand and Binnemans [36] have tabulated linear combinations of operators appropriate for the crystal-field Hamiltonians for all the point groups. Having defined the crystal-field Hamiltonian through the point group symmetry constraints, the Hamiltonian can be reexpressed as an arbitrary linear combination of the relevant operators. Specifically, terms may be grouped in such a manner that the sets of parameters are associated with higher symmetry crystal-field interactions. This approach allows small deviations in the interactions from a parent symmetry to be more readily apparent. For example, expressing a tetragonal crystal-field Hamiltonian in terms of cubic and non-cubic interactions may be relevant if it is thought that the interactions are dominated by a cubic environment, with a small non-cubic perturbation introduced through more remote ligands. The linear combination of the operators may also be chosen in such a way that the redefined operators associated with each parameter transform as specific irreducible representations of a group chain. For these reasons, and also for consis-

tency with the common recent practice for investigation of the trivalent rare-earths in fluorite-type crystals [72, 74, 96, 103], the following Hamiltonians are employed for the different symmetry centers encountered in this work.

$$V_{O_h} = B_C^4 \left[C_0^{(4)} + \sqrt{\frac{5}{14}}(C_4^{(4)} + C_{-4}^{(4)}) \right] + B_C^6 \left[C_0^{(6)} - \sqrt{\frac{7}{2}}(C_4^{(6)} + C_{-4}^{(6)}) \right] \tag{2.5}$$

$$\begin{aligned} V_{C_{4v}} &= B_A^2 C_0^{(2)} + B_A^4 \left[C_0^{(4)} - \sqrt{\frac{7}{10}}(C_4^{(4)} + C_{-4}^{(4)}) \right] + B_A^6 \left[C_0^{(6)} + \sqrt{\frac{1}{14}}(C_4^{(6)} + C_{-4}^{(6)}) \right] + \\ &\quad B_C^4 \left[C_0^{(4)} + \sqrt{\frac{5}{14}}(C_4^{(4)} + C_{-4}^{(4)}) \right] + B_C^6 \left[C_0^{(6)} - \sqrt{\frac{7}{2}}(C_4^{(6)} + C_{-4}^{(6)}) \right] \end{aligned} \tag{2.6}$$

$$\begin{aligned} V_{C_{3v}} &= B_A^2 C_0^{(2)} + B_A^4 \left[C_0^{(4)} - \frac{1}{2}\sqrt{\frac{7}{10}}(C_3^{(4)} - C_{-3}^{(4)}) \right] + \\ &\quad B_A^6 \left[\sqrt{\frac{11}{42}}(C_3^{(6)} - C_{-3}^{(6)}) + \sqrt{\frac{5}{21}}(C_6^{(6)} + C_{-6}^{(6)}) \right] + \\ &\quad B_A^{6\prime} \left[C_0^{(6)} + \frac{4}{7}\sqrt{\frac{10}{21}}(C_3^{(6)} - C_{-3}^{(6)}) - \frac{4}{7}\sqrt{\frac{11}{21}}(C_6^{(6)} + C_{-6}^{(6)}) \right] + \\ &\quad B_C^4 \left[C_0^{(4)} + \sqrt{\frac{10}{7}}(C_3^{(4)} - C_{-3}^{(4)}) \right] + B_C^6 \left[C_0^{(6)} - \sqrt{\frac{35}{96}}(C_3^{(6)} - C_{-3}^{(6)}) + \frac{1}{8}\sqrt{\frac{77}{3}}(C_6^{(6)} + C_{-6}^{(6)}) \right] \end{aligned} \tag{2.7}$$

The identity between the cubic Hamiltonian and the cubic part of the tetragonal C_{4v} Hamiltonian is readily apparent. The cubic part of the trigonal C_{3v} Hamiltonian differs because of a change in the coordinate system used to describe these two Hamiltonians. The identity of the cubic parts can be reestablished by an appropriate rotation of the coordinate system of the cubic Hamiltonian. For reference, the cubic and C_{4v} Hamiltonians are given for a basis with the z-axis along a four-fold rotation axis. The C_{3v} Hamiltonian corresponds to a z-axis along a three-fold axis.

In evaluating matrix elements of the crystal-field interaction the tensor operator characteristics of the C_q^k enable the Wigner-Eckart theorem to be employed, which greatly simplifies such calculations through a factorisation of the matrix elements. Following Wybourne [105] such matrix elements are evaluated from the expression

$$\langle 4f^n\alpha SLJM|C_q^k|4f^n\alpha SL'J'M'\rangle = \langle f||C^k||f\rangle\langle 4f^n\alpha SLJM|U_q^k|4f^n\alpha SL'J'M'\rangle$$

$$= -7(-1)^{2J-M+S+L'+k}\sqrt{(2J+1)(2J'+1)}\begin{pmatrix} 3 & k & 3 \\ 0 & 0 & 0 \end{pmatrix}\begin{pmatrix} J & k & J' \\ -M & q & M \end{pmatrix}$$

$$\times\begin{Bmatrix} J & J' & k \\ L' & L & S \end{Bmatrix}\langle \alpha SL||U^k||\alpha SL'\rangle \qquad (2.8)$$

The 3jm and 6j values can be found from the tabulations of Rotenberg et.al. [91] or evaluated directly from formulas given in the same reference. The reduced matrix elements of $\langle\ ||\ ||\ \rangle$ can be found from Nielson and Koster [77].

The free-ion and crystal-field calculations presented in this thesis are based on the above formalism. Such calculations were generally performed with the *f-shell empirical* programs written by Dr. M.F. Reid of this Department.

2.2 Group Theory

Through the application of group theory to spectroscopy, considerable insight into the properties of various interactions can be obtained. It is through group theory that the decomposition of multiplets into energy levels may be established in a simple manner, the properties of transitions between states determined, and the multitude of calculations that may be encountered simplified.

The basis for applying group theory to spectroscopic problems lies in the fact that the wavefunction of each state transforms as a particular irreducible representation (irrep) of the symmetry group corresponding to the symmetry of the surrounding environment [102].

2.2.1 Multiplet decomposition

The free-ion multiplets, corresponding to wavefunctions in a spherically symmetric potential, can each be labelled according to the irreps of the rotation group O_3. The dimension of the irrep corresponds to the total degeneracy of that multiplet, which in terms of the quantum number J is given simply as $(2J+1)$. Reduction of the symmetry of the environment upon embedding the ion in a crystal leads to consideration of the branching rules associated with the group chain reduction from the rotation group to the point group of the site symmetry. From these branching rules the remaining degeneracy of the crystal-field split multiplet can be inferred. When considering the crystal-field degeneracy the parity of the f^n configuration is to be taken into account.

J	C_{4v} irreps	C_{3v} irreps
15/2	$4\Gamma_6 + 4\Gamma_7$	$5\Gamma_4 + 3(\Gamma_5 + \Gamma_6)$
13/2	$3\Gamma_6 + 4\Gamma_7$	$5\Gamma_4 + 2(\Gamma_5 + \Gamma_6)$
11/2	$3\Gamma_6 + 3\Gamma_7$	$4\Gamma_4 + 2(\Gamma_5 + \Gamma_6)$
9/2	$3\Gamma_6 + 2\Gamma_7$	$3\Gamma_4 + 2(\Gamma_5 + \Gamma_6)$
7/2	$2\Gamma_6 + 2\Gamma_7$	$3\Gamma_4 + (\Gamma_5 + \Gamma_6)$
5/2	$\Gamma_6 + 2\Gamma_7$	$2\Gamma_4 + (\Gamma_5 + \Gamma_6)$
3/2	$\Gamma_6 + \Gamma_7$	$\Gamma_4 + (\Gamma_5 + \Gamma_6)$
1/2	Γ_6	Γ_4

Table 2.1: The Kramers ion irrep decomposition for each multiplet in C_{4v} and C_{3v} symmetry.

J	C_{4v} irreps
6	$2\Gamma_1+\Gamma_2+2\Gamma_3+2\Gamma_4+3\Gamma_5$
5	$\Gamma_1+2\Gamma_2+\Gamma_3+\Gamma_4+3\Gamma_5$
4	$2\Gamma_1+\Gamma_2+\Gamma_3+\Gamma_4+2\Gamma_5$
3	$\Gamma_2+\Gamma_3+\Gamma_4+2\Gamma_5$
2	$\Gamma_1+\Gamma_3+\Gamma_4+\Gamma_5$
1	$\Gamma_2+\Gamma_5$
0	Γ_1

Table 2.2: The non-Kramers ion irrep decomposition for each multiplet in C_{4v} symmetry.

As the individual f electrons are of odd parity, the total parity of the f^n configuration will be even for an even number of electrons (non-Kramers ions) and the parity will be odd for an odd number of electrons (Kramers ions). The irrep of a particular free-ion multiplet with angular momentum J is denoted as $D_J^{\pm}$, where the $\pm$ sign indicates the parity appropriate for the Kramers $(-)$ and non-Kramers $(+)$ ions. The multiplet decompositions for both Kramers ions and non-Kramers ions are listed in Tables 2.1 and 2.2, for the two main symmetries discussed in this thesis (C_{4v} and C_{3v}). Non-Kramers ions in C_{3v} symmetry centers are not discussed in this work, therefore those decompositions are not presented here.

The majority of the work discussed in this thesis is concerned with Kramers ions. For Kramers ions each crystal field state will remain doubly degenerate. This Kramers degeneracy is a consequence of Kramers theorem [58, 1], which shows that as a consequence of time-reversal symmetry applied to odd-electron systems, this double degeneracy can only be removed by time-odd interactions. This then implies that the (electrostatic) crystal-field cannot remove the two-fold degeneracy regardless of the symmetry of the crystal-field. However, application of a magnetic field will in general remove this residual degeneracy of the odd-electron states.

It is noted that while the Γ_5 and Γ_6 irreps of the C_{3v} symmetry are of dimension one, the states associated with these irreps will be degenerate, and constitute a Kramers conjugate pair.

2.3 Selection rules and polarisation behaviour.

By consideration of the group transformation properties of the electric-dipole and magnetic-dipole operators the selection rules for optical transitions between states can be inferred, along with polarisation characteristics of the allowed transitions.

The electric-dipole operator is proportional to $\boldsymbol{E} \cdot \boldsymbol{r}$ and for the free-ion transforms as the D_1^- irrep of the O_3 group. Similarly the magnetic dipole operator is proportional to $\boldsymbol{B}\cdot(\boldsymbol{L}+2\boldsymbol{S})$ and transforms as the D_1^+ irrep. For a particular symmetry of the ion that results upon embedding in a host lattice the branching of the transition operator irrep to the subgroup of the site symmetry is considered. This thesis is primarily concerned with the subgroups of C_{4v} and C_{3v} , for which the irreps of the transition operators in the reduced symmetry are

$$\begin{aligned} C_{4v} \qquad D_1^- &\rightarrow \Gamma_1(\pi) + \Gamma_5(\sigma) \\ D_1^+ &\rightarrow \Gamma_2(\pi') + \Gamma_5(\sigma') \\ C_{3v} \qquad D_1^- &\rightarrow \Gamma_1(\pi) + \Gamma_3(\sigma) \\ D_1^+ &\rightarrow \Gamma_2(\pi') + \Gamma_3(\sigma') \end{aligned} \tag{2.9}$$

The different irreps of the decomposition are identified with transitions of different polarisation, indicated by the π, σ notation. A π-polarised transition is one in which the electric field of the light is polarised parallel to the principal (z) axis of the symmetry center. Similarly, a σ-polarised transition is one in which the light is polarised orthogonal to the principal axis. For the magnetic dipole transitions the π' and σ' transitions involve light with the magnetic field parallel or perpendicular to the principal axis, remembering that the magnetic field will itself be orthogonal to the electric field. The prime notation is employed to signify polarisation with respect to the magnetic field.

A non-zero transition moment between states transforming as Γ_i and Γ_f via an operator transforming as Γ_{op} requires

$$\Gamma_{op} \times \Gamma_i \supset \Gamma_f. \tag{2.10}$$

From consideration of the irrep multiplication tables [60] the (point-group) allowed transitions can be inferred, along with the polarisation characteristic of those transitions. The selection rules for Kramers and non-Kramers ions, in both C_{4v} and C_{3v} symmetries, are summarised in Table 2.3.

As well as selection rules associated with the point group symmetry, there are additional selection rules associated with the LSJ quantum numbers. These selection rules will break down to some extent in the crystal-field states, as the LSJ cannot necessarily be considered good quantum numbers. However, by consideration of the LSJ components

Electric Dipole **Magnetic Dipole**

C_{3v}, Kramers ions

C_{3v}	Γ_4	$\Gamma_5+\Gamma_6$
Γ_4	π,σ	σ
$\Gamma_5+\Gamma_6$	σ	π

C_{3v}	Γ_4	$\Gamma_5+\Gamma_6$
Γ_4	π',σ'	σ'
$\Gamma_5+\Gamma_6$	σ'	π'

C_{4v}, Kramers ions

C_{4v}	Γ_6	Γ_7
Γ_6	π,σ	σ
Γ_7	σ	π,σ

C_{4v}	Γ_6	Γ_7
Γ_6	π',σ'	σ'
Γ_7	σ'	π',σ'

C_{3v}, non-Kramers ions

C_{3v}	Γ_1	Γ_2	Γ_3
Γ_1	π		σ
Γ_2		π	σ
Γ_3	σ	σ	π,σ

C_{3v}	Γ_1	Γ_2	Γ_3
Γ_1		π'	σ'
Γ_2	π'		σ'
Γ_3	σ'	σ'	π',σ'

C_{4v}, non-Kramers ions

C_{4v}	Γ_1	Γ_2	Γ_3	Γ_4	Γ_5
Γ_1	π				σ
Γ_2		π			σ
Γ_3			π		σ
Γ_4				π	σ
Γ_5	σ	σ	σ	σ	π

C_{4v}	Γ_1	Γ_2	Γ_3	Γ_4	Γ_5
Γ_1		π'			σ'
Γ_2	π'				σ'
Γ_3				π'	σ'
Γ_4			π'		σ'
Γ_5	σ'	σ'	σ'	σ'	π'

Table 2.3: Polarisation transition selection rules for Kramers and non-Kramers ions in the point group symmetries of C_{4v} and C_{3v} .

of a particular state an indication of the validity or otherwise of these selection rules can be obtained. For magnetic dipole transitions these free-ion selection rules are

$$\Delta S, \Delta L = 0, \qquad \Delta J = 0, \pm 1 \quad \text{but not} \quad 0 \leftrightarrow 0 \tag{2.11}$$

For the electric dipole transitions the situation is more complicated as transitions between pure f^n states are forbidden by parity considerations. Simply stated, the odd parity electric-dipole operator cannot connect two states of the same parity. However, electric dipole transitions are allowed through admixtures of the f^n configuration with configurations of opposite parity. The theory of such transitions is due to Judd [52] and Ofelt [78]. In the Judd-Ofelt theory the admixtures with opposite parity configurations are provided by the odd crystal-field interactions. These interactions do not influence the position of the f^n crystal-field energy levels in first order, and so are not included in the Hamiltonians of equations 2.5–2.7. The odd contributions to the

crystal-field Hamiltonians can be found in the review of Görller-Walrand and Binnemans [36]. Of note is that for centro-symmetric symmetries, such as that for centers in a cubic environment, there are no odd parity contributions to the crystal-field Hamiltonian, and therefore electric dipole transitions remain forbidden. For centers in which odd crystal-field interactions are present, the electric dipole LSJ selection rules are

$$\Delta S = 0, \qquad |\Delta L| \leq 6, \qquad |\Delta J| \leq 6 \tag{2.12}$$

2.4 Zeeman Theory.

The application of an external magnetic field to an ion can be treated as a perturbation on the crystal-field states. The Zeeman interaction is given by

$$H = \mu_{\mathrm{B}} \boldsymbol{B} \cdot (\boldsymbol{L} + 2\boldsymbol{S}) \tag{2.13}$$

where $\boldsymbol{B}$ is the applied magnetic field and μ_{B} is the Bohr magneton $\frac{e\hbar}{2m_e}$.

Within a given multiplet the matrix elements of the Zeeman interaction can be simplified such that an effective Hamiltonian can be given by

$$H = \mu_{\mathrm{B}} g_{\mathrm{L}} \boldsymbol{B} \cdot \boldsymbol{J} \tag{2.14}$$

where g_{L} is known as the Landé g-factor, with a value given algebraically as [6]

$$g_{\mathrm{L}} = 1 + \frac{J(J+1) + S(S+1) - L(L+1)}{2J(J+1)}. \tag{2.15}$$

Therefore only matrix elements of the form $\langle JJ'_z|\boldsymbol{J}|JJ_z\rangle$ need to be considered, with the SL dependence being accounted for by the Landé g-factor. The elements of $\boldsymbol{J_z}$ are diagonal in J_z and hence the parallel Zeeman interaction can be given somewhat trivially as

$$\mu_{\mathrm{B}} B_z g_{\mathrm{L}} \langle SLJJ'_z|J_z|SLJJ_z\rangle = \mu_{\mathrm{B}} g_{\mathrm{L}} B_z J_z \delta_{J_z J'_z} \tag{2.16}$$

where $\delta_{J_z J'_z}$ has a value of unity for $J_z = J'_z$ and zero otherwise. The matrix elements of J_x, J_y can be found by expressing these operators in terms of the ladder operators defined as

$$\begin{aligned} J_+ &= J_x + iJ_y & J_x &= \frac{1}{2}(J_+ + J_-) \\ J_- &= J_x - iJ_y & J_y &= \frac{-i}{2}(J_+ - J_-) \end{aligned} \tag{2.17}$$

and the matrix elements of the ladder operators can be found from the relations

$$\begin{aligned} J_+|J, J_z\rangle &= \sqrt{J(J+1) - J_z(J_z+1)}|J, J_z+1\rangle \\ J_-|J, J_z\rangle &= \sqrt{J(J+1) - J_z(J_z-1)}|J, J_z-1\rangle, \end{aligned} \tag{2.18}$$

The matrix elements of the perpendicular Zeeman interaction, for states of the same LSJ, are therefore

$$\mu_B B_x g_L \langle SLJ, J_z+1|J_x|SLJ, J_z\rangle = \frac{\mu_B B_x g_L}{2}\sqrt{J(J+1)-J_z(J_z+1)}$$
$$\mu_B B_y g_L \langle SLJ, J_z-1|J_y|SLJ, J_z\rangle = \frac{i\mu_B B_y g_L}{2}\sqrt{J(J+1)-J_z(J_z-1)} \qquad (2.19)$$

Forbidden transitions - Kramers ions

Under the influence of an applied magnetic field, a Kramers doublet will undergo a splitting into Zeeman levels. These levels will transform as the subgroup corresponding to the symmetry of the crystal-field combined with the magnetic field. This symmetry will in general depend on the orientation of the applied field with respect to the crystal-field axes. For particular orientations of the magnetic field, selection rules may still exist for transitions between the Zeeman split doublets.

For the C_{4v} center, a field applied along the direction of the principal C_{4v} z-axis will reduce the site symmetry to C_4. The branching of the C_{4v} Kramers ion states is such that the following irreps are assigned to the non-degenerate Zeeman levels

$$\Gamma_6 \rightarrow \gamma_5 + \gamma_6 \qquad \Gamma_7 \rightarrow \gamma_7 + \gamma_8 \qquad (2.20)$$

where the irreps of the C_4 subgroup have been denoted by γ_i. The electric dipole and magnetic dipole operators transform as $\gamma_2(\pi)+\gamma_3(\sigma)+\gamma_4(\sigma)$ and $\gamma_1(\pi)+\gamma_3(\sigma)+\gamma_4(\sigma)$ respectively.

In the particular setup of the Zeeman absorption experiments in this work, the direction of propagation of the light is parallel to the magnetic field. Hence the π-polarised transitions are not able to be observed. From consideration of the C_4 multiplication table for operators transforming as $\gamma_3+\gamma_4$ it is found that the allowed transitions are

$$\begin{aligned} \gamma_5 &\rightarrow \gamma_6+\gamma_8 & \gamma_6 &\rightarrow \gamma_5+\gamma_7 \\ \gamma_7 &\rightarrow \gamma_6+\gamma_8 & \gamma_8 &\rightarrow \gamma_7+\gamma_5 \end{aligned} \qquad (2.21)$$

The implication of these selection rules is that for the C_{4v} centers with the magnetic field parallel to the z-axis, only two of the four possible absorption transitions between a pair of Zeeman split Kramers doublets will be observed.

Similar considerations of C_{3v} centers with a magnetic field applied along the z-axis also reveals that some transitions are forbidden. Specifically, in such a geometry the appropriate subgroup is C_3 and the irrep decompositions will be

$$\Gamma_5 \rightarrow \gamma_4+\gamma_5 \qquad \Gamma_5+\Gamma_6 \rightarrow 2\gamma_6. \qquad (2.22)$$

As σ-polarised transitions between like C_3 irreps are forbidden the allowed transitions are

$$\gamma_4 \rightarrow \gamma_5 + \gamma_6 \qquad \gamma_5 \rightarrow \gamma_4 + \gamma_6 \qquad \gamma_6 \rightarrow \gamma_5 + \gamma_4 \tag{2.23}$$

For all other orientations of the magnetic field, all transitions between the Zeeman split doublets will be allowed, at least from the perspective of the point-group symmetry.

Chapter 3

Experimental

3.1 Crystal growth and preparation.

The CaF_2:RE^{3+} and SrF_2:RE^{3+} single crystals used in the studies reported in this thesis were grown and prepared within the Department of Physics and Astronomy. The majority of samples were grown and prepared by the author, while in a few cases samples previously grown by other members of the department have been employed.

The starting CaF_2 and SrF_2 material consisted of off-cuts of the fluorites supplied by Optovac Inc. To the crushed off-cuts small quantities of REF_3 were added. The dopant concentrations reported are based on the mol% addition of the rare-earth fluoride. Typical concentrations were 0.05%, with some particular samples having dopants concentrations of between 0.15% and 0.01%. The prepared material was placed in graphite crucibles in an Arthur D. Little rf induction furnace, under a vacuum of $\approx 2\times10^{-5}$ torr. The sample was slowly heated over an extended period of several hours to allow time for out-gassing of the starting material. When the appropriate temperature was obtained the crucible was lowered through the hot zone of the furnace at a rate of 4-5 mm per hour, over a range of $\approx$50 mm. Following the lowering of the crucible an automatic arrangement would continuously lower the input rf power of the furnace over a period of $\approx$5 hours. This slow cooling was the only annealing conditions to which the sample was treated. Through this procedure single crystal boules of the rare-earth doped fluorite-type crystals were obtained, with the boule having dimensions of $\approx$30 mm length and 10 mm diameter.

Unoriented samples were prepared from slices cut from the boule using a diamond saw. Surfaces were polished on a succession of emery paper of lowering grit sizes, and a final finish provided by polishing with a wet tin-oxide paste. For the Zeeman infrared absorption and polarised laser spectroscopy experiments oriented samples were required. As a matter of notation, in this thesis when discussing the crystal axes, ⟨ijk⟩ and [ijk] refer to a general and a specific crystallographic direction respectively, while {ijk} will refer to a general crystal plane and (ijk) to a specific crystal plane.

For samples in which the {111} planes of the crystal were required for mounting, the boule was cleaved along two parallel planes. These cleavage planes are known to constitute the {111} planes of the fluorites. Occasionally these cleavage faces provided an indication of several separate but closely aligned crystal domains in the sample. If required the sample would be regrown to obtain a single crystal of satisfactory quality. Samples with oriented (100) and (010) faces were also required. To obtain such an orientation, the boule would be cleaved along two intersecting {111} planes. An appropriate pair of planes intersecting at 109.5^o, with the intersection along a ⟨110⟩ direction were used to define the crystallographic axes. The sample was mounted by these intersecting cleavage faces into a chuck in which a wedge of the appropriate angle had been cut. This chuck was then in turn mounted on the diamond saw to cut the required (100) and (010) surfaces.

3.2 Cryogenics.

For the experiments described in this thesis, cryogenic temperatures and a method of temperature control was required. For the majority of experiments, the cryogenic temperatures were obtained by CTI cryogenics cryodyne model 22C closed cycle helium refrigerator units. Samples were mounted on copper sample holders, which in turn were mounted on the refrigerator cold-finger. To aid thermal contact a thin layer of indium foil was placed between the copper holder and the cold-finger, and also between the mounting surfaces of the sample and the copper holder. Sample temperatures of 12-15 K could be reached with the cryogenic unit that was used for the laser spectroscopy and optical absorption measurements. The unit used for the infrared absorption measurements was able to reach a slightly lower temperature of ≈10 K.

For some of the polarised fluorescence experiments temperature control between 15 K and 270 K was required. This was provided by a Department built temperature controller, which provided heating to the cold-finger via a pair of attached resistors. Temperature measurements were made via a diode temperature sensor that was also attached to the cold-finger of the cryostat. Temperature stability of better than ±2.5 K could be obtained.

On occasions temperatures lower than those achievable with the closed cycle refrigeration systems were required. For such measurements a Department built liquid helium cryostat was employed. This cryostat possesses a liquid nitrogen cooled heat-shield and a 5 litre capacity helium reservoir, in which the sample was immersed. After filling of the helium reservoir, the helium chamber was pumped by a high capacity rotary pump which further cooled the helium past the super-fluid point, providing sample

temperatures of $\approx$2 K.

3.3 Infrared and Zeeman infrared absorption.

Infrared absorption was performed using a Bio-Rad FTS-40 Fourier transform spectrometer. For the absorption measurements of Dy^{3+} a quartz beam-splitter was used in conjunction with a quartz-halogen source and liquid nitrogen cooled Indium Antimonide detector. With this combination of optical elements transmission spectra could be obtained over an approximate region of 3000 cm^{-1} to 9000 cm^{-1}. The spectrometer has a maximum resolution of 0.1 cm^{-1}, although a large beam-splitter interference ripple is present in the resulting spectra at this resolution. For the Zeeman infrared absorption experiments, spectra at a resolution of 0.25 cm^{-1} were more commonly measured, to reduce the the time taken to record the spectrum at each field strength. At a resolution of 0.25 cm^{-1} the beam-splitter interference is greatly reduced through aliasing effects.

For the Zeeman infrared measurements, samples were mounted in a Department built magnet cryostat, which in turn was mounted in a shielded compartment of the Bio-Rad spectrometer. The magnet cryostat incorporated on Oxford Instruments 4-Tesla superconducting magnet, which was operated in persistent current mode. The magnet was energised by a British Oxygen Company DPS 60-72/2A power supply. The magnet was immersed in liquid helium, surrounded by a liquid nitrogen jacket. However the sample itself was not immersed in the helium, but housed, under vacuum, in a tube in the bore of the magnet. Sample cooling was provided by thermal contact between the sample holder and the helium reservoir, resulting in an estimated sample temperature of 10 K. The magnet is not of a split solenoid configuration, constraining the experimental geometry to one in which the infrared radiation propagated down the bore of the magnet. With such an arrangement, with the propagation direction parallel to the magnetic field, π (or π') polarised transitions cannot be observed, as the electric (or magnetic) field of the propagating radiation will always be perpendicular to the applied magnetic field.

For infrared absorption measurements without an applied magnetic field, samples were mounted in a CTI closed cycle refrigeration unit.

Because some absorption features of the Dy^{3+} centers are quite weak, particularly in the higher field Zeeman spectra, it was desirable to reduce or remove the beam-splitter interference from the spectra.

To accomplish this aim, a filtering procedure was written, employing the mathematical processing package Matlab. The measured spectrum was first Fourier transformed, effectively reconstructing the interferogram. The raw interferogram available from the Bio-Rad spectrometer was not used, as this would have then eliminated the apodization procedures that are employed by the spectrometer software. In this Fourier transformed spectra an anomalous peak associated with the beam splitter interference was removed by setting the Fourier coefficients in this narrow region to zero. The filtered spectrum found from the inverse Fourier transform of this altered interferogram is considerably improved, allowing a much clearer examination of small absorption features. No adverse effects such as line-broadening of the absorption transitions were observed following such a procedure, and it is concluded that that any distortion introduced into the spectra by removal of the very narrow region of the Fourier spectrum is negligible. An example of the improvement in the absorption spectrum obtained from such filtering is shown in Figure 3.1.

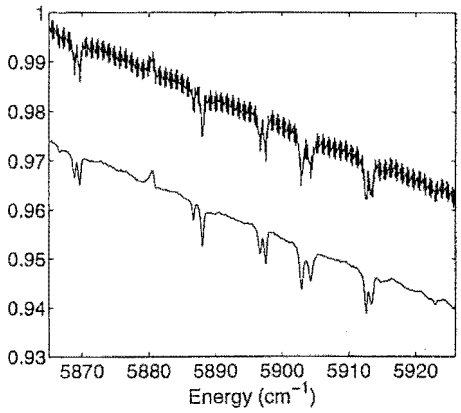

Figure 3.1: An example of weak absorption transitions before and after application of the spectral filtering.

3.4 Optical absorption.

For optical absorption measurements a sample boule would be mounted in the closed cycle cryostat, and cooled to 15 K. Typically a 100 watt tungsten-iodide lamp powered by a regulated power supply was employed as the light source. For later experiments, an alternative power supply providing 20 watts to the lamp was used as this resulted in better stability in the light output. The spectra were obtained with a Spex model 1700, 0.75 m monochromator. The detection was provided by the combination of an EMI-9659 QA photomultiplier tube and Keithley Instruments model 610 electrometer The photomultiplier tube was thermo-electrically cooled to -25°C. The signal from the Keithley electrometer was recorded via a voltage to frequency converter and a Department built integration counter, interfaced to a computer control and data acquisition system.

3.5 Laser spectroscopy.

Tunable laser radiation for the laser spectroscopy experiments was provided by an argon ion laser pumping one of two dye lasers.

Depending on the period in which the work was carried out, the argon ion laser was either a Spectra-Physics model 2045E 30 watt laser, or a Spectra-Physics model 2080-25S with "BeamLok". The spectroscopy of Dy^{3+} required tunable lasing in the region of 460 nm–480 nm. This was obtained from a Spectra-Physics model 375B dye laser fitted with an intra-cavity birefringent filter, operated with Coumarin 460 (C460) dye. Up to 2.5 W of ultraviolet pumping was provided by the argon laser. Although additional UV power was (often) available, it was found that stable lasing of the C460 dye could not be obtained with higher pump powers. The C460 dye becomes unstable with use, and degrades over a period of approximately 20 hours of UV pumping. During the later stages of this period the lasing of the dye is quite erratic, and the lasing spectral range is significantly reduced from that obtainable from a fresh batch of dye. The dye was circulated with a Spectra-Physics model 376 dye circulator. An additional external dye cooling heat exchanger that was added specifically for use with the C460 dye was found to offer improvements on the lasing stability. Typical lasing powers of the blue C460 dye used for the spectroscopy experiments were 5-15 mW.

For experiments involving the pumping of the $^1D_2$ multiplet of Pr^{3+} or $^5D_0$ of Eu^{3+} the tunable lasing was obtained with either the above mentioned dye laser operated with Rhodamine 590 (R590) dye, or with the combination of a Coherent model 590 dye laser and 591 dye circulator with R590 dye. The pumping of these dye lasers was provided by the 488-514 nm output of the argon laser.

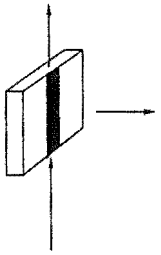

The samples were mounted in a cryostat and illuminated by the laser which was projected to a vertical propagation direction. The fluorescence was collected in the orthogonal direction, with the vertical image produced by the region of laser excitation collimated and then refocused onto the vertical slits of the spectrometer.

Three spectrometers were employed in this work, each performing a separate function. A low resolution Bausch and Lomb 0.25 m spectrometer was used for obtaining fluorescence detected absorption, or "broad-band excitation" spectra. For such spectra the Bausch and Lomb was used to monitor a broad $10-20$ nm spectral region while the laser frequency was scanned over an appropriate range.

Because of the broad bandpass of the Bausch and Lomb spectrometer such spectra

are not generally site selective, although with monitoring of appropriate wavelengths fluorescence from a particular rare-earth can usually achieved. Not all absorption transitions will necessarily give rise to a corresponding broadband excitation transition, as some centers will decay non-radiatively and hence go undetected in an excitation spectrum. The Bausch and Lomb was most commonly used in conjunction with the EMI-9659 QA photomultiplier tube and Keithley electrometer. Such a setup also enabled the laser to be manually tuned onto a specific absorption transition, as required for the fluorescence measurements.

A Spex 1403 double monochromator was employed for the majority of the fluorescence studies. While this spectrometer is capable of a resolution of $\sim$0.1 cm^{-1}, considerations of fluorescence throughput meant that it was more commonly operated with slit widths that provided a resolution of 0.5-1.0 cm^{-1}. An RCA-C31034 photomultiplier tube, thermo-electrically cooled to -25°C was used in conjunction with this spectrometer. The PMT output was monitored by photon counting equipment. For earlier work the photon counting was performed by a Princeton Applied Research model 1112 photon counter, while after an upgrade of the computerised data acquisition systems in the laser laboratory this function was carried out by a Department built photon-counting system.

The Spex 1403 was also used for obtaining "narrow-band excitation" spectra. This is essentially an analog of the broad-band excitation described above, with the exception that the the spectrometer was tuned to monitor a specific fluorescence transition. The excitation spectrum then only includes those absorption transitions giving rise to this specific fluorescence, and is therefore site-selective.

The Spex 1403 monochromator is driven by a Czerny-Turner configuration which limits the available scanning range to 11000 cm^{-1} to 33000 cm^{-1}. For fluorescence below 11000 cm^{-1} a Spex 1700 single monochromator was used, with a liquid nitrogen cooled RCA-7102 photomultiplier tube providing the infrared detection. This infrared photomultiplier tube was operated in conjunction with the Keithley electrometer, rather than photon-counting.

3.6 Polarised fluorescence.

As the CaF_2 structure is cubic, centers with a specific axis, such as the C_{4v} centers, can exist is several orientations. The C_{4v} center has an interstitial fluorine–rare-earth axis parallel to any of the orthogonal [100], [010] or [001] directions. Therefore, despite polarisation dependent selection rules, the identification of the energy level irreps is

not possible in absorption as the crystal will appear isotropic. However fluorescence following polarised absorption does reveal polarisation behaviour. This polarisation behaviour will be explained by means of an example.

As a matter of notation, a particular polarisation configuration will be described by two letters, AB, with A$\in${Y,Z} and B$\in${X,Y}. The first letter is taken to represent the polarisation of the laser, while the second represents the fluorescence polarisation. For all experiments discussed here, the laser direction of propagation is taken as the X-axis, with the orthogonal direction in which the fluorescence is monitored defining the Z-axis. A crystal with $\langle 100 \rangle$ axes coinciding with the lab axes defined above will be described as a $\langle 100 \rangle$ oriented sample.

For a $\langle 100 \rangle$ oriented sample, the different orientations of the C_{4v} centers are shown schematically in Figure 3.2, along with the experimental geometry. For an excitation transition which proceeds via a σ-polarised transition moment, with the laser polarised in the Y direction, then only centers oriented with their principal axes along the X and Z directions will be excited. Referring to Figure 3.2, these centers are represented by those labelled (A) and (C). If the monitored fluorescence is, say, a π-polarised emission transition, then for the orthogonal direction in which the the fluorescence is collected, center (C) will not be observed. The observed fluorescence will therefore originate from the (A)-oriented centers, and will be polarised in the X-direction.

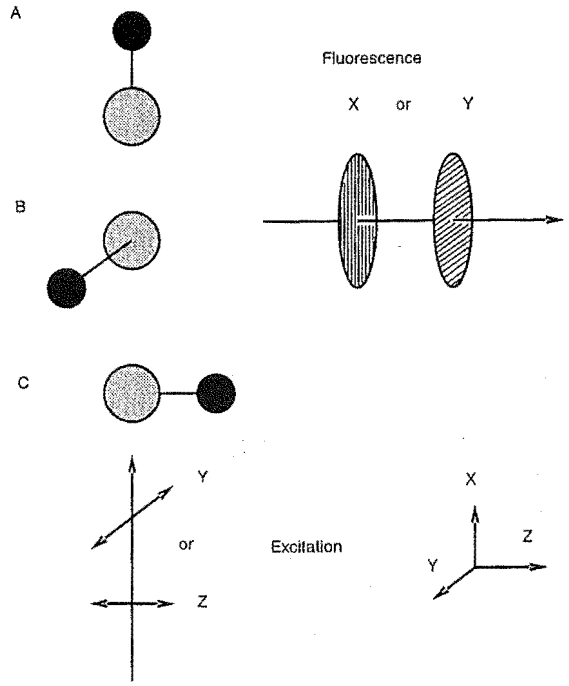

Figure 3.2: A schematic representation of the three orthogonal orientations of the C_{4v} center principal axes, and the experimental geometry employed for polarised fluorescence measurements.

So far these considerations are based solely on the geometrical arrangement of the fluorescence measurements, including the sample orientation. Considerations of the transition selection rules presented on page 16 will now be added to the discussion. For non-Kramers ions in C_{4v} symmetry, transitions involving a Γ_5 state may proceed

Pump	Decay	YX:YY:ZX
$\Gamma_{6,7} \rightarrow \Gamma_{6,7}$	$\Gamma_{6,7} \rightarrow \Gamma_{6,7}$	arbitrary
	$\Gamma_{6,7} \rightarrow \Gamma_{7,6}$	arbitrary
$\Gamma_{6,7} \rightarrow \Gamma_{7,6}$	$\Gamma_{6,7} \rightarrow \Gamma_{6,7}$	arbitrary
	$\Gamma_{6,7} \rightarrow \Gamma_{7,6}$	1:2:1

Table 3.1: Expected polarisation ratios for possible excitation and fluorescence transitions in a $\langle 100 \rangle$ oriented sample for Kramers ions in a C_{4v} center. Only ratios for purely electric dipole transitions are given.

Pump	Decay	YX:YY:ZX
$\Gamma_i \rightarrow \Gamma_i$	$\Gamma_i \rightarrow \Gamma_i$	0:1:0
	$\Gamma_i \leftrightarrow \Gamma_5$ $(\Gamma_5 \not\rightarrow \Gamma_5)$	1:0:1
$\Gamma_i \leftrightarrow \Gamma_5$	$\Gamma_i \rightarrow \Gamma_i$	1:0:1
$(\Gamma_5 \leftrightarrow \Gamma_5)$	$\Gamma_i \leftrightarrow \Gamma_5$ $(\Gamma_5 \not\rightarrow \Gamma_5)$	1:2:1

Table 3.2: Expected polarisation ratios for possible excitation and fluorescence transitions in a $\langle 100 \rangle$ oriented sample for non-Kramers ions in a C_{4v} center. Only ratios for purely electric dipole transitions are given. The indices i are taken such that $i \in \{1, \cdots, 5\}$

by both electric- and magnetic dipole processes. In practice it is usually found that a transition will be dominated by the electric dipole processes. For Kramers ions in C_{4v} symmetry any transition between states of like irreps will be allowed in both σ- and π-polarisations. In such cases the relative intensities of the polarised fluorescence are usually considered arbitrary, in that they depend on the relative magnitudes of unknown transition moments. The polarisation behaviour can be further obscured by the inclusion of magnetic dipole transitions moments.

The expected polarisation behaviour of transitions for the C_{4v} centers in $\langle 100 \rangle$ oriented samples is summarised in Tables 3.1 and 3.2. As shall be shown in the discussions of the SrF_2:Dy^{3+} and CaF_2:Dy^{3+} C_{4v} center fluorescence, a more detailed examination of the "arbitrary" ratios enables information on the irreps of states to be retrieved from the degraded Kramers ion polarised intensities that are encountered.

For C_{3v} centers the principal axes are oriented along any of the $\langle 111 \rangle$ directions. In a $\langle 100 \rangle$ oriented sample all C_{3v} centers will therefore be equally inclined to the laser propagation and monitored fluorescence directions, and no polarisation behaviour will be observed. For a sample oriented with a $\langle 111 \rangle$ axis along the fluorescence direction some polarisation behaviour will be displayed, as described by Cockroft [21].

Two methods were employed to observe the polarisation behaviour of transitions. The first, and simplest, involved orienting the laser polarisation using a Spectra Physics model 310A polarisation rotator. The laser would be polarised in either the Y or Z direction. The collected fluorescence was filtered through polarising sheets, oriented for either the X or Y polarisation. This enabled polarisation ratios of all four configurations (YX, YY, ZX, ZY) to be obtained. However, for observing the polarisation behaviour of Dy^{3+} under blue excitation it was found that the relatively small polarisation anisotropy, together with the instability of the Coumarin-460 dye, often led to ratios being obtained with rather limited precision.

For some purposes, this lack of precision was found to be unsatisfactory, and in such cases a photoelastic modulator (PEM) was employed. This enabled simultaneous recording of YY and YX (or ZX and ZY) polarised spectra. A Hinds International model PEM-IF4 photo-elastic modulator, operating at 50 kHz, was used for these experiments.

The procedure for these measurements was to place the PEM between the sample and spectrometer, with its oscillation axis at an angle of 45°, followed by a horizontal linear polariser. The DC signal and the AC signal at twice the PEM frequency, were simultaneously recorded for a fluorescence spectrum. The AC signal was measured by a Stanford Research Systems SR830 lock-in amplifier. The YY and YX spectra can be deduced from the AC and DC signal provided the different gain of the AC and DC recording electronics can be calibrated. To achieve this calibration, a subsequent scan would be made in identical circumstances, with the exception of an additional vertical linear polariser placed before the PEM. This would therefore produce a spectra of known polarisation (vertical only) and the AC/DC calibration could be made. This repetition of the scan enables any non-linearities in the calibration curve to be taken into account, as a calibration is obtained for each transition frequency and for an intensity relevant for that transition. As the PEM oscillates at 50 kHz any laser intensity fluctuations or frequency drift slower than this will not affect the results.

Although the YX:YY and ZX:ZY polarisation ratios can be obtained by the above procedure, intensity ratios involving two different laser polarisations cannot be established. For this reason the PEM was primarily used to establish the presence of 1:1 intensity ratios. For such a measurement no calibration of the AC and DC signals is required, as for a 1:1 intensity ratio the AC signal will be zero. Therefore a zero AC signal directly infers the equivalence of the two polarised intensities.

While the theory of the photelastic modulator has been discussed in various references [55, 49], it is considered worthwhile to discuss this theory for the specific geometrical arrangement used here, and also to clarify several mis-prints and errors present in these papers.

3.6.1 The Photoelastic modulator.

Two coordinate frames of reference are used in this discussion, a laboratory frame (X_l, Y_l, Z_l) and a reference frame for the PEM oscillating element (X_p, Y_p, Z_p), as shown in Figure 3.3. The PEM is taken to be oscillating along the Y_p axis.

A linearly polarised beam travelling in the Z_l direction, and polarised along the X_l-axis, has an amplitude of oscillation in the laboratory coordinates given by (using Jones

vector notation [42])

$$\boldsymbol{A}_l = A_{\mathrm{x}} e^{i\omega t} \begin{pmatrix} 1 \\ 0 \end{pmatrix} \tag{3.1}$$

Transforming the coordinates into the frame of reference of the PEM by a rotation of 45^o gives the amplitude as

$$\boldsymbol{A}_p = A_{\mathrm{x}} e^{i\omega t}/\sqrt{2} \begin{pmatrix} 1 \\ 1 \end{pmatrix}. \tag{3.2}$$

In this frame only the Y_{p} component of the amplitude is affected by the PEM compression and expansion. Specifically, the Y_{p} component gains an extra phase shift due to the instantaneous state of compression of the PEM optical element. This extra phase shift ϕ_{p} leaves the amplitude of the wave, in the PEM frame of reference, as

$$\boldsymbol{A}_p = A_{\mathrm{x}} e^{i\omega t}/\sqrt{2} \begin{pmatrix} 1 \\ e^{i\phi_{\mathrm{p}}} \end{pmatrix}. \tag{3.3}$$

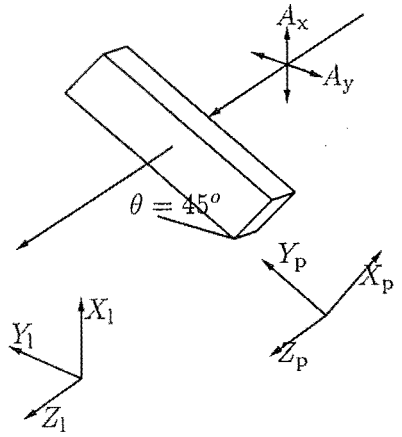

Figure 3.3: The orientation of the photoelastic modulator and the laboratory and PEM frames of reference discussed in the text.

The phase shift is itself sinusoidal in time, oscillating at the bar frequency ω_{p}, and will be defined as

$$\phi_{\mathrm{p}} = \chi \sin(\omega_{\mathrm{p}} t) \tag{3.4}$$

where χ is the peak retardation. Transforming the coordinates back into the laboratory frame of reference gives the amplitude of the polarised wave after passing through the PEM as

$$\boldsymbol{A}_l = A_{\mathrm{x}} e^{i\omega t}/2 \begin{pmatrix} 1 + e^{i\phi_{\mathrm{p}}} \\ -1 + e^{i\phi_{\mathrm{p}}} \end{pmatrix}, \tag{3.5}$$

By extension of this result the amplitude of an arbitrary linearly polarised beam in the laboratory frame, after passing through the PEM, is given in terms of the amplitudes of the input light $(A_{\mathrm{x}}, A_{\mathrm{y}})$ as

$$\boldsymbol{A}_l = A_{\mathrm{x}} e^{i\omega t}/2 \begin{pmatrix} 1 + e^{i\phi_{\mathrm{p}}} \\ -1 + e^{i\phi_{\mathrm{p}}} \end{pmatrix} + A_{\mathrm{y}} e^{i\omega t}/2 \begin{pmatrix} -1 + e^{i\phi_{\mathrm{p}}} \\ 1 + e^{i\phi_{\mathrm{p}}} \end{pmatrix} \tag{3.6}$$

Passing the resultant light through a linear polariser oriented to pass only Y_l polarised light, the resultant intensity is given by

$$I_l = \frac{I_{\mathrm{x}}}{2}(1 - \cos(\phi_{\mathrm{p}})) + \frac{I_{\mathrm{y}}}{2}(1 + \cos(\phi_{\mathrm{p}})) \tag{3.7}$$

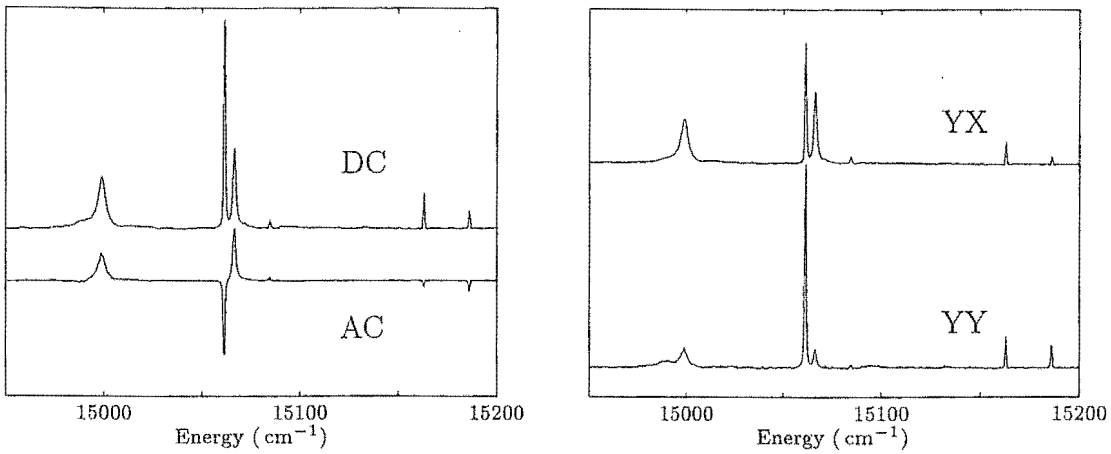

Figure 3.4: An example of polarised spectra obtained with the photo-elastic modulator. The AC and DC signals are shown together with the deduced polarised spectra.

The DC and AC components of the intensity signal can be evaluated from equation 3.7. The AC component at twice the PEM frequency ($2\omega_p$) is required as the PEM passes through a position of zero compression twice each cycle. These components of the intensity are, in terms of the Bessel functions [43] of the peak retardation:

$$\langle I_l \rangle = \frac{I_x}{2}(1 - J_0(\chi)) + \frac{I_y}{2}(1 + J_0(\chi)) \tag{3.8}$$

$$I_l|_{2\omega_p} = -I_x J_2(\chi) + I_y J_2(\chi) \tag{3.9}$$

It can be seen from equations 3.8-3.9 that with insertion of a pre-polariser in the vertical orientation, which sets $I_y = 0$, a clear relation between the AC and DC components is obtained. Specifically

$$\frac{\langle I_l \rangle}{I_l|_{2\omega_p}} = \frac{-1 + J_0(\chi)}{J_2(\chi)}. \tag{3.10}$$

Comparison of this value with that obtained experimentally establishes a calibration factor for the relative AC and DC intensities. With this calibration, equations 3.8-3.9 can be used to obtain the initial intensities I_x and I_y. Figure 3.4 shows an example of the results obtained from the photoelastic modulator.

3.7 Fluorescence lifetimes.

For measuring the fluorescence lifetimes of states, selective excitation was provided by a Photochemical Research Associates model LN107 dye laser pumped by a model LN1000 pulsed nitrogen laser. Either Coumarin 460 or Rhodamine 590 dyes were used, depending on the particular states to be excited.

The decay transients were detected and recorded using the Spex 1700 monochromator and EMI-9659 QA photomultiplier in conjunction with a Hitachi VC-6275 digital storage oscilloscope. The recorded transients were fitted to an appropriate exponential function with routines written to take advantage of non-linear fitting procedures incorporated into the Matlab package.

Chapter 4

Spectroscopy of $SrF_2:Dy^{3+}$.

4.1 Introduction.

Previous work.

The spectroscopy of the $SrF_2:Dy^{3+}$ system has not been previously investigated in great detail and there appears to be no studies reported in the literature that have used laser selective excitation. The tetragonal centers in particular seem to have attracted the least discussion and analysis. Al'tshuler, Eremin, Luks and Stolov [3] have reported energy level data and analysis of cubic and rhombic centers produced when the system is co-doped with Na^+ cations. The tetragonal centers of $CaF_2:Dy^{3+}$ are investigated in a paper by Antipin, Davydova, Eremin, Luks and Stolov [5], who note that a center possessing similar Stark structure in the luminescence is also present in $SrF_2:Dy^{3+}$ and that the spectroscopy of this center is complicated by overlapping trigonal emission. While there is some EPR data on the $CaF_2:Dy^{3+}$ centers [8], there appears to be no EPR work on $SrF_2:Dy^{3+}$ in the literature. Luks, Livanova and Stolov [65] have discussed the experimentally determined energy level structure of the lower multiplets for the oxygen centers of $SrF_2:Dy^{3+}$ and $CaF_2:Dy^{3+}$, while Eremin, Luks and Stolov [34] have presented the most information to date on the $SrF_2:Dy^{3+}$ fluorine compensated trigonal center, identifying a total of 16 energy levels. A crystal-field analysis based on a subset of 10 of these levels has also been presented by Eremin et.al. Their analysis leads them to state that no EPR of the C_{3v} center would be observable because of a calculated $g_\perp = 0$. They also note the observation of some vibronic transitions associated with this center. The SrF_2 tetragonal center is not discussed except in the context that emission of this center partially overlaps that of the trigonal center. Separation of these overlapping spectra was aided by comparison with the fluorescence of $BaF_2:Dy^{3+}$, for which only the trigonal center is observed.

In summary, for the $SrF_2:Dy^{3+}$ system the tetragonal centers have not been addressed in the literature, and the fluorine compensated trigonal centers have only a small amount of data and a somewhat limited crystal-field calculation reported.

This work.

The multiplets of Dy^{3+} lying below 25 000 cm^{-1} are shown in Fig. 4.1 at the calculated free-ion energies. These energy levels have been calculated from the free-ion parameters for $LaCl_3$:Dy^{3+} given by Carnell [12] and the Slater and spin-orbit parameters found from the C_{4v} SrF_2:Dy^{3+} crystal-field calculation of Section 4.3.3. These free-ion energy levels are insensitive to the particular host and therefore serve as a general description of the Dy^{3+} multiplet barycenters. The dominant LSJ compositions of the free-ion wavefunctions are tabulated in Table 4.1.

The majority of the multiplets are not accessible by optical absorption, with 12 multiplets below 14000 cm^{-1} and the next highest multiplet at approximately 21000 cm^{-1}. This work has focused on the laser excitation of the $^4F_{9/2}$ multiplet at $\approx$21000 cm^{-1}, using the resulting fluorescence to determine the energy levels of the lower lying multiplets. Because nine of the twelve lower multiplets are greater than 9000 cm^{-1} from the emitting $^4F_{9/2}$ levels, it has been possible to obtain fluorescence data for a large number of levels with visible and near infrared photomultiplier detection. Infrared absorption of several of the lower multiplets has also been measured.

For the SrF_2:0.05%Dy^{3+} system two dominant centers have been characterised. The first of these is identified as a tetragonal C_{4v} center analogous to that observed for SrF_2:RE^{3+} samples where the rare-earth is from the early part of the lanthanide series. The second center is assigned as a trigonal C_{3v} J center corresponding to that present in SrF_2:Er^{3+}[21]. This trigonal center does not correspond to the trigonal B center of SrF_2:Ho^{3+}[72]. The optical absorption of the $^4F_{9/2}$ multiplet suggests that both the tetragonal and trigonal centers are present in SrF_2:Dy^{3+} in approximately equal concentrations, assuming that there is not a dramatic difference in the oscillator strengths of these centers.

Following identification of energy levels of the two centers the irreducible representation labels of these levels have been determined through crystal-field calculations, and where possible with reference to polarised fluorescence data. The crystal-field analysis allows correlation of the C_{3v} center with that observed in SrF_2:Er^{3+}, thereby confirming the trigonal center reported for SrF_2:Ho^{3+} to be anomalous.

Zeeman infrared measurements have enabled an independent check on the accuracy of the wavefunctions that are obtained from the crystal-field calculations. The Zeeman data supports both the symmetry assignment of the centers, and the wavefunctions that are determined from the crystal-field calculation.

An often overlooked ambiguity in the crystal-field parameters, and in the corresponding

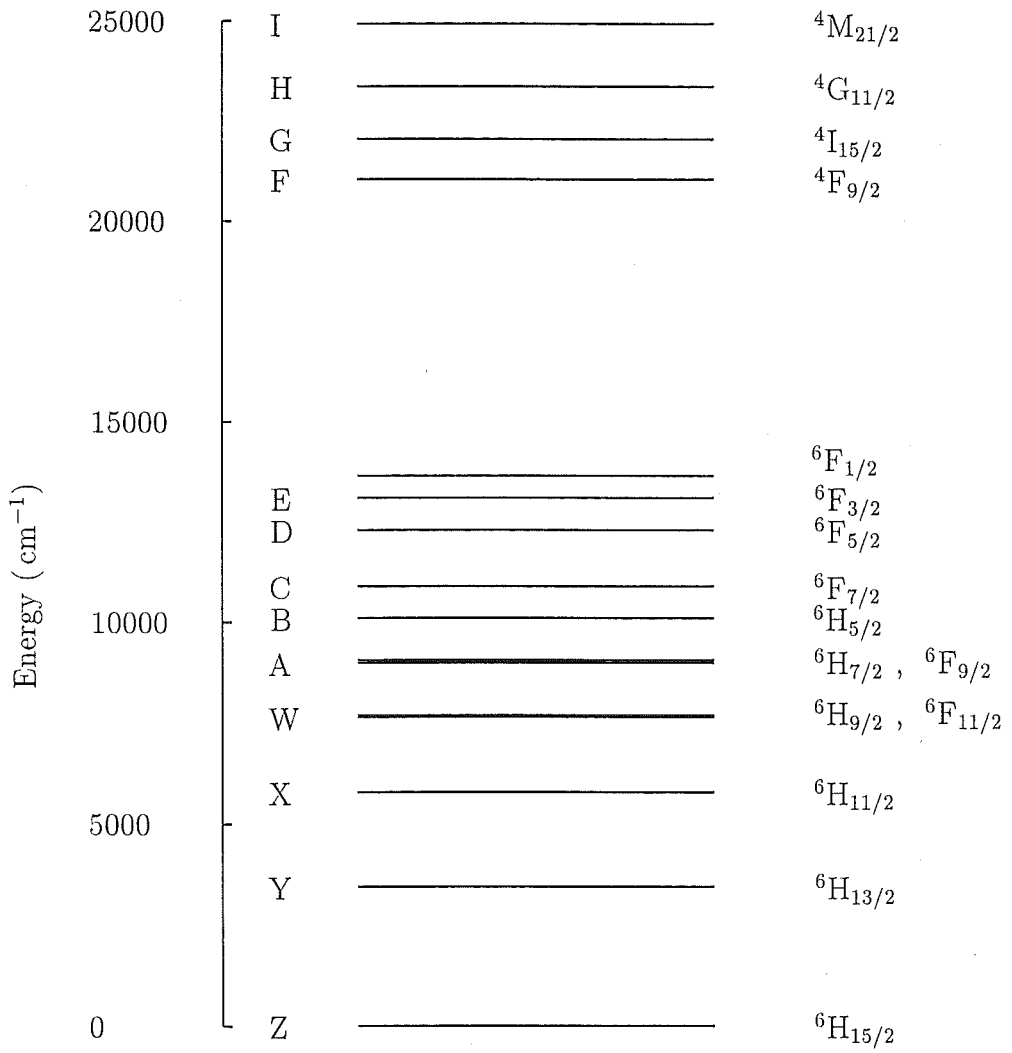

Figure 4.1: The free-ion energy levels of Dy^{3+}. Both the $^{2S+1}L_J$ and alphabetical multiplet labels are used in this thesis.

wavefunctions, is discussed in the context of Zeeman infrared absorption experiments. This ambiguity stems from the use of a Hamiltonian which does not uniquely specify the coordinate basis. It has been attempted, with some limited success, to determine the appropriate basis for the crystal-field parameters and wavefunctions through consideration of the expected experimental differences in the Zeeman infrared absorption for the two possible bases.

4.2 Optical absorption, laser excitation.

The optical absorption of the $^4F_{9/2}$ multiplet of a 3 cm long SrF_2:0.1%Dy^{3+} boule, at a sample temperature of 15 K, is presented in Figure 4.2. The absorption to this

Multiplet Composition		Barycenter Energy (cm^{-1})
0.97 $\|^6H_{15/2}\rangle$	- 0.21 $\|^4I_{15/2}\rangle^3$	0
-0.98 $\|^6H_{13/2}\rangle$	+ 0.15 $\|^4I_{13/2}\rangle^3$	3460
0.96 $\|^6H_{11/2}\rangle$	+ 0.17 $\|^6F_{11/2}\rangle$	5790
-0.97 $\|^6H_{9/2}\rangle$	- 0.17 $\|^4G_{9/2}\rangle^4$	7645
0.96 $\|^6F_{11/2}\rangle$	- 0.19 $\|^6H_{11/2}\rangle$	7665
-0.94 $\|^6F_{9/2}\rangle$	- 0.26 $\|^4F_{9/2}\rangle^3$	8985
-0.96 $\|^6H_{7/2}\rangle$	- 0.20 $\|^4G_{7/2}\rangle^4$	9060
-0.96 $\|^6H_{5/2}\rangle$	- 0.21 $\|^4G_{5/2}\rangle^4$	10113
0.96 $\|^6F_{7/2}\rangle$	+ 0.21 $\|^4F_{7/2}\rangle^3$	10900
0.96 $\|^6F_{5/2}\rangle$	+ 0.14 $\|^4F_{5/2}\rangle^3$	12305
0.95 $\|^6F_{3/2}\rangle$	- 0.18 $\|^4D_{3/2}\rangle^2$	13105
0.96 $\|^6F_{1/2}\rangle$	- 0.19 $\|^4D_{1/2}\rangle^2$	13650
0.67 $\|^4F_{9/2}\rangle^3$	- 0.32 $\|^4F_{9/2}\rangle^1$	21040
0.67 $\|^4I_{15/2}\rangle^3$	+ 0.34 $\|^4K_{15/2}\rangle^1$	21965

Table 4.1: Free-ion multiplet energies and composition for Dy^{3+}, based on free ion parameters of Carnell et al. [12] and the Slater and spin-orbit parameters of the SrF_2:Dy^{3+} C_{4v} center. The superscript labels in the decomposition distinguishes the LSJ multiplets with different LS term parentage.

multiplet is quite weak (less than 2% absorption for this sample), which necessitated the use of a higher concentration sample for the absorption measurements than that used for the majority of the laser selective excitation measurements. Also shown in Figure 4.2 is the broadband excitation spectrum obtained while monitoring fluorescence at 665 nm with a bandwidth of ≈10 nm (200 cm^{-1}), which corresponds to $^4F_{9/2} \rightarrow {}^6H_{11/2}$ fluorescence transitions. The excitation spectrum was also obtained at 15 K, but with a lower concentration 0.05%Dy^{3+} sample. Laser excitation into this multiplet was the predominant source of excitation for the fluorescence measurements of SrF_2:Dy^{3+} which are discussed in the following sections. All the transitions seen in absorption are likewise seen in the broadband excitation spectrum, which rules out the presence of centers which decay by non-radiative means. Such cross relaxation quenching of excitation has been observed in the CaF_2:Sm^{3+} by Wells [103] and also in this work for CaF_2:Dy^{3+} (Chapter 5). As will be discussed more fully in the chapter on CaF_2:Dy^{3+} clusters, any centers involving more than a single Dy^{3+} ion will be expected to decay rapidly and non-radiatively by any of a number of available cross-relaxation pathways. It can therefore be inferred that all the transitions observed in the absorption and

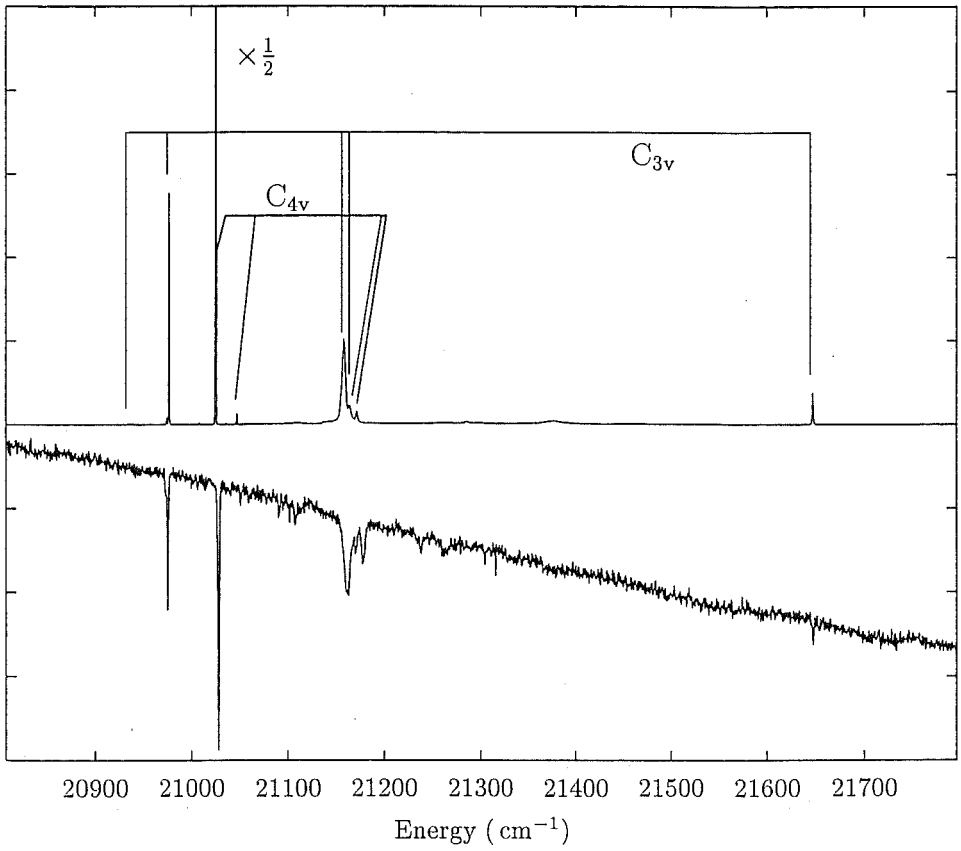

Figure 4.2: 15 K absorption spectrum of the $^4F_{9/2}$ multiplet of SrF_2:0.1%Dy^{3+} and the corresponding broadband excitation spectrum of SrF_2:0.05%Dy^{3+}.

broadband excitation spectra of Figure 4.2 are likely to belong to single ion centers. Also apparent from the spectra of Figure 4.2 is that broadband excitation is giving a true measure of the absorption strength, rather than being weighted by the relative emission strengths of the different centers. This is expected given the energy gap of $\approx 7000\,cm^{-1}$ from $^4F_{9/2}$ to the next lowest multiplet $^6F_{1/2}$. That is, all ions excited by absorption of the laser will decay radiatively. This is true despite a stronger coupling of the C_{3v} center to lattice phonons, as revealed by narrowband excitation spectra and further discussed in Section 4.4.

The absorption spectrum of $^4I_{15/2}$ is shown in Figure 4.3. In contrast to the weak absorption of $^4F_{9/2}$, the higher energy multiplet of $^4I_{15/2}$ possesses an absorption strength approximately ten times larger. However, this multiplet was generally not used for the laser excitation and fluorescence studies because of the lack of availability of a stable CW laser dye that could reach the higher energies of this multiplet. The $^4I_{15/2}$ multiplet was however measured in excitation with the pulsed dye laser which was pumped by a N_2 laser. For this excitation spectrum a boxcar integrator provided an observation window for the broadband fluorescence, while the laser wavelength was

scanned. Because of the weak intensities observed in fluorescence when observing any one particular transition, and the low pulse energy of the pulsed dye laser, it was found that selective excitation was not feasible for the $^4I_{15/2}$ multiplet. However, some partially center-selective excitation was achieved through exploitation of different lifetimes of the two centers. By setting the boxcar window to a short delay time after the excitation pulse it is possible to gain a relative increase in the broadband signal from the center with the shorter lifetime. Likewise, by increasing the window delay time, the relative excitation intensity of the center with the longer lifetime will be increased. A grouping of transitions was therefore able to be achieved. Identification with either of the two centers discussed above was made through obtaining a fluorescence spectrum while exciting the more intense transition shown in Figure 4.3. This fluorescence spectrum was quite noisy and of little value other than to allow a correlation with the fluorescence observed with CW excitation of the $^4F_{9/2}$ multiplet.

The infrared absorption obtained for the $^6H_{13/2}$ and $^6H_{11/2}$ multiplets, and the W manifold which consists of the mixed $^6H_{9/2}$, $^6F_{11/2}$ multiplets, is presented in Figures 4.4-4.6. Absorption transitions have been assigned from correlation with the energy levels obtained from the laser selective fluorescence. Several of these absorption transitions were investigated with Zeeman spectroscopy, as will be discussed in Section 4.5.3

The multitude of unlabelled transitions in the $^6H_{13/2}$ absorption spectrum are due to absorption of atmospheric water vapour. The spectrum was obtained after significant purging of the spectrometer with N_2 gas, which reduces this atmospheric absorption but cannot totally eliminate it.

All the infrared absorption spectra presented here have been processed to remove the beam-splitter interference, as described in Section 3.3.

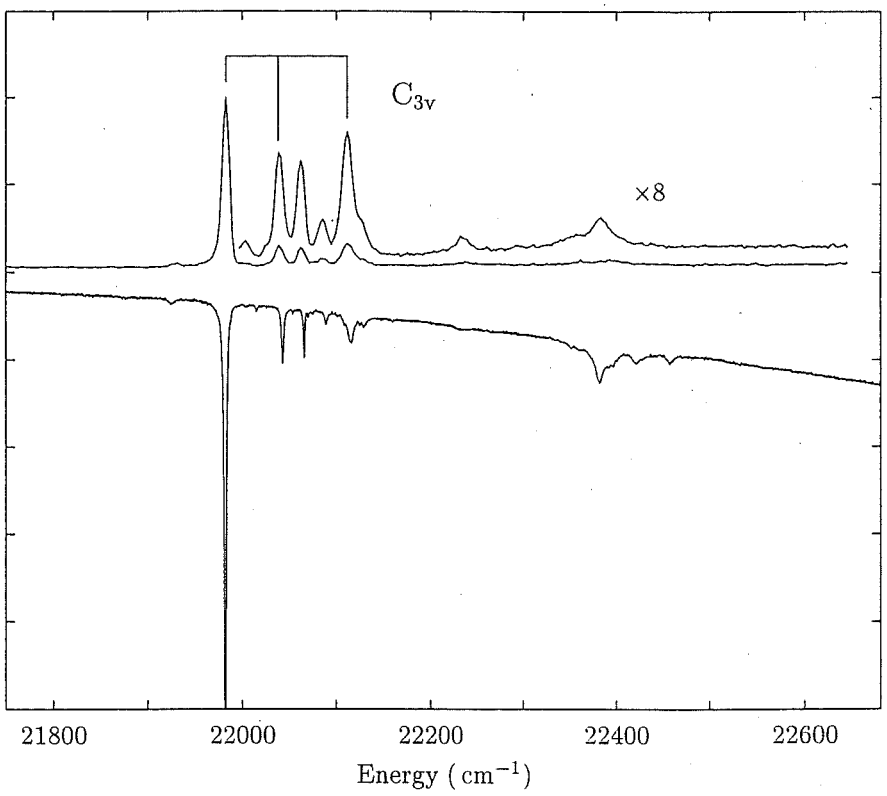

Figure 4.3: 15 K absorption spectrum of the $^4I_{15/2}$ multiplet of SrF_2:0.1%Dy^{3+} and the corresponding broadband pulsed excitation spectrum of SrF_2:0.05%Dy^{3+}.

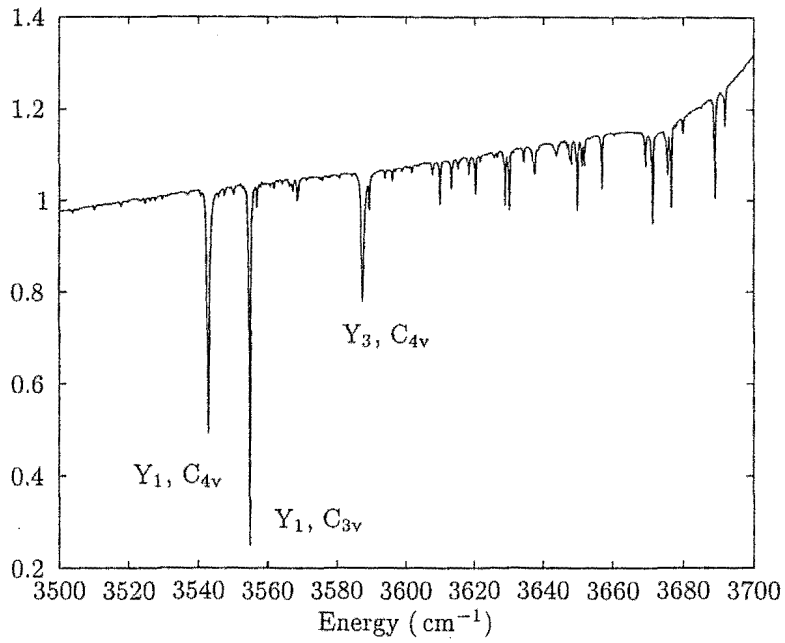

Figure 4.4: 15 K infrared absorption spectrum of the $^6H_{13/2}$ multiplet in SrF_2:0.05% Dy^{3+}.

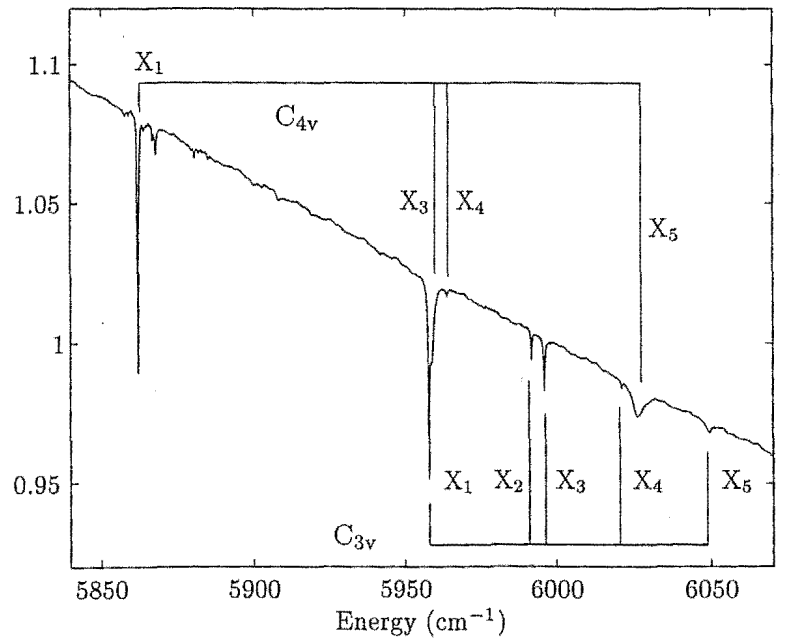

Figure 4.5: 15 K infrared absorption spectrum of the $^6H_{11/2}$ multiplet in SrF_2:0.05% Dy^{3+}.

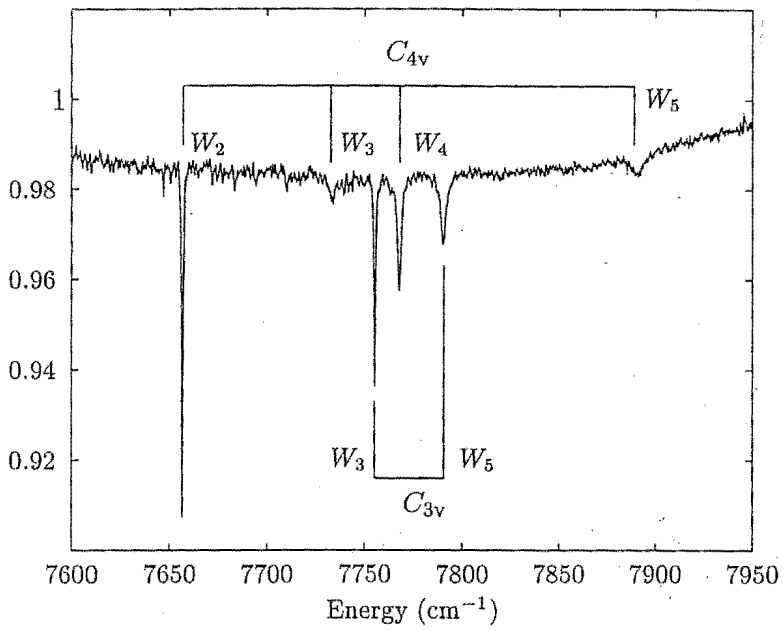

Figure 4.6: 15 K infrared absorption spectrum of the $^6H_{9/2}$ and $^6F_{11/2}$ multiplets (the W manifold) in SrF_2:0.05% Dy^{3+}. A steeply declining background response has been removed for clarity.

Figure 4.7 presents the narrowband excitation spectra of the $^4F_{9/2}$ multiplet, which clearly separates the various excitation transitions into two dominant centers. Both narrowband spectra were obtained by monitoring a specific $^4F_{9/2} \rightarrow {}^6H_{11/2}$ transition. The spectrum designated as corresponding to the C_{3v} center is that obtained for detection of fluorescence at 14898 cm^{-1}, corresponding to the $F_1 \rightarrow X_6$ emission, while that for the C_{4v} center was recorded while monitoring at 15058 cm^{-1}, corresponding to $F_1 \rightarrow X_4$ emission.

The C_{3v} center excitation spectrum reveals a 2.5 cm^{-1} splitting of the F_1 and F_2 energy levels. This splitting is observed repeatedly in the fluorescence, whenever the fluorescence transitions are sharp enough for the two transitions to be resolved. Also weakly visible are the $Z_2 \rightarrow F_1$,F_2 transitions. A distinctive feature in the broadband excitation spectra is the set of three transitions at approximately 21165 cm^{-1}. When compared to the narrowband excitation spectra of Figure 4.7 an indication is given of four transitions, two from each of the C_{3v} and C_{4v} centers. The possibility that both centers are observed in the narrowband excitation spectra, due to some fluorescence overlap, can be ruled out because of the clear distinction in the narrowband spectra when considering the other excitation transitions. Another feature of the narrowband spectra is the specific association of the broad features at approximately 21400 cm^{-1} with the C_{3v} center. These broad excitation features are associated with vibronic transitions, indicating that the C_{3v} center is more strongly coupled to lattice vibrations.

Table 4.2: Transition frequencies and assignments for excitation to the $^4F_{9/2}$ multiplet, and the inferred energy levels of $^4F_{9/2}$. All energies and transition frequencies are given in vacuum wavenumbers, with an uncertainty of $\pm 1\,cm^{-1}$. Splittings between transitions have an uncertainty of $\pm 0.5\,cm^{-1}$.

Excitation energy (cm^{-1})	Center	
	C_{4v}	C_{3v} "J"
21660		$Z_1 \rightarrow F_5$
21371		vibronic
21171	$Z_1 \rightarrow F_4$	
21162	$Z_1 \rightarrow F_3$	$Z_1 \rightarrow F_4$
21154		$Z_1 \rightarrow F_3$
21043	$Z_1 \rightarrow F_2$	
21020	$Z_1 \rightarrow F_1$	
20967.2		$Z_1 \rightarrow F_2$
20964.7		$Z_1 \rightarrow F_1$
20928.1		$Z_2 \rightarrow F_2$
20925.6		$Z_2 \rightarrow F_1$

$^4F_{9/2}$ Level	Energy (cm^{-1})	
	C_{4v}	C_{3v}
F_1	21020	20964.7
F_2	21043	20967.2
F_3	21162	21154
F_4	21171	21162
F_5	—	21660

Vibronic fluorescence transitions of the C_{3v} center have previously been reported by Eremin et.al. [34], and as will be discussed in a Section 4.4, the identification of vibronic transitions has been extended to include transitions associated with two distinct phonon frequencies, both of which are represented in the $^4F_{9/2}$ excitation spectrum.

The assignments and transition energies of the various transitions from the $^6H_{15/2}$ ground state multiplet to the $^4F_{9/2}$ multiplet are presented in Table 4.2. The $^4F_{9/2}$ energy levels inferred from the excitation data are also given in the same table.

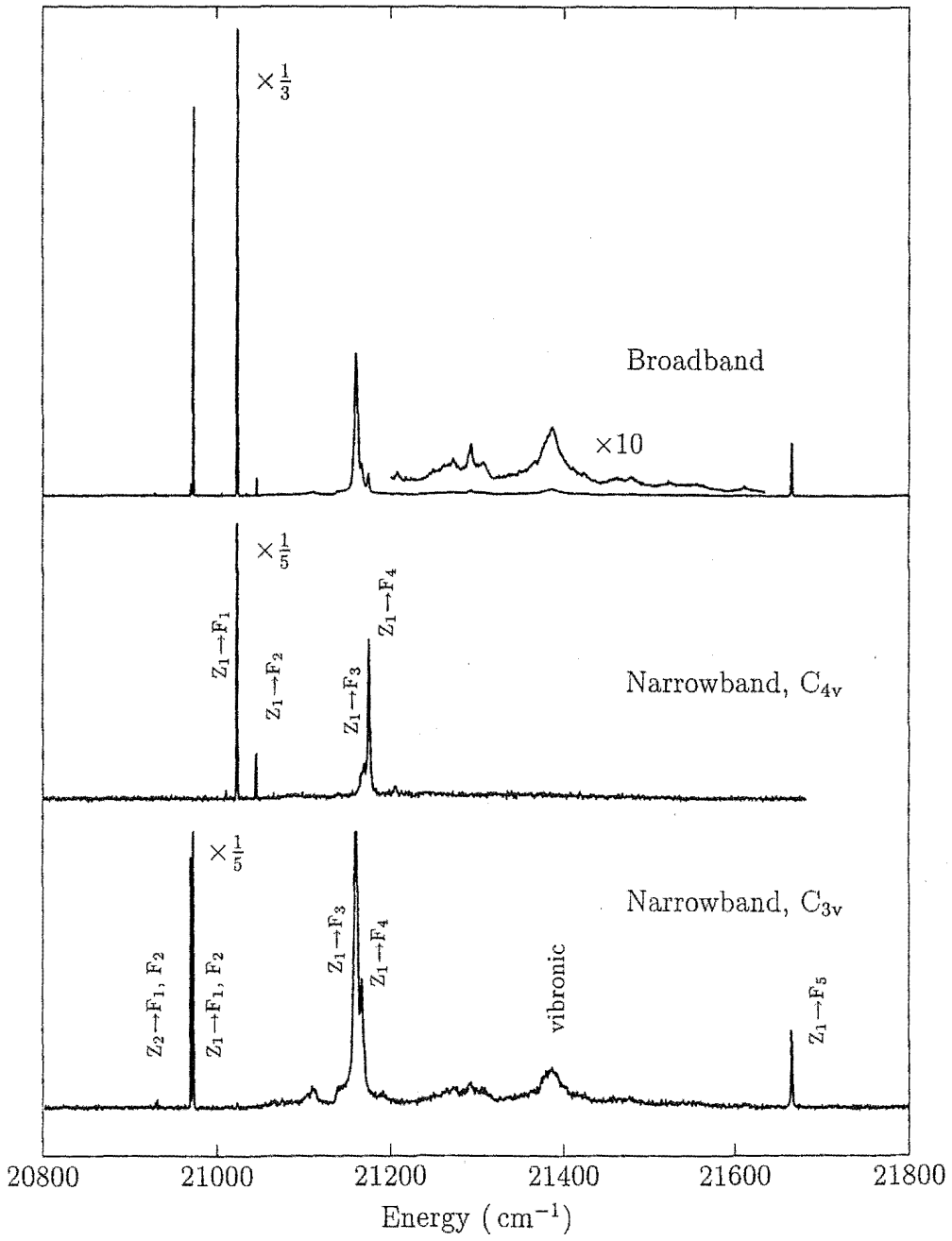

Figure 4.7: 15 K broadband and narrowband excitation spectra of SrF_2:0.05%Dy^{3+}. The spectra are: (top) broadband monitoring at 665 nm, corresponding to the $^4F_{9/2} \rightarrow {}^6H_{11/2}$ transitions. (center) narrowband spectrum of the C_{4v} centre, monitoring the $F_1 \rightarrow X_4$ transition at 15058 cm^{-1}. (bottom) narrowband spectrum of the C_{3v} centre, monitoring the $F_1 \rightarrow X_6$ transition at 14898 cm^{-1}. The most intense transition in each spectrum has been truncated to enable the minor features to be observed.

4.3 The $SrF_2:Dy^{3+}$ C_{4v} center.

Site-selective fluorescence from the $^4F_{9/2}$ multiplet to a number of the lower multiplets was obtained for both of the dominant centers observed in excitation and absorption. This section will discuss the $^4F_{9/2}$ fluorescence of the C_{4v} center, and the energy levels assignments that follow from analysis of this emission. For fluorescence energies between $\approx$21000 cm^{-1} and 11000 cm^{-1} the spectra were obtained with the Spex 1403 double monochromator and RCA C31034 photomultiplier tube with photon counting detection. For lower frequency fluorescence the liquid N_2 cooled infrared PMT was used in conjunction with the Spex 1700 single monochromator. The infrared PMT was not operated in photon counting detection, but rather with current detection performed by the Keithley electrometer. Because there is only a weak polarisation dependence of the fluorescence for most transitions, the discussion will first focus on the unpolarised fluorescence, with only occasional reference to polarisation results. The polarisation behaviour of the fluorescence will be discussed more fully in Section 4.3.2

4.3.1 Laser selective fluorescence

$^6H_{15/2}$ multiplet.

Figure 4.8 presents the unpolarised emission spectra for the $^4F_{9/2} \rightarrow {}^6H_{15/2}$ transitions of the $SrF_2:Dy^{3+}$ C_{4v} center. The top spectrum displays the emission obtained when the sample is at a temperature of 15 K and with laser excitation of the $Z_1 \rightarrow F_1$ transition at 21020 cm^{-1}. Apparent is a 23 cm^{-1} separation between several transitions. This 23 cm^{-1} splitting is also present in the excitation spectrum, indicating that emission from both the F_1 and F_2 energy levels is being observed. The F_2 emission occurs because at a temperature of 15 K the relatively small F_1–F_2 splitting enables the F_2 level to acquire a significant Boltzmann population, relative to the F_1 population. Figure 4.8 (b) presents the spectrum obtained for $Z_1 \rightarrow F_2$ excitation at 21043 cm^{-1}, which enables the observation of the $F_1 \rightarrow Z_1$ transition, confirming that the 21020 cm^{-1} energy level is the lowest emitting level of $^4F_{9/2}$.

Finally, Figure 4.8 (c) shows the spectrum obtained when the sample is cooled to 2 K in a pumped liquid helium cryostat. The excitation was via the $Z_1 \rightarrow F_1$ transition, and the spectrometer shutter was closed as it was scanned over the laser frequency. At this lower temperature the Boltzmann population of a level 23 cm^{-1} above F_1 will be negligible. As such it is expected that all emission from the F_2 level will be suppressed, and this can indeed be seen clearly in the spectrum.

For the $^6H_{15/2}$ multiplet in C_{4v} symmetry there are a total of eight Kramers doublets, of which energies of four doublets (three plus the ground state defined to be at $0\,cm^{-1}$) have been determined from the fluorescence spectra. Table 4.3 summarises the transition frequencies obtained for the $^4F_{9/2} \rightarrow {}^6H_{15/2}$ emission, together with the inferred energy levels of $^6H_{15/2}$.

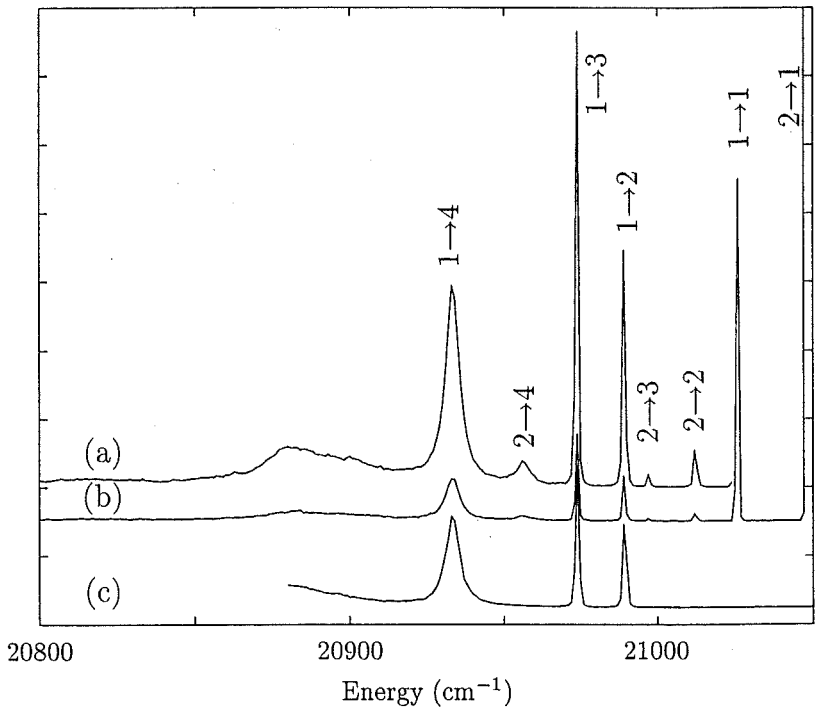

Figure 4.8: $^4F_{9/2} \rightarrow {}^6H_{15/2}$ fluorescence of the C_{4v} centre in SrF_2:0.05%Dy^{3+}. (a) exciting $Z_1 \rightarrow F_1$ at $21020\,cm^{-1}$, at a temperature of 15 K. (b) exciting $Z_1 \rightarrow F_2$ at $21043\,cm^{-1}$, at a temperature of 15 K. (c) exciting $Z_1 \rightarrow F_1$ at a temperature of 2 K with the spectrometer shutter closed as scanning over the laser frequency. Transitions are labelled by their emitting and terminating levels respectively.

Transition	Fluorescence energy
$F_2 \rightarrow Z_1$	21043
$F_1 \rightarrow Z_1$	21020
$F_2 \rightarrow Z_2$	21005
$F_2 \rightarrow Z_3$	20990
$F_1 \rightarrow Z_2$	20982
$F_1 \rightarrow Z_3$	20967
$F_2 \rightarrow Z_4$	20948
$F_1 \rightarrow Z_4$	20926

$^6H_{15/2}$ Level	Energy (cm^{-1})
Z_1	0
Z_2	38
Z_3	53
Z_4	94
Z_5 –Z_8	—

Table 4.3: The $^4F_{9/2} \rightarrow {}^6H_{15/2}$ transition frequencies and the inferred energy levels of the $^6H_{15/2}$ multiplet for the SrF_2:Dy^{3+} C_{4v} center. All transition frequencies and energy levels are given in vacuum wavenumbers, with an uncertainty of $\pm 1\,cm^{-1}$.

$^6H_{13/2}$ multiplet.

The emission to $^6H_{13/2}$ consists of a grouping of sharp transitions between $17510\,cm^{-1}$ and $17420\,cm^{-1}$ and three quite broad transitions at $17349\,cm^{-1}$, $17267\,cm^{-1}$ and $17259\,cm^{-1}$, as shown in Figure 4.9. As before, emission from the F_2 level has been eliminated by cooling the sample to 2 K in a helium cryostat (Fig. 4.9 (b)), simplifying considerably the spectrum of the group of sharp transitions. This enables an unambiguous identification of four transitions from the F_1 level and the corresponding transitions from F_2, from which the energies of the lower states of the $^5H_{13/2}$ can be determined. The emitting state for the three broad transitions is not known, and therefore the transitions assignments and energies of the terminating states are uncertain. A tentative assignment of $F_1 \rightarrow Y_5$ is given to the fluorescence transition at $17349\,cm^{-1}$. The remaining transitions are left unassigned.

The transition frequencies for the $^4F_{9/2} \rightarrow {}^6H_{13/2}$ fluorescence, and the inferred energy levels of $^6H_{13/2}$, are listed in Table 4.4.

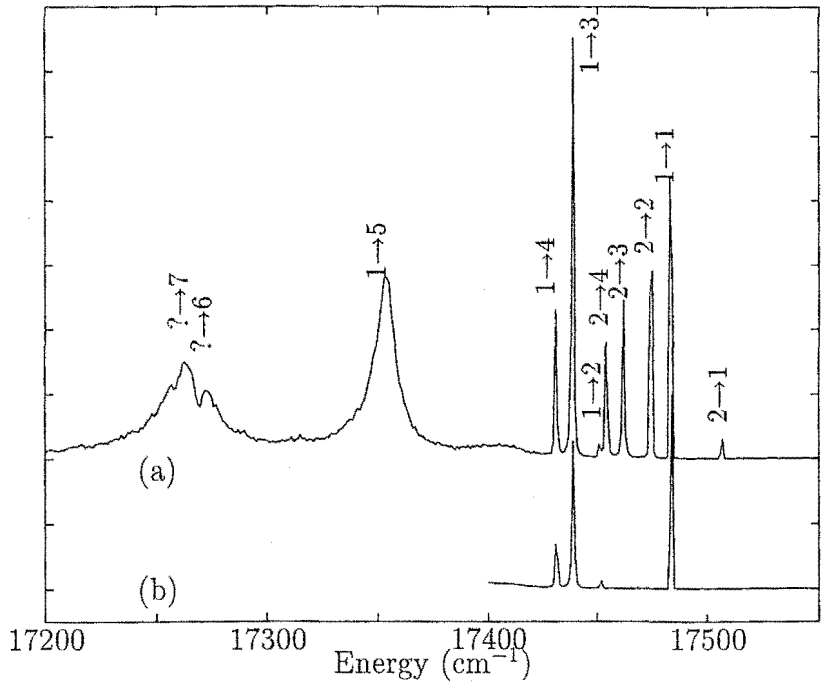

Figure 4.9: $^4F_{9/2} \rightarrow {}^6H_{13/2}$ fluorescence spectra of the C_{4v} center in SrF_2:0.05%Dy^{3+} at (a) 15 K (b) 2 K

Transition	Fluorescence energy
$F_2 \rightarrow Y_1$	17501
$F_1 \rightarrow Y_1$	17477
$F_2 \rightarrow Y_2$	17468
$F_2 \rightarrow Y_3$	17455
$F_2 \rightarrow Y_4$	17448
$F_1 \rightarrow Y_2$	17445
$F_1 \rightarrow Y_3$	17433
$F_1 \rightarrow Y_4$	17425
$F_1 \rightarrow Y_5$	17349±2
$F_? \rightarrow Y_6$ (?)	17267±5
$F_? \rightarrow Y_7$ (?)	17259±5

$^6H_{13/2}$ Level	Energy (cm^{-1})
Y_1	3543
Y_2	3575
Y_3	3587
Y_4	3595
Y_5	3671±2
Y_6	—
Y_7	—

Table 4.4: The $^4F_{9/2} \rightarrow {}^6H_{13/2}$ transition frequencies and the inferred energy levels of the $^6H_{13/2}$ multiplet for the $SrF_2:Dy^{3+}$ C_{4v} center. All transition frequencies and energy levels are given in vacuum wavenumbers, with an uncertainty of ±1 cm^{-1} unless otherwise stated.

$^6H_{11/2}$ multiplet.

The emission to the $^6H_{11/2}$ multiplet at temperatures of 15 K and 2 K is presented in the spectra of Figure 4.10. The fluorescence from F_2 is again suppressed in the spectrum obtained at 2 K. The two broad transitions at 14995 cm^{-1} and 14987 cm^{-1} are both present in the lower temperature spectrum, revealing that they are due to F_1 emission. These transitions are assigned as $F_1 \rightarrow X_5, X_6$. The broad features on the high energy side of these transitions are attributed to F_2 emission. The fluorescence with frequencies of 15160 cm^{-1}, 15063 cm^{-1} and 15058 cm^{-1} is assigned to the $F_1 \rightarrow X_1, X_3, X_4$ transitions.

In explaining the absence of an assigned $F_1 \rightarrow X_2$ transition it is noted that crystal-field calculations for the C_{4v} center predict the three energy levels X_2, X_3 and X_4 to all lie in close proximity. The broadening in the high energy tail of the $F_1 \rightarrow X_3$ transition is also indicative of another underlying transition, which is interpreted as the $F_1 \rightarrow X_2$ fluorescence. Reference to the infrared absorption is unable to clarify the accuracy of this assignment of the X_2 energy level. The levels here labelled X_3 and X_4 are indeed seen in absorption, but the presence of any level at the expected position of X_2 is masked by the relatively strong absorption to the X_1 state of the C_{3v} center at 5958 cm^{-1}. In an attempt to clarify this assignment of a C_{4v} energy level at approximately 5958 cm^{-1}, the polarised emission to this multiplet has been considered. Because of the generally small polarisation behaviour and the often unstable lasing of the Coumarin 460 dye, the photoelastic modulator was used to measure the polarisation dependence of the fluorescence. In Figure 4.11 both the AC and DC signal recorded with this system are presented, along with the inferred polarised intensities. From this data it is seen that the X_5 and X_6 transitions possess different polarisation behaviour, adding to the resolution of these two energy levels. Less obvious is any relative change in the intensities of the suspected X_2 transition and that of the transition to X_3. It is therefore concluded that the polarised fluorescence data is unable to confirm the separation of the X_2 and X_3 levels. The assignment of X_2 must therefore be considered tentative. For this reason the X_2 level has not been included in the crystal-field calculations, however it is expected that X_2 should lie within $\approx$5 cm^{-1} of X_3. Therefore, five of the six energy levels of the $^6H_{11/2}$ multiplet have been identified, and there is some constraint on the energy of the remaining level.

The transition frequencies for the $^4F_{9/2} \rightarrow {}^6H_{11/2}$ fluorescence, and the inferred energy levels of the terminating multiplet are shown in Table 4.5.

It is also noted that the $F_1 \rightarrow X_3$ and $F_1 \rightarrow X_4$ transitions have markedly different polarisation behaviour. As will be discussed in Section 4.3.2, this polarisation behaviour identifies the X_3 and X_4 levels to have the irrep assignments of Γ_7 and Γ_6 respectively.

Transition	Fluorescence energy
$F_2 \rightarrow X_1$	15183
$F_1 \rightarrow X_1$	15160
$F_2 \rightarrow X_4$	15081
$F_1 \rightarrow X_3$	15063
$F_1 \rightarrow X_4$	15058
$F_1 \rightarrow X_5$	14995
$F_1 \rightarrow X_6$	14987±2

$^6H_{11/2}$ Level	Energy (cm^{-1})
X_1	5860
X_2	—
X_3	5957
X_4	5962
X_5	6025
X_6	6033±2

Table 4.5: The $^4F_{9/2} \rightarrow {}^6H_{11/2}$ transition frequencies and the inferred energy levels of the $^6H_{11/2}$ multiplet for the $SrF_2:Dy^{3+}$ C_{4v} center. All transition frequencies and energy levels are given in vacuum wavenumbers, with an uncertainty of $\pm 1\,cm^{-1}$ unless otherwise stated.

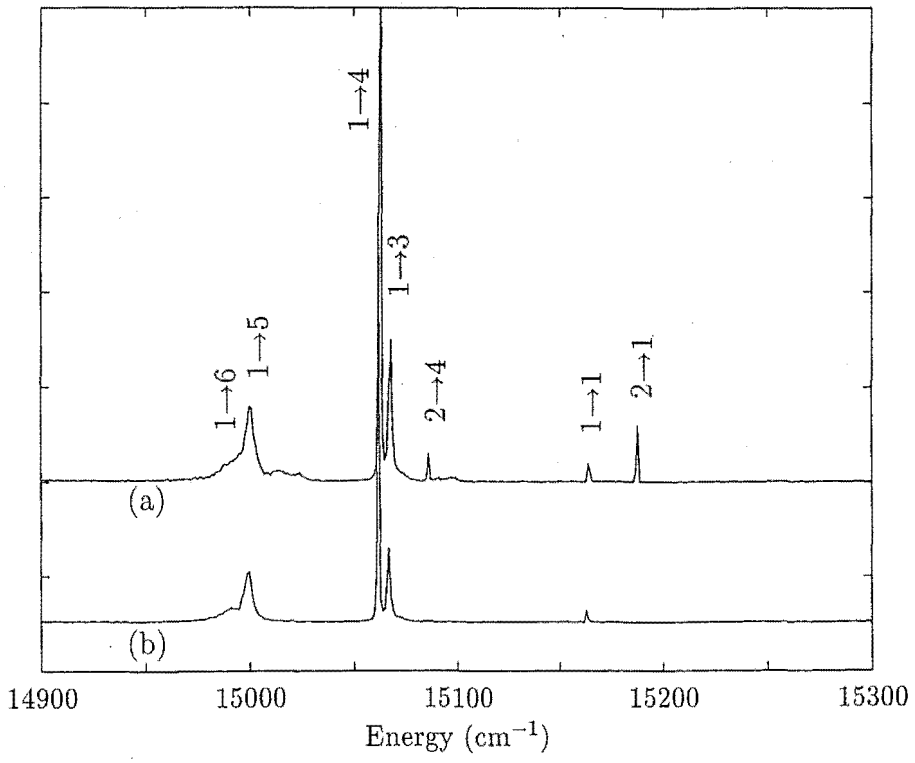

Figure 4.10: $^4F_{9/2} \rightarrow {}^6H_{11/2}$ fluorescence spectra of the C_{4v} center in SrF_2:0.05%Dy^{3+} at (a) 15 K (b) 2 K

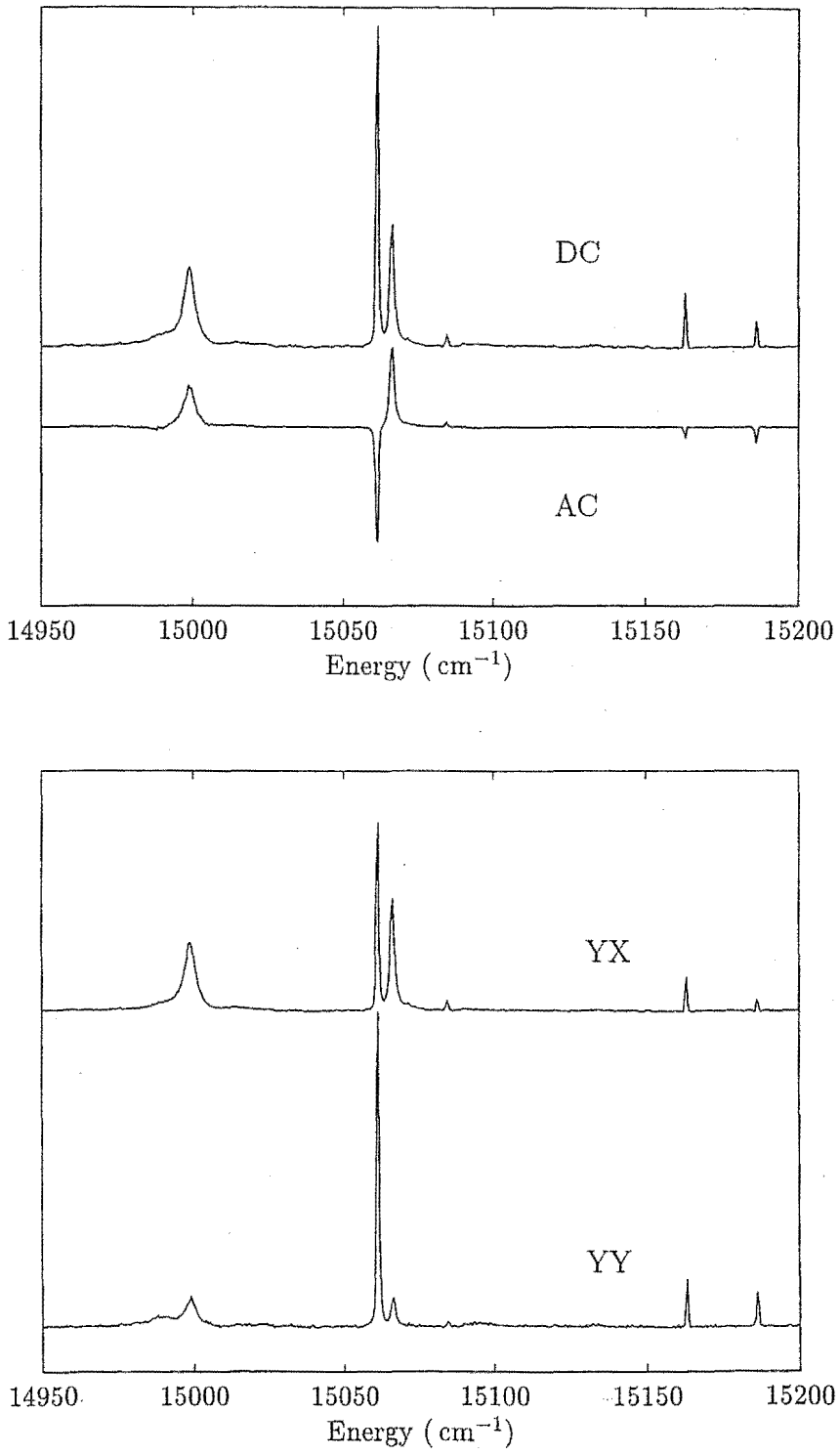

Figure 4.11: $^4F_{9/2} \rightarrow {}^6H_{11/2}$ polarised fluorescence of the C_{4v} center in $SrF_2 0.05\% Dy^{3+}$. The top figure shows the AC and DC signals obtained with the photoelastic modulator, while the lower figure displays the inferred polarised fluorescence spectra.

$^6H_{9/2}$ and $^6F_{11/2}$ multiplets.

The spin-orbit interaction in Dy^{3+} occurs with a magnitude that causes the $^6H_{9/2}$ and $^6F_{11/2}$ multiplets to be effectively overlapping. The small energy separation between levels of the two multiplets together with the crystal-field interactions causes a mixing of the two multiplets which effectively removes the validity of the LSJ labelling. These two multiplets will therefore be referred to by the single label W. The spectra for $^4F_{9/2} \rightarrow$W fluorescence at 15 K and 2 K are shown in Figure 4.12. The broad structure in the region between 13100 cm^{-1} and 13250 cm^{-1} shows no significant difference in appearance at the two temperatures, implying that this emission originates from the F_1 state. However, the possibility that this broad fluorescence is essentially of a vibronic character cannot be discounted. Assignment of transitions has therefore been limited to the ten transitions with energies greater than 13220 cm^{-1}. For all of these transitions a grouping into F_1 and F_2 emission is possible by appealing to the differences in the spectra at the two temperatures. This leads to the measurement of five energy levels, out of a total of eleven Kramers doublets for the intertwined multiplets of the W manifold. The frequencies for the assigned transitions and the energies of the associated levels of the W manifold are shown in Table 4.6.

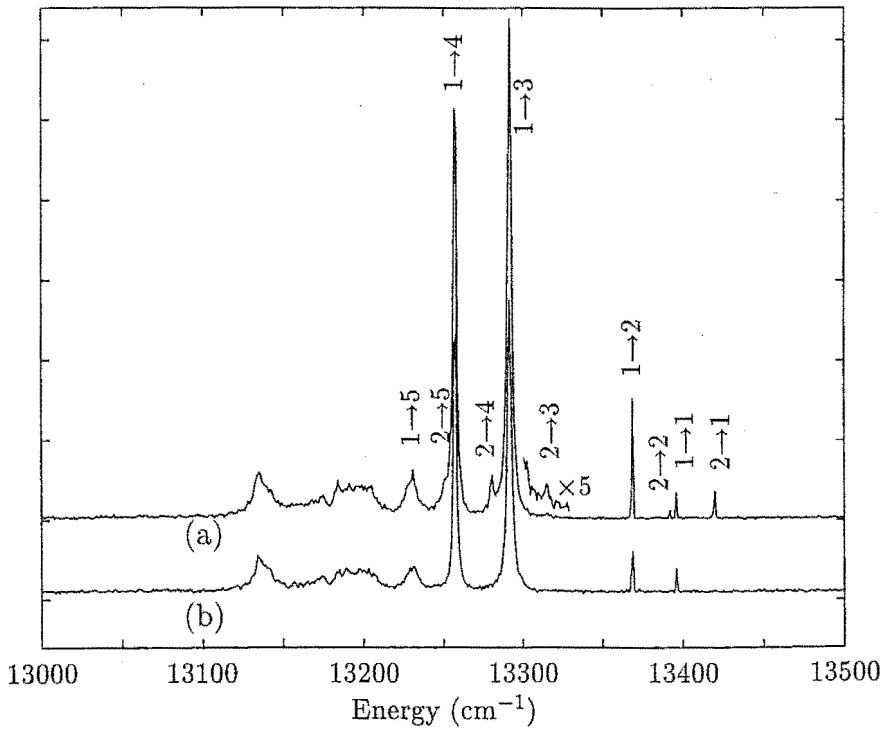

Figure 4.12: $^4F_{9/2} \rightarrow {}^6H_{9/2}$, $^6F_{11/2}$ (W manifold) fluorescence spectra of the C_{4v} center in SrF_2:0.05%Dy^{3+} at (a) 15 K (b) 2 K

Transition	Fluorescence energy
$F_2 \rightarrow W_1$	13416
$F_1 \rightarrow W_1$	13393
$F_2 \rightarrow W_2$	13388
$F_1 \rightarrow W_2$	13365
$F_1 \rightarrow W_3$	13288
$F_2 \rightarrow W_4$	13277
$F_1 \rightarrow W_4$	13254
$F_1 \rightarrow W_5$	13228

$^6H_{9/2}$, $^6F_{11/2}$ Level	Energy (cm^{-1})
W_1	7627
W_2	7655
W_3	7732
W_4	7766
W_5	7792
W_6 –W_{11}	—

Table 4.6: The $^4F_{9/2}$ →W transition frequencies and the inferred energy levels of the W manifold for the SrF_2:Dy^{3+} C_{4v} center. All transition frequencies and energy levels are given in vacuum wavenumbers, with an uncertainty of $\pm 1\,cm^{-1}$.

$^6H_{7/2}$ and $^6F_{9/2}$ multiplets.

As for the multiplets just discussed, the two multiplets of $^6H_{7/2}$ and $^6F_{9/2}$ are closely grouped. In the fluorescence spectrum of Figure 4.13 a separation of the fluorescence into two groups is observed. However this separation of $\approx 200\,cm^{-1}$ is relatively small compared to the possible crystal field splittings. The two multiplets will also be expected to posses considerable crystal-field mixing of the states, again making the use of the LSJ spectroscopic labelling invalid. This is supported by the crystal-field calculation of Section 4.3.3, where the mixing of states results in approximately equal contributions of the different LSJ components for many levels. The manifold of states comprising these two multiplets will be referred to by the label A.

The six transitions at a frequency greater than $11900\,cm^{-1}$ can be separated into two groups of three, with each group originating from an initial state of either F_1 or F_2. These transitions frequencies are tabulated in Table 4.7 along with the corresponding three energy levels of the A manifold.

To clarify the remaining transitions to the A manifold, those transitions with energies less than $11900\,cm^{-1}$, a further spectrum was obtained using the liquid N_2 cooled infrared PMT. Despite the fact that this PMT was not operated in conjunction with photon counting methods, the superior sensitivity in this spectral region enables a better signal to be obtained. The spectrum is presented in Figure 4.14, where transitions that could be tentatively identified through the observation of an approximate $23\,cm^{-1}$ F_1–F_2 splitting have been indicated.

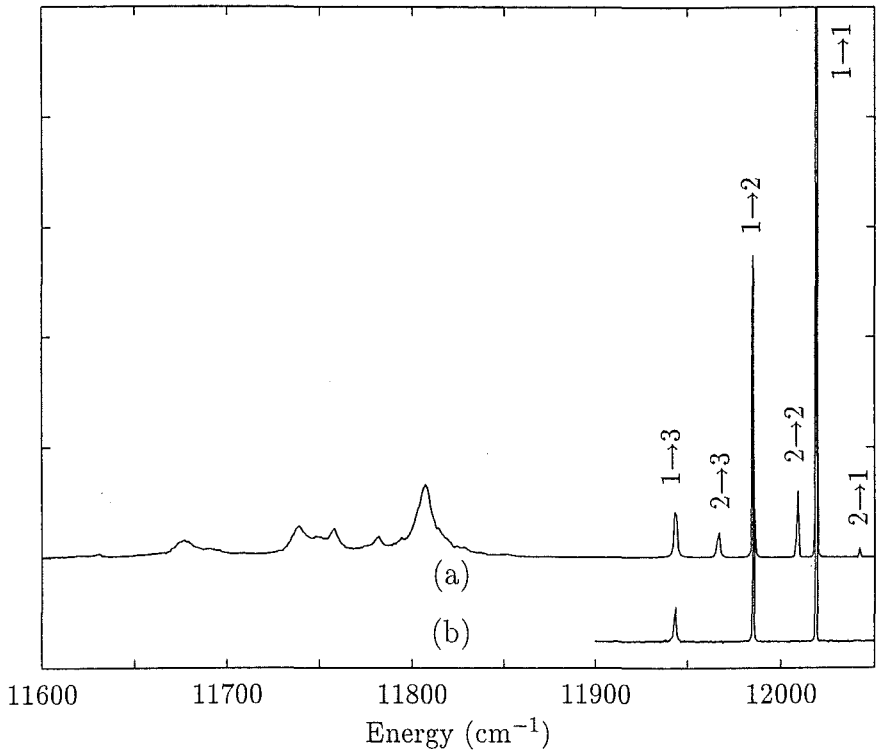

Figure 4.13: $^4F_{9/2} \rightarrow {}^6H_{7/2}$, $^6F_{9/2}$ (A manifold) fluorescence spectra of the C_{4v} center in SrF_2:0.05%Dy^{3+} at (a) 15 K (b) 2 K

Transition	Fluorescence energy
$F_2 \rightarrow A_1$	12039
$F_1 \rightarrow A_1$	12015
$F_2 \rightarrow A_2$	12005
$F_1 \rightarrow A_2$	11982
$F_2 \rightarrow A_3$	11963
$F_1 \rightarrow A_3$	11940

$^6H_{7/2}$, $^6F_{9/2}$ Level	Energy (cm^{-1})
A_1	9005
A_2	9038
A_3	9080

Table 4.7: The $^4F_{9/2} \rightarrow$A transition frequencies and the inferred energy levels of the A multiplets for the SrF_2:Dy^{3+} C_{4v} center. All transition frequencies and energy levels are given in vacuum wavenumbers, with an uncertainty of $\pm 1\,cm^{-1}$.

However, some ambiguity still remains due to the presence of still unassigned structure in the spectrum, particularly the pair of transitions at $\approx$11630 cm^{-1}. A less than satisfactory agreement is obtained between the energy levels inferred from these transitions and that found from a crystal-field calculation. For these reasons the energy levels and transitions listed in Table 4.8 should be considered quite tentative. The A_4–A_9 levels were not included in the least-squares crystal-field calculation of Section 4.3.3.

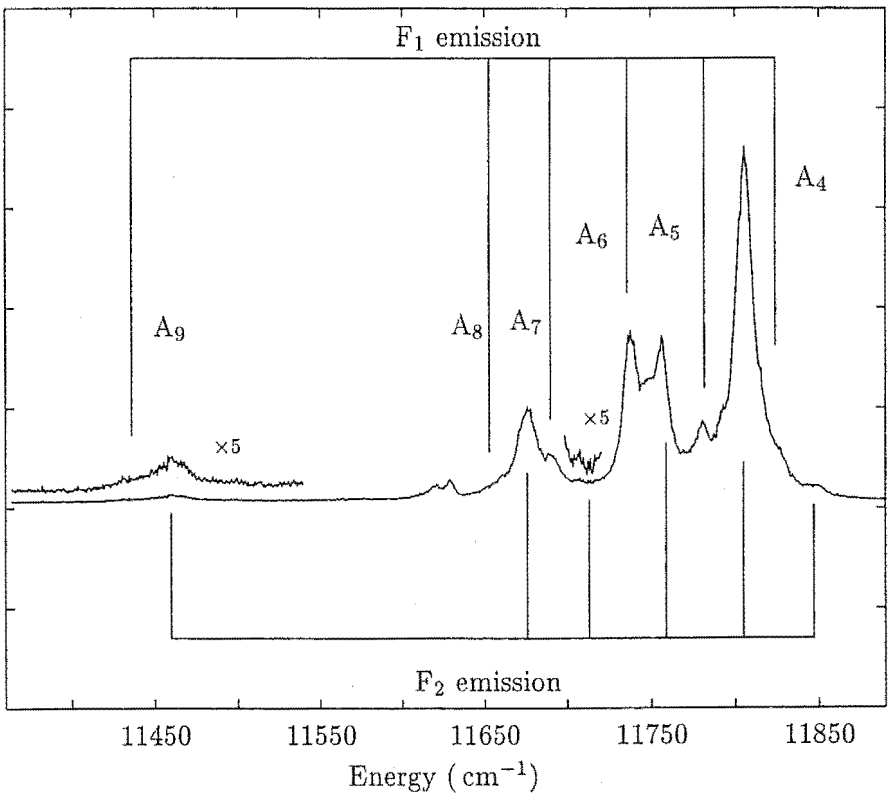

Figure 4.14: A partial spectrum of the $^4F_{9/2} \rightarrow {}^6H_{7/2}$, $^6F_{9/2}$ (A manifold) fluorescence of the C_{4v} center in SrF_2:0.05%Dy^{3+}. Transitions have been assigned on the basis of observation of an approximate 23 cm^{-1} splitting, indicating emission from both the F_1 and F_2 states. The sample is at a temperature of 15 K.

Transition	Fluorescence energy
$F_2 \rightarrow A_4$	11848
$F_2 \rightarrow A_5$	11807
$F_1 \rightarrow A_5$	11782
$F_2 \rightarrow A_6$	11758
$F_1 \rightarrow A_6$	11739
$F_1 \rightarrow A_7$	11691
$F_2 \rightarrow A_8$	11678
$F_2 \rightarrow A_9$	11461
$F_1 \rightarrow A_9$	11432

$^6H_{7/2}$, $^6F_{9/2}$ Level	Energy (cm^{-1})
A_4	9195
A_5	9236
A_6	9281
A_7	9329
A_8	9365
A_9	9582

Table 4.8: The SrF_2:Dy^{3+} C_{4v} center $^4F_{9/2} \rightarrow$A transitions of the A multiplets for transition energies less than 11900 cm^{-1}. All transition frequencies and energy levels are given in vacuum wavenumbers, with an uncertainty of $\pm 2\,cm^{-1}$. These levels were not including in the fitting of crystal-field parameters because of some remaining uncertainty in their assignment.

$^6H_{5/2}$ multiplet.

For emission to the $^6H_{5/2}$ multiplet, as displayed in Figure 4.15, a single transition with narrow linewidth and several broader transitions are observed. Through the observation of the 23 cm^{-1} F_1 –F_2 splitting in the fluorescence spectrum transitions to all three levels of the $^6H_{5/2}$ can be assigned, and the energy levels of this multiplet inferred. The transition frequencies and the energies of all three $^6H_{5/2}$ levels are tabulated in Table 4.9.

Transition	Fluorescence energy
$F_1 \rightarrow B_1$	10848
$F_2 \rightarrow B_2$	10683±5
$F_1 \rightarrow B_2$	10660±5
$F_2 \rightarrow B_3$	10645±5
$F_1 \rightarrow B_3$	10630±5

$^6H_{5/2}$ Level	Energy (cm^{-1})
B_1	10172
B_2	10360±5
B_3	10390±5

Table 4.9: The SrF_2:Dy^{3+} C_{4v} center $^4F_{9/2} \rightarrow$ $^6H_{5/2}$ transition frequencies and energy levels for the C_{4v} center of SrF_2:Dy^{3+}. All transition frequencies and energy levels are given in vacuum wavenumbers, with an uncertainty of $\pm 2\,cm^{-1}$ unless otherwise stated.

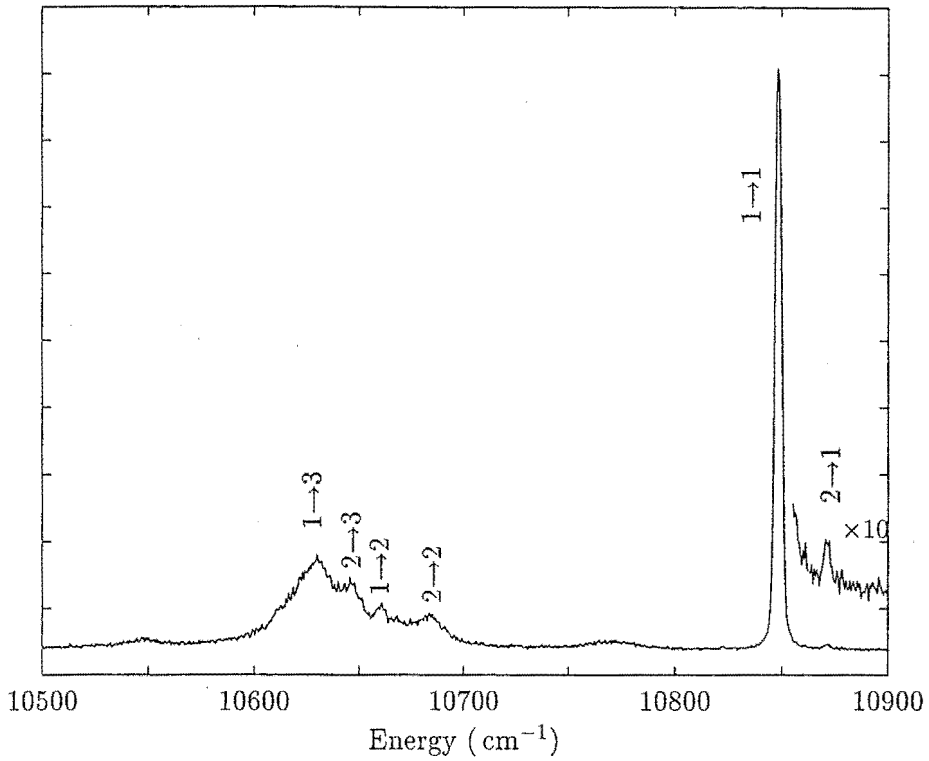

Figure 4.15: $^4F_{9/2} \rightarrow {}^6H_{5/2}$ fluorescence spectrum of the C_{4v} center in SrF_2:0.05%Dy^{3+}. The sample was at a temperature of 15 K.

$^6F_{7/2}$ multiplet.

The $^4F_{9/2} \rightarrow {}^6F_{7/2}$ fluorescence of the $SrF_2:Dy^{3+}$ C_{4v} center is shown in Figure 4.16, as recorded with the liquid N_2 cooled PMT. Taking the 23 cm^{-1} F_1–F_2 splitting into account, four transitions originating from each of the F_1 and F_2 states can be identified, and therefore the energies of all four states of the $^6F_{7/2}$ multiplet inferred. The transition frequencies and the energy levels of the terminating multiplet are given in Table 4.10.

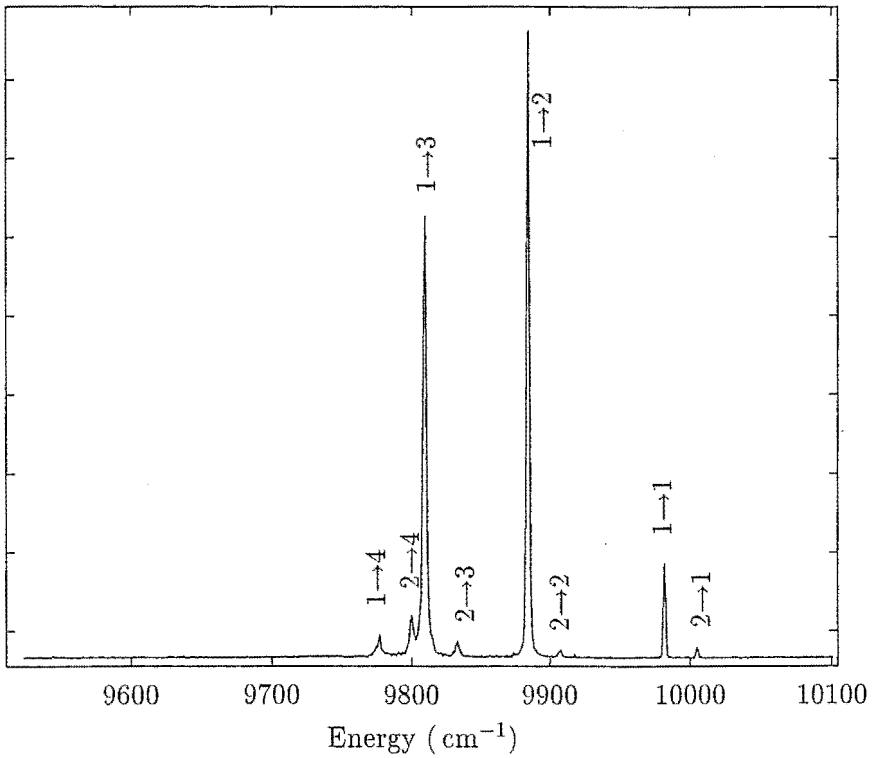

Figure 4.16: $^4F_{9/2} \rightarrow {}^6F_{7/2}$ fluorescence spectrum of the C_{4v} center in SrF_2:0.05%Dy^{3+}. The sample was at a temperature of 15 K.

Transition	Fluorescence energy
$F_2 \rightarrow C_1$	10002
$F_1 \rightarrow C_1$	9979
$F_2 \rightarrow C_2$	9904
$F_1 \rightarrow C_2$	9881
$F_2 \rightarrow C_3$	9830
$F_1 \rightarrow C_3$	9806
$F_2 \rightarrow C_4$	9796
$F_1 \rightarrow C_4$	9773

$^6F_{7/2}$ Level	Energy (cm^{-1})
C_1	11041
C_2	11139
C_3	11214
C_4	11247

Table 4.10: The $^4F_{9/2} \rightarrow {}^6F_{7/2}$ transition frequencies and the inferred energy levels of the $^6F_{7/2}$ multiplet for the SrF_2:Dy^{3+} C_{4v} center. All transition frequencies and energy levels are given in vacuum wavenumbers, with an uncertainty of $\pm 2\,cm^{-1}$.

4.3.2 Fluorescence polarisation.

Polarised fluorescence spectra were recorded to confirm the C_{4v} assignment of the center discussed here, and where possible gain additional information on the irrep label of energy levels. The general procedure for determining the polarisation properties of the fluorescence, the geometrical arrangement, and the notation used, have been described in Section 3.6 (page 25). The discussion here focuses on $\langle 100 \rangle$ oriented samples.

For the majority of RE^{3+} ions studied in CaF_2 and SrF_2, most transitions have been seen to occur via the electric dipole transition moment, with meaningful polarisation data obtained. However, for the CaF_2:Sm^{3+} C_{4v} centers, Wells [103] has reported that the electric and magnetic dipole moments appear to be of comparable magnitude, leading to degraded polarisation information. Similarly, the presence of significant magnetic-dipole transition moments degrades the clarity of the polarisation information in the SrF_2:Dy^{3+} C_{4v} center fluorescence. It has therefore been sought to further characterise the expected polarisation behaviour of the fluorescence transitions while allowing for the inclusion of both electric- and magnetic-dipole transition moments.

Table 4.11 lists the contributions to polarised emission for the C_{4v} center in a $\langle 100 \rangle$ oriented sample. In general the fluorescence intensity in any particular polarisation configuration will be a linear combination of the entries in Table 4.11 for the allowed absorption and emission transition moments. The coefficients of this linear combination are determined by the relative magnitudes of the transition moments. For Kramers ions, the selection rules (page 16) are such that for most pairs of excitation/fluorescence transitions the polarisation ratios will be arbitrary in that there is some dependence on the unknown relative magnitudes of the σ- and π-polarised transition moments. When the possibility of magnetic dipole transitions is included, then all transitions can be considered to have arbitrary polarisation behaviour in this sense, with the relative magnitudes of the electric-dipole and magnetic-dipole transition moments partially determining the relative polarised intensities.

Because all fluorescence polarisation measurements will include a possible degradation due to the polarisation properties of the excitation transition, it is important to clarify some aspects of the chosen excitation transition. From the various contributions to the polarised transition intensities shown in Table 4.11, it can be seen that for a purely electric dipole absorption, all possible emission moments will give rise to an equal weighting in emission if the laser is polarised in the Z direction. That is, ZX:ZY=1:1 for all fluorescence transitions if the absorption transition is purely electric dipole. Note that the emission itself may be magnetic dipole in nature and the above equality of polarised intensities still holds. The absorption may also contain some contribution of

absorption	emission	YX	YY	ZX	ZY
π	π	0	1	0	0
	σ	1	0	1	1
	π'	1	0	0	0
	σ'	0	1	1	1
σ	π	1	0	1	1
	σ	1	2	1	1
	π'	0	1	1	1
	σ'	2	1	1	1
π'	π	0	0	0	1
	σ	1	1	1	0
	π'	0	0	1	0
	σ'	1	1	0	1
σ'	π	1	1	1	0
	σ	1	1	1	2
	π'	1	1	0	1
	σ'	1	1	2	1

Table 4.11: The individual transition moment contributions to polarisation ratios for C_{4v} centers oriented in a ⟨100⟩ geometry. The labels π and σ refer to electric dipole transition moments, while π' and σ' refer to magnetic dipole moments.

both σ and π dipole moments. However, for the same electric dipole absorption the polarised fluorescence for Y polarised excitation will in general have YX:YY$\neq$1:1. For an excitation transition with both magnetic and electric dipole moments, the YX:YY and ZX:ZY intensity ratios will depend on the particular fluorescence transition, or more specifically on the relative magnitudes of the σ, π, σ' and π'-polarised transition moments of the fluorescence transition. Therefore, 1:1 intensity ratios will not be observed except for quite specific transitions for which there exists a fortuitous weighting of emission transition moments.

The results of polarised fluorescence measurements obtained with the photoelastic modulator (PEM) are presented in Figures 4.17 and 4.18. The PEM enables recording of a DC signal proportional to the addition of the orthogonally polarised intensities, and an AC signal proportional to the differences of the two intensities. The AC signal therefore gives a direct indication of any deviation from 1:1 intensity ratios. As it is this deviation, or lack of deviation, that is to be highlighted here, the raw signals are presented rather than the inferred polarised intensities. Figure 4.17 shows the $^4F_{9/2} \rightarrow {}^6H_{15/2}$

Table 4.12: Expected YX:YY:ZX polarised relative intensities for a purely electric-dipole σ-polarised absorption transition. The ratios are expressed in terms of the fluorescence transition moments.

Fluorescence transition	YX:YY:ZX relative intensities
$\Gamma_7 \rightarrow \Gamma_6$, $\Gamma_6 \rightarrow \Gamma_7$	$\sigma(1:2:1) + \sigma'(2:1:1)$
$\Gamma_7 \rightarrow \Gamma_7$, $\Gamma_6 \rightarrow \Gamma_6$	$\pi(1:0:1) + \sigma(1:2:1)$ $+\pi'(0:1:1) + \sigma'(2:1:1)$

emission spectra for both Z and Y polarised excitation for the $Z_1 \rightarrow F_2$ excitation transition. The $^4F_{9/2} \rightarrow {}^6H_{13/2}$ fluorescence is likewise shown in Figure 4.18. The spectra presented in these figures quite clearly indicate intensity ratios of ZX:ZY=1:1 for all fluorescence transitions (with a zero AC signal), whereas the YX:YY relative intensities are dependent on the particular transition. This equivalence of ZX and ZY intensities therefore implies that the absorption transition must be purely electric-dipole in character. However it is reemphasised that this in itself implies nothing regarding the irreps involved in the transitions, as both π and σ electric-dipole absorption (and any combination thereof) give rise to equal intensities for ZX and ZY spectra.

The expected relative polarised intensities are considerably simplified by this confirmation of a purely electric-dipole absorption transition. Further simplification is obtained through consideration of the particular irreps of the states involved in the absorption transition. For the SrF_2:$Dy^{3+}C_{4v}$ center, crystal-field calculations indicate that the Z_1, Z_2 and F_1 states transform as Γ_7 irreps and that F_2 transforms as the Γ_6 irrep. Hence, for an excitation transition of $Z_1(\Gamma_7) \rightarrow F_2(\Gamma_6)$ only the σ-polarised transition moment will be non-zero (c.f. the selection rules presented on page 15).

Table 4.12 presents the expected relative intensities for the YX:YY:ZX polarisation configurations, following an electric dipole σ-polarised absorption transition, such as the $Z_1(\Gamma_7) \rightarrow F_2(\Gamma_6)$ excitation transition. The irrep assignments of the levels involved in this absorption transition, initially based on a crystal-field calculation, are further justified by the self consistency of the relative polarised intensities obtained with this excitation.

From Table 4.12 constraints on the relative intensities for different polarisation configurations can be obtained. These constraints enable information on the irreps of the states involved in the fluorescence transitions to be determined from the degraded fluorescence polarisation data. These constrained relative intensities are shown in Table 4.13. Note that these constraints are not independent. For example, observed ratios of YX:YY:ZX=1:1:1 would satisfy each of the three constraints for a $\Gamma_6 \rightarrow \Gamma_7$

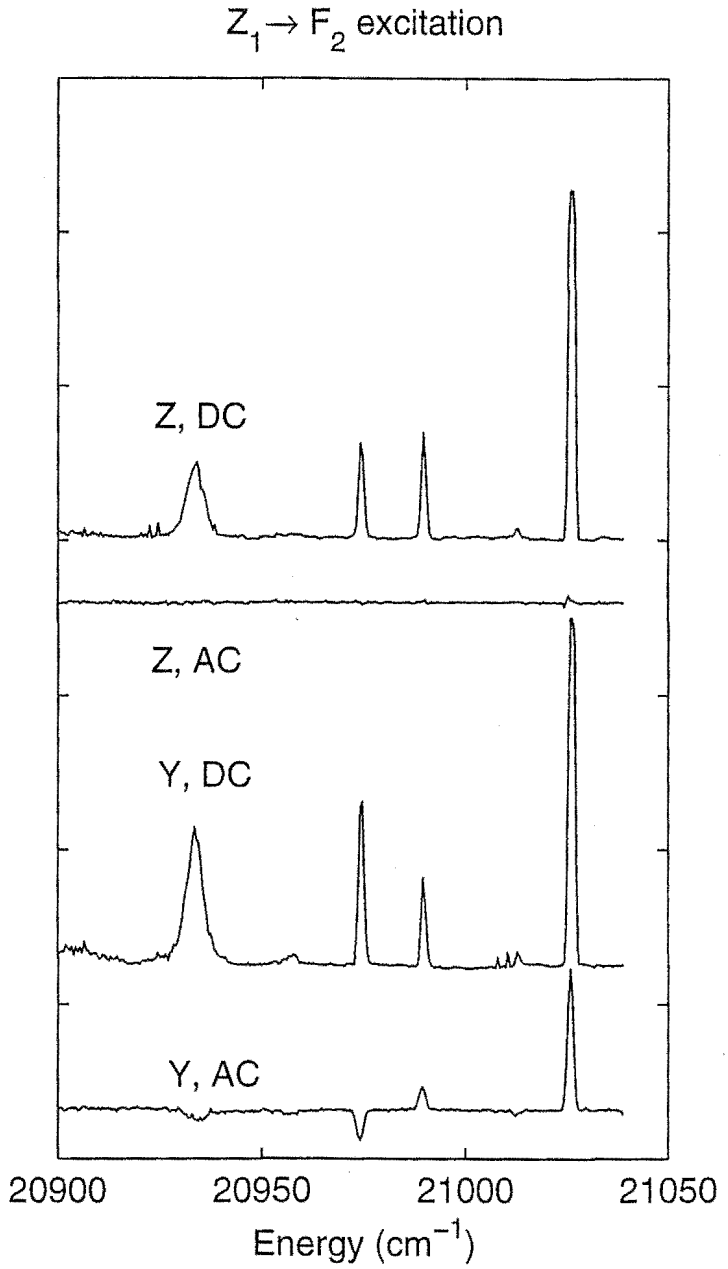

Figure 4.17: 15 K polarised fluorescence recorded for $^4F_{9/2} \rightarrow {}^6H_{15/2}$ with $Z_1 \rightarrow F_2$ excitation. All spectra are as obtained with the photoelastic modulator. The various spectra are, from the top: the DC signal recorded for Z polarised excitation; the AC signal with Z polarised excitation; the DC signal for Y polarised excitation; the AC signal for Y polarised excitation.

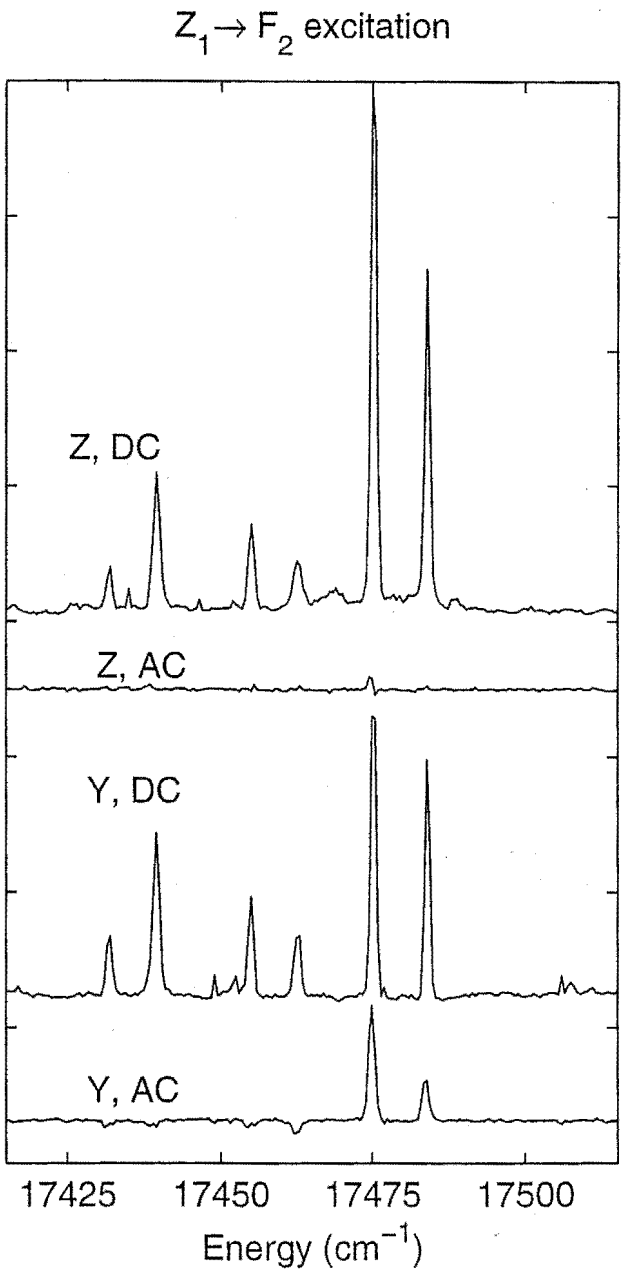

Figure 4.18: 15 K polarised fluorescence recorded for $^4F_{9/2} \rightarrow {}^6H_{13/2}$ with $Z_1 \rightarrow F_2$ excitation. All spectra are as obtained with the photoelastic modulator. The various spectra are, from the top: the DC signal recorded for Z polarised excitation; the AC signal with Z polarised excitation; the DC signal for Y polarised excitation; the AC signal for Y polarised excitation.

Table 4.13: Constraints on YX:YY:ZX polarised relative intensities for a purely electric-dipole σ-polarised absorption transition. No assumptions are made regarding the electric or magnetic dipole nature of the fluorescence transitions.

$\Gamma_7 \rightarrow \Gamma_6$, $\Gamma_6 \rightarrow \Gamma_7$	$\frac{1}{2} \leq \frac{YX}{YY} \leq 2$	$1 \leq \frac{YX}{ZX} \leq 2$	$1 \leq \frac{YY}{ZX} \leq 2$
$\Gamma_7 \rightarrow \Gamma_7$, $\Gamma_6 \rightarrow \Gamma_6$	$0 \leq \frac{YX}{YY} \leq \infty$	$0 \leq \frac{YX}{ZX} \leq 2$	$0 \leq \frac{YY}{ZX} \leq 2$

transition. However, a YX:YY=1:1 ratio would in that case imply an equal contribution from the σ electric dipole moment and the σ' magnetic dipole moment. This in turn implies a YX:YY:ZX=3:3:2 ratio. Therefore a 1:1:1 ratio is only consistent with a transition between like irreps.

As discussed in Section 3.6, the PEM was not amenable to obtaining relative intensities for different laser polarisations. Therefore polarised intensities were obtained by successive measurements of spectra in each of the four polarisation configurations, while simultaneously recording the laser power. Each spectrum was normalised with respect to the laser power. The polarised relative intensities of the SrF_2:Dy^{3+} C_{4v} center fluorescence are tabulated in Table 4.14. Some indication of the uncertainties in the polarisation data is obtained by consideration of the variation of the ZX:ZY ratios from the expected (and experimentally observed with the photoelastic modulator) 1:1 ratios. In Table 4.14 data is only presented for which the uncertainties of the measurement were not considered to be overwhelming.

The $F_2 \rightarrow W_1$ transition provides a good example of the failure of the naive approach of looking at only the YX:YY polarisation ratios. It is seen that the relative intensities of YX:YY=1:2 are consistent with a σ-polarised electric dipole fluorescence transition, and hence a transition between unlike irreps. However this assignment of a σ-polarised transition would also imply a 2:1 ratio for the YY:ZX intensities, whereas intensities of YY:ZX$\approx$1:1 are actually observed, which implies a σ' transition between unlike irreps. This contradiction is only resolved by recognising the transition as being between like irreps. Further, the relative intensities are not consistent with a purely electric dipole transition, as there is no solution for the transition moments σ and π for which $\pi(1:0:1) + \sigma(1:2:1)$ =1:2:2. Hence this transition further serves to make the point that magnetic dipole transition moments cannot be assumed to be insignificant in comparison to the electric dipole moments.

A number of transitions are observed to proceed via a significant magnetic dipole transition moment. To account for these transitions it is noted that an expansion of the free-ion wavefunctions beyond that given on page 35 shows the emitting $^4F_{9/2}$ multiplet

Table 4.14: Polarised fluorescence data for the SrF_2:$Dy^{3+}C_{4v}$ center, for $Z_1 \rightarrow F_2$ σ-polarised excitation. The dominant electric or magnetic dipole process is noted for fluorescence transitions between states transforming as unlike irreps.

Transition	Energy (cm^{-1})	irreps (C.F. Fit)	YX	YY	ZX	ZY	Notes
$F_1 \rightarrow Z_1$	21020	$\Gamma_7 \rightarrow \Gamma_7$	3.2	1.0	3.9	3.4	a
$F_2 \rightarrow Z_2$	21005	$\Gamma_6 \rightarrow \Gamma_7$	1.0	1.3	1.0	1.3	?
$F_1 \rightarrow Z_2$	20982	$\Gamma_7 \rightarrow \Gamma_7$	1.9	1.0	2.7	2.6	c
$F_1 \rightarrow Z_3$	20967	$\Gamma_7 \rightarrow \Gamma_6$	1.0	1.8	1.2	1.1	(e.d. transition)
$F_1 \rightarrow Z_4$	20926	$\Gamma_7 \rightarrow \Gamma_7$	1.0	1.5	1.2	1.3	?
$F_1 \rightarrow Y_1$	17477	$\Gamma_7 \rightarrow \Gamma_7$	1.9	1.0	1.9	1.8	c
$F_2 \rightarrow Y_2$	17468	$\Gamma_6 \rightarrow \Gamma_6$	8.9	1.0	9.4	7.8	a,c
$F_2 \rightarrow Y_3$	17455	$\Gamma_6 \rightarrow \Gamma_7$	1.0	1.7	1.1	1.0	(e.d. transition)
$F_2 \rightarrow Y_4$	17448	$\Gamma_6 \rightarrow \Gamma_6$	1.0	1.2	1.1	1.0	d
$F_1 \rightarrow Y_2$	17445	$\Gamma_7 \rightarrow \Gamma_6$	1.2	1.6	1.2	1.0	(e.d. transition)
$F_1 \rightarrow Y_3$	17433	$\Gamma_7 \rightarrow \Gamma_7$	1.0	1.1	1.0	1.0	d
$F_1 \rightarrow Y_4$	17425	$\Gamma_7 \rightarrow \Gamma_6$	1.0	1.6	1.0	1.1	(e.d. transition)
$F_2 \rightarrow X_1$	15183	$\Gamma_6 \rightarrow \Gamma_7$	2.0	1.3	1.6	1.0	(m.d. transition)
$F_1 \rightarrow X_1$	15160	$\Gamma_7 \rightarrow \Gamma_7$	1.2	1.0	1.2	1.1	d
$F_1 \rightarrow X_3$	15063	$\Gamma_7 \rightarrow \Gamma_7$	1.0	2.7	3.0	2.7	b
$F_1 \rightarrow X_4$	15058	$\Gamma_7 \rightarrow \Gamma_6$	1.8	1.1	1.1	1.0	(m.d. transition)
$F_1 \rightarrow X_5$	14995	$\Gamma_7 \rightarrow \Gamma_7$	1.0	1.8	1.9	2.0	b
$F_2 \rightarrow W_1$	13416	$\Gamma_6 \rightarrow \Gamma_6$	1.0	2.0	2.6	2.2	b
$F_1 \rightarrow W_1$	13393	$\Gamma_7 \rightarrow \Gamma_6$	2.0	1.0	1.4	1.1	(m.d. transition)
$F_1 \rightarrow W_2$	13365	$\Gamma_7 \rightarrow \Gamma_7$	1.0	1.2	1.8	1.4	b
$F_1 \rightarrow W_3$	13288	$\Gamma_7 \rightarrow \Gamma_6$	2.4	1.0	1.6	1.1	(m.d. transition)
$F_1 \rightarrow W_4$	13254	$\Gamma_7 \rightarrow \Gamma_7$	1.0	2.8	4.3	3.0	b
$F_1 \rightarrow A_1$	12015	$\Gamma_7 \rightarrow \Gamma_7$	1.8	1.0	1.9	1.2	c
$F_1 \rightarrow A_2$	11982	$\Gamma_7 \rightarrow \Gamma_6$	2.0	1.8	1.2	1.0	

a) $\frac{1}{2} \leq \frac{YX}{YY} \leq 2$ not satisfied
b) $1 \leq \frac{YX}{ZX} \leq 2$ not satisfied
c) $1 \leq \frac{YY}{ZX} \leq 2$ not satisfied
d) a$\rightarrow$c satisfied, but conflict in ratios

to contains an admixture of ≈9% $^6F_{9/2}$. Therefore the fluorescence transitions to the W manifold ($\sim {}^6F_{11/2}$) and the A manifold ($\sim {}^6F_{9/2}$) will satisfy the ΔL, $\Delta S = 0$, $|\Delta J| = 0, 1$ magnetic dipole selection rules. The magnetic dipole transitions to the $^6H_{11/2}$ multiplet are allowed through a small admixture of $^6F_{11/2}$ to the terminating multiplet.

The polarisation data has facilitated the irrep labelling of 19 of the 33 experimentally determined energy levels. Referring to the earlier discussion of the fluorescence to the $^6H_{11/2}$ multiplet, it is noted that the X_3 level is clearly identified as Γ_7 and transitions to the X_4 level are consistent with a Γ_6 assignment.

It is noted that this method of analysis of the polarised fluorescence in principle enables the relative magnitude of electric and magnetic transition moments to be determined. As the magnetic dipole moments can be calculated directly from the wavefunctions, this would lead to a determination of the electric dipole transition moments without the experimental difficulties involved in calibration of absolute intensities.

4.3.3 $SrF_2:Dy^{3+}$ C_{4v} crystal-field analysis.

A least-squares fitting program, f-shell empirical, written by Dr. Mike Reid, has been employed to evaluate crystal field parameters and generate wavefunctions from the experimentally determined energy levels. The irrep assignments implied from the polarisation data were also taken into account for this calculation.

The free-ion relativistic corrections and three-body parameters were taken as the values given by Carnell, Crosswhite and Crosswhite [12] for Dy^{3+} in $LaCl_3$. The free-ion Slater parameters, spin-orbit, and crystal field parameters were allowed to vary, with the initial Slater and spin-orbit parameters also taken from the $LaCl_3:Dy^{3+}$ values reported by Carnell et.al.

For initial irrep and level assignments a preliminary calculation was carried out using the free-ion parameters of Carnell et.al. and crystal-field parameters interpolated from the values reported for the C_{4v} centers of $SrF_2:Tb^{3+}$ [74] and $SrF_2:Ho^{3+}$ [72, 103]. The levels were then assigned according to this preliminary calculation, except for those cases where this assignment was in disagreement with the irreps inferred from the polarisation measurements. A least-squares fitting of a subset of these assigned levels was performed, and assignments altered where it was found that the resulting calculation placed levels inappropriately, for example by swapping the level ordering. Additional experimental levels were progressively added to the calculation in an iterative procedure. This procedure proved effective in providing irreps consistent with the polarisation data for all levels included, with the minor exception of the X_2 and X_3 lev-

els, where the ordering was swapped. However, given that the calculation places these levels within $3\,cm^{-1}$of each other, this was not considered to be a significant deviation outside of the general difference between calculated and experimental energy levels of $\leq 10\,cm^{-1}$.

A final standard deviation of $7.6\,cm^{-1}$ was obtained between the 33 experimental levels included in the least squares fitting and the calculated energy levels.

The wavefunctions obtained from this procedure were used in the analysis of the infrared-Zeeman measurements reported in Section 4.5. The calculated and experimental Zeeman splitting patterns match sufficiently well to add to the confidence in the crystal-field calculation.

The free-ion parameters that were not varied from those given by Carnell et.al. are tabulated in Table 4.15. The crystal-field, spin-orbit and Slater parameters that were found from the least-squares fitting procedure are given in Table 4.16. The calculated and experimental energy levels are presented in Table 4.17. Finally, Figure 4.19 presents the crystal-field parameters that have been reported for SrF_2:RE^{3+} C_{4v} centers for seven lanthanide ions (Ce, Pr, Nd, Sm, Eu, Tb, Ho) and those for the Dy^{3+} calculation reported here. The magnitude of the B_c^4 parameter obtained from the Dy^{3+} crystal-field calculation would appear to be too large to fit with a smooth trend across the rare-earth series. However, in light of the quite successful Zeeman measurements to be discussed in Section 4.5, this is not taken as an indication of any major inadequacy in the crystal-field calculation.

Attempts to constrain the B_c^4 parameter to a magnitude in line with the value interpolated from the Tb^{3+} and Ho^{3+} parameters have not proved successful. Fixing the B_c^4 parameter to a value of -1100 cm^{-1}, and allowing the remaining crystal-field parameters to vary in the least-squares calculation gives rise to significant changes in the calculated energy levels scheme, including a changed level ordering that is inconsistent with the irrep assignments derived from the polarised fluorescence data.

Table 4.15: Minor free-ion parameters for Dy^{3+} used in the crystal-field calculations. Parameters are as taken from Carnell, Crosswhite and Crosswhite [12].

Parameter	value (cm^{-1})	Parameter	value (cm^{-1})
M_{Tot}	3.92	T_2	-423
P_{Tot}	771	T_3	-50
α	17.64	T_4	-117
β	-608	T_6	334
γ	1498	T_7	-432
		T_8	-353

Table 4.16: The crystal-field and free-ion parameters for the C_{4v} center in $SrF_2:Dy^{3+}$ found from a least-squares fitting to the experimental data. For comparison the parameters for the C_{4v} center of $SrF_2:Ho^{3+}$ taken from reference [103] are also presented. All parameter values are given in units of cm^{-1}.

Parameter	SrF_2:Dy C_{4v}	SrF_2:Ho (A center)
F_2	94448	—
F_4	67892	—
F_6	45273	—
ζ	1916	—
B_a^2	346	338
B_a^4	434	297
B_a^6	322	325
B_c^4	-1334	-1030
B_c^6	502	488

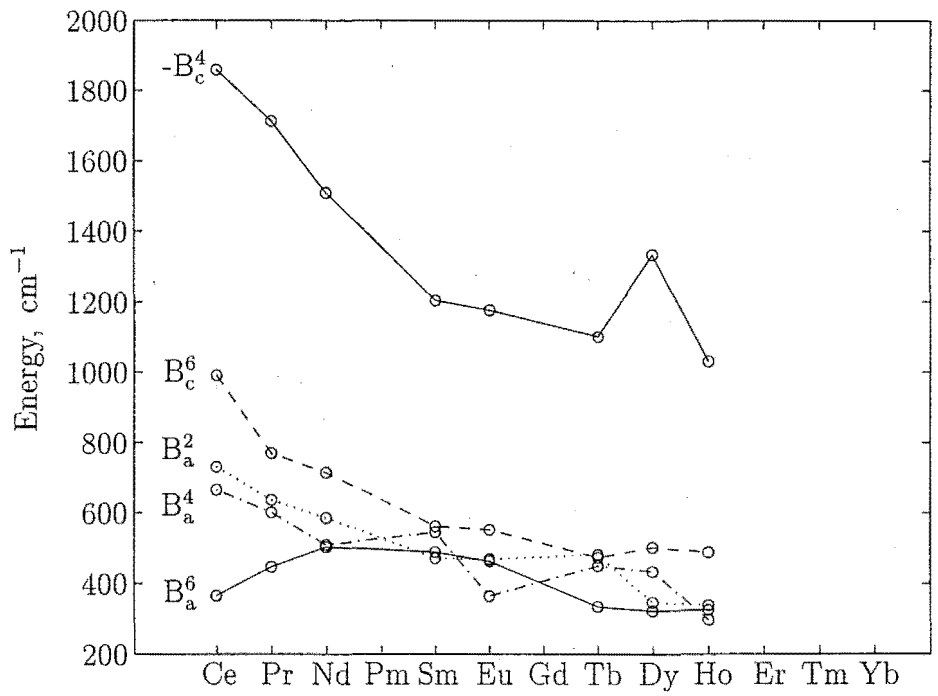

Figure 4.19: Reported crystal field parameters for C_{4v} center in SrF_2:RE^{3+}, and those found here for SrF_2:Dy^{3+}. The references for the parameters for rare-earths other than Dy are: Ce [35], Pr [85], Nd [38], Sm [103], Eu [103], Tb [74], Ho [72].

Table 4.17: Experimental and calculated energy levels for the SrF_2:Dy^{3+} C_{4v} center. † Levels not used in the least-squares calculation. * Levels with supporting polarisation data for irrep assignment.

Multiplet	Level	Irrep	Energy (cm^{-1})	
			Calc.	Expt.
$^6H_{15/2}$	Z_1*	γ_7	2.2	0.0
	Z_2*	γ_7	35	38
	Z_3*	γ_6	45	53
	Z_4*	γ_7	93	94
	Z_5	γ_6	157	
	Z_6	γ_6	227	
	Z_7	γ_6	441	
	Z_8	γ_7	472	
$^6H_{13/2}$	Y_1*	γ_7	3549	3543
	Y_2*	γ_6	3574	3575
	Y_3*	γ_7	3590	3587
	Y_4*	γ_6	3595	3595
	Y_5	γ_7	3669	3671
	Y_6	γ_7	3762	
	Y_7	γ_6	3791	
$^6H_{11/2}$	X_1*	γ_7	5859	5860
	X_2	γ_6	5953	
	X_3*	γ_7	5950	5957
	X_4*	γ_6	5965	5962
	X_5*	γ_7	6033	6025
	X_6	γ_6	6038	6033
$^6H_{9/2}$, $^6F_{11/2}$	W_1*	γ_6	7627	7627
	W_2*	γ_7	7646	7655
	W_3*	γ_6	7739	7732
	W_4*	γ_7	7772	7766
	W_5	γ_6	7797	7792
	W_6	γ_7	7844	
	W_7	γ_6	7875	
	W_8	γ_7	7892	
	W_9	γ_6	7987	
	W_{10}	γ_7	8124	
	W_{11}	γ_6	8131	

continued on next page

continued from previous page

Multiplet	Level	Irrep	Energy (cm^{-1})	
			Calc.	Expt.
$^6H_{7/2}$, $^6F_{9/2}$	A_1*	γ_7	9006	9005
	A_2	γ_6	9034	9038
	A_3	γ_6	9075	9080
	A_4	γ_7	9207	9195†
	A_5	γ_6	9258	9236†
	A_6	γ_7	9272	9281†
	A_7	γ_6	9287	9329†
	A_8	γ_7	9343	9365†
	A_9	γ_6	9560	9582 †
$^6H_{5/2}$	B_1	γ_7	10168	10172
	B_2	γ_6	10370	10360
	B_3	γ_7	10381	10390
$^6F_{7/2}$	C_1	γ_6	11048	11041
	C_2	γ_7	11141	11139
	C_3	γ_7	11205	11214
	C_4	γ_6	11241	11247
$^6F_{5/2}$	D_1	γ_7	12491	
	D_2	γ_6	12523	
	D_3	γ_7	12602	
$^6F_{3/2}$	E_1	γ_6	13337	
	E_2	γ_7	13340	
$^6F_{1/2}$	—	γ_6	13882	
$^4F_{9/2}$	F_1*	γ_7	21020	21020
	F_2*	γ_6	21038	21043
	F_3	γ_7	21151	21162
	F_4	γ_6	21187	21171
	F_5	γ_6	21483	

Number of data points	33
Number of free parameters	10
Standard deviation	7.6 cm^{-1}

4.4 The $SrF_2:Dy^{3+}$ C_{3v} center.

For the C_{3v} center in $SrF_2:Dy^{3+}$, one of the striking features apparent in the narrowband excitation spectrum is the increased (relative to the C_{4v} center) intensity of the vibronic absorption transitions to the $^4F_{9/2}$ multiplet. Figure 4.20 reproduces the C_{3v} narrowband spectrum of Section 4.2 (p. 42), with the added inclusion of vibronic transition assignments.

Through measurements of the far infrared reflection and transmission properties of pure SrF_2 Kaiser et.al. [53] have identified the transverse optical phonon to have an energy of $217\,cm^{-1}$. The $\approx 217\,cm^{-1}$ electronic-vibronic separation of the transitions indicated in the lower part of the excitation spectrum is consistent with these infrared measurements.

The physical origin of the $\approx 135\,cm^{-1}$ vibronic transitions indicated in Fig. 4.20 is not so apparent as there are no peaks in the SrF_2 phonon density of states in this region [28]. Richman [89] has reported similar vibronics of $\approx$140cm in the $SrF_2:Sm^{2+}$ system, but refrains from offering any particular assignment to the phonon involved in the transitions. Likewise, in a paper that discusses the luminescence of trigonal centers in $SrF_2:Dy^{3+}$, Eremin, Luks and Stolov [34] observe a $134\,cm^{-1}$ repetition in the fluorescence spectrum to the ground multiplet, which was also attributed to vibronic transitions.

The excitation spectrum of Figure 4.20, and the fluorescence spectra to be discussed in the following section, offer evidence for both the $\approx 217\,cm^{-1}$ transverse optical and $\approx 135\,cm^{-1}$ vibronics in $SrF_2:Dy^{3+}$ C_{3v} centers.

4.4.1 Laser selective fluorescence

The chosen $^4F_{9/2}$ excitation for the C_{3v} center fluorescence studies was the $Z_1 \rightarrow F_2$ transition at $20967\,cm^{-1}$. The F_1 level is placed only $2.5\,cm^{-1}$ below F_2. The choice of excitation into the F_2 level was made because of the greater absorption strength, as shown in the narrowband excitation spectra.

$^6H_{15/2}$ multiplet.

For C_{3v} center fluorescence to the ground state multiplet, the spectrometer shutter was closed when positioned within $5\,cm^{-1}$ of the laser frequency. Therefore transitions to the Z_1 level were not directly observed as this eliminated both the F_1 and F_2 emission

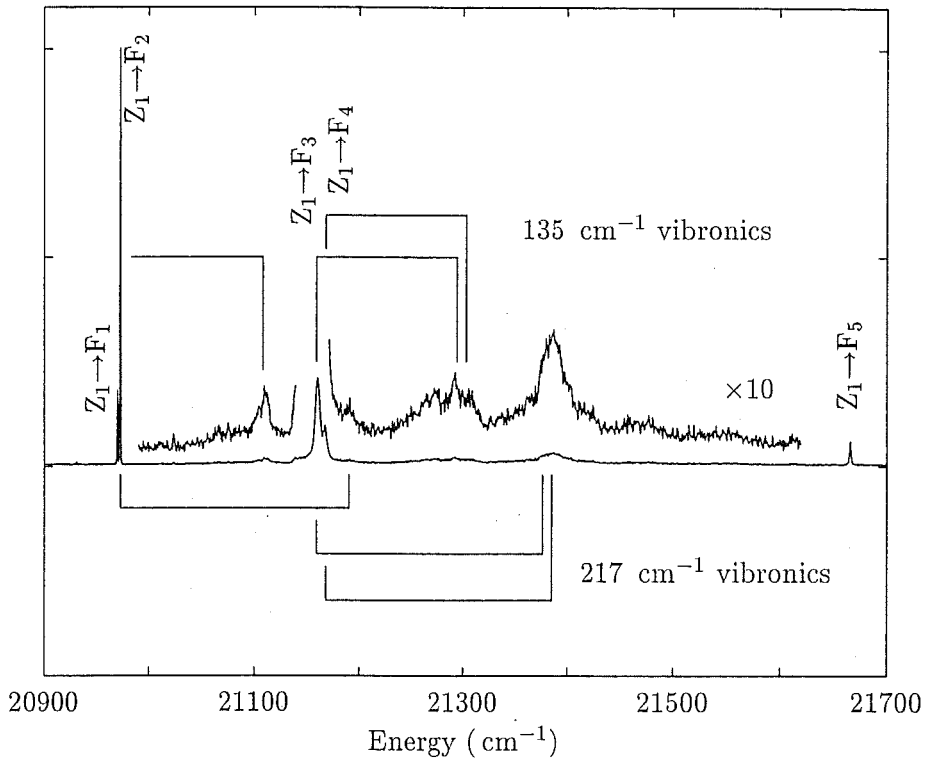

Figure 4.20: Narrowband excitation of the $^4F_{9/2}$ multiplet for the C_{3v} center in SrF_2. The vibronic interval of $134\,cm^{-1}$ is indicated for several transitions, along with the transverse optic interval of $217\,cm^{-1}$.

to that level.

In the fluorescence spectra of Figure 4.21 it is noticed that the F_1–F_2 splitting in the transitions to the Z_2 level is resolved. However, because of the broadening of the higher energy levels of $^6H_{15/2}$ this splitting is not resolved for any of the remaining transitions to this multiplet. The broadening of energy levels and transitions, and the consequent lack of resolution of the F_1 and F_2 emission, is a recurring feature of the C_{3v} center fluorescence. It has the consequence that when determining the energies of the terminating states from the fluorescence transition frequencies, less accuracy is obtained than would otherwise be possible. As this only introduces an additional uncertainty of $\approx 2\,cm^{-1}$ into the inferred energy levels, it is not considered to be a significant problem.

It is also apparent that the number of transitions to the ground multiplet by far exceeds that expected for the eight levels of $^6H_{15/2}$. These excess transitions are attributed to vibronic transitions, and a correlation with the phonon intervals observed in the excitation spectrum is observed. Many of these transitions are consistent with a $\approx 135\,cm^{-1}$

vibronic interval. Of those vibronic transitions so indicated in Figure 4.21, those associated with the $F_{1,2} \rightarrow Z_2, Z_3, Z_4$ electronic transitions were also identified by Eremin et.al. [34]. Clearly not all the excess transitions can be ascribed to vibronics involving a phonon of such a frequency. Further inclusion of a $217\,cm^{-1}$ interval, corresponding to the transverse optical phonon, enables assignments to be made for many of the remaining transitions.

Figure 4.21 includes an indication of the assigned electronic transitions to the Z_2, Z_3 and Z_4 energy levels, along with transitions that can be associated with the $\approx 134\,cm^{-1}$ and $217\,cm^{-1}$ vibronic emission to these levels. In assigning the remaining electronic transitions to the levels of $^6H_{15/2}$, the crystal-field calculation of Section 4.4.2 has been taken into account, which predicts the energy levels Z_6 and Z_7, Z_8 to lie at energies of $\approx 500\,cm^{-1}$ and $\approx 570\,cm^{-1}$ respectively. Transitions consistent with this calculation are observed and they also reveal some associated vibronic transitions. These transitions are appropriately indicated in Figure 4.21. Calculations also suggest a $\approx$5-10 cm^{-1} separation of the Z_4 and Z_5 states, and therefore transitions to the Z_5 level may well be masked by the broad $F_{1,2} \rightarrow Z_4$ transition and nearby vibronic transitions.

The $^4F_{9/2} \rightarrow {}^6H_{15/2}$ transition frequencies and their assignments are given in Table 4.18, along with the inferred energy levels of the $^6H_{15/2}$ multiplet.

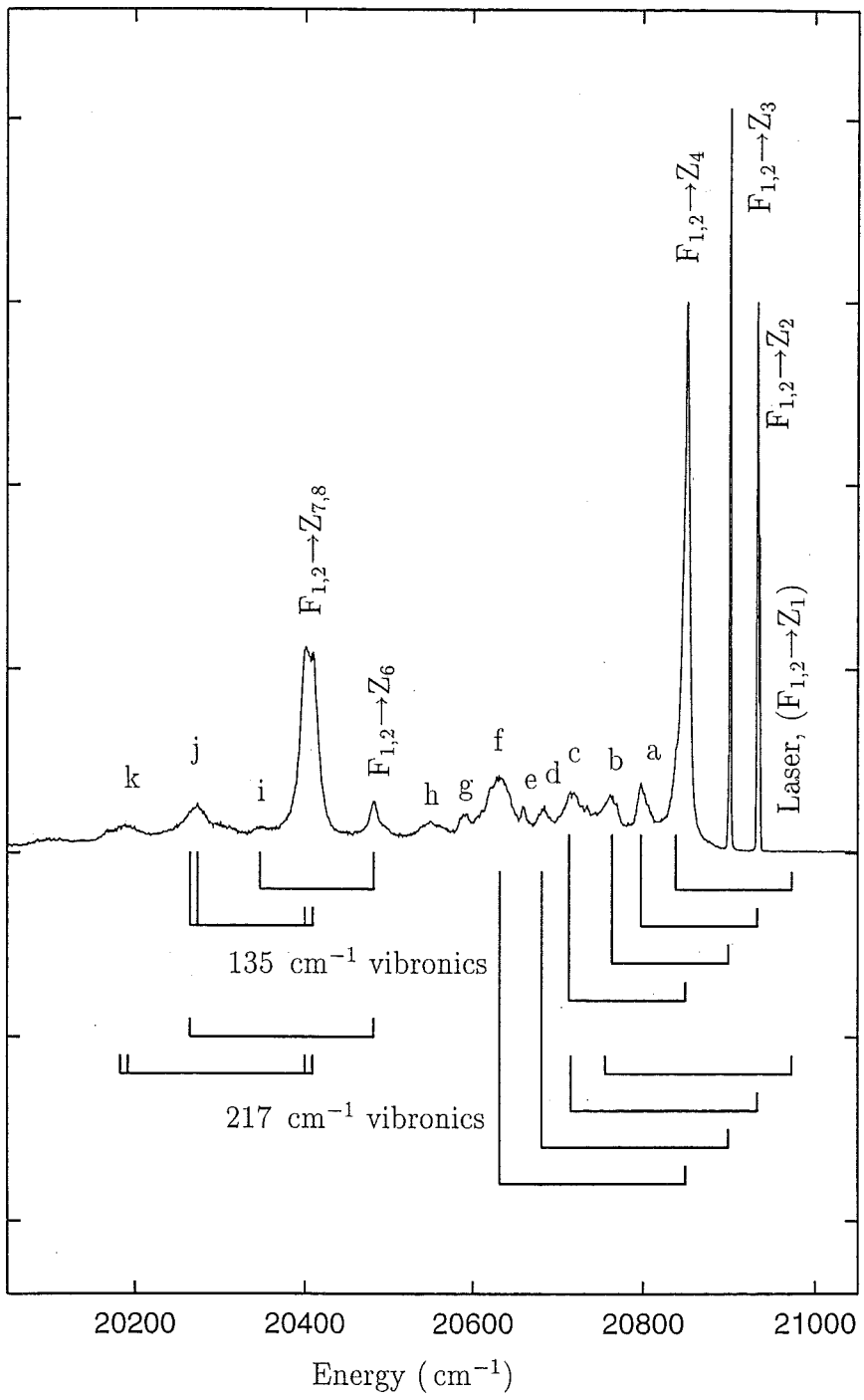

Figure 4.21: 15 K fluorescence spectrum of the C_{3v} center in SrF_2:Dy^{3+} for the $^4F_{9/2} \rightarrow {}^6H_{15/2}$ transitions. The vibronic interval of 134 cm^{-1} is indicated for several transitions, as are vibronic transitions associated with the 217 cm^{-1} transverse optical phonon. The spectrometer shutter was closed in the region of the laser frequency, hence masking the $F_{1,2}\rightarrow Z_1$ transitions.

Label	Fluorescence energy	Assignment
	20927.6 ±0.5	$F_2 \rightarrow Z_2$
	20925.4 ±0.5	$F_1 \rightarrow Z_2$
	20893.4 ±1	$F_{1,2} \rightarrow Z_3$
	20843.4 ±1	$F_{1,2} \rightarrow Z_4$
a	20790	$F_{1,2} \rightarrow Z_2 + 135\,cm^{-1}$
b	20754	$F_{1,2} \rightarrow Z_3 + 135\,cm^{-1}$
c	20704	$F_{1,2} \rightarrow Z_4 + 135\,cm^{-1}$
d	20677	$F_{1,2} \rightarrow Z_3 + 217\,cm^{-1}$
e	20652	
f	20624	$F_{1,2} \rightarrow Z_4 + 217\,cm^{-1}$
g	20582	
h	20542	
	20475	$F_{1,2} \rightarrow Z_6$
	20402	$F_{1,2} \rightarrow Z_7$
	20395	$F_{1,2} \rightarrow Z_8$
i	20340	$F_{1,2} \rightarrow Z_6 + 135\,cm^{-1}$
j	20267	$F_{1,2} \rightarrow Z_{7,8} + 135\,cm^{-1}$
k	20180	$F_{1,2} \rightarrow Z_{7,8} + 217\,cm^{-1}$

$^6H_{15/2}$ Level	Energy (cm^{-1})
Z_1	0
Z_2	39
Z_3	73
Z_4	123
Z_5	—
Z_6	491
Z_7	564
Z_8	571

Table 4.18: Transition frequencies for the $^4F_{9/2} \rightarrow {}^6H_{15/2}$ fluorescence of the SrF_2:Dy^{3+} C_{3v} center and the inferred energy levels of the $^6H_{15/2}$ multiplet. All transition frequencies are given in vacuum wavenumbers, with an uncertainty of $\pm 2\,cm^{-1}$ unless otherwise stated.

$^6H_{13/2}$ multiplet.

From the emission to the $^6H_{13/2}$ multiplet, as shown in Figure 4.22, four of the seven energy levels of this multiplet can be directly determined. Transitions to the remaining three levels are obscured by what are assigned as vibronic transitions. These vibronics, as indicated in the spectrum, have the same phonon offsets of 135 cm^{-1} and 217 cm^{-1} as discussed previously. The clear observation of the $F_{1,2}\rightarrow X_1+135\,cm^{-1}$ vibronic adds to the confidence in the assignment of 135 cm^{-1} phonons associated with the Dy^{3+} C_{3v} center. The broad peak at $\approx$17200 cm^{-1} is consistent with the possibility of several vibronic transitions of this frequency. However it is noted that crystal field calculations also place an electronic level (X_5) at an energy such that the $F_{1,2}\rightarrow Y_5$ transitions would also be expected to be in the region of 17200 cm^{-1}. Of the three peaks between 17100 cm^{-1} and 17150 cm^{-1} only the two lower frequency transitions are consistent with vibronics associated with the two phonon frequencies of 135 cm^{-1} and 217 cm^{-1}. The higher frequency transition is assigned as electronic, partially guided by crystal-field calculations which place both the Y_6 and Y_7 levels at an energy such that the $F_{1,2}\rightarrow Y_6, Y_7$ transitions have a frequency within 5 cm^{-1} of this observed emission. The remaining structure present in the fluorescence to the $^6H_{13/2}$ multiplet has not been accounted for. Transition frequencies and the inferred energy levels of the $^6H_{13/2}$ multiplet are shown in Table 4.19.

Label	Fluorescence energy	Transition
	17413	$F_2\rightarrow Y_1$
	17411	$F_1\rightarrow Y_1$
	17342	$F_2\rightarrow Y_2$
	17340	$F_1\rightarrow Y_2$
	17328	$F_{1,2}\rightarrow Y_3$
	17324	$F_2\rightarrow Y_4$
	17322	$F_1\rightarrow Y_4$
a	17273	$F_{1,2}\rightarrow Y_1$ +135 cm^{-1}
b	17193 ±5	$F_{1,2}\rightarrow Y_1$ +217 cm^{-1} and Y_5 ?
	17136	$F_{1,2}\rightarrow Y_{6,7}$
c	17124	$F_{1,2}\rightarrow Y_2$ + 217 cm^{-1}
d	17108	$F_{1,2}\rightarrow Y_{3,4}$ + 217 cm^{-1}

$^6H_{13/2}$ Level	Energy (cm^{-1})
Y_1	3554
Y_2	3625
Y_3	3638
Y_4	3643
Y_5	—
Y_6	3830±5 †
Y_7	3830±5 †

Table 4.19: Transition frequencies for the $^4F_{9/2} \rightarrow {}^6H_{13/2}$ fluorescence of the SrF_2:Dy^{3+} C_{3v} center, and the inferred energy levels of the terminating multiplet. All transition frequencies and energies are given in vacuum wavenumbers, with an uncertainty of ±2 cm^{-1} unless otherwise stated. † indicates a level not used in the least-squares crystal-field calculation.

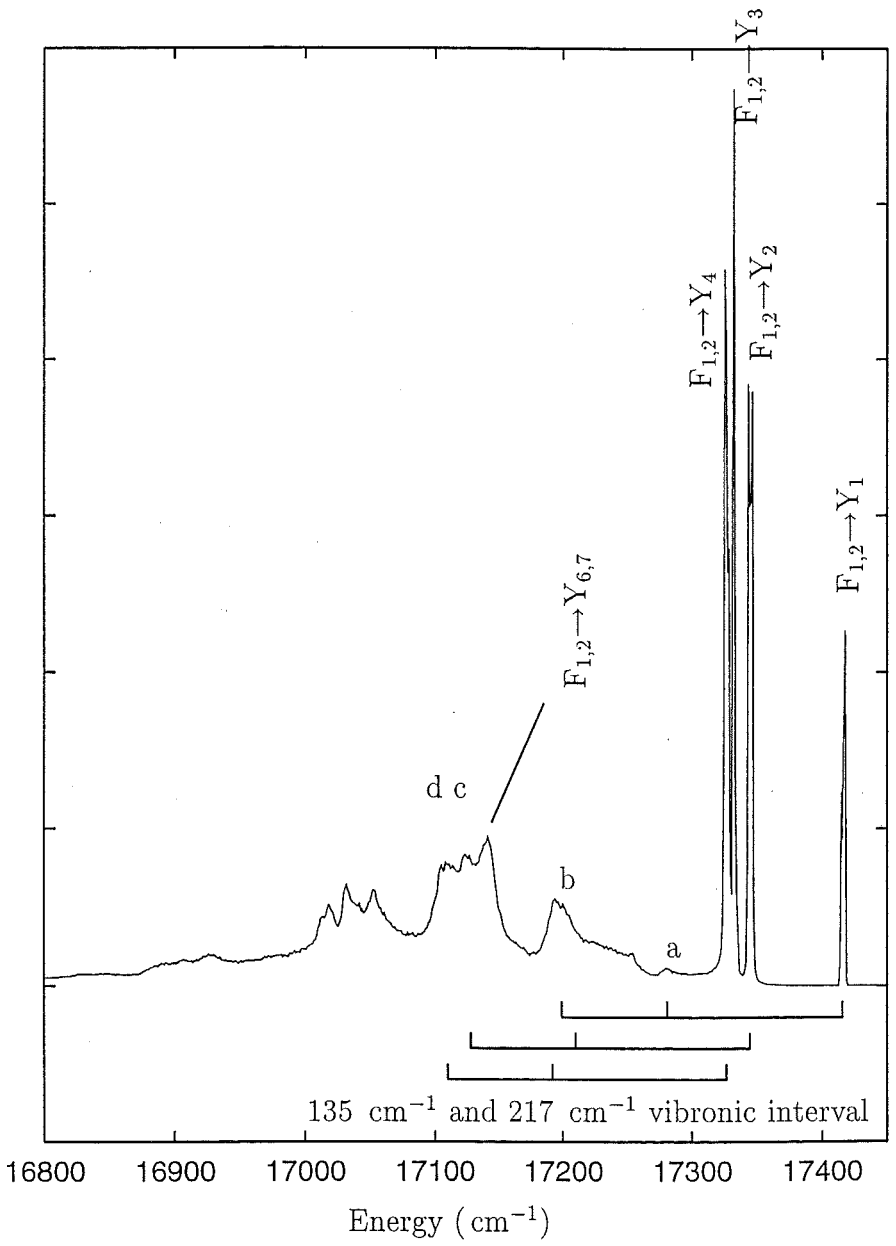

Figure 4.22: 15 K $^4F_{9/2} \rightarrow {}^6H_{13/2}$ fluorescence spectrum of the SrF_2:Dy^{3+} C_{3v} center.

$^6H_{11/2}$ multiplet.

The fluorescence to the $^6H_{11/2}$ multiplet, shown in Fig. 4.23, allows the determination of all six energy levels of this multiplet. The entire span of the energy levels is less than $150\,cm^{-1}$, and the transitions are sufficiently sharp for the F_1 -F_2 separation to be observed in the transitions to all six terminating energy levels. Transitions of note are those to the X_2 levels, as these were not resolved from the X_3 transitions by the work of Eremin, Luks and Stolov [34].

No vibronic transitions to this multiplet have been observed. The presence of strong vibronic transitions in only the fluorescence to the two lower multiplets ($^6H_{15/2}$ and $^6H_{13/2}$) is also observed for the CaF_2:Dy^{3+} cubic center. While not necessarily explaining this occurrence of vibronic transitions, it is interesting to note that from the C_{4v} center polarised fluorescence data it appears that transitions to the two lower multiplets are distinct in that they are predominately electric-dipole processes, while transitions to the higher multiplets tend to proceed with a large magnetic-dipole contribution.

The $^4F_{9/2} \rightarrow {}^6H_{11/2}$ transition frequencies and the $^6H_{11/2}$ energy levels are tabulated in Table 4.20.

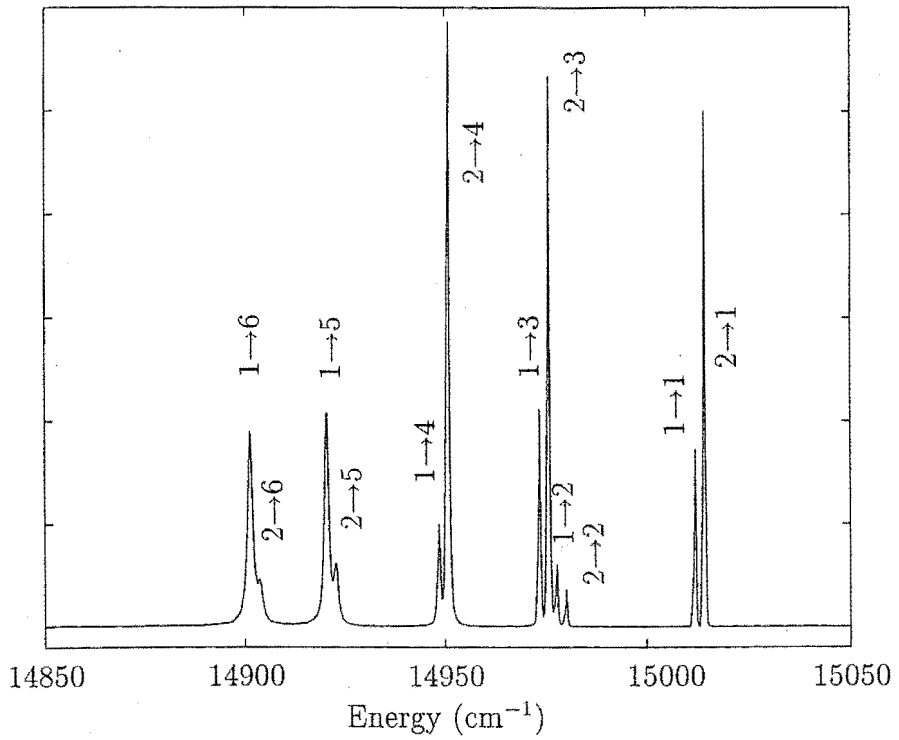

Figure 4.23: 15 K $^4F_{9/2} \rightarrow {}^6H_{11/2}$ fluorescence spectrum of the SrF_2:Dy^{3+} C_{3v} center.

Transition	Fluorescence energy
$F_2 \rightarrow X_1$	15010.5
$F_1 \rightarrow X_1$	15008.2
$F_2 \rightarrow X_2$	14976.4
$F_1 \rightarrow X_2$	14974.1
$F_2 \rightarrow X_3$	14972.2
$F_1 \rightarrow X_3$	14969.8
$F_2 \rightarrow X_4$	14947.1
$F_1 \rightarrow X_4$	14944.8
$F_2 \rightarrow X_5$	14918.6
$F_1 \rightarrow X_5$	14916.4
$F_2 \rightarrow X_6$	14899.7
$F_1 \rightarrow X_6$	14897.5

$^6H_{11/2}$ Level	Energy (cm^{-1})
X_1	5956.5
X_2	5990.0
X_3	5995.0
X_4	6020.0
X_5	6048.5
X_6	6067.0

Table 4.20: Transition frequencies for the $^4F_{9/2} \rightarrow {}^6H_{11/2}$ fluorescence of the SrF_2:Dy^{3+} C_{3v} center, and the inferred energy levels of the terminating multiplet. All transition frequencies and energies are given in vacuum wavenumbers, with an absolute uncertainty of $\pm 1\,cm^{-1}$ and an uncertainty in the splittings between transitions of $\pm 0.5\,cm^{-1}$.

$^6H_{9/2}$ and $^6F_{11/2}$ multiplets.

From emission to the W manifold, consisting of the mixed $^6H_{9/2}$ and $^6F_{11/2}$ multiplets, only a limited number of the terminating energy levels have been determined. Transitions to the first five energy levels, W_1 to W_5, are indicated in the spectrum of Figure 4.24. The F_1 -F_2 separation of $2.5\,cm^{-1}$ is resolved for transitions to W_1, W_2 and W_3, with a partially resolved splitting for transitions terminating on W_4. Transition frequencies and the inferred energy levels are shown in Table 4.21. The remaining six levels of this manifold could not be determined from the fluorescence spectrum.

The transition frequencies for the $F_{1,2}\rightarrow W_6$-W_9 expected on the basis of crystal-field calculations are also indicated in Figure 4.24. The transitions to W_{10} and W_{11} are predicted to be a further $\approx 300\,cm^{-1}$ lower in frequency, but were not observed.

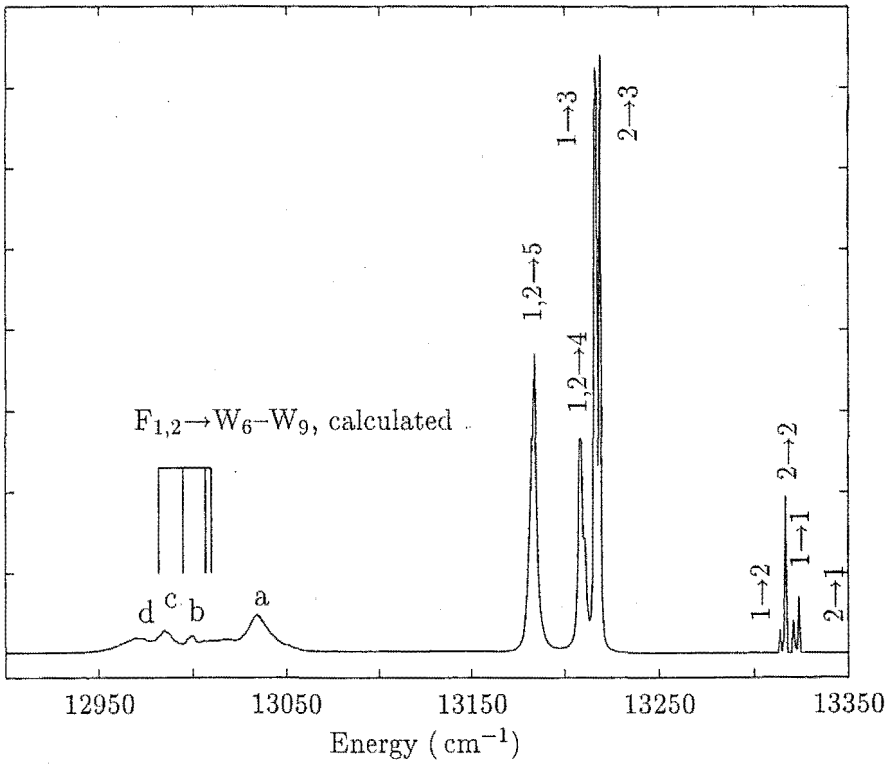

Figure 4.24: 15 K $^4F_{9/2} \rightarrow {}^6H_{9/2}$, $^6F_{11/2}$ (W manifold) fluorescence spectrum of the SrF_2:Dy^{3+} C_{3v} center.

line	Fluorescence energy	Transition
	13318	$F_2 \rightarrow W_1$
	13316	$F_1 \rightarrow W_1$
	13311	$F_2 \rightarrow W_2$
	13309	$F_1 \rightarrow W_2$
	13214	$F_2 \rightarrow W_3$
	13211	$F_1 \rightarrow W_3$
	13205	$F_{1,2} \rightarrow W_4$
	13179	$F_{1,2} \rightarrow W_5$
a	13030	
b	12995	
c	12981	
d	12966	

$^6H_{9/2}$, $^6F_{11/2}$ Level	Energy (cm^{-1})
W_1	7649
W_2	7655
W_3	7753
W_4	7761
W_5	7787
W_6 –W_{11}	—

Table 4.21: Transition frequencies for the $^4F_{9/2} \rightarrow {}^6H_{9/2}$, $^6F_{11/2}$ (W manifold) fluorescence of the SrF_2:Dy^{3+} C_{3v} center, and the inferred energies levels of the W manifold. All transition frequencies and energies are given in vacuum wavenumbers, with an uncertainty of $\pm 2\,cm^{-1}$.

$^6H_{7/2}$ and $^6F_{9/2}$ multiplets.

The fluorescence to the A manifold, consisting of the $^6H_{7/2}$ and $^6F_{9/2}$ multiplets, gives rise to a spectrum in which more than the nine expected transitions are observed (taking account of the F_1-F_2 splitting). In the spectrum of Figure 4.25 the fluorescence is grouped into two sets of transitions separated by $\approx 300\,cm^{-1}$. The fluorescence transitions terminating on the lower levels of the A manifold have narrow linewidths, and the F_1-F_2 splitting is resolved for transitions to A_1, A_2 and A_3. For the lower energy fluorescence it was advantageous to re-record the spectrum with the liquid N_2 cooled infrared photomultiplier tube, which is more sensitive in this region than the RCA C31034 tube, and this spectrum is also presented. Transitions frequencies for $F_{1,2} \rightarrow A_4$–A_8 predicted from the crystal-field calculations have also been indicated in Figure 4.25. The transition to the A_9 level is predicted to have a frequency of $\approx 11245\,cm^{-1}$, but is not observed. Some of these transitions below $11700\,cm^{-1}$have been tentatively assigned, but to avoid a circular argument the energy levels of the A manifold inferred from these transitions were not included in the crystal-field least-squares calculation.

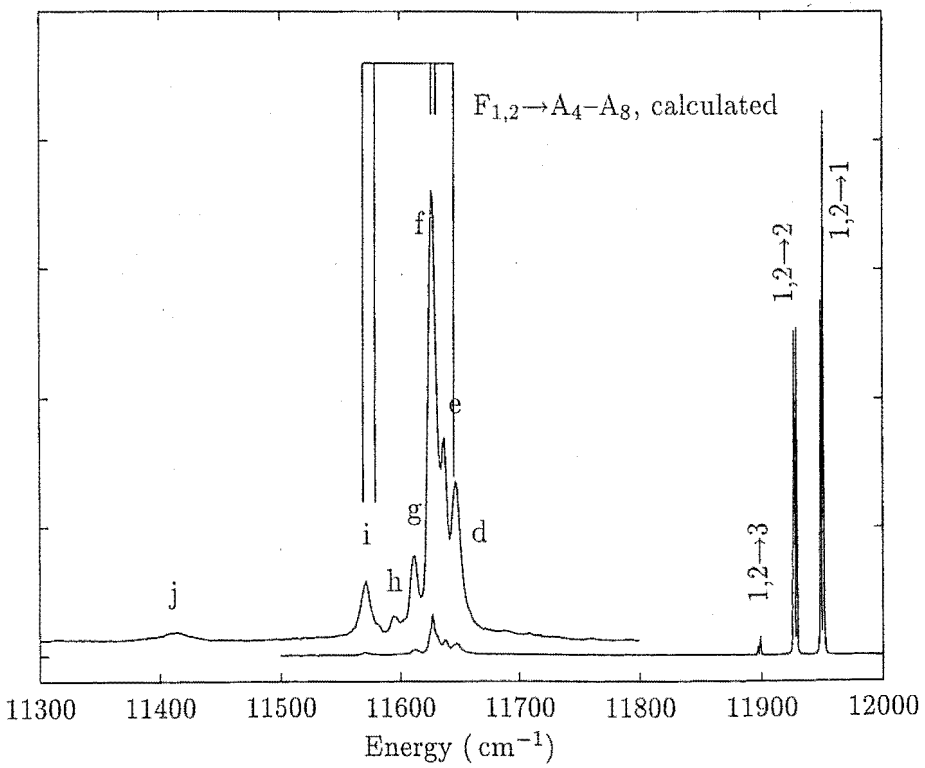

Figure 4.25: 15 K $^4F_{9/2} \rightarrow {}^6H_{7/2}$, $^6F_{9/2}$ (A manifold) fluorescence spectra of the SrF_2:Dy^{3+} C_{3v} center. The upper trace of the low energy fluorescence was recorded with the N_2 cooled infrared PMT.

Label	Fluorescence energy	Transition
	11948	$F_2 \rightarrow A_1$
	11946	$F_1 \rightarrow A_1$
	11926	$F_2 \rightarrow A_2$
	11923	$F_1 \rightarrow A_2$
	11896	$F_2 \rightarrow A_3$
	11894	$F_1 \rightarrow A_3$
d	11647	$F_{1,2} \rightarrow A_4$ †
e	11637	$F_{1,2} \rightarrow A_5$ †
f	11627	$F_{1,2} \rightarrow A_6$ †
g	11612	$F_{1,2} \rightarrow A_7$ †
h	11596	—
i	11572	$F_{1,2} \rightarrow A_8$ †
j	11414	$F_{1,2} \rightarrow A_6$ $+217\,cm^{-1}$ †

$^6H_{7/2}$ $^6F_{9/2}$ Level	Energy (cm^{-1})
A_1	9019
A_2	9041
A_3	9071
A_4	9319 †
A_5	9329 †
A_6	9339 †
A_7	9354 †
A_8	9394 †
A_9	—

Table 4.22: Transition frequencies for the $^4F_{9/2} \rightarrow {}^6H_{7/2}$, $^6F_{9/2}$ (A manifold) fluorescence of the SrF_2:Dy^{3+} C_{3v} center, and the inferred energies levels of the A manifold. All transition frequencies and energies are given in vacuum wavenumbers, with an uncertainty of $\pm 2\,cm^{-1}$. † indicates transitions and energy levels that are only tentatively assigned. Such energy levels were not included in the crystal-field least-squares calculation.

$^6H_{5/2}$ multiplet.

The $^4F_{9/2} \rightarrow {}^6H_{5/2}$ fluorescence as measured with the N_2 cooled infrared photomultiplier is presented in Fig. 4.26. The excited state splitting is not resolved for any of the three transitions. All the energy levels of the $^6H_{5/2}$ multiplet can be obtained from this fluorescence spectrum, and these energy levels are listed in Table 4.23, along with the transition frequencies.

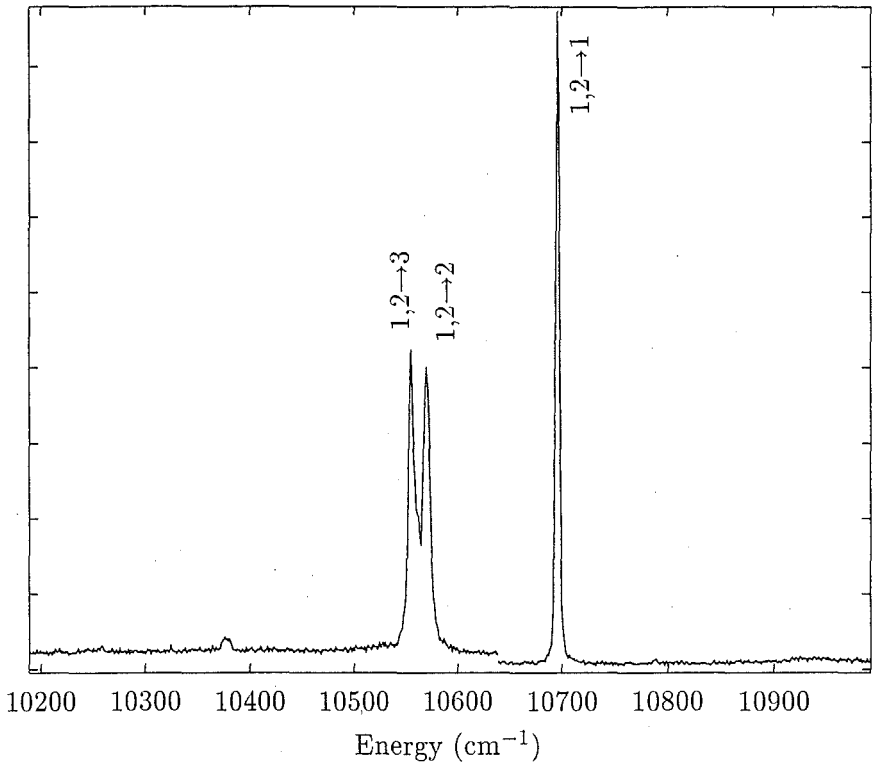

Figure 4.26: 15 K $^4F_{9/2} \rightarrow {}^6H_{5/2}$ fluorescence spectrum of the SrF_2:Dy^{3+} C_{3v} center.

Transition	Fluorescence energy
$F_{1,2} \rightarrow B_1$	10694
$F_{1,2} \rightarrow B_2$	10567
$F_{1,2} \rightarrow B_3$	10552

$^6H_{5/2}$ Level	Energy (cm^{-1})
B_1	10272
B_2	10399
B_3	10414

Table 4.23: Transition frequencies for the $^4F_{9/2} \rightarrow {}^6H_{5/2}$ fluorescence of the SrF_2:Dy^{3+} C_{3v} center, and the inferred energies levels of the terminating multiplet. All transition frequencies and energies are given in vacuum wavenumbers, with an uncertainty of $\pm 2\,cm^{-1}$.

$^6F_{7/2}$ multiplet.

The four energy levels of the $^6F_{7/2}$ multiplet have been determined from the fluorescence spectrum shown in Figure 4.27, and are tabulated in Table 4.24 along with the transition frequencies.

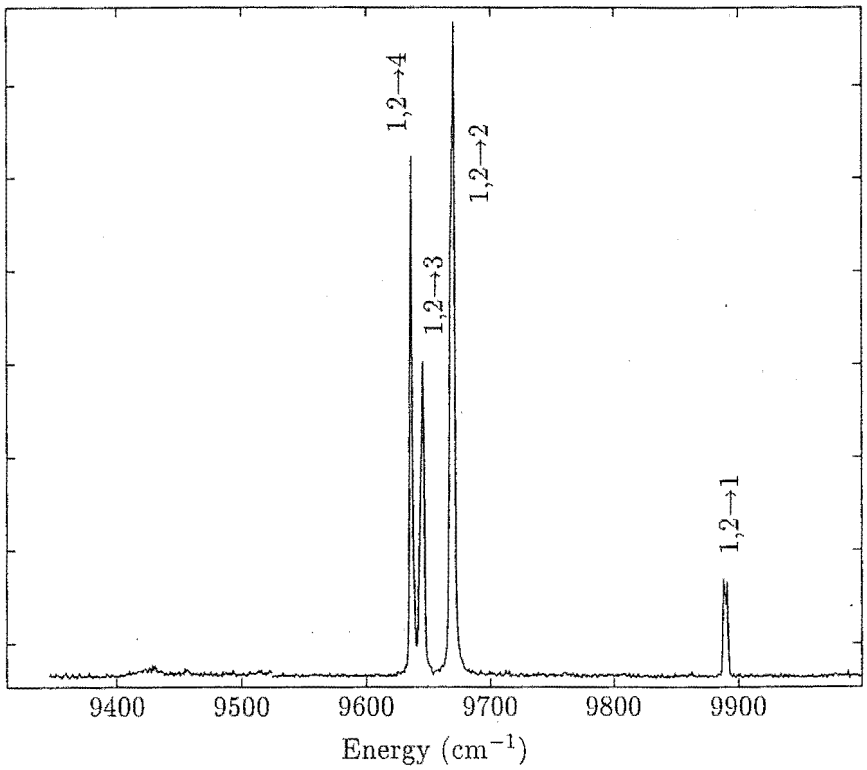

Figure 4.27: 15 K $^4F_{9/2} \rightarrow {}^6F_{7/2}$ fluorescence spectrum of the SrF_2:Dy^{3+} C_{3v} center.

Transition	Fluorescence energy
$F_2 \rightarrow C_1$	9885
$F_1 \rightarrow C_1$	9883
$F_{1,2} \rightarrow C_2$	9666
$F_{1,2} \rightarrow C_3$	9640
$F_{1,2} \rightarrow C_4$	9632

$^6F_{7/2}$ Level	Energy (cm^{-1})
C_1	11082
C_2	11300
C_3	11326
C_4	11334

Table 4.24: Transition frequencies for the $^4F_{9/2} \rightarrow {}^6F_{7/2}$ fluorescence of the SrF_2:Dy^{3+} C_{3v} center, and the inferred energy levels of the $^6F_{7/2}$ multiplet. All transition frequencies and energies are given in vacuum wavenumbers, with an uncertainty of $\pm 2\,cm^{-1}$.

4.4.2 $SrF_2:Dy^{3+}$ C_{3v} crystal-field analysis.

A crystal-field analysis was performed for the C_{3v} center with the same programs described in Section 4.3.3 (p. 64).

For the C_{3v} center it was not possible to use polarised fluorescence data to provide information on irrep assignment. The reasons for this are two-fold. First, the expected C_{3v} center polarisation ratios are intrinsically not well defined [21] due to the non-orthogonal nature of the eight possible orientations of the C_{3v} principal axis. Secondly, what polarisation behaviour there is will, for many transitions, be obscured by the overlapping and unresolved emission from both the F_1 and F_2 states (which are of different irreps). Therefore irrep assignment has been based solely on comparison between the calculated and experimentally determined energy levels. An initial calculation using the $SrF_2:Er^{3+}$ J center crystal field parameters [21] and the free-ion parameters of Carnell, Crosswhite and Crosswhite [12] was used to provide starting irrep assignments to the experimental energy levels. Further refinement of these assignments was carried out after a least squares fitting to the energy levels, and where a changed level ordering or large mismatch in calculated and experimental energies suggested a false assignment. For the calculation the minor free-ion parameters listed in Table 4.15, page 66, were held fixed and the Slater, spin-orbit and six C_{3v} crystal-field parameters were varied. The average energy of the configuration was also allowed to vary. A total of 38 experimental energy levels were used in the refinement of the parameters. A number of additional levels, which were not included in the calculation, are found to agree closely with the calculated energies. Such levels include the Y_6 and Y_7 states and several levels of the A manifold. These levels were not included in the calculations due to uncertainty in their measurement or assignment.

The resulting "best fit" parameters are shown in Table 4.25 along with the parameters reported for the trigonal center in $SrF_2:Ho^{3+}$ [71, 72, 103] and the trigonal J center in $SrF_2:Er^{3+}$ [21]. The reasonable similarity between the Dy^{3+} and Er^{3+} parameters is taken as an indication of the same structure of the two centers. Likewise, the disparity with the Ho^{3+} B center parameters indicates that the Ho^{3+} center is apparently anomalous in the lanthanide series. For comparison the parameters given by Eremin, Luks and Stolov [34] for the $SrF_2:Dy^{3+}$ C_{3v} center are also presented. Their analysis was based on fitting a total of 10 experimental energy levels (including the ground state) from the $^6H_{15/2}$ and $^6H_{13/2}$ multiplets to a crystal-field calculation which neglected J-mixing. A further 7 experimental levels from the $^6H_{11/2}$ and $^4F_{9/2}$ multiplets were also available for comparison but not directly included in the calculation because of the expected increased contribution of J-mixing to the calculations. The comparison of parameters required a transformation between the two different parametrisation schemes

used by Eremin et.al. and that used in this work. Eremin et.al. have employed a Hamiltonian of the form $\sum B_k^q V_k^q$ where the V_k^q are the homogeneous polynomials given by Al'tshuler [4], and are essentially the spherical harmonics with a different normalisation. Eremin et.al. also report only the absolute value of the B_4^3 and B_6^3 parameters, as the sign contains some ambiguity due to the possibility of different coordinate systems giving rise to different signs in these parameters [33]. To enable a comparison between parameters the following approach was employed. The parameters of both Eremin and those reported here were converted to the parametrisation scheme of Wybourne ($\sum B_q^k C_q^k$). The signs of Eremins B_3^4 and B_3^6 parameters were then chosen to match that found here. Eremins parameters were then further transformed from the Wybourne parametrisation to that used here. Note that any other choice of the signs for the B_3^4 and B_3^6 parameters gave a worse agreement than that obtained with the signs chosen as described. It is these twice transformed parameters of Eremin et.al. that are shown in Table 4.25. The relevant parameter transformations are given in Appendix A.

Table 4.26 presents a listing of all the calculated energy levels below $\approx$22000 cm^{-1} and the corresponding experimentally inferred energies. The standard deviation between the 38 experimental levels used in the least-squares procedure and the corresponding calculated levels is 6.6 cm^{-1}. A total of 11 parameters were varied in the calculation.

Table 4.25: The free-ion and crystal-field parameters found for the $SrF_2:Dy^{3+}$ C_{3v} center for refinement with 38 experimental energy levels. Parameters found by Eremin et.al., and those reported for other $SrF_2:RE^{3+}$ C_{3v} centers are given for comparison. All parameters are in units of cm^{-1}.

Parameter	SrF_2:Dy C_{3v} This work	SrF_2:Eu [103]	SrF_2:Ho (B) [71, 103]	SrF_2:Er (J) [21]	$SrF_2:Dy^{3+}$ [34]
F_2	94325	—	—	—	—
F_4	67516	—	—	—	—
F_6	45641	—	—	—	—
ζ	1913	—	—	—	—
B_a^2	184	221	52	189	206
B_a^4	99	171	-184	-142	-49
B_a^6	-18	-238	-526	-222	531
$B_a'^6$	85	-59	-149	106	-108
B_c^4	1423	1227	-58	1097	1369
B_c^6	1168	1152	605	999	972

Table 4.26: Experimental and calculated energy levels for the SrF_2:Dy^{3+} C_{3v} center. †: Levels not used in parameter refinement.

Multiplet	Level	Irrep	Energy (cm^{-1})	
			Calc.	Expt.
$^6H_{15/2}$	Z_1	$\gamma_{5,6}$	-1.7	0.0
	Z_2	γ_4	35	39
	Z_3	γ_4	69	73
	Z_4	$\gamma_{5,6}$	122	123
	Z_5	γ_4	128	
	Z_6	γ_4	499	491
	Z_7	$\gamma_{5,6}$	563	564
	Z_8	γ_4	567	571
$^6H_{13/2}$	Y_1	γ_4	3558	3554
	Y_2	γ_4	3620	3625
	Y_3	$\gamma_{5,6}$	3633	3638
	Y_4	γ_4	3643	3643
	Y_5	γ_4	3777	
	Y_6	γ_4	3837	3830†
	Y_7	$\gamma_{5,6}$	3840	3830†
$^6H_{11/2}$	X_1	γ_4	5968.5	5956.5
	X_2	$\gamma_{5,6}$	5984.5	5990.0
	X_3	γ_4	5991.5	5995.0
	X_4	γ_4	6029.5	6020.0
	X_5	$\gamma_{5,6}$	6057.0	6048.5
	X_6	γ_4	6077.9	6067.0
$^6H_{9/2}$, $^6F_{11/2}$	W_1	$\gamma_{5,6}$	7644	7649
	W_2	γ_4	7650	7655
	W_3	γ_4	7759	7753
	W_4	$\gamma_{5,6}$	7761	7761
	W_5	γ_4	7793	7787
	W_6	γ_4	7954	
	W_7	$\gamma_{5,6}$	7957	
	W_8	γ_4	7969	
	W_9	γ_4	7982	
	W_{10}	γ_4	8273	
	W_{11}	$\gamma_{5,6}$	8299	

continued on next page

continued from previous page

Multiplet	Level	Irrep	Energy (cm^{-1})	
			Calc.	Expt.
$^6H_{7/2}$, $^6F_{9/2}$	A_1	γ_4	9020	9019
	A_2	$\gamma_{5,6}$	9038	9041
	A_3	γ_4	9067	9071
	A_4	γ_4	9318	9319†
	A_5	$\gamma_{5,6}$	9334.5	9329†
	A_6	γ_4	9334.8	9339†
	A_7	$\gamma_{5,6}$	9384	9354†
	A_8	γ_4	9394	9394†
	A_9	γ_4	9722	
$^6H_{5/2}$	B_1	γ_4	10263	10272
	B_2	γ_4	10401	10399
	B_3	$\gamma_{5,6}$	10410	10414
$^6F_{7/2}$	C_1	γ_4	11088	11082
	C_2	γ_4	11288	11300
	C_3	γ_4	11327	11326
	C_4	$\gamma_{5,6}$	11336	11334
$^6F_{5/2}$	D_1	$\gamma_{5,6}$	12553	
	D_2	γ_4	12558	
	D_3	γ_4	12721	
$^6F_{3/2}$	E_1	$\gamma_{5,6}$	13408	
	E_2	γ_4	13412	
$^6F_{1/2}$	—	γ_4	13944	
$^4F_{9/2}$	F_1	$\gamma_{5,6}$	20970.7	20964.7
	F_2	γ_4	20971.8	20967.2
	F_3	$\gamma_{5,6}$	21152	21154
	F_4	γ_4	21157	21162
	F_5	γ_4	21658	21660
$^4I_{15/2}$	G_1	$\gamma_{5,6}$	21977	21976

Number of data points	38
Number of free parameters	11
Standard deviation	6.6 cm^{-1}

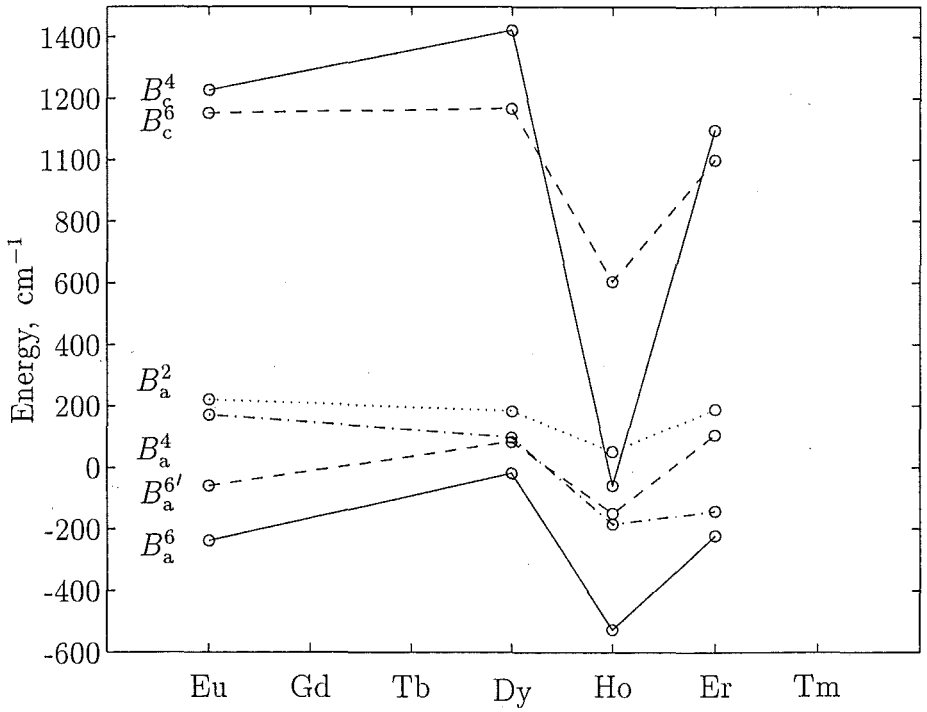

Figure 4.28: Reported crystal field parameters for C_{3v} center in SrF_2:RE^{3+}, and those found here for SrF_2:Dy^{3+}. References are given in Table 4.25.

4.5 Zeeman infrared, SrF_2:Dy^{3+}.

The Zeeman infrared absorption spectra of the C_{3v} and C_{4v} centers in samples oriented with the magnetic field along either the ⟨111⟩ or ⟨100⟩ crystal axes have been considered in order to test the crystal-field analyses. The Zeeman experiments have also provided a test of the coordinate basis appropriate for the crystal-field parameters determined in earlier sections. The 4 Tesla magnet that is operated in conjunction with the FTIR spectrometer is constrained to an experimental arrangement with the magnetic field aligned parallel to the infrared propagation direction. The sample is held at a temperature of approximately 10 K by indirect thermal contact to the cryogenic helium that is cooling the magnet coil. Because of the multiple orientations of the charge compensated centers in the fluorite crystals, the Zeeman splitting of centers aligned differently with respect to the magnetic field need to be considered. Each case will be discussed separately, with the implication that several magnetically inequivalent centers may arise simultaneously in any given spectrum. As a matter of notation, the magnitude of the magnetic field is written as B=|B|, and the angular brackets ⟨ijk⟩ are taken to refer to a general crystallographic direction, with [ijk] referring to a specific direction.

4.5.1 Crystal-field basis ambiguity.

The crystal-field analysis of the C_{3v} and C_{4v} centers contains an ambiguity, in that the coordinate bases for the centers are not uniquely defined by the Hamiltonian. It is found that this ambiguity can in principle be resolved by Zeeman absorption experiments. In this section the basis ambiguity is discussed, with an emphasis on possible experimental determination of the correct basis for the wavefunctions obtained by the crystal-field calculations.

The C_{4v} basis.

The C_{4v} basis is not uniquely determined by the crystal-field Hamiltonian, and there remains some additional arbitrariness in the choice of the x and y axes, in that both choices of the C_{4v} axes depicted in Figure 4.29 will possess a Hamiltonian of the same functional form. This ambiguity has the implication that the crystal-field parameters found from the calculation of energy levels in C_{4v} symmetry are not unique, and neither are the wavefunctions, as has been pointed out by Eremin and Leushin [33]. This arbitrariness in the basis is best discussed in the context of the Hamiltonian

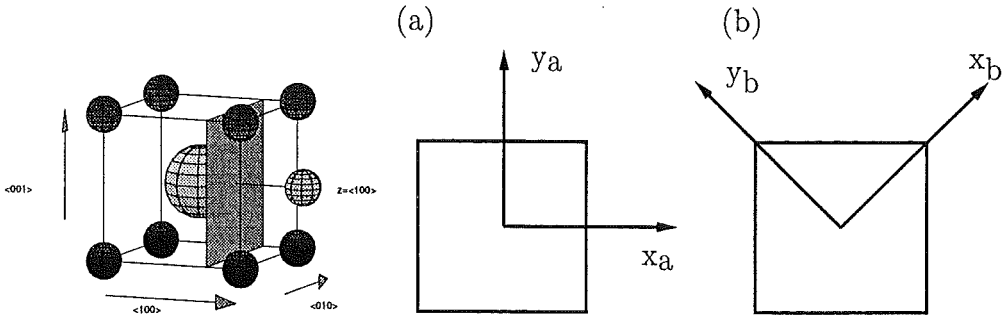

Figure 4.29: The two possible bases of the C_{4v} symmetry center for the Hamiltonian used here. The symmetry of the center is shown schematically as viewed looking down the z-axis. The square can be considered as representing the cross-section of the fluorine cage enclosing the rare-earth ion.

expressed in the following way:

$$H = B_0^2 C_0^2 + B_0^4 C_0^4 + B_0^6 C_0^6 + B_4^4 (C_4^4 + C_{-4}^4) + B_4^6 (C_4^6 + C_{-4}^6). \tag{4.1}$$

If it is assumed that the Hamiltonian of equation 4.1 corresponds to the basis depicted in Figure 4.29(a) and then perform a $\pi/4$ rotation about the z-axis, to arrive at the basis of Figure 4.29(b), then the transformed Hamiltonian, corresponding to the new basis, will be

$$H = B_0^2 C_0^2 + B_0^4 C_0^4 + B_0^6 C_0^6 - B_4^4 (C_4^4 + C_{-4}^4) - B_4^6 (C_4^6 + C_{-4}^6). \tag{4.2}$$

Because the B_q^k are treated as parameters, any change of sign such as that in the B_4^k parameters, will effectively be absorbed into the final fitted values. To notationally distinguish between these two sets of parameters, B_q^k is taken to signify parameters for the first basis and $\overline{B_q^k}$ represents the parameters for the rotated basis. The parameter equivalence can therefore be summarised as

$$B_4^4 \equiv -\overline{B_4^4}, \qquad B_4^6 \equiv -\overline{B_4^6} \tag{4.3}$$

It is further noted that this equivalence does not imply that the sign of the parameters is irrelevant. That is

$$B_4^4 \not\equiv -B_4^4, \qquad B_4^6 \not\equiv -B_4^6 \tag{4.4}$$

While Eremin and Leushin [33] have discussed this ambiguity in signs of the crystal-field parameters, and noted that this leads to an ambiguity in the wavefunction composition, the consequences of this ambiguity do not appear to have been addressed in the literature.

This ambiguity in the basis leads to a problem that is central to the calculation of the effects of the Zeeman interaction on the C_{4v} centers. Because the B_4^k parameters have been determined by fitting to the experimental energy levels, it is not immediately

known which basis these parameters are applicable to. That is, do the parameters and wavefunctions correspond to the basis of Figure 4.29(a) or Figure 4.29(b)? Because the wavefunctions obtained will only be applicable to the specific basis, all the calculations involving these wavefunctions should be carried out in the same basis. It is found that many, if not most, calculations involving these wavefunctions will be independent of the basis used. However, under certain circumstances the Zeeman splitting of states will distinguish between the bases. An example will be employed to clarify this point, and to highlight the requirements for there to be observable differences in the Zeeman splittings.

It is first noted that the relative signs of the wavefunction components will be changed by the $\pi/4$ rotation about the z-axis according to $|J_z\rangle \rightarrow \exp(-i\pi J_z/4)|J_z\rangle$. The wavefunctions of two C_{4v} Kramers doublets are defined below by listing their J_z composition, along with the corresponding transformed/rotated wavefunctions:

$$
\begin{array}{lcl}
|1\rangle \equiv a|\frac{13}{2}\rangle + b|\frac{5}{2}\rangle + c|\frac{-11}{2}\rangle & \xrightarrow{R_z(\pi/4)} & a|\frac{13}{2}\rangle - b|\frac{5}{2}\rangle - c|\frac{-11}{2}\rangle \\
|2\rangle \equiv a|\frac{-13}{2}\rangle + b|\frac{-5}{2}\rangle + c|\frac{11}{2}\rangle & \longrightarrow & a|\frac{-13}{2}\rangle - b|\frac{-5}{2}\rangle - c|\frac{11}{2}\rangle \\
|3\rangle \equiv g|\frac{9}{2}\rangle + h|\frac{-7}{2}\rangle & \longrightarrow & g|\frac{9}{2}\rangle + h|\frac{-7}{2}\rangle \\
|4\rangle \equiv g|\frac{-9}{2}\rangle + h|\frac{7}{2}\rangle & \longrightarrow & g|\frac{-9}{2}\rangle + h|\frac{7}{2}\rangle
\end{array}
$$

In listing the transformed wavefunctions, advantage has been taken of the freedom to introduce a phase factor to the complete wavefunctions. The wavefunctions $|1\rangle$, $|2\rangle$ and $|3\rangle$, $|4\rangle$ are Kramers conjugate pairs with C_{4v} irreps of γ_7 and γ_6 respectively. A rank one operator, such as that appropriate for the Zeeman interaction, can be written as $M{=}M_0^1 + M_1^1 + M_{-1}^1$. For such an operator the matrix elements between the three states, and their transformed counterparts, can be seen to be proportional to the component coefficients as follows:

$$
\begin{array}{lll}
\langle 1|M|1\rangle = \langle 2|M|2\rangle & \sim a^2 + b^2 + c^2 \equiv A & \xrightarrow{R_z(\pi/4)} \quad a^2 + b^2 + c^2 = A \\
\langle 1|M|2\rangle & \sim 2a.c \equiv B & \longrightarrow \quad -2a.c = -B \\
\langle 1|M|3\rangle = \langle 2|M|4\rangle & \sim 0 & \longrightarrow \quad 0 \\
\langle 1|M|4\rangle = \langle 2|M|3\rangle & \sim b.h + c.g \equiv E & \longrightarrow \quad -b.h - c.g = -E \\
\langle 3|M|3\rangle = \langle 4|M|4\rangle & \sim g^2 + h^2 \equiv C & \longrightarrow \quad g^2 + h^2 = C \\
\langle 3|M|4\rangle & \sim 2g.h \equiv D & \longrightarrow \quad 2g.h = D
\end{array}
$$

From the transformation properties of the individual matrix elements the eigenvalue

matrix in the original and rotated basis can be seen to be

M	$\|1\rangle$	$\|2\rangle$	$\|3\rangle$	$\|4\rangle$
$\langle 1\|$	A	B	0	E
$\langle 2\|$	B	A	E	0
$\langle 3\|$	0	E	$C+\Delta$	D
$\langle 4\|$	E	0	D	$C+\Delta$

$\xrightarrow{R_z(\pi/4)}$

M	$\|1\rangle$	$\|2\rangle$	$\|3\rangle$	$\|4\rangle$
$\langle 1\|$	A	$-B$	0	$-E$
$\langle 2\|$	$-B$	A	$-E$	0
$\langle 3\|$	0	$-E$	$C+\Delta$	D
$\langle 4\|$	$-E$	0	D	$C+\Delta$

,

where Δ is the zero-field separation of the two Kramers doublets. In general these two matrices will give rise to differing sets of eigenvalues. Hence it can be seen that interactions between states of different irreps can, if the wavefunction compositions are appropriate, lead to a basis dependent interaction.

The above discussion highlights that simply reporting the crystal-field parameters does not uniquely specify the crystal-field interactions physically occurring at the ion. Despite this, it is only rarely that crystal-field parameters are reported with an indication of the appropriate basis. In the past, some authors reported only the absolute magnitude of the ambiguous parameters, however this results in a loss of information as the relative signs of these parameters is still meaningful.

The problem at hand is summarised schematically in the following diagram. The parameters and wavefunctions have been determined for some particular basis. The crystal-field parameters and wavefunctions can be transformed between the two bases, however it is not known to which basis the initial calculations correspond. Therefore, knowing the transformation between bases does not remove the ambiguity of the wavefunctions. When considering Zeeman interactions the appropriate basis must be known in order to express the magnetic field components in that same basis. Failure to do so may lead to incorrect calculations of the Zeeman splittings.

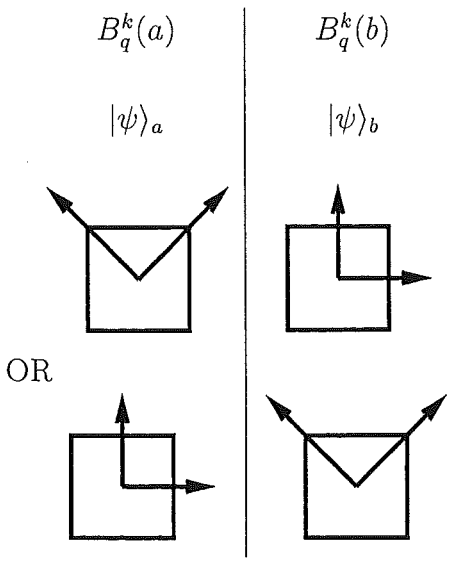

The reduction of the symmetry that is imposed by the application of a magnetic field at an oblique angle to the principal axis may therefore enable the appropriate basis to be determined. This is accomplished by calculating the Zeeman splittings with the wavefunctions obtained from the crystal-field calculations, and with the relevant magnetic field components for each of the two bases. Under certain conditions the calculated Zeeman splittings will be different for the two choices of x-y basis. These calculations can then be compared with experiment to finally deter-

mine the appropriate basis.

The appropriate magnetic field components for both bases of Figure 4.29 are calculated in Section 4.5.2 with the intention of experimentally determining the C_{4v} basis. The calculated Zeeman splittings in each basis have been compared with that obtained experimentally.

While the focus here is on an experimental determination of the C_{4v} basis, if the structure of the center is known such a determination may also be obtained through appealing to ab-initio calculations. Superposition model calculations for the C_{4v} center in $SrF_2:RE^{3+}$ and $CaF_2:RE^{3+}$ have been reported by Reid and Butler [88]. These calculations indicate that for the crystal-field parameters (and therefore the wavefunctions) obtained here, the appropriate x,y basis is that depicted in Figure 4.29(a).

The C_{3v} basis.

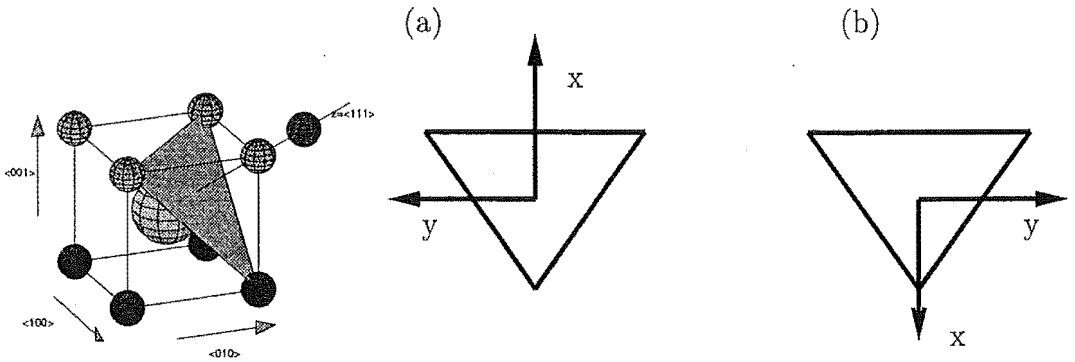

Figure 4.30: The two possible bases of the C_{3v} symmetry center for the Hamiltonian used here.

The problem of basis ambiguity also exists in the C_{3v} Hamiltonian, and therefore in the crystal-field parameters and wavefunctions. For the C_{3v} center bases can be chosen that are rotated by 180° around the z-axis relative to each other. Both bases possess a crystal-field Hamiltonian of the same functional form. As for the C_{4v} center, transformation of wavefunctions between bases involves changes in the relative signs of the wavefunction components. The two C_{3v} bases are shown schematically in Figure 4.30. This ambiguity in the C_{3v} basis is entirely analogous to that of the C_{4v} center, as can be seen from recognising the π rotation of the x,y-axes is also equivalent to a $\pi/3$ rotation.[1] It should be noted that there is another pair of x,y-bases available for the C_{3v} center, but that the particular Hamiltonian used distinguishes between these pairs of bases. For the Hamiltonian used here, the x-axis is defined as lying in

[1]The π rotation can be considered as a $\pi/3$ rotation followed by a $2\pi/3$ rotation. Because of the 3-fold rotation symmetry of the center, this second rotation does not alter the wavefunctions.

C_{3v}	Point-charge calc.		C.F. calc.	Lesniak et.al.
Parameter	Basis a	Basis b	page 85	ref. [62]
B_a^2	215	215	184	191
B_c^4	315	-150	1423	-643
B_a^4	3	468	99	2013
B_c^6	88	38	1168	492
B_a^6	0	109	-18	1433
$B_a^{6'}$	1	51	85	668

Table 4.27: Comparison of $SrF_2:Dy^{3+}$ C_{3v} crystal-field parameters with those calculated from a point-charge calculation in the two bases of Figure 4.30. The parameters of Lesniak et.al. have been transformed to the parametrisation used here according to the relations given in appendix A. All parameter values are given in units of cm^{-1}.

one of the reflection planes of the C_{3v} center, with the y-axis normal to this reflection plane [11].

Again, reference to experiments involving a reduction in the symmetry of the center, or to ab-initio calculations, is required to determine the appropriate basis. Calculations based on an effective charge model have been reported for $SrF_2:RE^{3+}$ C_{3v} centers by Lesniak and Richardson [62]. However, despite calculating the crystal-field parameters from the known structure of the C_{3v} center, the basis used for these calculations was not reported. This oversight not only eliminates the possibility of using these calculations to determine the appropriate basis of the C_{3v} center, but also highlights the prevalence of this basis ambiguity in the literature. Some indication of the appropriate basis can be obtained from a simple point-charge model calculation. Such a calculation has been performed here, for both bases of Figure 4.30, and the predicted parameters are shown in Table 4.27 along with the parameters obtained from the crystal-field calculation of Section 4.4.2. The calculated crystal-field parameters of Lesniak et.al. are also shown for comparison. While such a simple point-charge calculation should not be expected to produce particularly accurate parameters, the B_a^4/B_c^4 and $B_q^6/B_{q'}^6$ parameter ratios and the relative signs of the parameters can be expected to somewhat more meaningful, due to an effective cancellation of the inaccuracies in the radial integrals. This point-charge calculation suggests that the appropriate basis for the C_{3v} crystal-field parameters (and therefore wavefunctions) obtained in Section 4.4.2 is that depicted in Figure 4.30(a). It also appears that the calculations of Lesniak have been performed in the alternative basis of Figure 4.30(b).

To enable an experimental investigation into the C_{3v} basis, the magnetic field components appropriate for both C_{3v} bases have been calculated, and are presented in the following section.

4.5.2 Magnetic field components for Zeeman calculations.

In order to calculate the Zeeman splittings of the C_{4v} and C_{3v} center energy levels the magnetic field components are required for the specific geometrical arrangement of the applied field with respect to the C_{4v} and C_{3v} bases. Because there are multiple orientations of a given center in the host crystal, several magnetically inequivalent centers may be present in the sample for a given experimental arrangement. This section discusses each experimental arrangement in turn, presenting the magnetic field components for both bases of each of the C_{4v} and C_{3v} centers.

C_{4v} center, B$\|\langle 111\rangle$.

The C_{4v} center will have the charge compensating fluorine in any one of the six nearest-neighbour $\langle 100\rangle$ interstitial positions, thus defining the orientation of the particular site. For this particular configuration of the magnetic field with a C_{4v} center, all six orientations of the center have the principal axis equally inclined to the magnetic field, at an angle of 54.7^o. The x and y axes can be chosen to include an arbitrary rotation of 0^o, 90^o, 180^o or 270^o about the z-axis as the wavefunctions will be independent of such a rotation.

For the basis of Figure 4.29(a), with the x- and y-axes along the crystallographic [100] and [010] directions, by explicitly considering all six centers it is found that the magnetic field components can be expressed as

$$B_X = \frac{1}{\sqrt{3}}B, \qquad B_Y = \frac{1}{\sqrt{3}}B, \qquad B_Z = \pm\frac{1}{\sqrt{3}}B.$$

The sign on the B_Z component indicates whether a particular center has its' principal axis pointing in such a direction as to have the z-component of the magnetic field parallel or anti-parallel to the principal axis. The allowed $m\pi/2$ rotations of the x and y axes around the z-axis enable these axes to be chosen to have a positive magnetic field component.

For the alternative basis of Figure 4.29(b), with the x and y axes along the [110] and [$\bar{1}$10] directions, the magnetic field components can be expressed as

$$B_X = 0, \qquad B_Y = \sqrt{\frac{2}{3}}B, \qquad B_Z = \pm\frac{1}{\sqrt{3}}B.$$

The allowed $m\pi/2$ rotations about the z axis enables the B_Y component to always be chosen as positive.

C_{3v} center, B||⟨100⟩.

For the C_{3v} centers the z-axis of the site is in any one of the eight ⟨111⟩ directions. For the B||⟨100⟩ configuration of the magnetic field, all eight sites are equally inclined to the magnetic field, with an angle of 54.7° between the magnetic field and the principal axis. The magnetic field along the z direction is therefore $B_Z = \pm B/\sqrt{3}$. The sign accounts for the difference between the centers with parallel and anti-parallel components in the z direction, as for example in the [111] and $[\overline{1}\overline{1}\overline{1}]$ oriented centers.

The magnetic field components for Zeeman calculations for the basis of Figure 4.30(a) will be discussed first. In determining the x and y components of the magnetic field some degree of choice remains as a ±120° rotation about the z-axis will not alter any observables, as the wavefunctions are independent of this $m2\pi/3$ rotation. As an example, the center with a z-axis defined by the [111] direction may have the x and y directions given by $x \| [2\overline{1}\overline{1}]$ and $y \| [01\overline{1}]$. A rotation of these axes by ±120° about the z-axis will also give suitable *and equivalent* choices of the x and y axes. For the magnetic field along the [100] direction the magnetic field components can be given as $B_X = \sqrt{2/3}\,B$, $B_Y = 0$, and $B_Z = 1/\sqrt{3}\,B$. By taking account of the 3-fold rotation that is allowed in the choice of the x and y axes, it can be shown that all eight z-axis orientations of the C_{3v} center, with the basis depicted in Figure 4.30(a), will have magnetic field components given by

$$B_X = \pm\sqrt{\frac{2}{3}}B, \qquad B_Y = 0, \qquad B_Z = \pm\frac{1}{\sqrt{3}}B.$$

Note that the signs of the B_X and B_Z components are not independent, and a particular sign of B_X necessarily requires the same sign for B_Z. Different Zeeman splittings will be calculated for any other choice of signs, or x-y basis (other than that allowed for by the 3-fold rotation), unless the wavefunctions obtained from the crystal field calculation are specifically transformed by a rotation consistent with the new choice of axes.

By similarly considering the magnetic field components for the basis of Figure 4.30(b) it is found that the magnetic field components are given by

$$B_X = \mp\sqrt{\frac{2}{3}}B, \qquad B_Y = 0, \qquad B_Z = \pm\frac{1}{\sqrt{3}}B.$$

C_{4v} center, B||⟨100⟩.

For a magnetic field applied to the C_{4v} centers with the experimental configuration of B||⟨100⟩, there are effectively two types of sites in the crystal. These are

(a) The parallel sites. Those sites with the principal axis parallel or anti-parallel to the magnetic field. That is, sites with the charge compensating ion in the [100] or $[\bar{1}00]$ directions. Therefore B_X=B_y=0, and B_Z=$\pm$B. There is no ambiguity resulting from the two possible C_{4v} bases.

(b) The perpendicular sites, where the principal axis is perpendicular to the magnetic field: [010], $[0\bar{1}0]$, [001], and $[00\bar{1}]$. For these sites the magnetic field along the principal symmetry axis is zero: B_Z=0. However the choice of C_{4v} bases determines the form of the perpendicular magnetic field components. For the basis of Figure 4.29(a) the magnetic field components can be expressed as B_X=B, B_y=0 and B_Z=0. Note that there is freedom to choose either of B_X or B_y as zero as the x and y axes are effectively only defined to within an arbitrary rotation of 0^o, 90^o, 180^o or 270^o about the z-axis.

For the alternative basis of Figure 4.29(b) the magnetic field components are given by B_X=$1/\sqrt{2}$B, B_y=$1/\sqrt{2}$B and B_Z=0.

C_{3v} center, B$\|\langle 111\rangle$.

This particular configuration for the C_{3v} center results in two sets of inequivalent sites. Of the eight C_{3v} principal axis orientations there will be two sites in which the magnetic field is aligned parallel or anti-parallel with the magnetic field. The remaining six sites will be arranged at an oblique angle to the field.

(a) The parallel sites. [111], $[\bar{1}\bar{1}\bar{1}]$. The magnetic field components are given by B_X=B_y=0, B_Z=$\pm$B. Because both B_X and B_y are zero, no ambiguity in the Zeeman splittings results from the two possible C_{3v} bases.

(b) The oblique sites. $[\bar{1}11]$, $[1\bar{1}1]$, $[11\bar{1}]$, $[\bar{1}\bar{1}1]$, $[\bar{1}1\bar{1}]$, $[1\bar{1}\bar{1}]$. These sites have the principal axis at an angle of 70.5^o to the magnetic field. For the basis of Figure 4.30(a) all six oblique sites can be taken to have their magnetic field components given by

$$B_X = \mp\frac{2\sqrt{2}}{3}B, \qquad B_y = 0, \qquad B_Z = \pm\frac{1}{3}B,$$

where the signs of B_X and B_Z are not independent. The allowed 3-fold rotation of the x and y axes about the z-axis has been employed so that the B_y component can always be chosen to be zero. For the alternative C_{3v} basis, Figure 4.30(b), the magnetic field components are given by

$$B_X = \pm\frac{2\sqrt{2}}{3}B, \qquad B_y = 0, \qquad B_Z = \pm\frac{1}{3}B,$$

Note that the basis choice simply leads to a change in the relative signs of the B_X and B_Z components.

4.5.3 Experimental results and analysis.

Zeeman infrared absorption measurements were carried out on oriented SrF_2:Dy^{3+} samples using the 4 Tesla axial magnet incorporated into the Bio-Rad FTIR spectrometer. The nature of the splitting of absorption transitions with applied magnetic field can enable a confirmation of the center involved, along with information relating to the wavefunctions. Calculations were performed to predict the Zeeman splittings, based on the wavefunctions obtained from the crystal-field least-squares analyses. In many cases a very good agreement between theory and experiment was obtained, adding confidence to the crystal-field irrep assignments, and the crystal-field calculation as a whole. However, the small absorption strength of most of the accessible transitions, together with close lying transitions from different centers, has limited the number of transitions for which satisfactory analysis can be done.

Matlab routines were written to take the crystal-field wavefunctions and calculate the matrix elements, diagonalise the matrix for a given magnetic field, and hence determine the energy level splittings. The calculations were performed by generating the set of $\langle LSJJ_z|\mu_B g_L \boldsymbol{B}\cdot\boldsymbol{J}|LSJJ_z'\rangle$ matrix elements for the relevant states. The components J_x, J_y were calculated in terms of the ladder operators J_-, J_+. Only matrix elements diagonal in LSJ were included in the analysis. The matrix elements were evaluated taking into account all the J_z components for the LSJ of that multiplet for which the normalised coefficients were greater than 0.1 (1%). For the W manifold, the states considered contained a significant admixture of both $^6H_{9/2}$ and $^6F_{11/2}$ multiplets. Likewise, states of the A manifold consisted of significant contributions from both $^6H_{7/2}$ and $^6F_{9/2}$ multiplets. For calculating the splitting of states of these manifolds both LSJ contributions were taken into account. Where there were energy levels nearby to that of interest, these additional levels were included in the calculation to ensure that mixing of levels as a function of field strength was properly accounted for. For these purposes the definition "nearby" depended on the expected splitting values for a given multiplet and level, and on whether any quadratic behaviour was observed in the splitting patterns. In practice this meant that both the Z_1 and Z_2 levels were taken into account for both C_{3v} and C_{4v} centers, although the effects of mixing between these levels was minor. The components of the magnetic field $\boldsymbol{B}$ were taken as described in the previous section. The eigenvalues of the matrix containing elements evaluated in this way were then found as a function of magnetic field strength, giving the splittings of the ground and upper states, and therefore the transitions frequencies. To enable

comparison with experiment, the zero field transition frequencies for the calculations were set equal to that seen experimentally, rather than taking that obtained from the crystal-field calculation. Importantly, this sets the separation between energy levels to that obtained from experiment. It is this separation between levels that determines the magnitude of the interactions between levels when a magnetic field is applied, and the few cm^{-1} inaccuracies in the calculated energy level positions would then be expected to significantly alter the calculated Zeeman patterns. Because the X_2 level of the C_{4v} center has not been directly observed in absorption, due to an overlapping C_{3v} transition, or conclusively inferred from the laser-selective fluorescence, some ambiguity in the position of this level remains.

Where it was considered to add clarity, the thermal Boltzmann population of the ground state levels was considered with regard to transition intensities. The calculated transitions originating on a level $\approx 10\,cm^{-1}$ above the (split) ground state are not shown in such cases.

Zeeman results: C_{4v} center, $B\|\langle 111\rangle$

For the Zeeman interaction of the C_{4v} center in samples oriented with the crystal $\langle 111\rangle$ axis parallel to the magnetic field, as noted earlier all six possible orientations of the center are magnetically equivalent. The absorption spectra are therefore much simpler to analyse than the equivalent spectra for a $\langle 100\rangle$ oriented sample. The Zeeman splitting factor is defined by

$$S = \frac{\Delta E}{\mu_B B}. \tag{4.5}$$

The splitting of a doublet in the $B\,\|\langle 111\rangle$ configuration can be related to the perpendicular ($\perp$) and parallel ($\|$) splitting factors by taking the oblique angle of the magnetic field into account, by the following relationship

$$S_{\langle 111\rangle} = \sqrt{\frac{S_{\|}^2 + 2S_{\perp}^2}{3}} \tag{4.6}$$

This allows some comparison between the Zeeman splittings observed in the $\langle 111\rangle$ and $\langle 100\rangle$ oriented samples, as well as giving an indication of the relative importance of the parallel and perpendicular Zeeman effects.

Initially only the $S_{\langle 111\rangle}$ splitting values will be discussed, as it is these that are directly measured. The calculated parallel and perpendicular splitting values will also be presented later in this section.

Figure 4.31 shows the Zeeman splittings for the A_1 level, which has a zero field energy of $9007\,cm^{-1}$. The observation of all four transitions between the pair of split Kramers

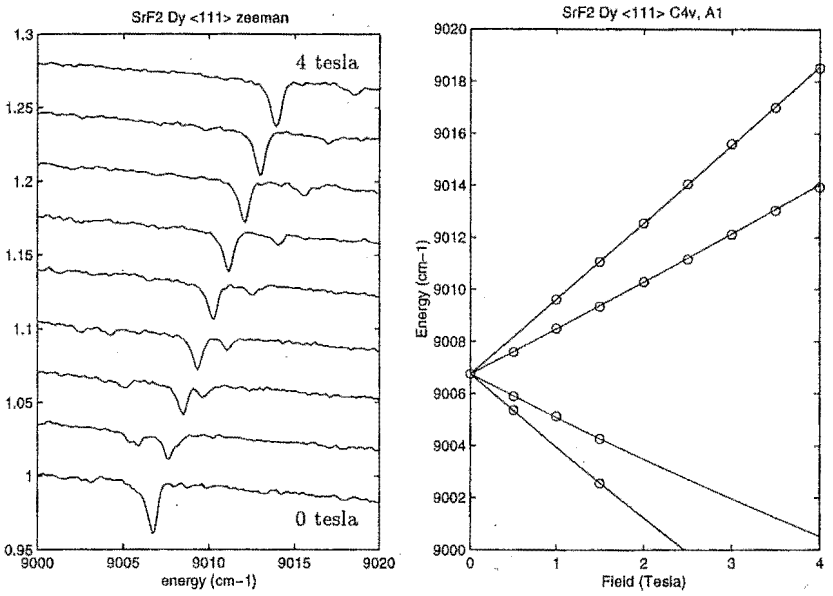

Figure 4.31: Zeeman infrared absorption spectra of SrF_2:Dy^{3+}, showing the ⟨111⟩ splittings of A_1 of the C_{4v} center. Both the ${}^6H_{7/2}$ and ${}^6F_{9/2}$ components of the wavefunction has been taken into account for the calculated splitting.

doublets enables the splitting factor of both the ground state and the A_1 level to be deduced. The decreasing intensity with increasing magnetic field identifies both of the lower frequency transitions as originating on the upper level of the split ground state, as this will have a reduced thermal population as the splitting of the doublet increases. This intensity decrease is seen in most spectra, and is a consequence of the large splitting factor of the ground state. Figure 4.31 also shows the transitions deduced from a Zeeman calculation based on the wavefunctions found from the crystal-field calculation. This calculation includes contributions from both $|{}^6H_{7/2}J_z\rangle$ and $|{}^6F_{9/2}J_z\rangle$ components. The wavefunctions used for this calculation, and all the C_{4v} Zeeman calculations discussed here, are given in Table 4.29 (page 116).

Quantitatively, the splitting factors are measured to be

$$S_{\langle 111\rangle}(Z_1)_{1.5T} = 9.7,$$

$$S_{\langle 111\rangle}(A_1)_{1.5T} = 2.4,$$

where the splitting factors are found from the 1.5 Tesla spectra, the highest field at which all four transitions are observed. It is also noted that the A_1 splitting factor remains unchanged up to 4 Tesla, as can be found from the energies of the two highest frequency transitions.

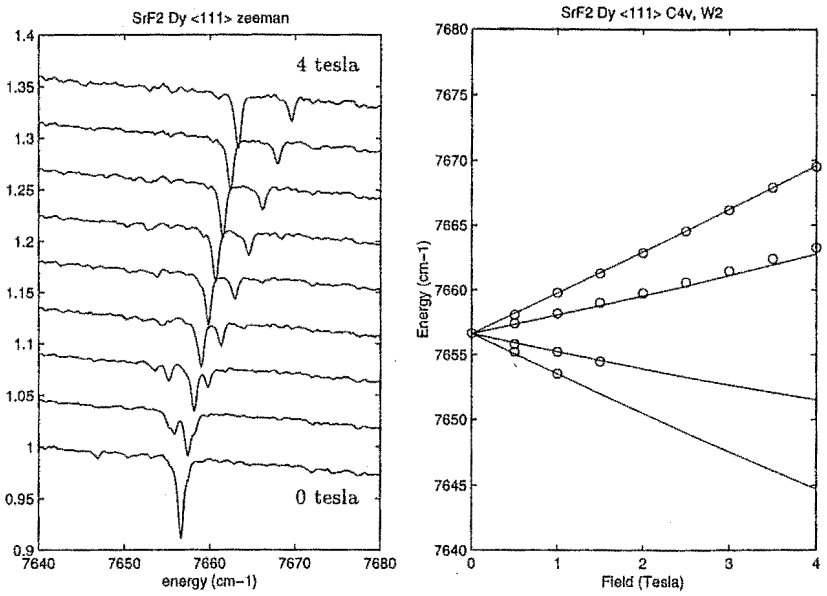

Figure 4.32: Zeeman infrared absorption spectra of SrF_2:Dy^{3+}, showing the $\langle 111 \rangle$ splittings of W_2 of the C_{4v} center. Both $^6H_{9/2}$ and $^6F_{11/2}$ components of the wavefunction have been taken into account for the calculated splitting.

The calculated splitting factors, at a field strength of 1.5 Tesla, are

$$S_{\langle 111 \rangle}(Z_1)_{\text{calc}} = 9.72,$$

$$S_{\langle 111 \rangle}(A_1)_{\text{calc}} = 2.43$$

which demonstrates the excellent agreement between theory and experiment which is readily apparent in the splitting diagram of Figure 4.31.

For the Zeeman splitting of the W_2 level shown in Figure 4.32, the observation of all four transitions again permits the determination of the splittings of the W_2 level and another independent measurement of that for the ground state. It is found that

$$S_{\langle 111 \rangle}(Z_1)_{1.0T} = 9.8,$$

$$S_{\langle 111 \rangle}(W_2)_{1.0T} = 3.5.$$

The calculated splitting value at the same field of 1.0 T is also in reasonable agreement with the measured value, with

$$S_{\langle 111 \rangle}(W_2)_{\text{calc}} = 3.66.$$

Because the W manifold consists of levels with significant admixtures of both the $^6H_{9/2}$ and $^6F_{11/2}$ multiplets, both $|LS\rangle$ components have been taken into account to

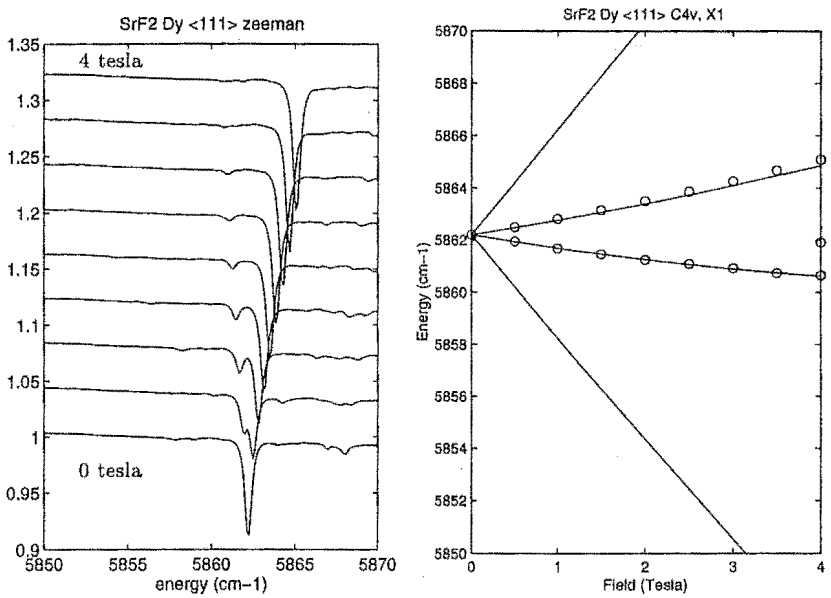

Figure 4.33: Zeeman infrared absorption spectra of SrF_2:Dy^{3+}, showing the $\langle 111 \rangle$ splitting of X_1 of the C_{4v} center. The decrease in intensity of the low energy line in simply due to thermal depopulation of the upper ground state level.

obtain the calculated splitting. Any possible perturbation caused by the W_1 level which lies $28\,cm^{-1}$ lower in energy has been neglected in the calculations. The lack of any appreciable quadratic behaviour in the observed splitting serves as a good indication of the validity of this approximation.

The Zeeman splittings of the X_1 level at $5862\,cm^{-1}$ are shown in Figure 4.33. Only transitions between either the lower split levels or the upper levels of the two split doublets are observed. Therefore to enable the splitting of the X_1 state to be deduced, the Z_1 splitting has been taken from the measurements discussed above. The measured and calculated splitting factors are again in excellent agreement:

$$S_{\langle 111 \rangle}(X_1)_{4T} = 7.4, \qquad S_{\langle 111 \rangle}(X_1)_{\text{calc}} = 7.41.$$

For the interaction of the Y_1 state with the magnetic field (Figure 4.34), the Z_1 splitting behaviour found from other transitions has again been employed in deducing the Y_1 splitting factors

$$S_{\langle 111 \rangle}(Y_1)_{2T} = 8.4, \qquad S_{\langle 111 \rangle}(Y_1)_{\text{calc}} = 8.30.$$

Because of the lack of influence of neighbouring energy levels in the Zeeman interactions of the levels discussed above, the calculated splitting patterns are independent of the

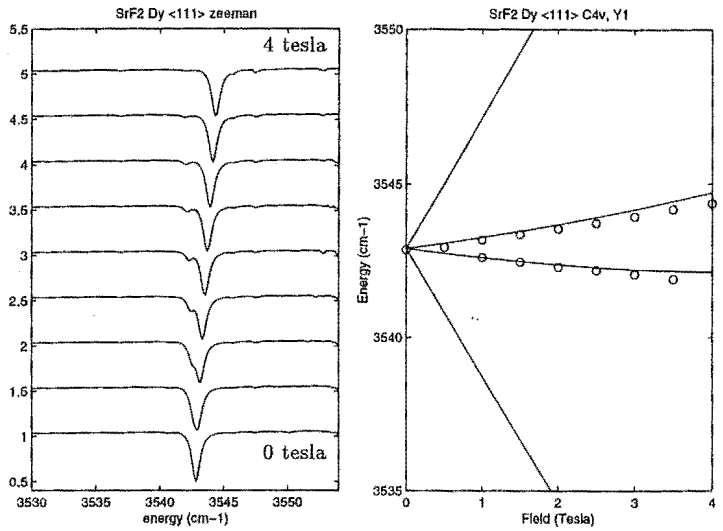

Figure 4.34: Zeeman infrared absorption spectra of SrF_2:Dy^{3+} for $\langle 111 \rangle$ sample, showing the experimental and calculated C_{4v} Y_1 splittings.

choice of x,y-basis. For the C_{4v} center an exception to this basis independence lies in the Zeeman splittings of the X_2,X_3 and X_4 levels at approximately $5960\,cm^{-1}$. As these three levels consist of the different irreps of $X_2(\gamma_6)$, $X_3(\gamma_7)$ and $X_4(\gamma_6)$, and all three levels lie within $\approx 20\,cm^{-1}$, there exists the possibility of considerable mixing of the wavefunctions and the associated repulsion of the energy levels as they split under the action of the magnetic field. In principle the Zeeman calculations can then distinguish between the two bases of the C_{4v} symmetry which are related by a $\pi/4$ rotation about the z-axis. Unfortunately the complications of having three levels, rather than just a γ_6, γ_7 pair, leads to a quite complicated splitting pattern. The zero field position of the X_2 level has also not been unambiguously identified, although there are indications from the laser selective fluorescence that it lies $\approx$1-2 cm^{-1} below X_3. One further complication to the analysis is the presence of a relatively strong absorption overlapping this region due to the C_{3v} X_1 level at $5958\,cm^{-1}$. Therefore the $\boldsymbol{B}\|\langle 111 \rangle$ Zeeman spectra for the C_{4v} X_2,X_3 and X_4 levels and the C_{3v} X_1 level have been analysed concurrently. The Zeeman infrared absorption spectra for this these states are shown in Figure 4.35.

Figures 4.36, 4.37 show the experimental and calculated splitting diagrams for the two choices of C_{4v} basis. The choice of C_{3v} basis is not an issue for these calculations, as the isolation of the C_{3v} X_1 level precludes there being any difference between the basis choices.

There are significant differences in the calculated splitting patterns for the two choices of C_{4v} basis. It is considered that the calculation with the basis of Figure 4.29(a), with

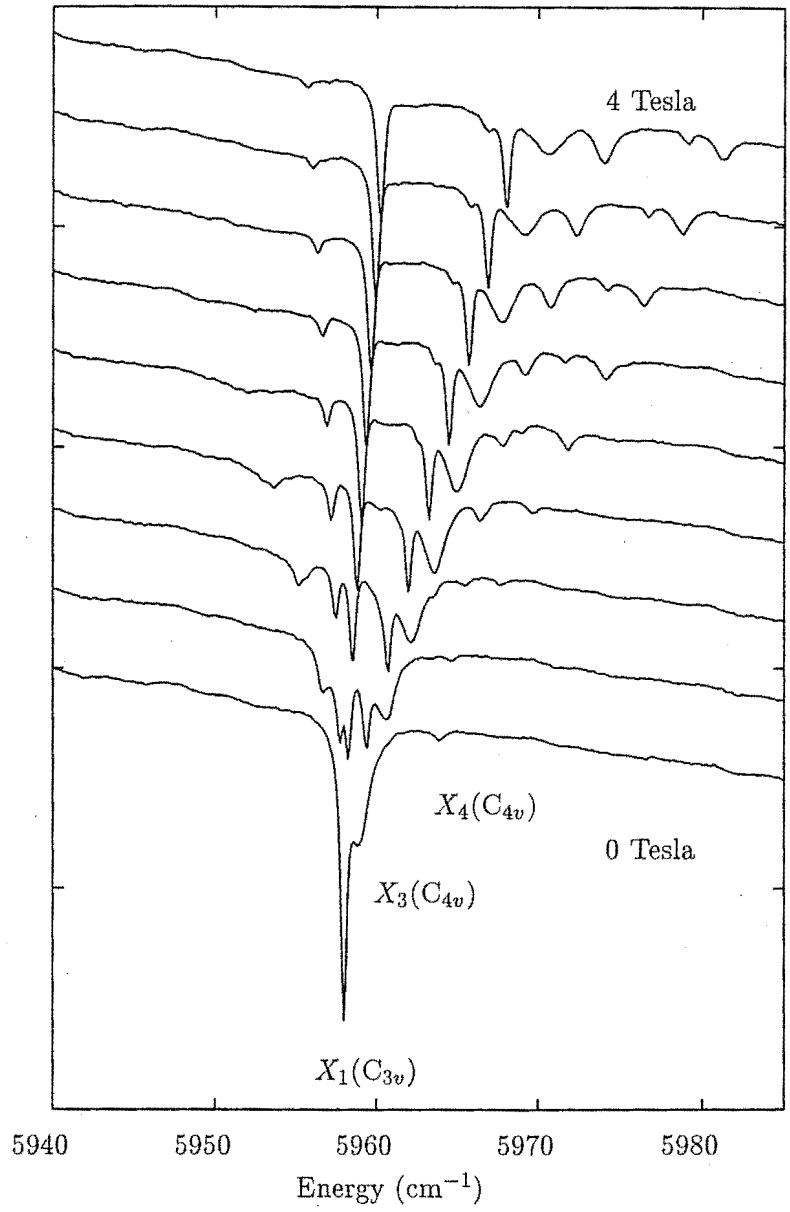

Figure 4.35: Zeeman infrared absorption spectra of SrF_2:Dy^{3+} showing the C_{4v} and C_{3v} absorption spectra in the region of 5960 cm^{-1} for magnetic field strength between 0 and 4 Tesla, with $B \| \langle 111 \rangle$. Note that the zero-field position of X_2 of the C_{4v} center is not observed, but calculations put it in this region.

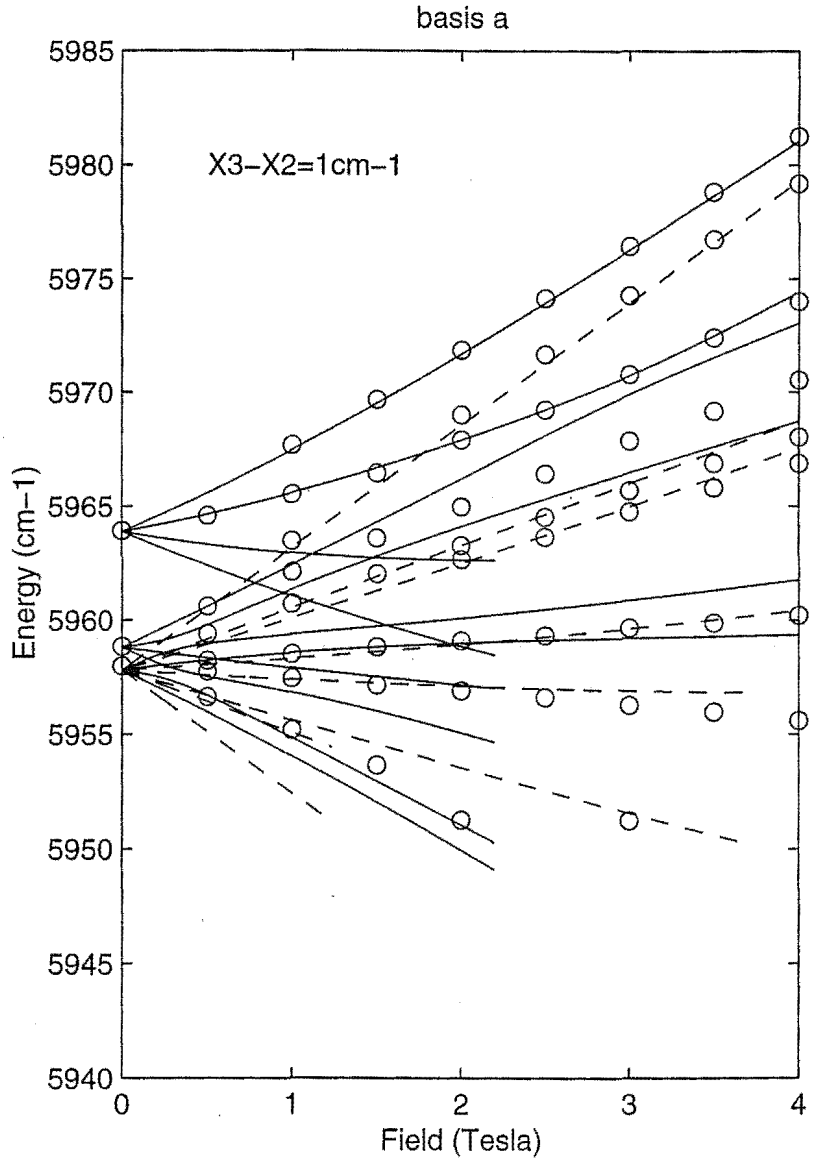

Figure 4.36: Calculated and measured splitting diagram for the X_2, X_3 and X_4 levels of the C_{4v} center and the X_1 level of the C_{3v} center. The calculation are for the C_{4v} basis choice A of Fig.4.29, and for the X_2 level lying $1\,cm^{-1}$ below X_3. The solid line is the calculated splittings of the the C_{4v} center, with the dashed lines showing the C_{3v} center splittings.

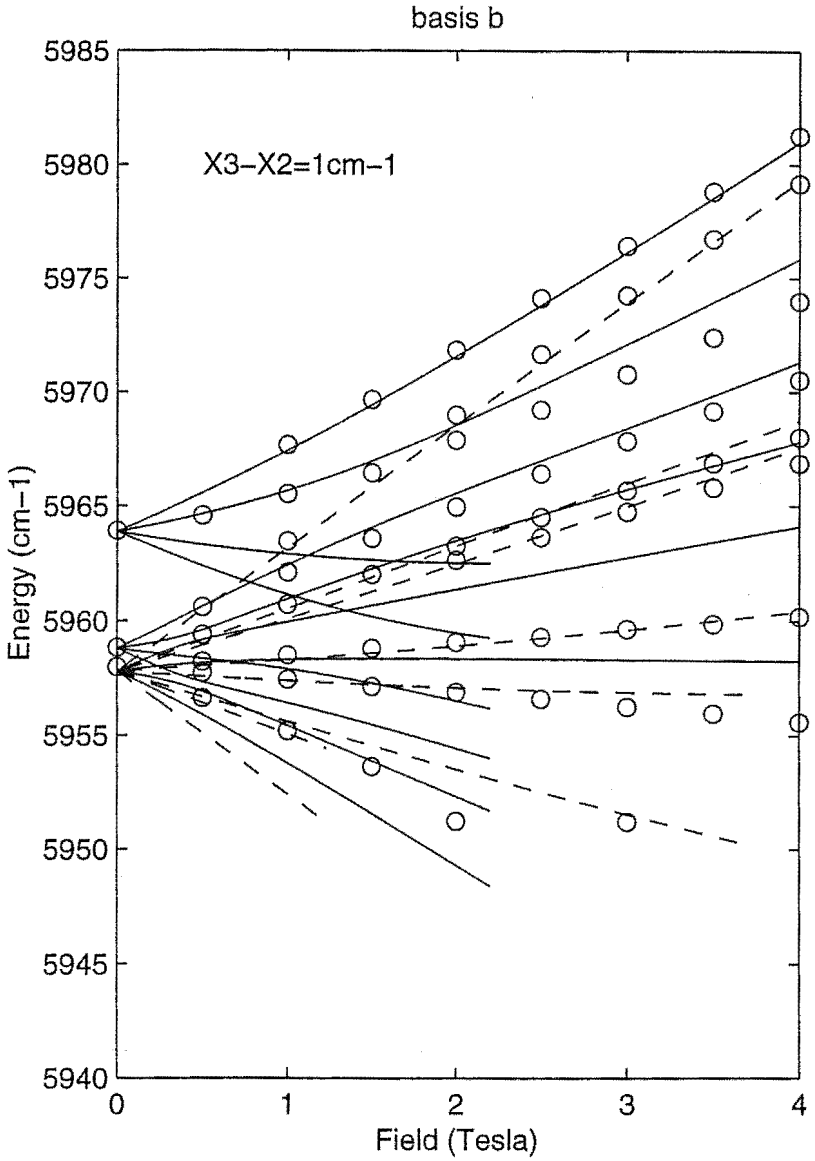

Figure 4.37: Calculated and measured splitting diagram for the X_2, X_3 and X_4 levels of the C_{4v} center and the X_1 level of the C_{3v} center. The calculation are for the C_{4v} basis choice B of Fig.4.29, and for the X_2 level lying $1\,cm^{-1}$ below X_3. The solid line is the calculated splittings of the the C_{4v} center, with the dashed lines showing the C_{3v} center splittings.

the x,y axes along the $\langle 100 \rangle$ and $\langle 010 \rangle$ crystal axes, gives a more accurate description of the observed data. However, as both calculations show some discrepancy with the experimental results, this assignment cannot be made with absolute certainty, and it must be considered somewhat subjective.

With this uncertainty in mind, the tentative conclusion is reached that the basis of Figure 4.29(a) is the correct choice for the crystal-field parameters reported in Section 4.3.3 (p. 64). This basis is also that predicted from the superposition model calculations of Reid and Butler [88].

The good agreement found between the calculated and experimental Zeeman splittings leads to confidence in the accuracy of the C_{4v} wavefunctions, and therefore to the energy level and irrep assignments that have gone into the crystal-field calculation.

It is also noted that the splittings corresponding to the C_{3v} X_1 level are adequately described by the calculation depicted in Figures 4.36, 4.37.

The experimental and calculated splitting factors for the C_{4v} center are listed in Table 4.28. Splitting factors for the X_2, X_3 and X_4 states are not readily determined from experiment, and therefore no comparison between theory and experiment can be made on the basis of splitting factors.

C_{4v}	Field	Calculated			Expt.
Level	(Tesla)	$S_{\parallel}$	$S_{\perp}$	$S_{\langle 111 \rangle}$	$S_{\langle 111 \rangle}$
Z_1	1.5	16.79	0.65	9.72	9.7
Y_1	2.0	14.38	0.09	8.30	8.4
X_1	4.0	12.83	0.13	7.41	7.4
W_2	1.0	2.27	4.18	3.66	3.5
A_1	1.5	0.07	2.97	2.43	2.4

Table 4.28: Experimental and calculated splitting factors for the $SrF_2:Dy^{3+}$ C_{4v} center.

Zeeman results: C_{3v} center, $\boldsymbol{B}\|\langle 100\rangle$

For the C_{3v} centers, a geometry of $\boldsymbol{B}\|\langle 100\rangle$ leads to the simplest spectra as all eight C_{3v} orientations are then magnetically equivalent. It is therefore in this geometry that the wavefunctions obtained from the crystal-field analysis can be most easily tested. The C_{3v} wavefunctions used in the calculations discussed here, and that of the X_1 level already discussed in the context of the C_{4v} spectra, are presented in Table 4.30 (page 116).

Figure 4.38 presents the Zeeman spectra of the X_2 and X_3 levels of the C_{3v} center. Because of the small separation of these two levels it is expected that there will be some repulsion of the split energy levels as they move closer together with increasing field strength. This small separation, together with the opposite irrep character of these levels, leads to the possibility that the particular x,y-basis choice used in the calculations will show different calculated Zeeman splittings. This is indeed found to be the case. Figure 4.38 shows the calculated Zeeman splittings for both bases (a) and (b) of Figure 4.30(page 94). Clearly the two calculations differ considerably, with basis (a) showing a smaller repulsive effect than that for basis (b). However, the correct basis cannot be directly determined due to issues of sample misalignment, which will now be discussed.

A feature of the C_{3v} $\boldsymbol{B}\|\langle 100\rangle$ splittings, is that what would be expected to be a single transition, does in fact split into several resolvable transitions at high magnetic fields. The initial suspicion is that the sample is slightly misaligned and that the eight C_{3v} center orientations can no longer be considered to be equally inclined to the magnetic field direction. To estimate the magnitude of misalignment required to produce these excess splittings, and therefore make some judgement on the validity of this explanation, Zeeman calculations have been performed in which a small misalignment of the magnetic field is included. These calculations have been carried out in the same manner as above, but with the allowance for some misalignment of the field in one crystallographic direction, such that $\boldsymbol{B}=B\langle 100\rangle \rightarrow B\langle \cos\theta,0,\sin\theta\rangle$. It is found that due to the large splitting factors present in Dy^{3+}, a misalignment of as small as 3^o could give rise to resolvable splittings such as that seen in Figure 4.38. For the X_2,X_3 splittings, it is found that a 4 Tesla field with 3^o misalignment as mentioned above, gives rise to two inequivalent centers with a difference of $\approx 1\,cm^{-1}$ in the transition energies corresponding to the absorption shown at $\approx 6010\,cm^{-1}$ in the splitting diagrams. Allowing for some small misalignment in the $\langle 010\rangle$ direction would further reduce the equivalence of the differently oriented centers. It would then be expected that the eight C_{3v} center orientations would exist as four pairs of centers which are magnetically distinct.

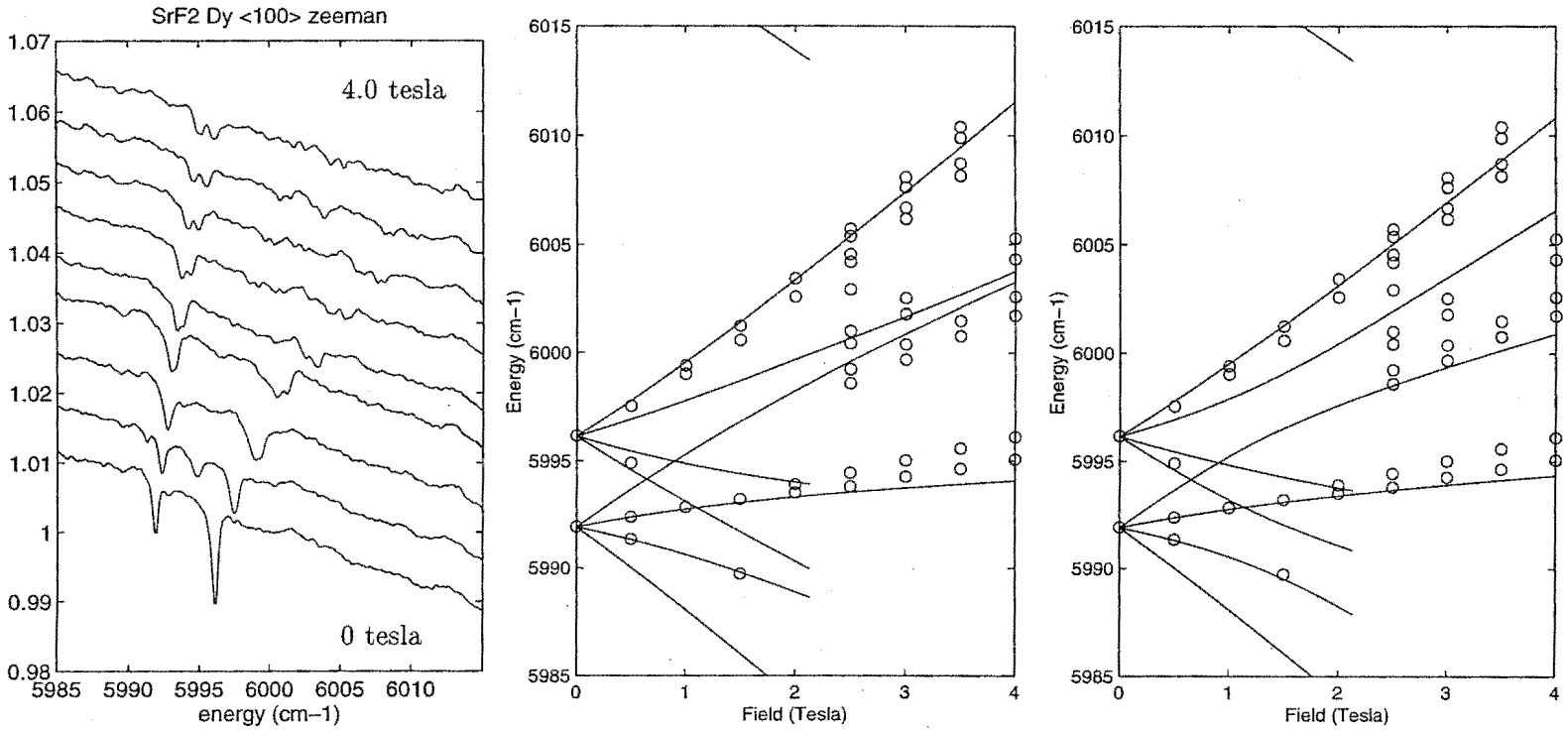

Figure 4.38: Zeeman infrared absorption spectra of SrF_2:Dy^{3+}, showing the ⟨100⟩ splittings of X_2 and X_3 of the C_{3v} center. The X_4 level was also included in the calculations. Transitions originating from levels greater than 10 cm^{-1} above ground state are not shown in the calculations. The two calculations are for the x,y-basis of Fig4.30(A) (center), and Fig4.30(B) (right).

With the possible misalignment taken into account for both C_{3v} basis choices it is found that for the two transitions displaying repulsion the misalignment causes the calculated transitions for basis (a) to improve their agreement with experiment. The same misalignment for calculations with basis (b) causes these repelling transitions to display even greater disparity with experiment. It is therefore concluded that if sample misalignment is indeed the true cause of the excess splittings in the Zeeman absorption transitions, then the appropriate basis for the C_{3v} center parameters of Section 4.4.2 is that depicted in Figure 4.30(a). This is also the basis that is expected from comparison of the C_{3v} center point-charge calculations and the crystal-field parameters obtained here.

The magnet used for these experiments is constructed in such a way that the sample orientation can not be modified once the magnetic has been cooled. The cryogenic vacuum space is required to be opened before any adjustment can be made to the sample alignment. It is therefore not possible with the present setup to make adjustments in the sample alignment on the basis of high field spectra.

It should be noted that the same anomalous splittings have consistently been observed for Zeeman studies of the trigonal Er^{3+} centers in the fluorites [23]. Because of the occurrence of these splittings with different samples, it raised the possibility that the origin of the anomalous splittings is in fact some off-axis distortion of the center itself, rather than an issue of the sample mounting. However because those erbium studies and the dysprosium Zeeman work reported here have been carried out on the same apparatus, it may in fact be an indication of misalignment of the magnetic itself with respect to the mounting assembly. Both dysprosium and erbium have quite large splitting factors in comparison to the rest of the lanthanides studied with the apparatus used here, and it is likely that it is only with these ions that the issue of such a small misalignment arises.

The presence of both C_{3v} and C_{4v} centers in SrF_2:Dy^{3+} makes it is possible to perform a check on whether the apparent misalignment of the C_{3v} centers is due to some off-axis distortion of the centers themselves, or an external effect of crystal (mis)orientation. By considering the Zeeman splittings of the C_{4v} center obtained at the same time as those of the C_{3v} center, the effects of misalignment on each of these centers can be compared.

The C_{4v} centers in the $\boldsymbol{B}\|\langle 100\rangle$ geometry will be expected to provide a sensitive test of alignment. Focusing on the C_{4v} X_1 Zeeman absorption, the C_{4v} centers arranged perpendicular to the magnetic field will exhibit a quite small splitting due to the small $S_\perp$ factors of the ground and excited states (c.f. Table 4.28). As $S_\| \gg S_\perp$ for these states, any misalignment will introduce relatively large effects from the parallel splitting

factor and a considerable change in the observed Zeeman splittings would be expected to result. With this in mind, Figure 4.39 presents the $\boldsymbol{B}\|\langle 100\rangle$ Zeeman absorption spectra and splitting diagrams for the X_1 level of the C_{4v} center. The calculated splitting pattern expected for $\boldsymbol{B}\|\langle 100\rangle$ is shown, along with that expected for a small misalignment of the form $\boldsymbol{B}=B\langle\cos\theta,0,\sin\theta\rangle$. The calculations for the misaligned case are for an angle of 4^o off axis. The results of this calculation do indeed tend to indicate that the sample is misaligned. It is therefore considered that the excess splittings of C_{3v} transitions observed in the $\boldsymbol{B}\|\langle 100\rangle$ samples are a result of misalignment of the sample with respect to the magnetic field. To fully test this conclusion it would be necessary to perform the Zeeman measurements with a magnet that is capable of having the sample alignment adjusted while the sample is at cryogenic temperatures, and with real time reference to the Zeeman spectra.

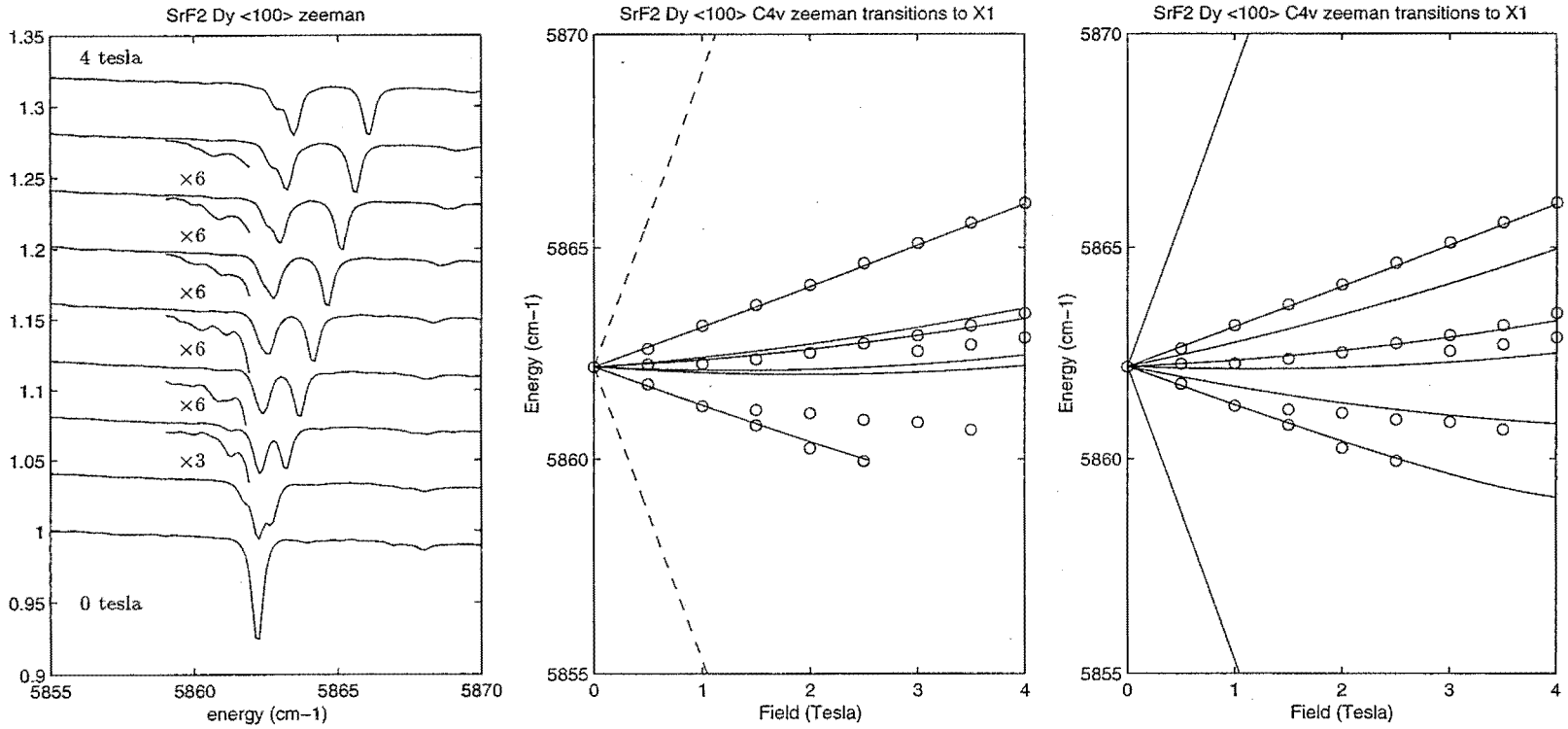

Figure 4.39: The $B\|\langle 100\rangle$ Zeeman infrared absorption spectra of the X_1 level of the SrF_2:Dy^{3+} C_{4v} center and the associated splitting diagrams. The calculated splittings are for perfect alignment (center), and for a misalignment of 4^o such that $B{=}B(\cos\theta, 0, \sin\theta)$.

The Zeeman spectra of the C_{3v} Y_1 level at $3555\,cm^{-1}$ is now discussed. The absorption spectra and the splitting diagram are presented in Figure 4.40. Because only two of the four transitions between the Zeeman sublevels are observed, the $\langle 100 \rangle$ splitting factors for both the Z_1 and Y_1 states cannot be directly determined. Only the difference in the splitting factors $\Delta S_{\langle 100 \rangle} \equiv |S_{\langle 100 \rangle}(Z_1) - S_{\langle 100 \rangle}(Y_1)|$ can be inferred from experiment, as the observed splittings will be due to the difference in the Zeeman splittings of the two states, as schematically shown in the adjacent figure. It is therefore this quantity which is compared with calculations based on the wavefunctions obtained from the crystal-field analysis. Experimentally the difference in splitting factors at 2 Tesla is measured to be

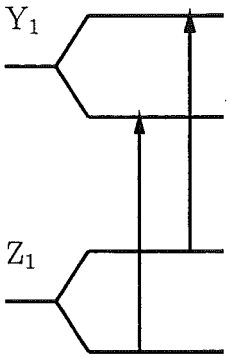

$$\Delta S_{\langle 100 \rangle 2T} = 1.07.$$

From calculation it is found that $S_{\langle 100 \rangle}(Z_1)_{2T} = 10.03$ and $S_{\langle 100 \rangle}(Y_1)_{2T} = 9.15$, and therefore

$$\Delta S_{\langle 100 \rangle \mathrm{calc}} = 0.88.$$

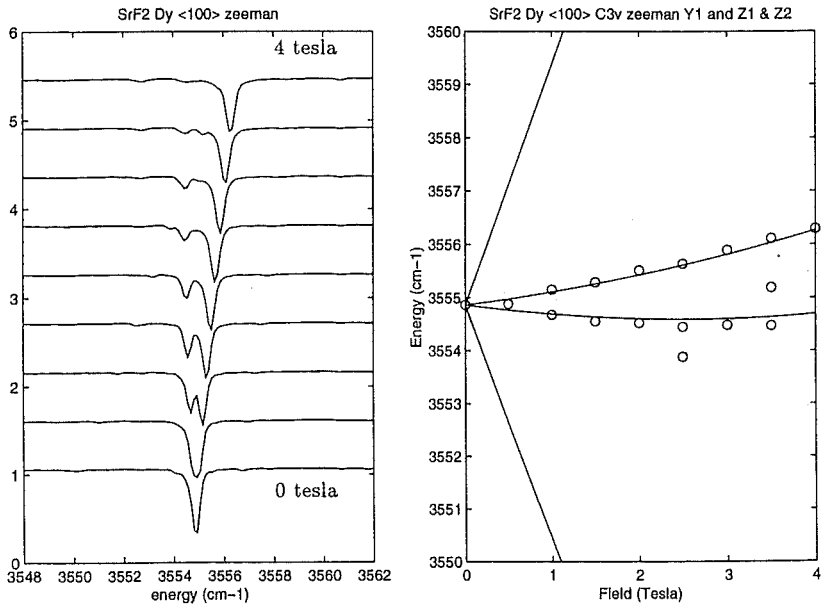

Figure 4.40: Zeeman infrared absorption spectra of SrF_2:Dy^{3+} for $\langle 100 \rangle$ sample, showing the experimental and calculated C_{3v} Y_1 splittings.

Summarising the C_{3v} center Zeeman results, the additional splittings observed in the Zeeman transitions of $\langle 100 \rangle$ oriented samples have been shown to be consistent with sample misalignment. Reasonable qualitative agreement between experimental

and calculated Zeeman splittings of the absorption transitions to the X_2, X_3 and Y_1 levels has been obtained. Some degree of quantitative agreement for the Y_1 level is also obtained. Qualitative agreement between calculation and experiment for the C_{3v} X_1 level was shown earlier in the context of the C_{4v} $\langle 111 \rangle$ Zeeman splittings. Weak absorption strengths of the C_{3v} center transitions accessible in the infrared have hampered investigation of further Zeeman transitions.

Table 4.29: SrF_2:Dy^{3+} C_{4v} wavefunctions used in the Zeeman calculations of this section.

level	energy	irrep	wavefunction
Z_1	0	γ_7	$-0.9836\|\frac{\mp 13}{2}\rangle - 0.1300\|\frac{\mp 5}{2}\rangle + 0.0944\|\frac{\pm 3}{2}\rangle - 0.0659\|\frac{\pm 11}{2}\rangle$
Z_2	38	γ_7	$0.1235\|\frac{\mp 13}{2}\rangle - 0.2464\|\frac{\mp 5}{2}\rangle + 0.3190\|\frac{\pm 3}{2}\rangle - 0.9057\|\frac{\pm 11}{2}\rangle$
Y_1	3543	γ_7	$-0.0342\|\frac{\mp 11}{2}\rangle - 0.0237\|\frac{\mp 3}{2}\rangle + 0.4604\|\frac{\pm 5}{2}\rangle - 0.8837\|\frac{\pm 13}{2}\rangle$
Y_2	3575	γ_6	$\pm 0.2207\|\frac{\mp 7}{2}\rangle \mp 0.2909\|\frac{\pm 1}{2}\rangle \pm 0.9272\|\frac{\pm 9}{2}\rangle$
X_1	5860	γ_7	$\mp 0.9825\|\frac{\mp 11}{2}\rangle \pm 0.1332\|\frac{\mp 3}{2}\rangle \pm 0.0738\|\frac{\pm 5}{2}\rangle$
X_2	—	γ_6	$\pm 0.7821\|\frac{\mp 9}{2}\rangle \pm 0.3766\|\frac{\mp 1}{2}\rangle \pm 0.4716\|\frac{\pm 7}{2}\rangle$
X_3	5957	γ_7	$-0.1376\|\frac{\mp 11}{2}\rangle - 0.5561\|\frac{\mp 3}{2}\rangle - 0.8089\|\frac{\pm 5}{2}\rangle$
X_4	5962	γ_6	$-0.5608\|\frac{\mp 9}{2}\rangle + 0.1549\|\frac{\mp 1}{2}\rangle + 0.8039\|\frac{\mp 7}{2}\rangle$
W_2	7655	γ_7	$-0.4964\|^6H_{9/2}, \frac{\mp 5}{2}\rangle - 0.6886\|^6H_{9/2}, \frac{\pm 3}{2}\rangle$ $\pm 0.3019\|^6F_{11/2}, \frac{\pm 11}{2}\rangle \pm 0.4055\|^6F_{11/2}, \frac{\pm 3}{2}\rangle \mp 0.1230\|^6F_{11/2}, \frac{\mp 5}{2}\rangle$
A_1	9005	γ_7	$\mp 0.4193\|^6H_{7/2}, \frac{\mp 5}{2}\rangle \mp 0.4090\|^6H_{7/2}, \frac{\pm 3}{2}\rangle$ $-0.4649\|^6F_{9/2}, \frac{\mp 5}{2}\rangle - 0.6457\|^6F_{9/2}, \frac{\pm 3}{2}\rangle$

Table 4.30: SrF_2:Dy^{3+} C_{3v} wavefunctions used in the Zeeman calculations of this section.

level	energy	irrep	wavefunction
Z_1	0	$\gamma_{5,6}$	$\mp 0.8716\|\frac{\mp 15}{2}\rangle - 0.4149\|\frac{\mp 9}{2}\rangle \mp 0.2131\|\frac{\mp 3}{2}\rangle$ $+0.1383\|\frac{\pm 3}{2}\rangle \mp \|\frac{\pm 9}{2}\rangle$
Z_2	39	γ_4	$\mp 0.7294\|\frac{\mp 13}{2}\rangle - 0.5137\|\frac{\mp 7}{2}\rangle \mp 0.3824\|\frac{\mp 1}{2}\rangle$ $+0.2214\|\frac{\pm 5}{2}\rangle \mp 0.0726\|\frac{\pm 11}{2}\rangle$
Y_1	3554	γ_4	$0.9615\|\frac{\mp 13}{2}\rangle \pm 0.2056\|\frac{\mp 7}{2}\rangle + 0.1400\|\frac{\mp 1}{2}\rangle$ $\mp 0.0401\|\frac{\pm 5}{2}\rangle + 0.0219\|\frac{\pm 11}{2}\rangle$
X_1	5957	γ_4	$-0.5996\|\frac{\mp 11}{2}\rangle \pm 0.6452\|\frac{\mp 5}{2}\rangle \pm 0.4368\|\frac{\pm 7}{2}\rangle$
X_2	5990	$\gamma_{5,6}$	$\mp 0.9251\|\frac{\mp 9}{2}\rangle + 0.3245\|\frac{\mp 3}{2}\rangle + 0.0262\|\frac{\pm 9}{2}\rangle$
X_3	5995	γ_4	$0.3280\|\frac{\mp 11}{2}\rangle \mp 0.2711\|\frac{\mp 5}{2}\rangle$ $+0.2648\|\frac{\pm 1}{2}\rangle \pm 0.8463\|\frac{\pm 7}{2}\rangle$
X_4	6020	γ_4	$0.7061\|\frac{\mp 11}{2}\rangle \pm 0.6593\|\frac{\mp 5}{2}\rangle - 0.1889\|\frac{\pm 1}{2}\rangle$

4.6 Summary of the SrF_2:Dy^{3+} spectroscopy.

Through laser selective excitation into the $^4F_{9/2}$ multiplet of Dy^{3+} at an energy of approximately 21000 cm^{-1}, and studies of the subsequent fluorescence, the two dominant centers in SrF_2:Dy^{3+}have been characterised. These centers have been found to be of C_{4v} and C_{3v} symmetry.

For the C_{4v} symmetry center 33 energy levels from eight different multiplets or manifolds have been identified. The fluorescence of the C_{4v} center was found to have degraded polarisation properties, similar in nature to that reported for the conjugate lanthanide ion, Sm^{3+}. The expected polarisation behaviour of fluorescence transitions between like or dislike irreps has been considered with the inclusion of both electric and magnetic dipole transition moments. Together with the experimental determination of the pure electric-dipole nature of the excitation transition, constraints of the fluorescence polarisation behaviour have been determined, and it has therefore been possible to draw conclusions on the irreps of many of the energy levels. It was also shown that magnetic-dipole processes cannot be overlooked in explaining the fluorescence polarisation behaviour. A least-squares crystal-field calculation has been carried out for the C_{4v} center using the experimentally determined energy levels. The resulting crystal-field parameters are found to agree with the general trends through the lanthanide series, with the possible exception of the B_c^4 parameter, which is approximately 20% larger in magnitude than expected from consideration of the parameters reported for the same center for the neighbouring ions in the lanthanide series, Tb^{3+} and Ho^{3+}. The crystal-field calculation gave a standard deviation between the 33 experimental and calculated energy levels of 7.6 cm^{-1}. The calculation also positioned further energy levels at energies consistent with several broad fluorescence transitions that could not be assigned from the spectroscopy alone.

Through examination of the splitting of some of these energy levels under the influence of a magnetic field, the accuracy of the wavefunctions determined from the crystal-field calculation has been tested. While the number of transitions examined was limited by the prevalence of weak absorption strengths, the results of this Zeeman infrared absorption investigation provide confidence in the accuracy of the crystal-field calculation.

An often overlooked ambiguity present in the crystal-field parametrisation, due to the two possible choices of co-ordinate bases has been addressed from an experimental point of view. This basis choice is not determined by the crystal-field Hamiltonian. While the existence of two sets of "equivalent" parameters is well known, as is to a lesser extent that this leads to some ambiguity in the signs of the wavefunction components, it has been sought to highlight that the different bases can indeed lead to observable

differences. Specifically, when two levels of different irreps mix under the influence of the Zeeman interaction, with the magnetic field not directed along the C_{4v} (or C_{3v}) axis, these two bases and wavefunctions can result in quite distinct Zeeman spectra. Unfortunately the availability of only one set of C_{4v} absorption transitions in which the mixing would be sufficient to test the basis choice, and the quite complicated nature of these transitions, which include an overlapping C_{3v} center absorption, has hampered a definitive determination of the appropriate basis for the crystal-field parameters of Section 4.3.3.

For the C_{3v} center a total of 38 energy levels from eight multiplets or manifolds have been identified. It has been found that this center has a stronger coupling to the SrF_2 lattice, as revealed by the large number of vibronic transitions with an increased relative intensity compared to the C_{4v} center. Vibronics associated with an unassigned phonon of energy $135\,cm^{-1}$ have been identified, in agreement with Eremin et.al. [34]. A number of transitions associated with the transverse optical phonon with an energy of $217\,cm^{-1}$ are also observed. The energy levels obtained are in agreement with the limited data set of Eremin et.al. A crystal-field calculation based on the determined energy levels has been performed. Irrep assignments were based on the results of this calculation. The trigonal crystal-field parameters found give approximate agreement with the calculation of Eremin et.al (which was based on only 10 energy levels), with the exception of the two axial B_A^6 and $B_A^{6\prime}$ parameters. General agreement is obtained with of the parameters reported for the SrF_2:Eu^{3+} and SrF_2:Er^{3+}(J) trigonal centers, indicating that the center discussed here has the same structure. In contrast, the crystal-field parameters display considerable disparity with those reported for the C_{3v} center of SrF_2:Ho^{3+}, indicating that it is the Ho^{3+} trigonal center that is to be considered anomalous in the SrF_2:RE^{3+} series.

The Zeeman infrared absorption spectra of the C_{3v} center in a $\boldsymbol{B}\|\langle 100\rangle$ configuration has revealed additional anomalous splittings that initially do not appear to be consistent with a true C_{3v} center. Such anomalous splittings have previously been observed in Er^{3+} trigonal centers, and the possibility of a small off axis distortion that is revealed by the large splitting values has been raised. However, it has been shown that the anomalous splittings in SrF_2:Dy^{3+} can be accounted for by a quite small misalignment of the sample, by only a few degrees. Because the SrF_2:Dy^{3+} samples posses both trigonal and tetragonal centers, is was possible to consider, and observe, effects on the Dy^{3+} C_{4v} center Zeeman spectra that show these "anomalous" splittings are not due to an off-axis distortion, but the result of small alignment errors and the large $S_\parallel$ value and small $S_\perp$ value of these centers. The basis choice involved in the C_{3v} crystal-field calculation has also been addressed. As with C_{4v} symmetry, the C_{3v} Hamiltonian is consistent with two different coordinate bases, but with a trans-

formation of the wavefunctions required to move from one basis to the other. The C_{3v} basis appropriate for the crystal-field parameters reported here has been experimentally determined from Zeeman infrared absorption measurements. Point-charge model calculations, based on the known structure of the SrF_2:RE^{3+} C_{3v} center, support this experimentally determined basis.

Chapter 5

Spectroscopy of $CaF_2:Dy^{3+}$.

5.1 Introduction.

Previous work.

In contrast to $SrF_2:Dy^{3+}$, there exists a reasonable quantity of work in the literature discussing the $CaF_2:Dy^{3+}$ system. Unfortunately much of this early work is lacking in firm conclusions, or remains in a state of contradiction between differing researchers. Due to the complexities of the spectroscopy, much of this earlier work tended to focus on the cubic centers. It also appears that the spectroscopy of this system has not previously been investigated by the techniques of laser-selective excitation. The early EPR work of CaF_2:0.1%$Dy^{3+}$by Bierig and Weber in 1963 [8] established a cubic center with Γ_8 ground state and a Γ_7 level lying $8.5\pm1\,cm^{-1}$higher in energy. Two trigonal centers were also reported with g values of $g_{\|}=16\pm1$, $g_{\perp}<1$ and $g_{\|}=4.93\pm0.05$, $g_{\perp}=1.50\pm0.05$, although it was not firmly established that these g values corresponded to two separate centers, and not two levels of the same center [34]. A tetragonal center with $g_{\|}=1.78$, $g_{\perp}=2.84$ was also attributed to a Dy^{3+}center, but as noted later by Antipin et.al. [5], these g values correspond closely to that of a Nd^{3+} tetragonal center. One of the earliest studies of the fluorescence of $CaF_2:Dy^{3+}$ is due to Rabbiner [83] who investigated centers assumed to be cubic in CaF_2:0.1%Dy^{3+}:0.1%Na^{+}, at liquid nitrogen temperatures. An energy level scheme for the three lowest multiplets was constructed from the observed fluorescence. This included a Γ_7 ground state, in disagreement with the EPR results of Bierig et.al. Voron'ko et.al. [99] discussed the optical properties of $CaF_2:Dy^{3+}$ with reference to characterising crystals before γ-irradiation creating Dy^{2+} impurities. Luks, Saitkulov and Stolov [66] also examined the luminescence spectra of $CaF_2:Dy^{3+}$ and identified transitions of four centers which were grouped according to fluorescence lifetimes. The centers were arbitrarily labelled A, B, C and D. The D center is a center involving Na^{+} and is of no further interest here. The C center was assigned as cubic. Neither the A or B centers were assigned to any particular structure, although the B center was later considered to be tetragonal by Antipin [5]. The Stark

level schemes for the two lowest multiplets were constructed for centers B, C and D. As with Rabbiner, the emitting multiplet was incorrectly ascribed to be $^6F_{11/2}$ rather than $^4F_{9/2}$. The fluorescent lifetimes of the three centers A, B and C were given as 1.8 ms, 2.9 ms and 6.6 ms respectively, at a temperature of 77 K. Al'tshuler et.al. [3] have analysed the $^4F_{9/2} \rightarrow {}^6H_{15/2}$, $^6H_{13/2}$, $^6H_{11/2}$ luminescence of Dy^{3+} cubic centers in fluorite structure crystals, including CaF_2. The energy levels of these lower multiplets were inferred from the fluorescence, and in the first reported crystal-field calculation for CaF_2:Dy^{3+} centers, the cubic crystal-field parameters were obtained. Schlesinger and Kwan [93] investigated the thermoluminescence and luminescence of CaF_2:0.1%Dy^{3+}. Narrowband excitation of the samples was employed in an effort to obtain site-selective fluorescence. However, with a bandwidth of $\approx$40 cm^{-1} it is unlikely that the obtained fluorescence was truly site selective. No analysis of the results is given and only some minor qualitative points made. Nara and Schlesinger [75] have also carried out a crystal-field calculation for the cubic centers in CaF_2:Dy^{3+}, based on the $^6H_{15/2}$ and $^6H_{13/2}$ energy levels inferred from thermoluminescence. Crystal-field parameters similar to those of Al'tshuler et.al. [3] were obtained. In a subsequent paper Nara and Schlesinger [76] presented a crystal-field analysis for a proposed tetragonal energy level scheme, based on the $^6H_{15/2}$ and $^6H_{13/2}$ multiplets. Antipin et.al. [5] also addressed the tetragonal centers in CaF_2:Dy^{3+}, assigning the B center of Luks, Satitkulov and Stolov [66] as tetragonal, and on the basis of their reported levels of the $^6H_{15/2}$ and $^6H_{13/2}$ multiplets calculated tetragonal crystal-field parameters. From the resulting ground state wavefunctions they calculate g values of $g_{\|}$=17.06, $g_{\perp}$=0. Salva and Tovar [92] looked at the anisotropy of EPR g-values for the CaF_2:Dy^{3+} cubic centers, which occurs due to the interaction of the Γ_8 ground state and the nearby Γ_7 level, determining a splitting between the two lowest levels of 9.5$\pm$0.4 cm^{-1}. Sivaram et.al. [94] have presented the results of an investigation into CaF_2:Dy^{3+} luminescence for Dy^{3+} concentration ranging from 0.01% to 1.08% by weight. The excitation was provided by Ar^+ and N_2 lasers. Two centers, labelled A and B, were observed and assigned as tetragonal and cubic respectively. The fluorescence lifetimes for the 1.08% sample were reported as 1.3 ms for the tetragonal and 3.5 ms for the cubic center. This work represents the only laser excitation (although non-selective) study of the CaF_2:Dy^{3+} system, and also the only attempt to extend the energy level scheme above the first three multiplets (excluding the emitting $^4F_{9/2}$ levels). They have given the inferred energy levels of their tetragonal center for the $^6H_{15/2}$, $^6H_{13/2}$, $^6H_{11/2}$, ($^6H_{9/2}$, $^6F_{11/2}$), ($^6H_{7/2}$, $^6F_{9/2}$) and $^4F_{9/2}$ multiplets. No crystal-field analysis is given.

While many of the energy levels of Sivaram et.al. are in agreement with that of the B center of Luks et.al. [66] and the analysis of Antipin et.al., there are also significant differences. Further, both Sivaram and Antipin have energy levels schemes that are

considerably different from that proposed by Nara and Schlesinger [76]. All three energy level schemes are also inconsistent with superposition model calculations for the CaF_2:Dy^{3+} tetragonal center [88].

The tetragonal center to be described in this work is in substantial disagreement with both that of Antipin et.al., Luks et.al., Sivaram et.al. and Nara et.al. A feature of the $^6H_{15/2}$ multiplet in the first two of these papers is a ground state splitting of $6\,cm^{-1}$. No such tetragonal center ground state splitting is observed here, and disagreement with these tetragonal energy level schemes is found.

With regard to trigonal centers, it is noted that Eremin, Luks and Stolov [34] have carried out crystal-field analyses of trigonal centers in Dy^{3+} doped crystals of the fluorite structure. However, for the case of CaF_2, only O_2^- and OH^- trigonal centers were discussed.

To summarise the previous work on the CaF_2:Dy^{3+} centers, a considerable amount of analysis and data exists for the cubic centers, predominately from EPR and luminescence experiments. The tetragonal centers have received some attention, with two similar energy level schemes inferred from luminescence data, and a crystal-field calculation based on the two lowest multiplets of one of these schemes reported. However there is some doubt as to the accuracy of the tetragonal center assignments, as they are inconsistent with point-charge model calculations and with the CaF_2:RE^{3+} crystal-field parameters determined for other lanthanide ions in the C_{4v} centers. For the trigonal centers, some EPR data exists, although the assignment of these centers (or center) is not clear. The O_2^- and OH^- trigonal centers have been analysed in terms of crystal field calculations. No information on a center assigned to a trigonal Dy^{3+}-F^- center has been reported. There is also no site-selective laser excitation studies of CaF_2:Dy^{3+} reported in the literature.

This work.

This chapter reports the first laser selective studies of the C_{4v} and C_{3v} Dy^{3+}-F^- centers in CaF_2. For both centers, energy levels from eight multiplets have been inferred from the fluorescence and excitation data. In the case of the C_{4v} center, additional polarised fluorescence information has been obtained, aiding in the assignment of irreps to the energy levels. A crystal-field calculation is presented, and the resulting C_{4v} crystal-field parameters are shown to be consistent with that expected by comparison with other CaF_2:RE^{3+} tetragonal centers. The energy level scheme of the C_{4v} center to be presented here is in disagreement with that of Antipin et.al. [5], Sivaram et.al. [94] and Nara et.al [75]. Zeeman experiments, analysed in terms of wavefunctions derived from

crystal-field calculations, support the accuracy of the C_{4v} center data and energy level assignments. The energy level scheme for the second center presented in this chapter has been assigned as C_{3v} :F^-on the basis of crystal-field calculations, which are also consistent with such centers in CaF_2 doped with other rare-earth ions towards the end of the lanthanide series.

The spectroscopy presented in this chapter was obtained with doping concentrations $\leq$0.05%Dy^{3+}, minimising both cluster center and cubic center formation. Because the cubic center is best observed in more highly doped samples, and is formed partly as a consequence of the "gettering" action of cluster formation [97], the CaF_2:Dy^{3+} cubic center data and analysis is presented in Chapter 6, in conjunction with results on the more complex cluster centers that have been observed in CaF_2:Dy^{3+} and CaF_2:Dy^{3+}:RE^{3+} crystals with higher dopant concentrations.

5.2 Optical absorption, laser excitation.

The broadband excitation spectrum of the $^4F_{9/2}$ multiplet of Dy^{3+} at $\approx$21000 cm^{-1} is presented in Figure 5.1. The dominant transitions were determined to be associated with the C_{4v} :F^- center. Much weaker transitions are also observed, flanking the dominant C_{4v} :F^- excitation transition, and were determined as being associated with a C_{3v} :F^- center. In the optical absorption spectrum of the $^4F_{9/2}$ multiplet, which is also shown in Figure 5.1, several transitions are observed that are not present in the broadband excitation spectrum. This discrepancy is attributed to the presence of multi-ion Dy^{3+} centers, which can efficiently and non-radiatively cross-relax, giving rise to an absorption feature without the corresponding fluorescence. These multi-ion "cluster" centers will be discussed more fully in Chapter 6. The excitation frequencies of the radiative centers are presented in Table 5.1, along with corresponding transition assignments.

The infrared absorption to the lower multiplets will be discussed in Section 5.5, with an emphasis on transitions that can be associated with the C_{4v} or C_{3v} centers and which have been investigated with Zeeman infrared measurements.

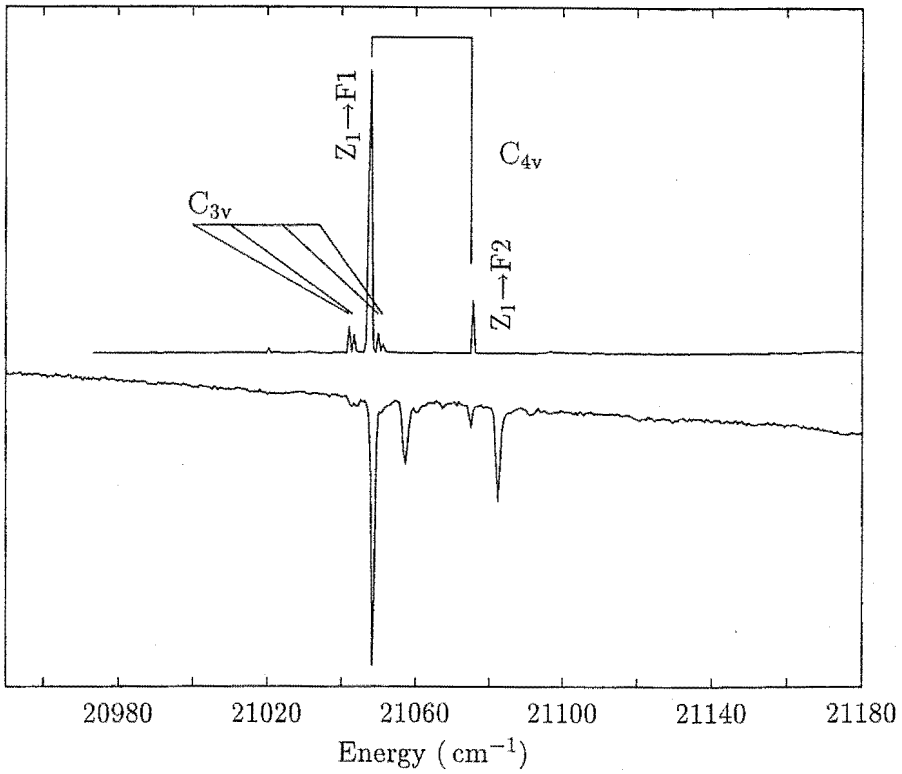

Figure 5.1: 15 K broadband excitation spectrum of the $^4F_{9/2}$ multiplet in CaF_2:Dy^{3+}, and the corresponding absorption spectrum revealing the presence of non-radiative centers. Note that the abscissa is in air cm^{-1}.

Transition frequency (cm^{-1})	Transition assignment	
	C_{4v} :F^-	C_{3v} :F^-
21037.0		$Z_2 \rightarrow F_1$
21038.5		$Z_1 \rightarrow F_1$
21042.5	$Z_1 \rightarrow F_1$	
21044.5		$Z_2 \rightarrow F_2$
21046.0		$Z_1 \rightarrow F_2$
21070.0	$Z_1 \rightarrow F_2$	

$^4F_{9/2}$ Level	Energy (cm^{-1})	
	C_{4v}	C_{3v}
F_1	21042.5	21038.5
F_2	21070.0	21046.0

Table 5.1: Transition frequencies for the $^6H_{15/2} \rightarrow {}^4F_{9/2}$ excitation of the CaF_2:Dy^{3+} C_{4v} and C_{3v} centers, and the corresponding energy levels of $^4F_{9/2}$. All transition frequencies and energies are given in vacuum wavenumbers, with an absolute uncertainty of $\pm 1\,cm^{-1}$. The uncertainty associated with the splitting between the transitions is $\pm 0.5\,cm^{-1}$.

5.3 The CaF_2:Dy^{3+} C_{4v} center

5.3.1 Laser selective fluorescence

$^6H_{15/2}$ multiplet.

The $Z_1 \rightarrow F_1$ transition at 21043 cm^{-1} was used to selectively excite the CaF_2:Dy^{3+} C_{4v} center. In the spectrum of the fluorescence back to the ground multiplet, as shown in Figure 5.2, emission is observed from the F_1 state and the thermally populated F_2 level. The F_1–F_2 separation of 27 cm^{-1} is a recurring feature in 15 K fluorescence spectra. To aid the assignment of transitions, fluorescence spectra to the $^6H_{15/2}$ multiplet, and many other multiplets, were also obtained with the sample cooled to 2 K in a liquid helium immersion dewar. This quite effectively reduces the Boltzmann population of F_2 and eliminates emission from that level. Only a limited number of the transitions to $^6H_{15/2}$ have been identified. The transition frequencies and the inferred $^6H_{15/2}$ energy levels are given in Table 5.2. The assignment of the level at 185 cm^{-1} as Z_5 rather than Z_4 is based on polarisation behaviour of transitions to this state, which requires it to have Γ_6 irrep symmetry, and the level ordering predicted from crystal-field calculations.

Fluorescence energy	Transition
21070	$F_2 \rightarrow Z_1$
21043	$F_1 \rightarrow Z_1$; laser line
20991	$F_2 \rightarrow Z_2$
20964	$F_1 \rightarrow Z_2$
20915	$F_1 \rightarrow Z_3$
20884	$F_2 \rightarrow Z_5$
20858	$F_1 \rightarrow Z_5$

$^6H_{15/2}$ Level	Energy (cm^{-1})
Z_1	0
Z_2	79
Z_3	128
Z_4	—
Z_5	185
Z_6–Z_8	—

Table 5.2: Transition frequencies for the $^4F_{9/2} \rightarrow {}^6H_{15/2}$ fluorescence of the CaF_2:Dy^{3+} C_{4v} center and the inferred energy levels of $^6H_{15/2}$. All transition frequencies and energies are given in vacuum wavenumbers, with an absolute uncertainty of ± 1 cm^{-1}.

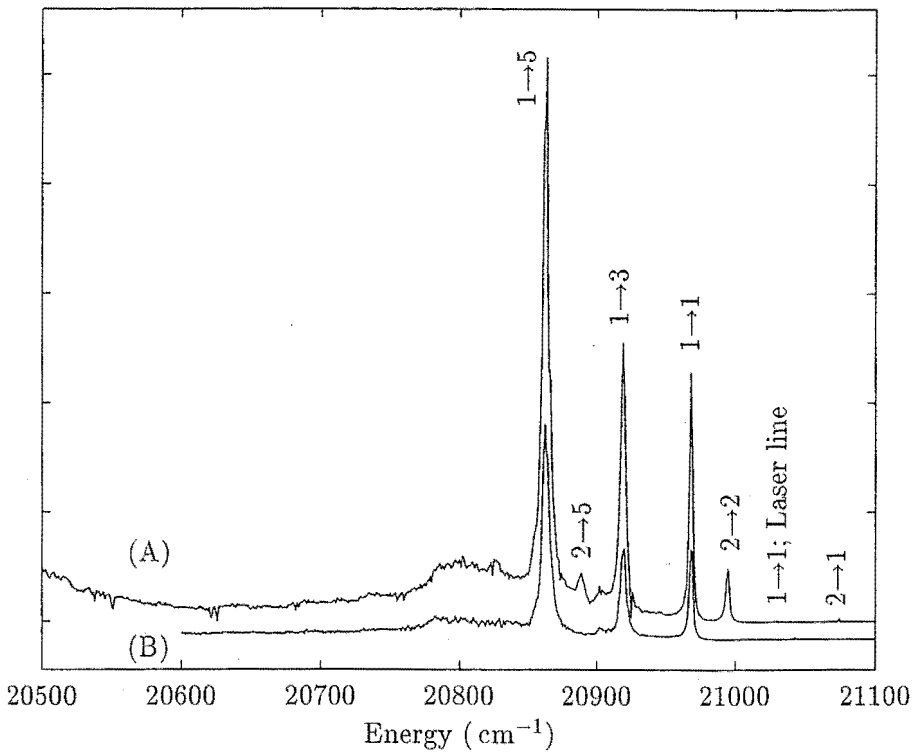

Figure 5.2: $^4F_{9/2} \rightarrow {}^6H_{15/2}$ fluorescence spectra of the CaF_2:Dy^{3+} C_{4v} center. (A) 15 Kelvin; (B) 2 Kelvin. The spectrometer shutter was closed in the vicinity of the laser frequency, at 21043 cm^{-1}.

$^6H_{13/2}$ multiplet.

The fluorescence of the C_{4v} center terminating on the $^6H_{13/2}$ multiplet is relatively complex and only four of the seven energy levels of this multiplet have been determined. Three transitions at ≈17410 cm^{-1} overlap each other to some extent, and are shown enlarged in the inset of Figure 5.3. A comparison between the 15 K and 2 K spectra, and observation of the 27 cm^{-1} separation in the F_1 and F_2 emission, enables a satisfactory assignment of the higher frequency transitions. Comparing the spectra at both temperatures, no significant difference is observed for the transitions with frequencies between 17300 cm^{-1} and 17100 cm^{-1}, and it has not been possible to assign the four broad transitions in terms of emission to the remaining three levels (Y_5–Y_7) of $^6H_{13/2}$. These transitions have therefore been left unassigned. Apparent in the 2 K spectrum is a number of weak transitions for which no 15 K emission was observed. It is thought that these transitions are due to cluster center fluorescence. The "cluster" centers, those with more than one Dy^{3+} ion in close proximity, are expected to undergo rapid non-radiative cross-relaxation. It is possible that at the reduced temperature of 2 K these cross-relaxation processes become less efficient, allowing some fluorescence to be observed.

Fluorescence energy	Transition
17531	$F_2 \rightarrow Y_1$
17504	$F_1 \rightarrow Y_1$
17440	$F_2 \rightarrow Y_2$
17438	$F_2 \rightarrow Y_3$
17413	$F_1 \rightarrow Y_2$
17410	$F_1 \rightarrow Y_3$
17407	$F_2 \rightarrow Y_4$
17380	$F_1 \rightarrow Y_4$
17311	a
17294	b
17267	c
17179	d

$^6H_{13/2}$ Level	Energy (cm^{-1})
Y_1	3539
Y_2	3630
Y_3	3633
Y_4	3663
Y_5–Y_7	—

Table 5.3: Transition frequencies for the $^4F_{9/2} \rightarrow {}^6H_{13/2}$ fluorescence of the CaF_2:Dy^{3+} C_{4v} center, and the inferred energy levels of $^6H_{13/2}$. All transition frequencies and energies are given in vacuum wavenumbers, with an absolute uncertainty of $\pm 1\,cm^{-1}$.

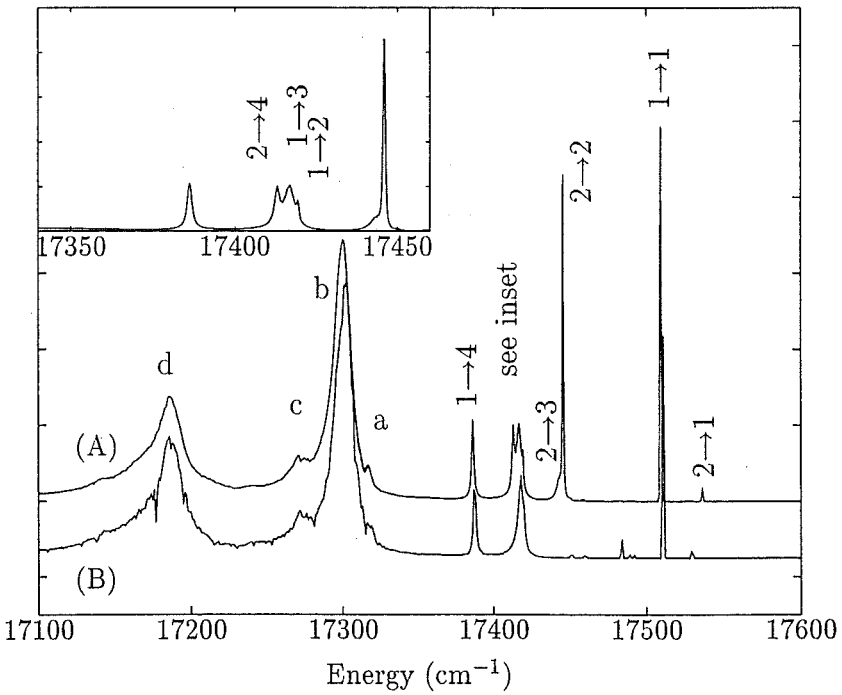

Figure 5.3: $^4F_{9/2} \rightarrow {}^6H_{13/2}$ fluorescence spectra of the CaF_2:Dy^{3+} C_{4v} center. (A) 15 Kelvin; (B) 2 Kelvin. The spectrum in the inset is for a sample temperature of 15 K.

The fluorescence transition frequencies and the inferred energy levels of $^6H_{13/2}$ are presented in Table 5.3.

$^6H_{11/2}$ multiplet.

Site selective emission to the levels of the $^6H_{11/2}$ is shown in Figure 5.4. All six energy levels have been determined with the assistance of the observed emission from both F_1 and F_2. One complication in the fluorescence, highlighted in the expanded spectrum in the inset of Figure 5.4, is a weak feature $2\,cm^{-1}$ below the $F_2 \rightarrow X_4$ transition. This unassigned transition is also present in the 2 K spectrum. A satisfactory explanation of this weak transition has not been found.

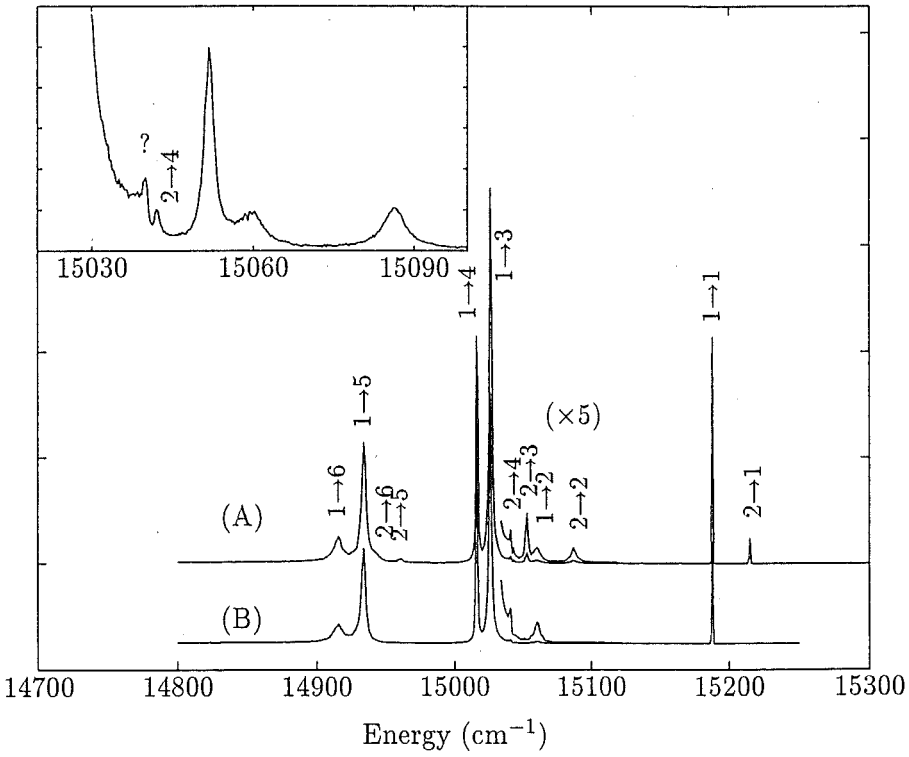

Figure 5.4: $^4F_{9/2} \rightarrow {}^6H_{11/2}$ fluorescence spectra of the $CaF_2:Dy^{3+}$ C_{4v} center. (A) 15 Kelvin; (B) 2 Kelvin. The spectrum in the inset is for a sample temperature of 15 K.

Fluorescence energy	Transition
15210	$F_2 \rightarrow X_1$
15184	$F_1 \rightarrow X_1$
15083	$F_2 \rightarrow X_2$
15056	$F_1 \rightarrow X_2$
15048	$F_2 \rightarrow X_3$
15038	$F_2 \rightarrow X_4$
15036	?
15022	$F_1 \rightarrow X_3$
15012	$F_1 \rightarrow X_4$
14956	$F_2 \rightarrow X_5$
14938	$F_2 \rightarrow X_6$
14930	$F_1 \rightarrow X_5$
14912	$F_1 \rightarrow X_6$

$^6H_{11/2}$ Level	Energy (cm^{-1})
X_1	5859
X_2	5987
X_3	6021
X_4	6031
X_5	6113
X_6	6131

Table 5.4: Transition frequencies for the $^4F_{9/2} \rightarrow {}^6H_{11/2}$ fluorescence of the CaF_2:Dy^{3+} C_{4v} center, and the inferred energy levels of $^6H_{11/2}$. All transition frequencies and energies are given in vacuum wavenumbers, with an absolute uncertainty of $\pm 1\,cm^{-1}$.

$^6H_{9/2}$, $^6F_{11/2}$ multiplets.

As already discussed in Chapter 4 on the spectroscopy of SrF_2:Dy^{3+}, the $^6H_{9/2}$ and $^6F_{11/2}$ multiplets are intertwined, and these combined multiplets are referred to as the W manifold. From the fluorescence to this manifold, as shown in Figure 5.5, the energies of five states have been unambiguously identified, with emission from both F_1 and F_2 terminating on these states. Two remaining features are observed, and are attributed to F_1 emission because of their persistence in the 2 K spectrum. These transitions at $13155\,cm^{-1}$ and $13092\,cm^{-1}$ have been assigned to emission terminating on the W_6 and W_8 levels respectively, by comparison with the energy levels found from the subsequent crystal-field calculation of Section 5.3.3. To avoid a circular argument these levels have not been included in the least-squares crystal-field calculation.

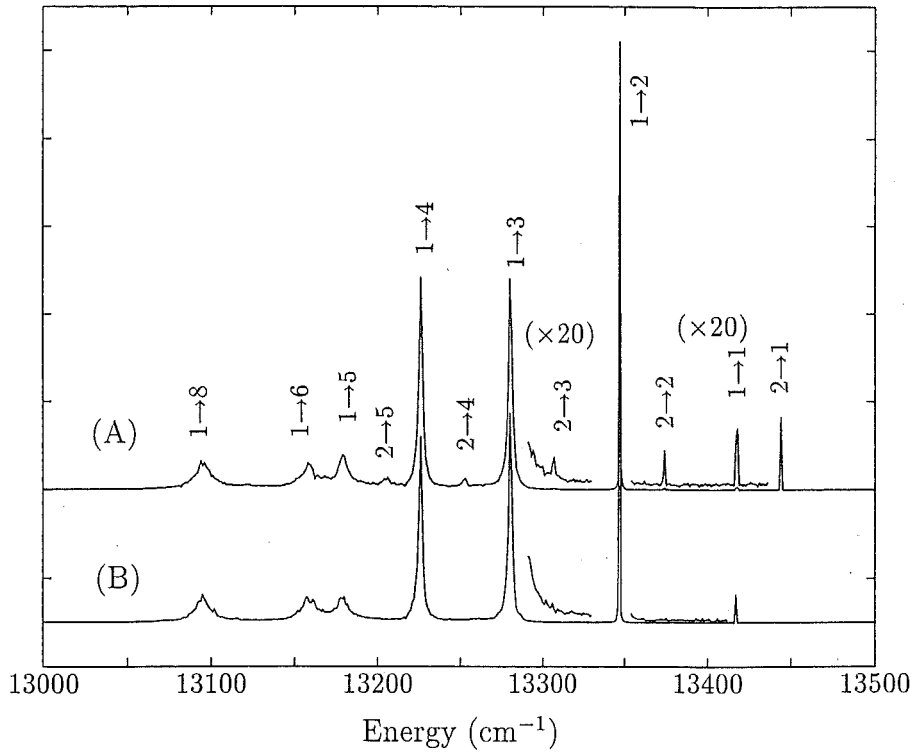

Figure 5.5: $^4F_{9/2} \rightarrow {}^6H_{9/2}$, $^6F_{11/2}$ (W manifold) fluorescence spectra of the CaF_2:Dy^{3+} C_{4v} center. (A) 15 Kelvin; (B) 2 Kelvin.

Fluorescence energy	Transition
13440	$F_2 \rightarrow W_1$
13414	$F_1 \rightarrow W_1$
13371	$F_2 \rightarrow W_2$
13343	$F_1 \rightarrow W_2$
13304	$F_2 \rightarrow W_3$
13277	$F_1 \rightarrow W_3$
13250	$F_2 \rightarrow W_4$
13223	$F_1 \rightarrow W_4$
13202	$F_2 \rightarrow W_5$
13176	$F_1 \rightarrow W_5$
13155	$F_1 \rightarrow W_6$ †
13092	$F_1 \rightarrow W_8$ †

$^6H_{9/2}$, $^6F_{11/2}$ Level	Energy (cm^{-1})
W_1	7629
W_2	7700
W_3	7766
W_4	7820
W_5	7867
W_6†	7888
W_7	—
W_8†	7951
W_9–W_{11}	—

Table 5.5: Transition frequencies for the $^4F_{9/2} \rightarrow {}^6H_{9/2}$, $^6F_{11/2}$ (W manifold) fluorescence of the CaF_2:Dy^{3+} C_{4v} center, and the inferred energy levels of the W manifold. All transition frequencies and energies are given in vacuum wavenumbers, with an absolute uncertainty of $\pm 1\,cm^{-1}$. † Tentatively assigned transitions and the corresponding energy levels which were not used in the crystal-field calculation.

$^6H_{7/2}$, $^6F_{9/2}$ multiplets.

A limited number of energy levels of the A manifold have been unambiguously identified from the fluorescence spectra of Figure 5.6. For transitions terminating on A_1, A_2 and A_3 emission is observed from both F_1 and F_2, aiding in their assignment. To enable a tentative assignment of further transitions reference has been made to the results of the crystal-field calculation, which indicates that the transition at 11342 cm^{-1} is approximately that expected for $F_1 \rightarrow A_9$. This transition has a high energy shoulder that would be appropriate for associated F_2 emission adding confidence to this assignment. The transitions labelled as terminating on A_5 in Figure 5.6 also display the appropriate 27 cm^{-1} F_1–F_2 splitting. The remaining (tentatively) assigned transitions are taken as originating on the F_1 state through reference to the similarity of the 2 K and 15 K spectra. Transitions to A_6 are not assigned, as any remaining features in the spectra are both ambiguous and inconsistent with crystal-field calculations. The transition at 11537 cm^{-1} is left unassigned for the same reasons.

Because of the difficulties in the above mentioned transitions assignments, only the levels A_1, A_2 and A_3 have been used in the crystal-field calculations.

Fluorescence energy	Transition
12040	$F_2 \rightarrow A_1$
12014	$F_1 \rightarrow A_1$
12008	$F_2 \rightarrow A_2$
11981	$F_1 \rightarrow A_2$
11925	$F_2 \rightarrow A_3$
11898	$F_1 \rightarrow A_3$
11766	$F_1 \rightarrow A_4$ †
11741	$F_2 \rightarrow A_5$ †
11712	$F_1 \rightarrow A_5$ †
11690	$F_1 \rightarrow A_7$ †
11613	$F_1 \rightarrow A_8$ †
11537	a
11342	$F_1 \rightarrow A_9$ †

$^6H_{7/2}$, $^6F_{9/2}$ Level	Energy (cm^{-1})
A_1	9029
A_2	9062
A_3	9145
A_4†	9277
A_5†	9331
A_6	—
A_7†	9354
A_8†	9430
A_9†	9701

Table 5.6: Transition frequencies for the $^4F_{9/2} \rightarrow {}^6H_{7/2}$, $^6F_{9/2}$ (A manifold) fluorescence of the CaF_2:Dy^{3+} C_{4v} center, and the inferred energy levels of the A manifold. All transition frequencies and energies are given in vacuum wavenumbers, with an absolute uncertainty of ±1 cm^{-1}. † Tentatively assigned transitions, and the corresponding energy levels which were not used in the crystal-field calculation.

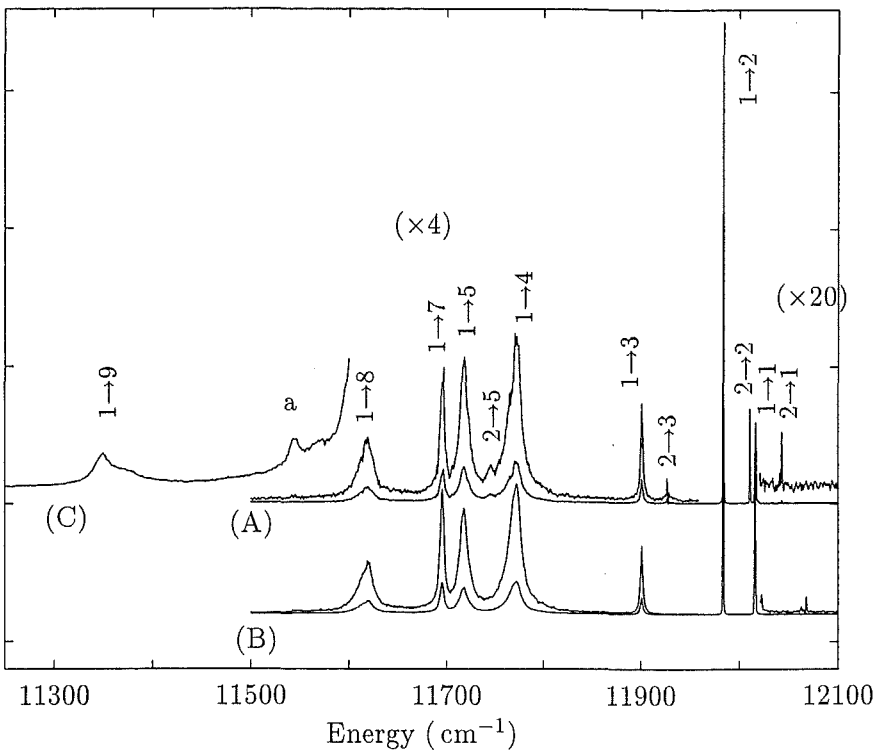

Figure 5.6: $^4F_{9/2} \rightarrow {}^6H_{7/2}$, $^6F_{9/2}$ (A manifold) fluorescence spectra of the CaF_2:Dy^{3+} C_{4v} center. (A) 15 Kelvin; (B) 2 Kelvin; (C) 15 Kelvin, recorded with infrared PMT.

$^6H_{5/2}$ multiplet.

The fluorescence to the $^6H_{5/2}$ multiplet (Figure 5.7) is quite weak in intensity, and despite there being only three states of this multiplet, it has been difficult to assign the observed transitions. The only transition that can be assigned with any confidence is the $F_1 \rightarrow B_1$ transition at 10852 cm^{-1}. A shoulder observed on the high energy side of this transition is consistent with the $F_2 \rightarrow B_1$ transition. The remaining transitions and energy levels were not able to be assigned.

Fluorescence energy	Transition
(shoulder)	$F_2 \rightarrow B_1$
10852	$F_1 \rightarrow B_1$
10632	b
10562	c
10516	d

$^6H_{5/2}$ Level	Energy (cm^{-1})
B_1	10191
B_2	—
B_3	—

Table 5.7: Transition frequencies for the $^4F_{9/2} \rightarrow {}^6H_{5/2}$ fluorescence of the CaF_2:Dy^{3+} C_{4v} center, and the inferred energy levels of $^6H_{5/2}$. All transition frequencies and energies are given in vacuum wavenumbers, with an absolute uncertainty of ± 2 cm^{-1}.

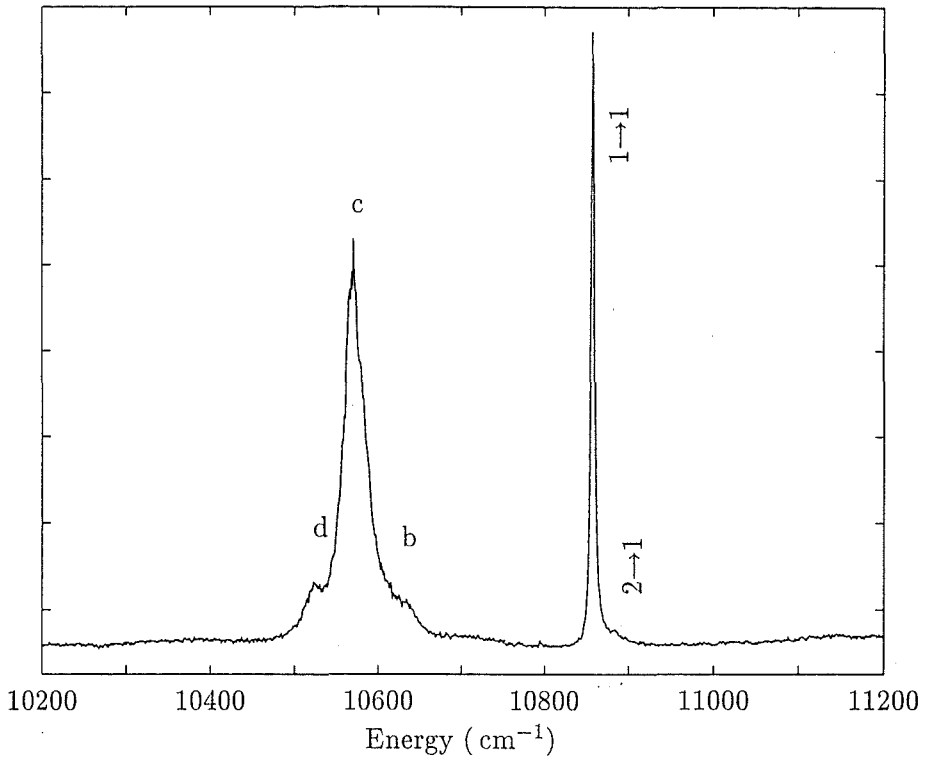

Figure 5.7: 15 K $^4F_{9/2} \rightarrow {}^6H_{5/2}$ fluorescence spectrum of the CaF_2:Dy^{3+} C_{4v} center. Recorded with infrared PMT.

$^6F_{7/2}$ multiplet.

The fluorescence to the $^6F_{7/2}$ multiplet is quite clear in its interpretation, and all four energy levels of this multiplet can be easily and unambiguously inferred from the spectra of Figure 5.8. Fluorescence from both emitting levels is observed for each of the four terminating states. The fluorescence frequencies and the inferred energy levels are presented in Table 5.8.

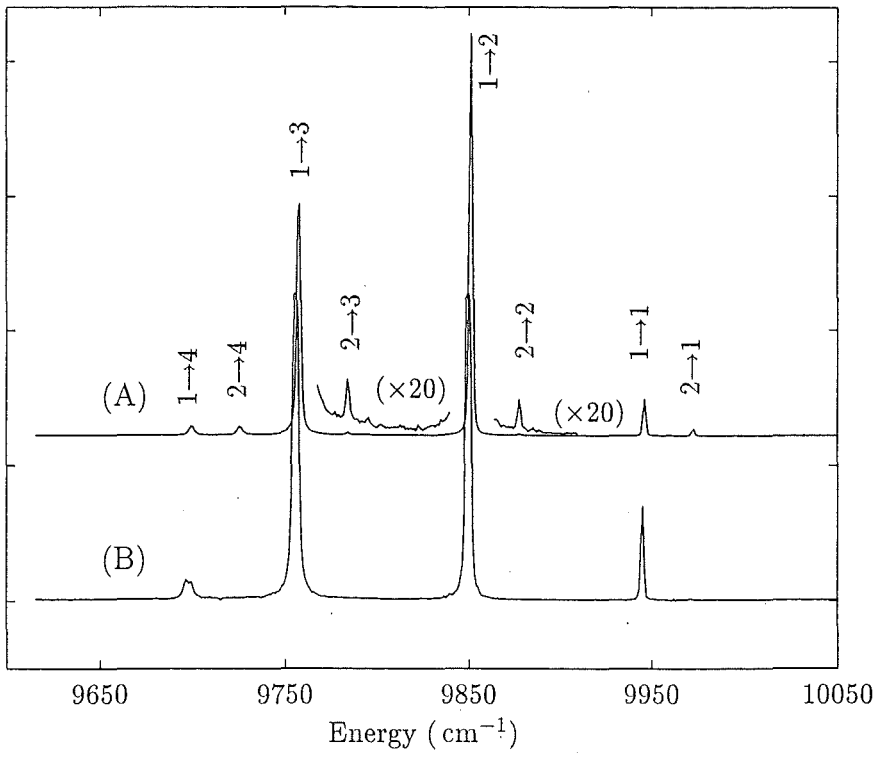

Figure 5.8: $^4F_{9/2} \rightarrow {}^6F_{7/2}$ fluorescence spectra of the CaF_2:Dy^{3+} C_{4v} center. Recorded with infrared PMT. (A) 15 Kelvin; (B) 2 Kelvin

Fluorescence energy	Transition
9967	$F_2 \rightarrow C_1$
9941	$F_1 \rightarrow C_1$
9874	$F_2 \rightarrow C_2$
9847	$F_1 \rightarrow C_2$
9781	$F_2 \rightarrow C_3$
9754	$F_1 \rightarrow C_3$
9723	$F_2 \rightarrow C_4$
9696	$F_1 \rightarrow C_4$

$^6F_{7/2}$ Level	Energy (cm^{-1})
C_1	11102
C_2	11196
C_3	11289
C_4	11347

Table 5.8: Transition frequencies for the $^4F_{9/2} \rightarrow {}^6F_{7/2}$ fluorescence of the CaF_2:Dy^{3+} C_{4v} center, and the inferred energy levels of $^6F_{7/2}$. All transition frequencies and energies are given in vacuum wavenumbers, with an absolute uncertainty of $\pm 2\,\mathrm{cm}^{-1}$.

5.3.2 Fluorescence polarisation.

To determine information on the irrep assignments of the C_{4v} energy levels laser selective polarised fluorescence measurements were made on the CaF_2:$Dy^{3+}C_{4v}$ center, in the same manner as previously discussed for SrF_2:Dy^{3+}. Again it is found that the polarisation ratios are such that the YX:YY ratios, by themselves, are often ambiguous for determining or checking irrep assignments.

As discussed in Section 4.3.2, interpretation of the polarisation data in terms of irrep assignments becomes tractable if the absorption transition is purely electric-dipole or purely magnetic-dipole in character, and also between states transforming as unlike irreps. The first issue, that of establishing the electric-dipole (or magnetic-dipole) nature of an absorption transition, has been addressed by use of the photoelastic modulator for determining the similarity or otherwise of the ZX:ZY and YX:YY polarisation intensities. When used for this purpose, the photoelastic modulator minimises any issues of laser stability and monochromator reproducibility. As shown in Figure 5.9, the AC signal, representing a difference in the polarised intensities, reveals that the $^4F_{9/2} \rightarrow {}^6H_{13/2}$ and $^4F_{9/2} \rightarrow {}^6H_{15/2}$ emission, following $Z_1 \rightarrow F_2$ excitation, has polarised intensities such that in general $I_{ZX}=I_{ZY}$ and $I_{YX} \neq I_{YY}$. This establishes the absorption transition as a purely electric-dipole process.

The second requirement for obtaining meaningful polarisation data is that the chosen absorption transition must be between states transforming as different irreps. This ensures that the transition proceeds via a σ- (or σ'-) polarised transition moment. Preliminary crystal-field calculations indicate that the Z_1, F_1 and F_2 levels transform as the Γ_7, Γ_7 and Γ_6 irreps respectively. These irrep assignments are confirmed by the fluorescence polarisation data which will shortly be discussed. Hence the polarisation studies of the CaF_2:Dy^{3+} C_{4v} center were performed with $Z_1(\Gamma_7) \rightarrow F_2(\Gamma_6)$ excitation, which unfortunately is considerably weaker than the $Z_1(\Gamma_7) \rightarrow F_1(\Gamma_7)$ transition.

The information discussed above leads to the consideration of the polarised fluorescence following excitation by a purely electric dipole σ-polarised transition. This situation is therefore analogous in all relevant respects to that encountered for the SrF_2:Dy^{3+} C_{4v} center. The discussion of Section 4.3.2 (page 57) can therefore be directly carried over to the present situation, and the polarised intensities will be constrained as given in Tables 4.12,4.13 on page 59.

Polarised fluorescence spectra were recorded in each of the four polarisation configurations (YX, YY, ZX, ZY), and normalised with respect to laser power to minimise the problems of laser power instability. The relative intensities of various transitions for these configurations are presented in Table 5.9, along with the irrep assignments

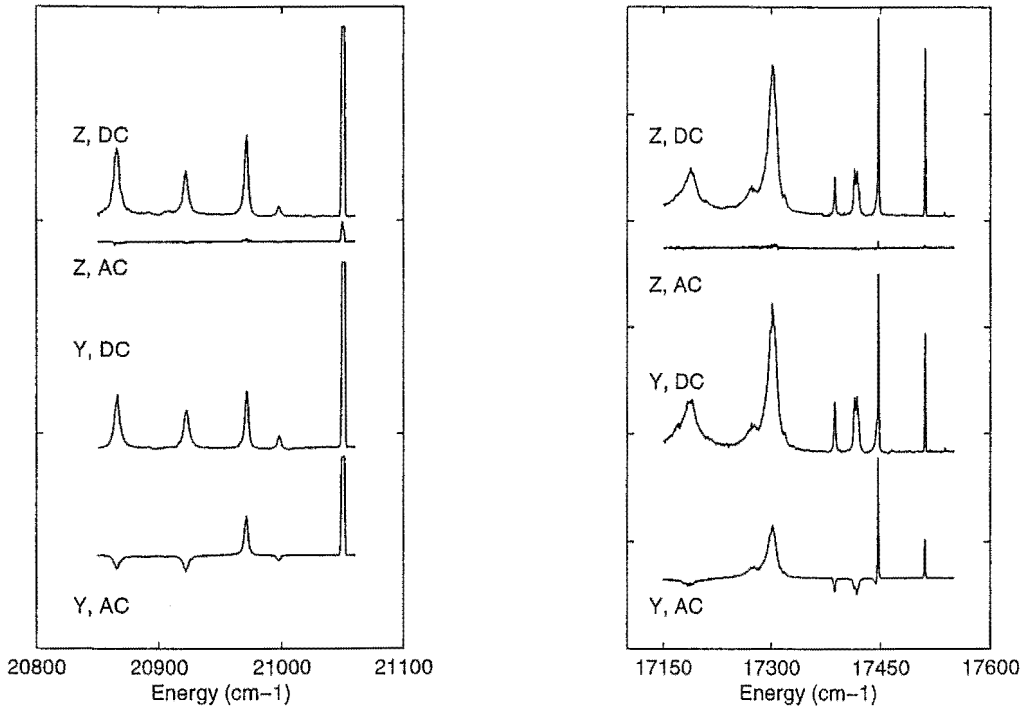

Figure 5.9: The $^4F_{9/2} \rightarrow {}^6H_{15/2}$ and $^6H_{13/2}$ fluorescence of the CaF_2:Dy^{3+} C_{4v} center, as recorded with the PEM. The AC and DC spectra are given for the two cases of laser excitation polarised in either the Y direction or the Z direction.

for the states involved in each transition. Both ZX and ZY relative intensities are given, and while these are expected to be equal in magnitude, in practice they differ slightly due to laser (frequency) instability and the limited spectral reproducibility for transitions of narrow linewidth. Low intensity transitions obviously have more noise in the intensity ratios, and many of these transitions are not listed for this reason. When considering the significance, or otherwise, of a given set of ratios the ZX:ZY ratio was taken into account along with the transition linewidth and intensity.

It is noted that the $F_1 \rightarrow Z_5$ transition is consistent with the Z_5 state transforming as the Γ_6 irrep. The crystal-field calculations place Z_4 and Z_5 in close proximity and with opposite irrep character. As transitions to only one state in the region of the expected Z_4, Z_5 energy levels is observed, it is unclear whether the observed transitions are to Z_4 or Z_5. However it is clear that the level at $186\,cm^{-1}$ is consistent with a Γ_6 irrep labelling. The final crystal-field calculation suggests that this is the Z_5 level, with $Z_4(\Gamma_7)$ lying $\approx 6\,cm^{-1}$ lower in energy. Therefore, although the level ordering in this case is not absolutely certain, the $186\,cm^{-1}$ state has been assigned as $Z_5(\Gamma_6)$.

As for the SrF_2:Dy^{3+} C_{4v} center, several transitions from $^4F_{9/2}$ to the W and A manifolds possess the characteristics of a magnetic dipole transition moment.

Table 5.9: Polarised fluorescence data for the CaF_2:Dy^{3+} C_{4v} center, for $Z_1 \rightarrow F_2$ σ-polarised absorption. † Terminating levels not used in the crystal-field parameter refinement calculations. The dominant fluorescence transition moment is given for transitions between states transforming as unlike irreps.

transition	Energy (cm^{-1})	irreps (C.F. Fit)	YX	YY	ZX	ZY	Notes
$F_1 \rightarrow Z_1$	21043	$\Gamma_7 \rightarrow \Gamma_7$	3.1	1.0	3.8	3.7	a
$F_2 \rightarrow Z_2$	20991	$\Gamma_6 \rightarrow \Gamma_7$	1.1	2.1	1.0	1.1	σ
$F_1 \rightarrow Z_2$	20964	$\Gamma_7 \rightarrow \Gamma_7$	4.8	1.0	5.1	4.9	a
$F_1 \rightarrow Z_3$	20915	$\Gamma_7 \rightarrow \Gamma_6$	1.0	1.8	1.1	1.1	σ
$F_1 \rightarrow Z_5$	20884	$\Gamma_7 \rightarrow \Gamma_6$	1.0	1.5	1.1	1.1	σ
$F_1 \rightarrow Y_1$	17504	$\Gamma_7 \rightarrow \Gamma_7$	2.1	1.0	2.2	2.1	c
$F_2 \rightarrow Y_2$	17440	$\Gamma_6 \rightarrow \Gamma_6$	7.1	1.0	8.9	7.1	a
$F_1 \rightarrow Y_2$	17413	$\Gamma_7 \rightarrow \Gamma_6$	1.0	1.6	1.2	1.1	σ
$F_1 \rightarrow Y_3$	17410	$\Gamma_7 \rightarrow \Gamma_7$	1.0	1.5	1.2	1.2	?
$F_2 \rightarrow Y_4$	17407	$\Gamma_6 \rightarrow \Gamma_6$	1.0	1.3	1.4	1.2	?
$F_1 \rightarrow Y_4$	17380	$\Gamma_7 \rightarrow \Gamma_6$	1.0	1.6	1.2	1.2	σ
	17311	—	1.6	1.0	2.4	2.1	c
	17294	—	1.9	1.0	2.7	2.4	c
	17267	—	1.9	1.0	2.9	2.5	c
	17179	—	1.0	1.5	1.9	1.6	b
$F_2 \rightarrow X_1$	15210	$\Gamma_6 \rightarrow \Gamma_7$	2.3	1.3	1.3	1.0	σ'
$F_1 \rightarrow X_1$	15184	$\Gamma_7 \rightarrow \Gamma_7$	1.3	1.0	1.3	1.1	ambig.
$F_1 \rightarrow X_2$	15056	$\Gamma_7 \rightarrow \Gamma_6$	1.1	1.5	1.1	1.0	σ
$F_2 \rightarrow X_3$	15048	$\Gamma_6 \rightarrow \Gamma_6$	1.3	1.0	2.1	1.5	c
$F_1 \rightarrow X_3$	15022	$\Gamma_7 \rightarrow \Gamma_6$	1.8	1.3	1.3	1.0	σ
$F_1 \rightarrow X_4$	15012	$\Gamma_7 \rightarrow \Gamma_7$	1.0	2.8	2.9	2.6	b
$F_1 \rightarrow X_5$	14930	$\Gamma_7 \rightarrow \Gamma_7$	1.0	1.9	2.1	1.8	b
$F_1 \rightarrow X_6$	14912	$\Gamma_7 \rightarrow \Gamma_6$	1.6	1.3	1.2	1.0	σ
$F_2 \rightarrow W_1$	13440	$\Gamma_6 \rightarrow \Gamma_6$	1.0	2.3	2.4	2.1	b
$F_1 \rightarrow W_1$	13414	$\Gamma_7 \rightarrow \Gamma_6$	2.3	1.0	1.2	1.0	σ'
$F_1 \rightarrow W_2$	13343	$\Gamma_7 \rightarrow \Gamma_7$	1.0	1.7	1.9	1.8	b
$F_1 \rightarrow W_3$	13277	$\Gamma_7 \rightarrow \Gamma_6$	2.2	1.0	1.2	1.1	σ'
$F_1 \rightarrow W_4$	13223	$\Gamma_7 \rightarrow \Gamma_7$	1.0	2.9	3.4	3.2	b
$F_1 \rightarrow W_5$	13176	$\Gamma_7 \rightarrow \Gamma_6$	2.1	1.0	1.3	1.2	σ'
$F_1 \rightarrow W_6$†	13155	$\Gamma_7 \rightarrow \Gamma_7$	1.0	1.1	1.3	1.2	d
$F_1 \rightarrow W_8$†	13092	$\Gamma_7 \rightarrow \Gamma_7$	2.7	1.0	2.3	2.1	b
$F_1 \rightarrow A_1$	12014	$\Gamma_7 \rightarrow \Gamma_7$	1.0	1.0	1.5	1.3	b
$F_1 \rightarrow A_2$	11981	$\Gamma_7 \rightarrow \Gamma_6$	1.0	2.1	1.6	1.3	σ
$F_1 \rightarrow A_3$	11898	$\Gamma_7 \rightarrow \Gamma_6$	2.2	1.0	1.4	1.1	σ'
$F_1 \rightarrow A_4$†	11766	$\Gamma_7 \rightarrow \Gamma_7$	1.6	1.0	1.5	1.2	c
$F_1 \rightarrow A_5$†	11712	$\Gamma_7 \rightarrow \Gamma_7$	1.1	1.2	1.2	1.0	d
$F_1 \rightarrow A_7$†	11690	$\Gamma_7 \rightarrow \Gamma_6$	2.0	1.2	1.3	1.0	σ'
$F_1 \rightarrow A_8$†	11613	$\Gamma_7 \rightarrow \Gamma_7$	4.0	1.0	4.4	3.3	a

Reasons for concluding a transition is between like irreps:

a) $\frac{1}{2} \leq \frac{YX}{YY} \leq 2$ not satisfied

b) $1 \leq \frac{YX}{ZX} \leq 2$ not satisfied

c) $1 \leq \frac{YY}{ZX} \leq 2$ not satisfied

d) a→c satisfied, but conflict in ratios

5.3.3 CaF_2:Dy^{3+} C_{4v} crystal-field analysis.

Values interpolated from those for the CaF_2 C_{4v} centers of the neighbouring lanthanide ions, Tb^{3+} [74] and Ho^{3+} [72], were used for initial crystal-field parameters in the the crystal-field analysis of the CaF_2:Dy^{3+} C_{4v} center. The initial spin-orbit and Slater parameters were those of $LaCl_3Dy^{3+}$ reported by Carnell et.al. [12]. All of the above parameters and the configuration average were allowed to vary to find the best match between experimental and calculated energy levels. Parameters associated with the relativistic corrections and the three body parameters were held fixed at the values of Carnell et.al. as listed in Table 4.15 on page 66. The same procedure discussed for the SrF_2:Dy^{3+} calculations was employed here, with experimental energy levels progressively added to the calculation while maintaining consistency with level ordering and irrep assignments based on polarisation data. A total of 29 energy levels were included in the least-squares refinement of parameters. Of these 29 levels, information on the irrep assignment was available for 22 levels. A resulting standard deviation between experimental and calculated energy levels of $6\,cm^{-1}$ was obtained. The crystal-field, Slater and spin-orbit parameters found from this calculation are shown in Table 5.10, and a full listing of the experimental and calculated energy levels, along with irrep assignments, is given in Table 5.11. The crystal-field parameters of the CaF_2:Dy^{3+} C_{4v} centers are compared with the equivalent parameters reported for other rare-earth ions in Figure 5.10, and the Dy^{3+} parameters are found to be in general agreement with the trends across the lanthanide series. Wavefunctions obtained from the final crystal-field calculation were employed for analysis of Zeeman infrared absorption experiments, which will be discussed in Section 5.5.2.

Table 5.10: The crystal-field, spin-orbit and Slater parameters of the CaF_2:Dy^{3+} C_{4v} center found from a least-squares calculation fitting to the experimental energy levels and irrep assignments reported here. The crystal-field parameters obtained from the superposition model calculation of Reid and Butler [88] are given for comparison. Parameter values are given in units of cm^{-1}.

Parameter	B_c^4	B_c^6	B_a^2	B_a^4	B_a^6	ζ	F^2	F^4	F^6
This work	-1360	588	628	484	428	1917	94010	68180	44945
Reid et.al. [88]	-1269	584	671	472	465	—	—	—	—

Table 5.11: Experimental and calculated energy levels for the CaF_2:Dy^{3+} C_{4v} center. † Levels not used in the least-squares calculation. * Levels with supporting polarisation data for irrep assignment.

Multiplet	Level	Irrep	Energy (cm^{-1})	
			Calc.	Expt.
$^6H_{15/2}$	Z_1*	γ_7	-5	0.0
	Z_2*	γ_7	77	79
	Z_3*	γ_6	122	128
	Z_4	γ_7	179	-
	Z_5 *	γ_6	186	185
	Z_6	γ_6	260	
	Z_7	γ_6	549	
	Z_8	γ_7	589	
$^6H_{13/2}$	Y_1*	γ_7	3543	3539
	Y_2*	γ_6	3628	3630
	Y_3	γ_7	3636	3633
	Y_4	γ_6	3663	3663
	Y_5	γ_7	3750	
	Y_6	γ_7	3861	
	Y_7	γ_6	3900	
$^6H_{11/2}$	X_1*	γ_7	5858	5859
	X_2*	γ_6	5994	5987
	X_3*	γ_6	6023	6021
	X_4*	γ_7	6026	6031
	X_5*	γ_7	6122	6113
	X_6*	γ_6	6133	6131
$^6H_{9/2}$, $^6F_{11/2}$	W_1*	γ_6	7629	7629
	W_2*	γ_7	7692	7700
	W_3*	γ_6	7774	7766
	W_4*	γ_7	7825	7820
	W_5*	γ_6	7869	7867
	W_6*	γ_7	7897	7888†
	W_7	γ_6	7944	
	W_8*	γ_7	7944	7951†
	W_9	γ_6	8082	
	W_{10}	γ_6	8221	
	W_{11}	γ_7	8223	
$^6H_{7/2}$, $^6F_{9/2}$	A_1*	γ_7	9029	9029

continued on next page

continued from previous page

Multiplet	Level	Irrep	Energy (cm^{-1})	
			Calc.	Expt.
	A_2*	γ_6	9058	9062
	A_3*	γ_6	9141	9145
	A_4*	γ_7	9264	9277†
	A_5*	γ_7	9331	9331†
	A_6	γ_6	9331	
	A_7*	γ_6	9339	9354†
	A_8*	γ_7	9430	9430†
	A_9	γ_6	9685	9701†
$^6H_{5/2}$	B_1	γ_7	10184	10191
	B_2	γ_6	10464	
	B_3	γ_7	10467	
$^6F_{7/2}$	C_1	γ_6	11107	11102
	C_2	γ_7	11198	11196
	C_3	γ_7	11278	11289
	C_4	γ_6	11342	11347
$^6F_{5/2}$	D_1	γ_7	12553	
	D_2	γ_6	12595	
	D_3	γ_7	12668	
$^6F_{3/2}$	E_1	γ_6	13403	
	E_2	γ_7	13408	
$^6F_{1/2}$	—	γ_6	13950	
$^4F_{9/2}$	F_1*	γ_7	21046	21043
	F_2*	γ_6	21067	21070
	F_3	γ_7	21173	
	F_4	γ_6	21232	
	F_5	γ_6	21553	

Number of data points	29
Number of free parameters	10
Standard deviation	6.0 cm^{-1}

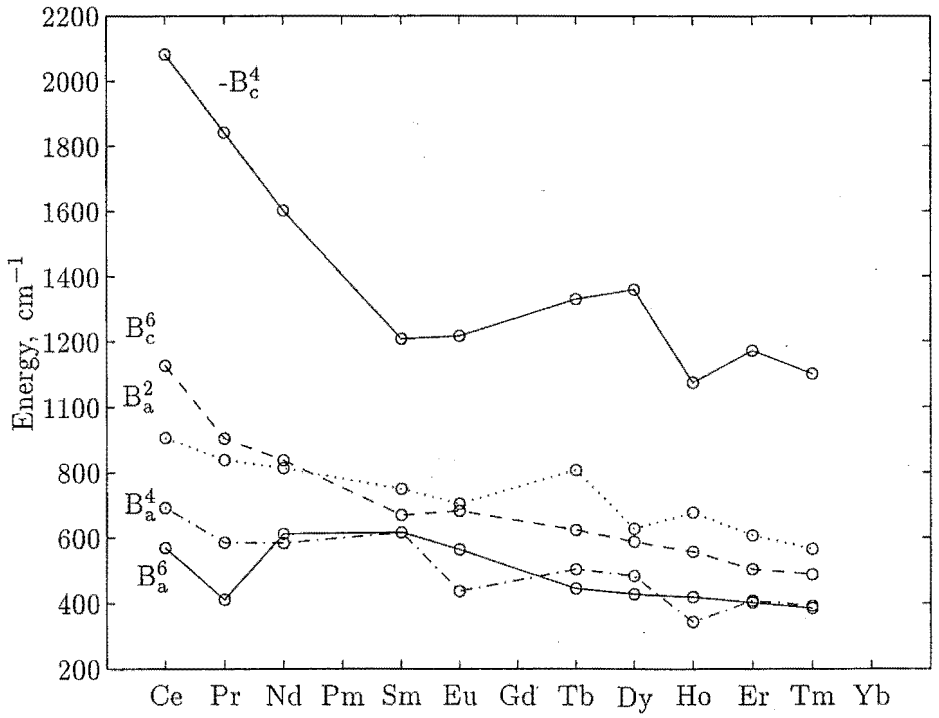

Figure 5.10: Comparison across the lanthanide series of the crystal-field parameters for the CaF_2:RE^{3+} C_{4v} centers. Parameter values for rare-earths other than Dy^{3+} have been taken from the summary provided by Wells [103].

5.4 The $CaF_2:Dy^{3+}$ C_{3v} center

The secondary single-ion center observed in the excitation spectra on page 124 has been assigned as C_{3v} in symmetry and corresponding to the C_{3v} :F^-centers observed in $CaF_2:Er^{3+}$ [21] and $CaF_2:Ho^{3+}$ [72]. This assignment is based on a crystal-field calculation for this symmetry, in which the derived parameters are in reasonable agreement with that of $CaF_2:Er^{3+}$ and $CaF_2:Ho^{3+}$ B centers and in which the energy level scheme is adequately reproduced. Polarisation data for the fluorescence was not sought for similar reasons as for the $SrF_2:Dy^{3+}$ C_{3v} center, namely the inherent ambiguity of such information for Kramers ions, particularly with the presence of both electric and magnetic dipole transitions, and the added experimental difficulty associated with the weak fluorescence intensities observed for this center. These weak transition intensities are presumed due to the low relative concentration of the C_{3v} center compared to the dominant C_{4v} center.

5.4.1 Laser selective fluorescence

As has been discussed in connection with the excitation and absorption spectra of the $^4F_{9/2}$ multiplet (page 124) a small ground state splitting of $1.5\,cm^{-1}$ is present along with a splitting of $8\,cm^{-1}$ between the F_1 and F_2 levels. For the fluorescence experiments, excitation was provided via the $Z_1 \rightarrow F_2$ transition at $21046\,cm^{-1}$. The use of excitation into the F_2 state has allowed direct observation of the ground state Z_1-Z_2 splitting through the $F_1 \rightarrow Z_{1,2}$ fluorescence as shown in Figure 5.11. This splitting is measured as $1.4\,cm^{-1}$ in fluorescence, and $1.6\,cm^{-1}$ in laser excitation.

At 15 K emission is observed from both F_1 and F_2 levels due to the small ($8\,cm^{-1}$) splitting between the excited state levels. Therefore for all multiplets considered here, the $^6H_{15/2}$, $^6H_{13/2}$, $^6H_{11/2}$, W, A, $^6H_{5/2}$ and $^6F_{7/2}$ multiplets and manifolds, the fluorescence has been measured at both 15 K and 2 K. The elimination of emission from the F_2 level in the 2 K spectra has assisted in the assignment of fluorescence transitions, and increased the number of energy levels determined for this center. The fluorescence spectra are presented in Figures 5.11–5.17, on pages 144–150.

The 2 K fluorescence spectra to several multiplets display weak additional transition which are considered to be due to cluster centers for which cross-relaxation processes are inhibited at the lower temperature. Investigations of the cluster center fluorescence in double doped $CaF_2:Dy^{3+}:Gd^{3+}$ (Chapter 6) support this interpretation of the additional weak fluorescence transitions.

From the fluorescence terminating on seven distinct manifolds, 29 energy levels below

11500 cm^{-1} have been determined, along with an additional 2 energy levels of the $^4F_{9/2}$ multiplet at ≈21000 cm^{-1}. The transition frequencies and inferred energy levels of the C_{3v} center are given in Tables 5.12–5.18, together with the relevant fluorescence spectra.

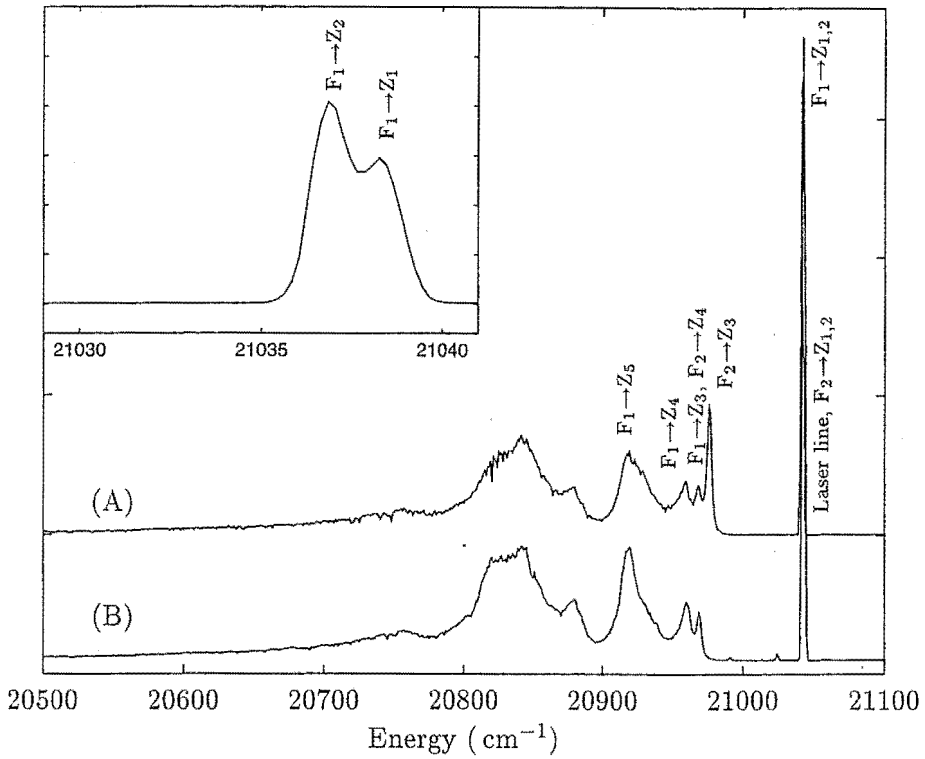

Figure 5.11: $^4F_{9/2} \rightarrow {}^6H_{15/2}$ fluorescence spectra of the CaF_2:Dy^{3+} C_{3v} center. (A) 15 Kelvin; (B) 2 Kelvin. The figure inset shows the just resolved $F_1 \rightarrow Z_1$, Z_2 transitions measured at 15 K.

Fluorescence energy	Transition
Laser line	$F_2 \rightarrow Z_{1,2}$
21038.3±0.5	$F_1 \rightarrow Z_1$
21036.9±0.5	$F_1 \rightarrow Z_2$
20972	$F_2 \rightarrow Z_3$
20964	$F_1 \rightarrow Z_3$, $F_2 \rightarrow Z_4$
20955	$F_1 \rightarrow Z_4$
20913	$F_1 \rightarrow Z_5$

$^6H_{15/2}$ Level	Energy (cm^{-1})
Z_1	0
Z_2	1.4±0.2 cm^{-1}
Z_3	74
Z_4	83
Z_5	125
Z_6–Z_8	—

Table 5.12: Transition frequencies for the $^4F_{9/2} \rightarrow {}^6H_{15/2}$ fluorescence of the CaF_2:Dy^{3+} C_{3v} center, and the inferred energy levels of $^6H_{15/2}$. All transition frequencies and energies are given in vacuum wavenumbers, with an absolute uncertainty of ±1 cm^{-1} unless otherwise stated.

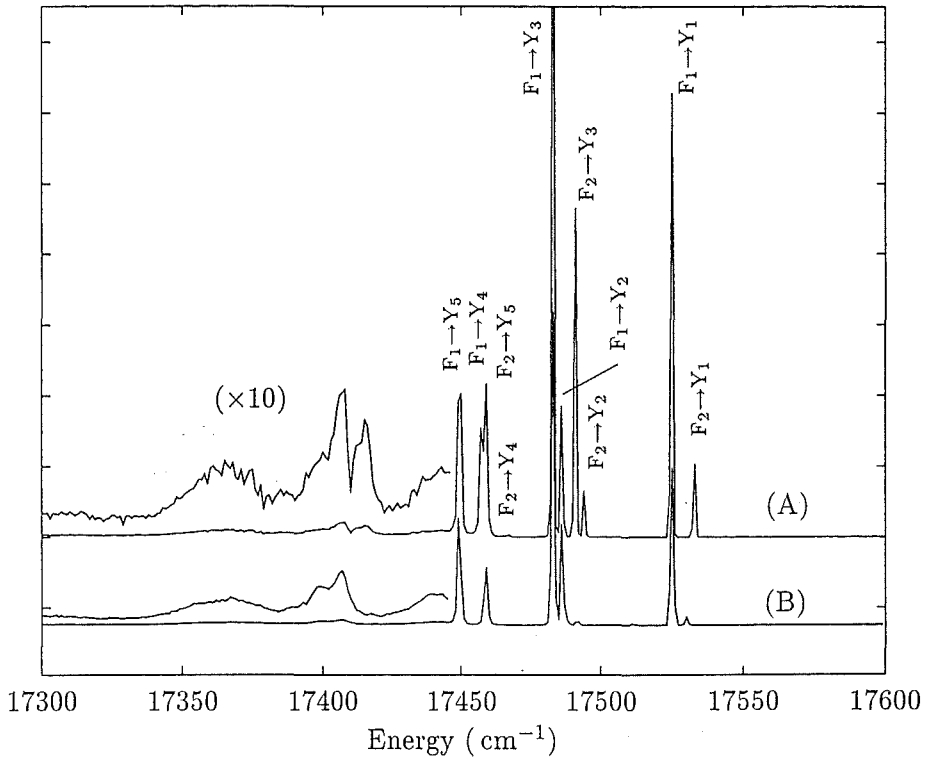

Figure 5.12: $^4F_{9/2} \rightarrow {}^6H_{13/2}$ fluorescence spectra of the CaF_2:Dy^{3+} C_{3v} center. (A) 15 Kelvin; (B) 2 Kelvin.

Fluorescence energy	Transition
17529	$F_2 \rightarrow Y_1$
17521	$F_1 \rightarrow Y_1$
17490	$F_2 \rightarrow Y_2$
17487	$F_2 \rightarrow Y_3$
17483	$F_1 \rightarrow Y_2$
17479	$F_1 \rightarrow Y_3$
17463	$F_2 \rightarrow Y_4$
17455	$F_2 \rightarrow Y_5$
17454	$F_1 \rightarrow Y_4$
17446	$F_1 \rightarrow Y_5$

$^6H_{13/2}$ Level	Energy (cm^{-1})
Y_1	3517
Y_2	3555
Y_3	3559
Y_4	3584
Y_5	3592
Y_6–Y_7	—

Table 5.13: Transition frequencies for the $^4F_{9/2} \rightarrow {}^6H_{13/2}$ fluorescence of the CaF_2:Dy^{3+} C_{3v} center, and the inferred energy levels of $^6H_{13/2}$. All transition frequencies and energies are given in vacuum wavenumbers, with an absolute uncertainty of $\pm 1\,cm^{-1}$.

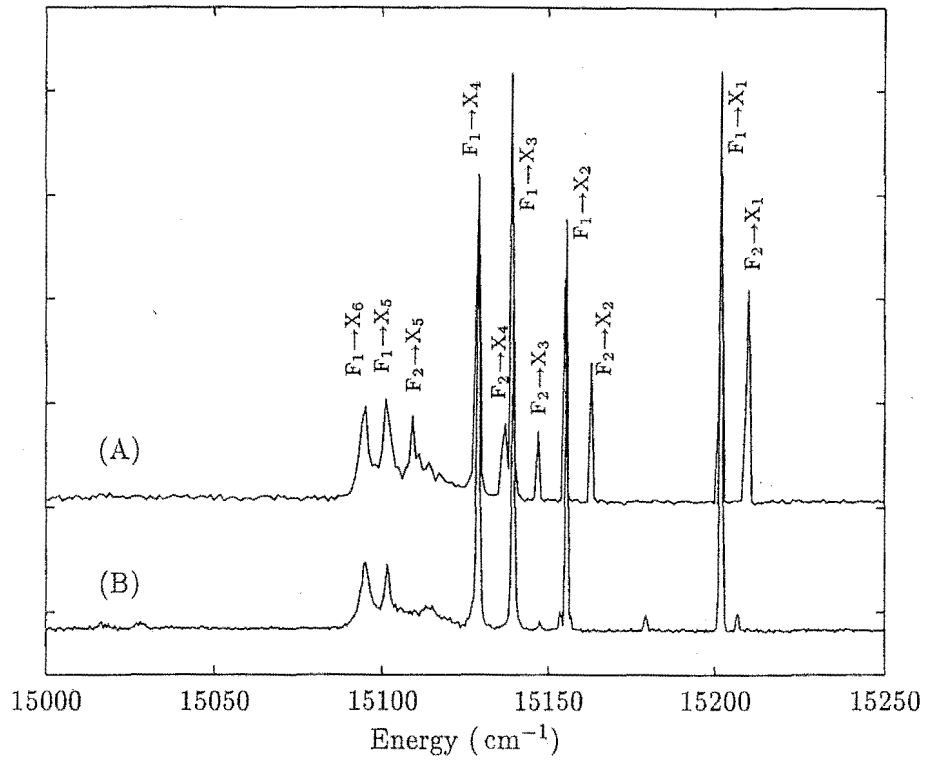

Figure 5.13: $^4F_{9/2} \rightarrow {}^6H_{11/2}$ fluorescence spectra of the CaF_2:Dy^{3+} C_{3v} center. (A) 15 Kelvin; (B) 2 Kelvin.

Fluorescence energy	Transition
15206	$F_2 \rightarrow X_1$
15198	$F_1 \rightarrow X_1$
15160	$F_2 \rightarrow X_2$
15152	$F_1 \rightarrow X_2$
15143	$F_2 \rightarrow X_3$
15135	$F_1 \rightarrow X_3$
15133	$F_2 \rightarrow X_4$
15125	$F_1 \rightarrow X_4$
15105	$F_2 \rightarrow X_5$
15098	$F_1 \rightarrow X_5$, $F_2 \rightarrow X_6$
15091	$F_1 \rightarrow X_6$

$^6H_{11/2}$ Level	Energy (cm^{-1})
X_1	5840
X_2	5886
X_3	5903
X_4	5913
X_5	5940
X_6	5947

Table 5.14: Transition frequencies for the $^4F_{9/2} \rightarrow {}^6H_{11/2}$ fluorescence of the CaF_2:Dy^{3+} C_{3v} center, and the inferred energy levels of $^6H_{11/2}$. All transition frequencies and energies are given in vacuum wavenumbers, with an absolute uncertainty of $\pm 1\,cm^{-1}$.

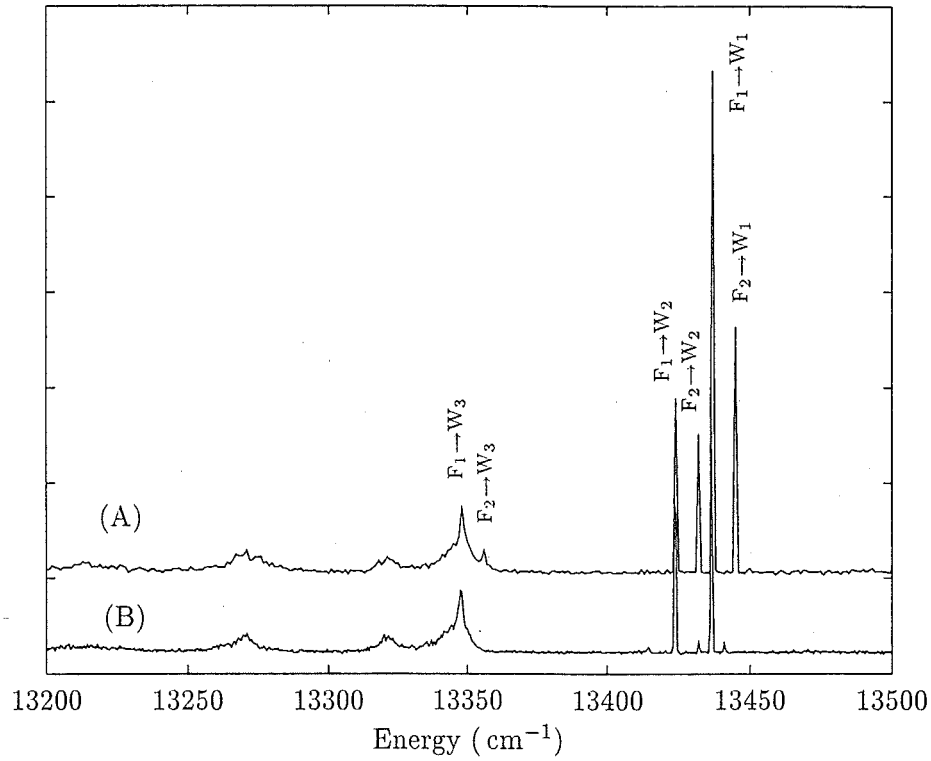

Figure 5.14: $^4F_{9/2} \rightarrow {}^6H_{9/2}$, $^6F_{11/2}$ (W manifold) fluorescence spectra of the CaF_2:Dy^{3+} C_{3v} center. (A) 15 Kelvin; (B) 2 Kelvin.

Fluorescence energy	Transition
13442	$F_2 \rightarrow W_1$
13434	$F_1 \rightarrow W_1$
13429	$F_2 \rightarrow W_2$
13421	$F_1 \rightarrow W_2$
13352	$F_2 \rightarrow W_3$
13344	$F_1 \rightarrow W_3$

$^6H_{9/2}$, $^6F_{11/2}$ Level	Energy (cm^{-1})
W_1	7604
W_2	7617
W_3	7694
W_4–W_{11}	—

Table 5.15: Transition frequencies for the $^4F_{9/2} \rightarrow$W manifold fluorescence of the CaF_2:Dy^{3+} C_{3v} center, and the inferred energy levels of $^6H_{9/2}$ and $^6F_{11/2}$. All transition frequencies and energies are given in vacuum wavenumbers, with an absolute uncertainty of $\pm 1\,cm^{-1}$.

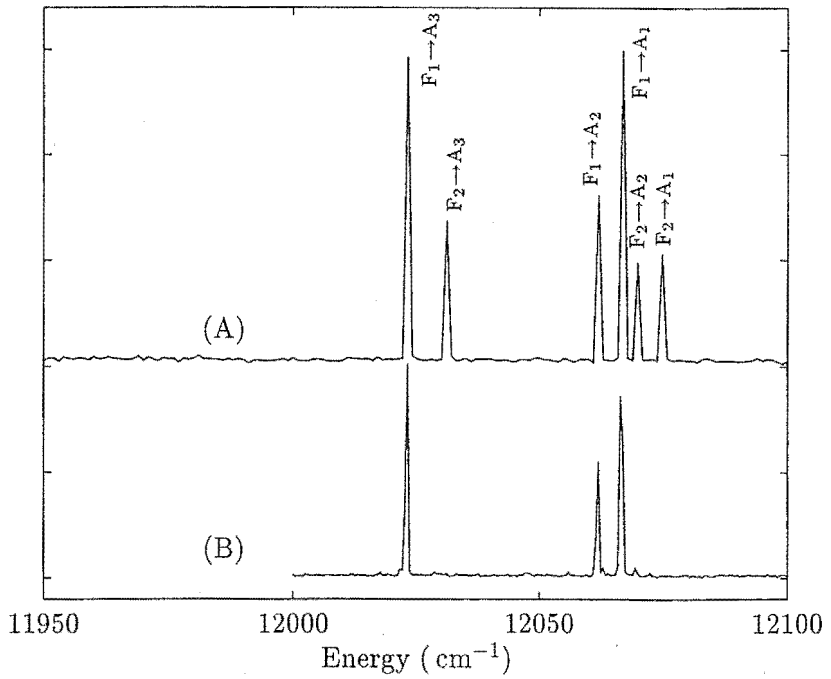

Figure 5.15: $^4F_{9/2} \rightarrow {}^6H_{7/2}$, $^6F_{9/2}$ (A manifold) fluorescence spectra of the CaF_2:Dy^{3+} C_{3v} center. (A) 15 Kelvin; (B) 2 Kelvin.

Fluorescence energy	Transition
12072	$F_2 \rightarrow A_1$
12067	$F_2 \rightarrow A_2$
12064	$F_1 \rightarrow A_1$
12059	$F_1 \rightarrow A_2$
12028	$F_2 \rightarrow A_3$
12020	$F_1 \rightarrow A_3$

$^6H_{7/2}$, $^6F_{9/2}$ Level	Energy (cm^{-1})
A_1	8974
A_2	8979
A_3	9018
A_4–A_9	—

Table 5.16: Transition frequencies for the $^4F_{9/2} \rightarrow$A manifold fluorescence of the CaF_2:Dy^{3+} C_{3v} center, and the inferred energy levels of $^6H_{7/2}$ and $^6F_{9/2}$. All transition frequencies and energies are given in vacuum wavenumbers, with an absolute uncertainty of $\pm 1\,cm^{-1}$.

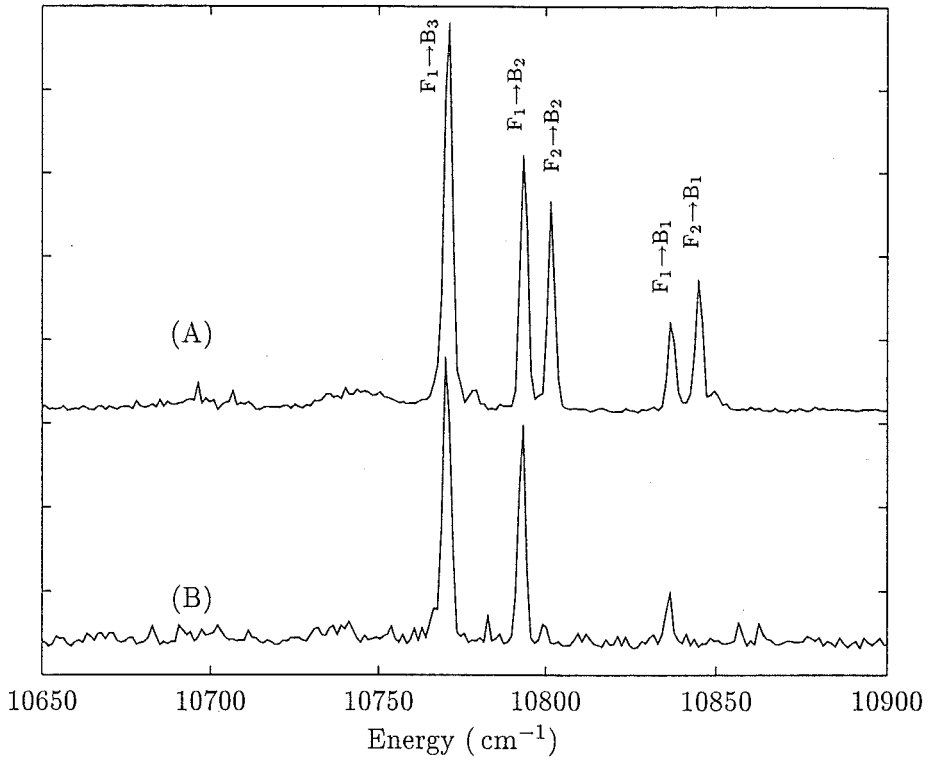

Figure 5.16: $^4F_{9/2} \rightarrow {}^6H_{5/2}$ fluorescence spectra of the CaF_2:Dy^{3+} C_{3v} center as recorded with the liquid N_2 cooled infrared PMT. (A) 15 Kelvin; (B) 2 Kelvin.

Fluorescence energy	Transition
10845	$F_2 \rightarrow B_1$
10837	$F_1 \rightarrow B_1$
10801	$F_2 \rightarrow B_2$
10794	$F_1 \rightarrow B_2$
10771	$F_1 \rightarrow B_3$

$^6H_{5/2}$ Level	Energy (cm^{-1})
B_1	10201
B_2	10244
B_3	10267

Table 5.17: Transition frequencies for the $^4F_{9/2} \rightarrow {}^6H_{5/2}$ fluorescence of the CaF_2:Dy^{3+} C_{3v} center, and the inferred energy levels of $^6H_{5/2}$. All transition frequencies and energies are given in vacuum wavenumbers, with an absolute uncertainty of $\pm 2\,cm^{-1}$.

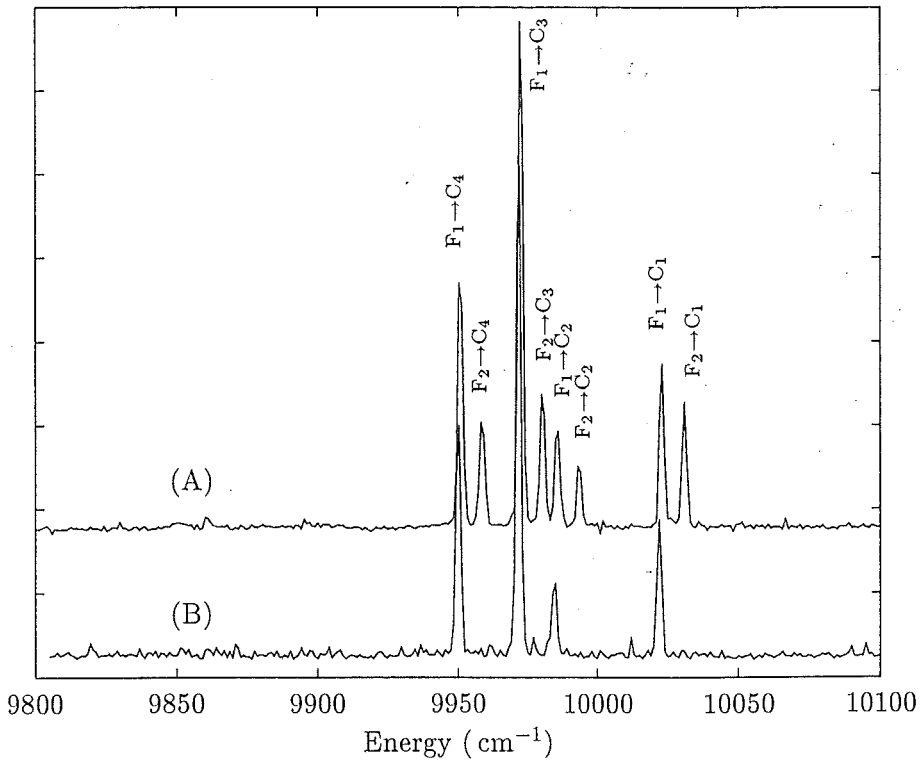

Figure 5.17: $^4F_{9/2} \rightarrow {}^6F_{7/2}$ fluorescence spectra of the CaF_2:Dy^{3+} C_{3v} center as recorded with the liquid N_2 cooled infrared PMT. (A) 15 Kelvin; (B) 2 Kelvin.

Fluorescence energy	Transition
10028	$F_2 \rightarrow C_1$
10020	$F_1 \rightarrow C_1$
9990	$F_2 \rightarrow C_2$
9982	$F_1 \rightarrow C_2$
9977	$F_2 \rightarrow C_3$
9969	$F_1 \rightarrow C_3$
9956	$F_2 \rightarrow C_4$
9948	$F_1 \rightarrow C_4$

$^6F_{7/2}$ Level	Energy (cm^{-1})
C_1	11018
C_2	11056
C_3	11069
C_4	11090

Table 5.18: Transition frequencies for the $^4F_{9/2} \rightarrow {}^6F_{7/2}$ fluorescence of the CaF_2:Dy^{3+} C_{3v} center, and the inferred energy levels of $^6F_{7/2}$. All transition frequencies and energies are given in vacuum wavenumbers, with an absolute uncertainty of $\pm 2\,cm^{-1}$.

5.4.2 CaF_2:Dy^{3+} C_{3v} crystal-field analysis.

For the crystal-field analysis of the center discussed in the preceding section, the initial assumption of a trigonal B center was made. This assumption is considered to be justified *a-posteri* by the good agreement obtained between the theoretical and experimental energy level scheme and with the crystal-field parameters for the B center of other lanthanide ions in the CaF_2 host. The B center in CaF_2:Er^{3+} has been shown to be inconsistent with the model configuration of a single charge compensating interstitial fluorine ion in the next-nearest neighbour position, along the $\langle 111 \rangle$ direction [62]. Therefore it is expected that the parameters for the CaF_2:Dy^{3+} trigonal center will be considerably different from that found for the J center in SrF_2:Dy^{3+}. The parameters reported for the B center in CaF_2:Ho^{3+}[72] have been taken as the starting parameters in the least-squares refinement calculation for the CaF_2:Dy^{3+} C_{3v} center. The calculation was performed in the same manner as discussed in previous sections. A standard deviation of 5.6 cm^{-1} was obtained between the calculated levels and the 31 experimental energy levels included in the calculation. A total of 11 parameters, comprising of the six trigonal crystal-field parameters, the spin-orbit parameter, the three Slater integrals, and the configuration average, were varied in the calculation. The remaining free-ion parameters were held fixed at the values of Carnell et.al. [12] given on page 66. The resulting C_{3v} crystal-field parameters are in good general agreement with those of the B center in CaF_2:Ho^{3+} and CaF_2:Er^{3+}, leading to the conclusion that this center can likewise be described as a trigonal B center. The parameters obtained from the crystal-field calculation are given in Table 5.19, and the calculated energy levels are compared to those of experiment in Table 5.20.

Table 5.19: The crystal-field, spin-orbit and Slater parameters of the CaF_2:Dy^{3+} C_{3v} center found from a least-squares calculation fitting to the experimental energy levels. All parameters are in units of cm^{-1}.

Parameter	B_c^4	B_c^6	B_a^2	B_a^4	B_a^6	$B_a^{6'}$	ζ	F^2	F^4	F^6
CaF_2:Dy^{3+}	-44	735	128	-89	-49	-626	1918	93743	68793	44431
CaF_2:Ho^{3+} [72]	46	681	197	-72	-223	-676	—	—	—	—
CaF_2:Er^{3+} [21]	83	581	141	77	-342	-531	—	—	—	—

Table 5.20: Experimental and calculated energy levels for the CaF_2:Dy^{3+} C_{3v} B center. The irrep assignments are based solely on the crystal-field calculation.

Multiplet	Level	Irrep	Energy (cm^{-1})	
		(Calc.)	Calc.	Expt.
$^6H_{15/2}$	Z_1	γ_4	-8.5	0.0
	Z_2	$\gamma_{5,6}$	2.3	1.4
	Z_3	γ_4	72	74
	Z_4	γ_4	95	83
	Z_5	$\gamma_{5,6}$	125	125
	Z_6	γ_4	203	
	Z_7	γ_4	216	
	Z_8	$\gamma_{5,6}$	224	
$^6H_{13/2}$	Y_1	γ_4	3518	3517
	Y_2	γ_4	3554	3555
	Y_3	$\gamma_{5,6}$	3557	3559
	Y_4	γ_4	3588	3584
	Y_5	γ_4	3598	3592
	Y_6	$\gamma_{5,6}$	3632	
	Y_7	γ_4	3674	
$^6H_{11/2}$	X_1	γ_4	5839	5840
	X_2	$\gamma_{5,6}$	5884	5886
	X_3	γ_4	5898	5903
	X_4	γ_4	5910	5913
	X_5	$\gamma_{5,6}$	5935	5940
	X_6	γ_4	5940	5947
$^6H_{9/2}$, $^6F_{11/2}$	W_1	$\gamma_{5,6}$	7607	7604
	W_2	γ_4	7613	7617
	W_3	γ_4	7697	7694
	W_4	$\gamma_{5,6}$	7699	
	W_5	γ_4	7723	
	W_6	γ_4	7765	
	W_7	$\gamma_{5,6}$	7826	
	W_8	γ_4	7837	
	W_9	γ_4	7899	
	W_{10}	$\gamma_{5,6}$	7969	
	W_{11}	γ_4	8003	

continued on next page

continued from previous page

Multiplet	Level	Irrep (Calc.)	Energy (cm^{-1}) Calc.	Expt.
$^6H_{7/2}$, $^6F_{9/2}$	A_1	γ_4	8970	8974
	A_2	$\gamma_{5,6}$	8985	8979
	A_3	γ_4	9024	9018
	A_4	γ_4	9099	
	A_5	$\gamma_{5,6}$	9146	
	A_6	γ_4	9158	
	A_7	γ_4	9279	
	A_8	$\gamma_{5,6}$	9287	
	A_9	γ_4	9379	
$^6H_{5/2}$	B_1	γ_4	10202	10201
	B_2	$\gamma_{5,6}$	10247	10244
	B_3	γ_4	10274	10267
$^6F_{7/2}$	C_1	γ_4	11020	11018
	C_2	γ_4	11053	11056
	C_3	$\gamma_{5,6}$	11063	11069
	C_4	γ_4	11089	11090
$^6F_{5/2}$	D_1	γ_4	12447	
	D_2	γ_4	12451	
	D_3	$\gamma_{5,6}$	12453	
$^6F_{3/2}$	E_1	$\gamma_{5,6}$	13246	
	E_2	γ_4	13247	
$^6F_{1/2}$	—	γ_4	13796	
$^4F_{9/2}$	F_1	γ_4	21038.5	21038.5
	F_2	$\gamma_{5,6}$	21045.6	21046.0
	F_3	γ_4	21127	
	F_4	$\gamma_{5,6}$	21253	
	F_5	γ_4	21274	

Number of data points	31
Number of free parameters	11
Standard deviation	5.6 cm^{-1}

5.5 Infrared absorption and Zeeman infrared.

5.5.1 Infrared absorption.

This section reports the results of Zeeman infrared experiments which have been performed with the aim of testing the accuracy of the crystal-field calculation and the laser selective fluorescence measurements. The absorption spectra to the accessible multiplets, namely $^6H_{13/2}$, $^6H_{11/2}$, and ($^6H_{9/2}$, $^6F_{11/2}$) will be discussed first. Because of the tendency of CaF_2:RE^{3+} systems to undergo preferential clustering at only modest dopant concentration, particularly with the heavier lanthanide ions, the absorption spectra presented are for a CaF_2:0.01%Dy^{3+} sample. The sample thickness was 9 mm. For these multiplets and at this low concentration of Dy^{3+}, the C_{4v} center is the only site with appreciable absorption strength. However, a number of transitions associated with the C_{3v} center are observed, with a characteristic 1.5 cm^{-1} splitting due to the Z_1–Z_2 energy separation.

For the spectra presented here the transmission spectrum for each multiplet has been normalised in such a manner that an indication of the absorption strength is given. All infrared spectra have been processed in the manner described in Section 3.3 to remove the beam-splitter interference.

$^6H_{13/2}$ multiplet.

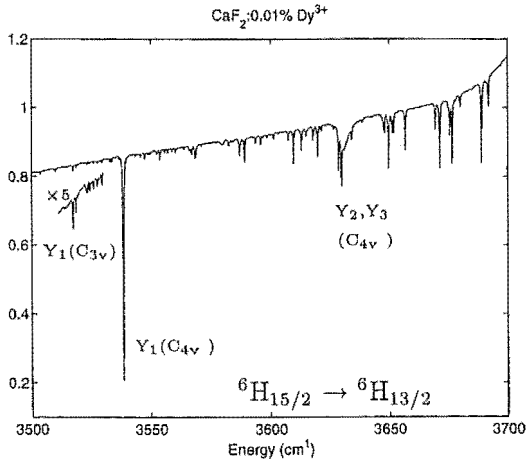

In the absorption spectrum of the $^6H_{13/2}$ multiplet the strong absorption at 3538.4 cm^{-1} corresponds to the C_{4v} $Z_1 \rightarrow Y_1$ transition, while a broad absorption at $\approx$3631 cm^{-1} reveals the $Z_1 \rightarrow Y_2, Y_3$ transitions. Superimposed on this broad absorption feature are several atmospheric absorptions that could not be eliminated completely with purging of the spectrometer with dry N_2 gas. This atmospheric absorption limits the ability to observe any higher frequency transitions to this multiplet. Weak absorptions at 3517.3 cm^{-1} and 3518.7 cm^{-1} correspond to the $Z_1, Z_2 \rightarrow Y_1$ transitions of the C_{3v} center. For this multiplet only the transition to Y_1 of the C_{4v} center was suitable for further investigation through Zeeman infrared absorption experiments.

$^6H_{11/2}$ multiplet.

In the transmission spectrum of the $^6H_{11/2}$ multiplet, the three absorption features at 5860.3 cm^{-1}, 6032.0 cm^{-1} and 6114.3 cm^{-1} correspond to absorption to the X_1, X_4 and X_5 energy levels of the C_{4v} center. Absorption to the X_2, X_3 and X_6 energy levels is completely absent, which at first appears anomalous given that the Kramers ion selection rules do not forbid any transitions for a C_{4v} symmetry center. In anticipation of the Zeeman results to be discussed later, it is noted that the Zeeman splitting of the X_4 transition is only well described by the inclusion of mixing effects with the unobserved X_3 energy level, which has been placed at an energy of 10 cm^{-1} below X_4 by laser-selective fluorescence.

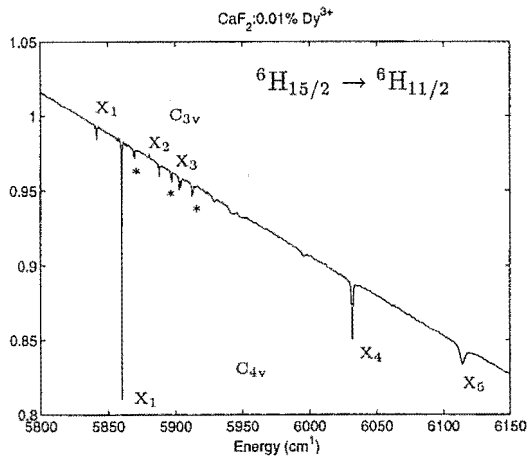

The particular wavefunction compositions of the C_{4v} states have been examined in an attempt to explain the absence of these transitions. The wavefunctions of energy levels discussed here, and in relation to the Zeeman experiments, are tabulated on page 164 in Table 5.21. Two features of the wavefunctions present themselves for further attention. Firstly the ground state is composed almost entirely of a single J_z component, with a 99% contribution from $J_z = \pm\frac{13}{2}$. Secondly, all observed transitions are between the like irreps $\Gamma_7 \rightarrow \Gamma_7$, while the absent transitions are of the form $\Gamma_7 \rightarrow \Gamma_6$. It might be supposed that the almost pure $J_z = \pm\frac{13}{2}$ composition of the ground state will provide some constraint on the observable transitions in addition to the group theory selection rules. However, this is not the case, as will now be shown.

The electric dipole selection rules of $\Delta S = 0$, $|\Delta L|, |\Delta J| \leq 6$ are satisfied for the $^6H_{15/2}$ $\rightarrow$ $^6H_{11/2}$ transitions, while magnetic dipole transitions are forbidden as $|\Delta J| > 1$. Therefore only electric dipole transitions, which are allowed through the odd crystal-field interactions, need to be considered. For C_{4v} symmetry the operators that appear in the odd part of the crystal-field Hamiltonian are [36] C_0^1, C_0^3, C_0^5, C_0^7, $C_{\pm4}^5$ and $C_{\pm4}^7$. Therefore, the electric dipole transition matrix elements will only be non-zero for the wavefunction components that satisfy $\Delta J_z = q \pm 1$, where $q = 0, 4$. Returning to the particular situation here, with a (almost) pure ground state with $J_z = \pm\frac{13}{2}$, then transitions to states containing $J_z = \pm\frac{11}{2}, \pm\frac{7}{2}, \pm\frac{5}{2}, \pm\frac{3}{2}$ will be allowed. From the wavefunctions presented in Table 5.21 it can be seen that at least some of the

unobserved transitions are to states with a considerable $J_z = \pm\frac{7}{2}$ component, and are therefore allowed, even with the pure J_z composition of the ground state. To further pursue the issue of absent transitions would involve consideration of an intensity parametrisation scheme, however due to the limited quantity of transition intensity data available for this system this is not possible here.

The Zeeman absorption transitions to the X_1 and X_4 states have been investigated and are discussed in the following section. Transitions to the X_5 level are too broad to provide useful Zeeman data.

Three pairs of transitions associated with the C_{3v} center have been indicated in the absorption spectrum of the $^6H_{11/2}$ multiplet. These absorptions correspond to the X_1–X_3 levels at 5840 cm^{-1}, 5886 cm^{-1} and 5903 cm^{-1}, and the pairing of transitions is due to the Z_1-Z_2 ground state splitting of 1.5 cm^{-1}. Three other absorption transitions marked by an asterisk display a 0.8 cm^{-1} splitting and are attributed to cluster centers, which will be discussed in Chapter 6. That cluster centers are observed in a 0.01%Dy^{3+} sample demonstrates the preferential nature of the clustering mechanisms in CaF_2:Dy^{3+}.

$^6H_{9/2}$, $^6F_{11/2}$ (W) manifold.

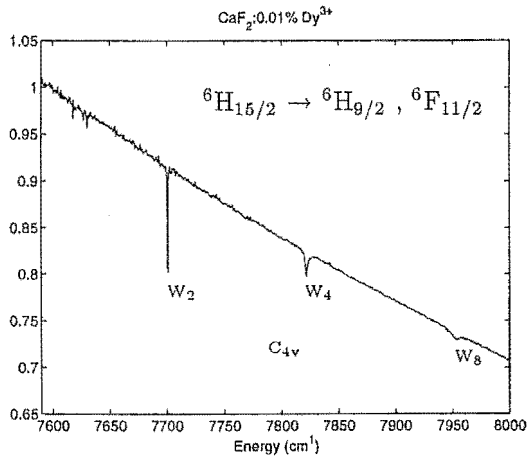

The W manifold absorption spectrum reveals only a small number of the possible transitions, with transitions to the W_2, W_4 and W_8 states observed at the energies 7701.0 cm^{-1}, 7821.8 cm^{-1} and 7952 cm^{-1}. The absence of absorption transitions to other states of the W manifold also appears to be anomalous given the Kramers ion selection rules.

In the following section the Zeeman transitions to the W_2 state are discussed, while the broad linewidth of transitions to W_4 and W_8 render them unsuitable for the Zeeman investigations.

5.5.2 CaF_2:Dy^{3+} C_{4v} Zeeman infrared absorption.

For the theoretical splitting values and diagrams of this section calculations were based on the wavefunctions presented in Table 5.21, as obtained from the crystal-field calculation. Only matrix elements diagonal in J have been considered, however, for transitions to the W manifold both the $|\ ^6H_{9/2}\ J_z\rangle$ and $|\ ^6F_{11/2}\ J_z\rangle$ components have been taken into account. For the remaining multiplets only the dominant LSJ components are included in the calculation. The calculations were performed by expressing the Zeeman interaction Hamiltonian in terms of the raising and lowering operators J_+, J_- along with the J_z operator. The individual matrix elements were then evaluated and the matrix diagonalised as a function of magnetic field strength and orientation. Further details of the Zeeman calculations have been given in Section 4.5.3 (page 99).

The magnetic field components for a given sample orientation have been given in Section 4.5.2. The issue of basis choice discussed for the SrF_2:Dy^{3+} centers does not arise here, as all transitions considered have insufficient mixing with nearby states for an observable distinction between Zeeman splittings of each basis to be made.

No C_{3v} center transitions were amenable to Zeeman investigation due to their weak absorption strengths and the small $1.5\,cm^{-1}$ separation of the Z_1 and Z_2 states.

Zeeman absorption of the C_{4v} W_2 state.

The Zeeman infrared spectra of the W_2 state of the C_{4v} center at $7701\,cm^{-1}$ are shown in Figure 5.18. The Zeeman effect for samples oriented with $\boldsymbol{B}\|\ \langle 100\rangle$ and $\boldsymbol{B}\|\ \langle 111\rangle$ has been considered. For the first case of $\boldsymbol{B}\|\ \langle 111\rangle$, all six orientations of the C_{4v} principal axis are equally inclined to the magnetic field, and therefore all centers are magnetically equivalent. Therefore four transitions between the pair of split Kramers doublets are expected. In practice, for field strengths greater than 2 Tesla additional small splittings of the transitions are observed, which is attributed to small sample alignment errors, which render the different orientations of the C_{4v} center inequivalent. Because of the large $S_\|$ and small $S_\perp$ for the ground state, the Zeeman transitions will be rendered quite sensitive to misalignment. This is the equivalent problem of alignment discussed for the Zeeman results for the SrF_2 C_{3v} center in a $\boldsymbol{B}\|\ \langle 100\rangle$ geometry. The misalignment of the C_{4v} center is more straight forward as it will only cause the creation of two sets of magnetically inequivalent centers, with a resulting maximum of eight transitions.

In gaining a quantitative measure of the agreement between theory and experiment the problem of misalignment has been partially avoided by considering the splitting factors

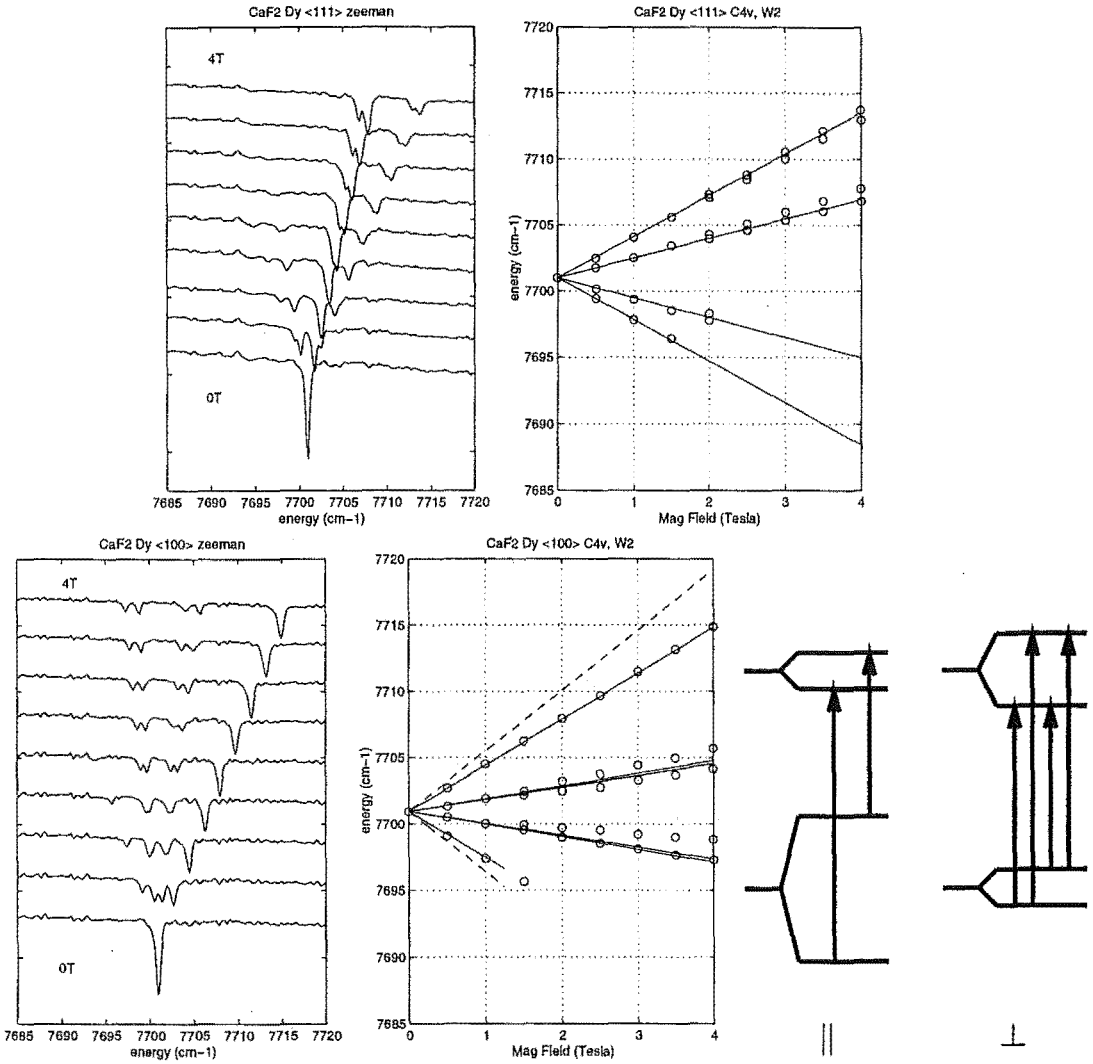

Figure 5.18: The Zeeman splittings of the CaF_2:Dy^{3+} C_{4v} W_2 absorption transition, for the magnetic field configurations of $\boldsymbol{B}\|\langle 100\rangle$ and $\boldsymbol{B}\|\langle 111\rangle$.

at 1.5 Tesla. The observation of all four transitions between the two Kramers doublets at this field strength also enables both the W_2 and Z_1 ground state splitting factors to be evaluated directly from experiment. From the measured transition frequencies and the wavefunctions derived from the crystal-field calculation, the experimental and theoretical splitting factors of W_2 and Z_1 are found to be

$$S_{\langle 111\rangle}(W_2)_{\text{expt.}} = 3.1 \pm 0.1 \qquad S_{\langle 111\rangle}(W_2)_{\text{calc.}} = 3.5$$

$$S_{\langle 111\rangle}(Z_1)_{\text{expt.}} = 10.1 \pm 0.1 \qquad S_{\langle 111\rangle}(Z_1)_{\text{calc.}} = 9.9$$

The behaviour of this transition in a $\boldsymbol{B}\|\langle 100\rangle$ configuration, enables a direct measure of $S_\parallel$ and $S_\perp$. In this configuration there are two inequivalent centers that are oriented parallel or perpendicular to the magnetic field. For the perpendicular centers all four transitions are allowed, while for the parallel center two of the transitions will be forbidden by group theory considerations (Section 2.4). In Figure 5.18 the forbidden parallel center transitions are shown as dashed lines.

In the splitting diagram of Figure 5.18 the transitions of the perpendicular centers are those which display the smallest splittings. By consideration of this set of transitions, at a field strength of 1.5 T, it is found that

$$S_\perp(W_2)_{\text{expt.}} = 3.7 \pm 0.1 \qquad S_\perp(W_2)_{\text{calc.}} = 4.0$$

$$S_\perp(Z_1)_{\text{expt.}} = 0.4 \pm 0.2 \qquad S_\perp(Z_1)_{\text{calc.}} = 0.13$$

There is insufficient information in the pair of observed parallel center transitions to directly measure the parallel splitting factor of W_2. Therefore, an experimental value for the parallel splitting value for the ground state is indirectly evaluated from the relationship between the three splitting values, $S_{\langle 111\rangle} = \sqrt{(S_\parallel^2 + 2S_\perp^2)/3}$. With this value for $S_\parallel(Z_1)$ there is enough information to determine $S_\parallel(W_2)$ from the Zeeman spectra. The calculated and experimental parallel splitting factors are found to be

$$S_\parallel(W_2)_{\text{expt.}} = 2.4 \pm 0.1 \qquad S_\parallel(W_2)_{\text{calc.}} = 2.3$$

$$S_\parallel(Z_1)_{\text{expt.}} = 17.5 \pm 0.1; \qquad S_\parallel(Z_1)_{\text{calc.}} = 17.2$$

Zeeman absorption of the C_{4v} X_4 state.

Figure 5.19 presents the Zeeman splittings of the X_4 absorption transition at 6032 cm^{-1} for the two configurations of the magnetic field with respect to the crystal axes. To correctly account for the Zeeman splittings interactions between the X_4 and X_3 states

have been included in the calculations. No absorption to the X_3 level has been observed but the fluorescence to this multiplet places it at an energy of $10\,cm^{-1}$ below X_4. The nonlinear Zeeman splittings display clear evidence of interaction with the nearby unobserved state, and the excellent agreement between theory and experiment demonstrates the accuracy of the calculated wavefunctions and the position of the X_3 level. For clarity of presentation the theoretical transitions to X_3 are not displayed in the splitting diagram for the $\boldsymbol{B}\|\ \langle 100\rangle$ geometry. The forbidden parallel center transitions are shown as dashed lines.

To give some quantitative indication of the agreement between the experimental and theoretical splitting values of X_4, the splitting factors evaluated at a field strength of 1.5 T are compared. For the $\boldsymbol{B}\|\ \langle 100\rangle$ configuration, $S_\parallel$ has been obtained by using the previously determined ground state splitting, while for $S_\perp$, the ground state splitting is not resolved at 1.5 T. The experimental splitting factor $S_{\langle 111\rangle}$ has been inferred directly from the experimental transition frequencies. The splitting values obtained are (for $B = 1.5\,T$)

$$S_\parallel(X_4)_{\text{expt.}} = 3.5 \pm 0.1 \qquad S_\parallel(X_4)_{\text{calc.}} = 3.5$$

$$S_\perp(X_4)_{\text{expt.}} = 4.8 \pm 0.1 \qquad S_\perp(X_4)_{\text{calc.}} = 5.3$$

$$S_{\langle 111\rangle}(X_4)_{\text{expt.}} = 4.6 \pm 0.1 \qquad S_{\langle 111\rangle}(X_4)_{\text{calc.}} = 4.9$$

The general agreement displayed in the splitting values is quite good given the complications of the mixing with the X_3 state. It is noted that the simple relationship between the splitting factors will no longer be valid because of this interaction between states. From the splitting diagrams of Figure 5.19 it is clear that the perpendicular splitting factor for the ground state is underestimated by the calculations, as shown by the small splittings of the inner set of transitions of the $\boldsymbol{B}\|\ \langle 100\rangle$ splitting diagram, and the even smaller prediction of theory.

Zeeman absorption of the C_{4v} X_1 state.

The Zeeman splittings of the C_{4v} X_1 absorption transition are presented in Figure 5.20. For the $\boldsymbol{B}\|\ \langle 111\rangle$ geometry only two of the four transitions are observed, despite all transitions being allowed by group theory. However, the observation of only two transitions can be explained through consideration of the particular wavefunction composition of these Kramers doublets. With the ground state an almost pure $|\pm\frac{13}{2}\rangle$ doublet and the X_1 state likewise almost pure in its J_z composition of $|\pm\frac{11}{2}\rangle$, only the $|\pm\frac{13}{2}\rangle \rightarrow |\pm\frac{11}{2}\rangle$ transitions will be expected to be observed, with the $|\pm\frac{13}{2}\rangle \rightarrow |\mp\frac{11}{2}\rangle$ transitions only allowed through the quite small admixtures of other J_z components. To

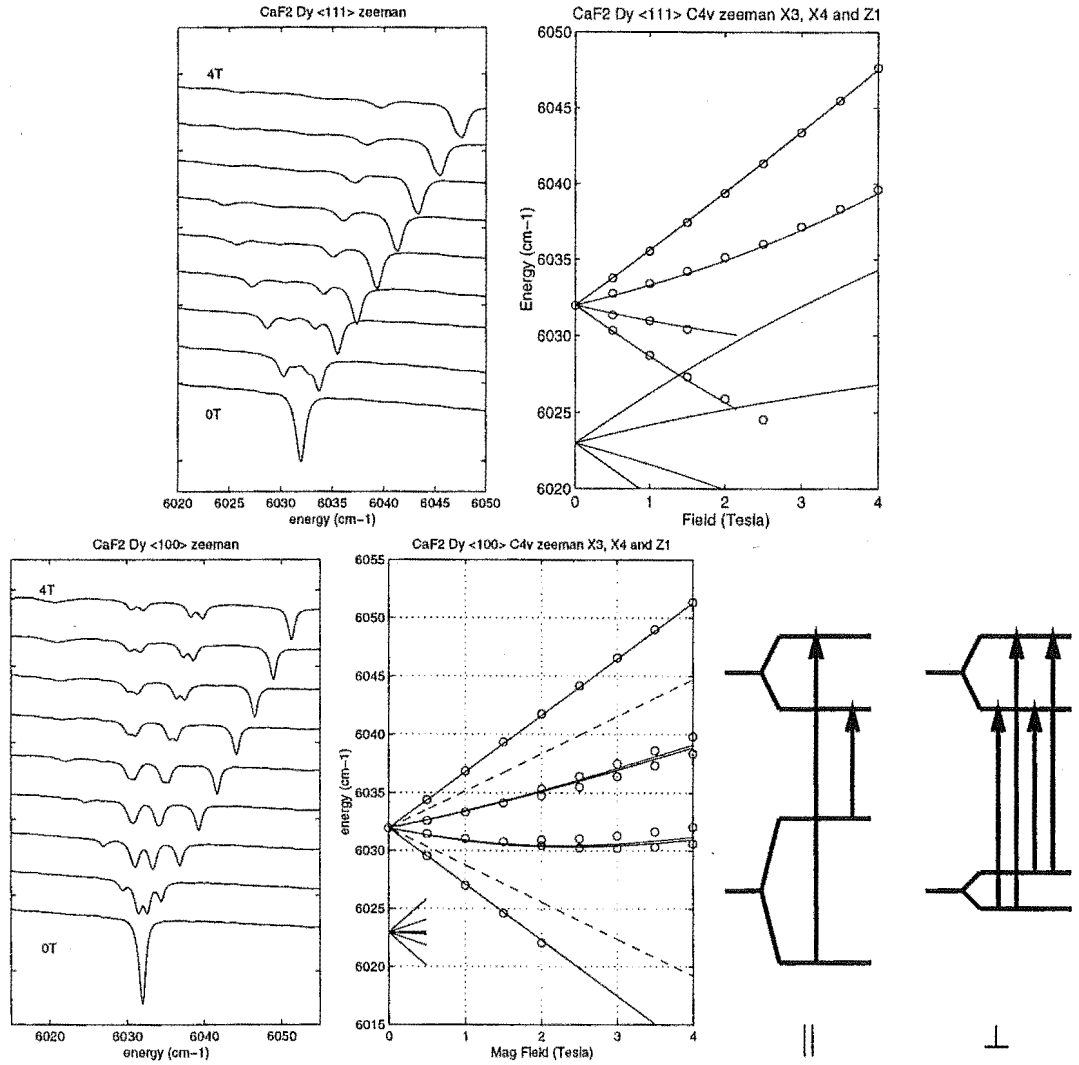

Figure 5.19: The Zeeman splittings of the CaF_2:Dy^{3+} C_{4v} X_4 absorption transition, for the magnetic field configurations of $\boldsymbol{B}\|\langle 100\rangle$ and $\boldsymbol{B}\|\langle 111\rangle$.

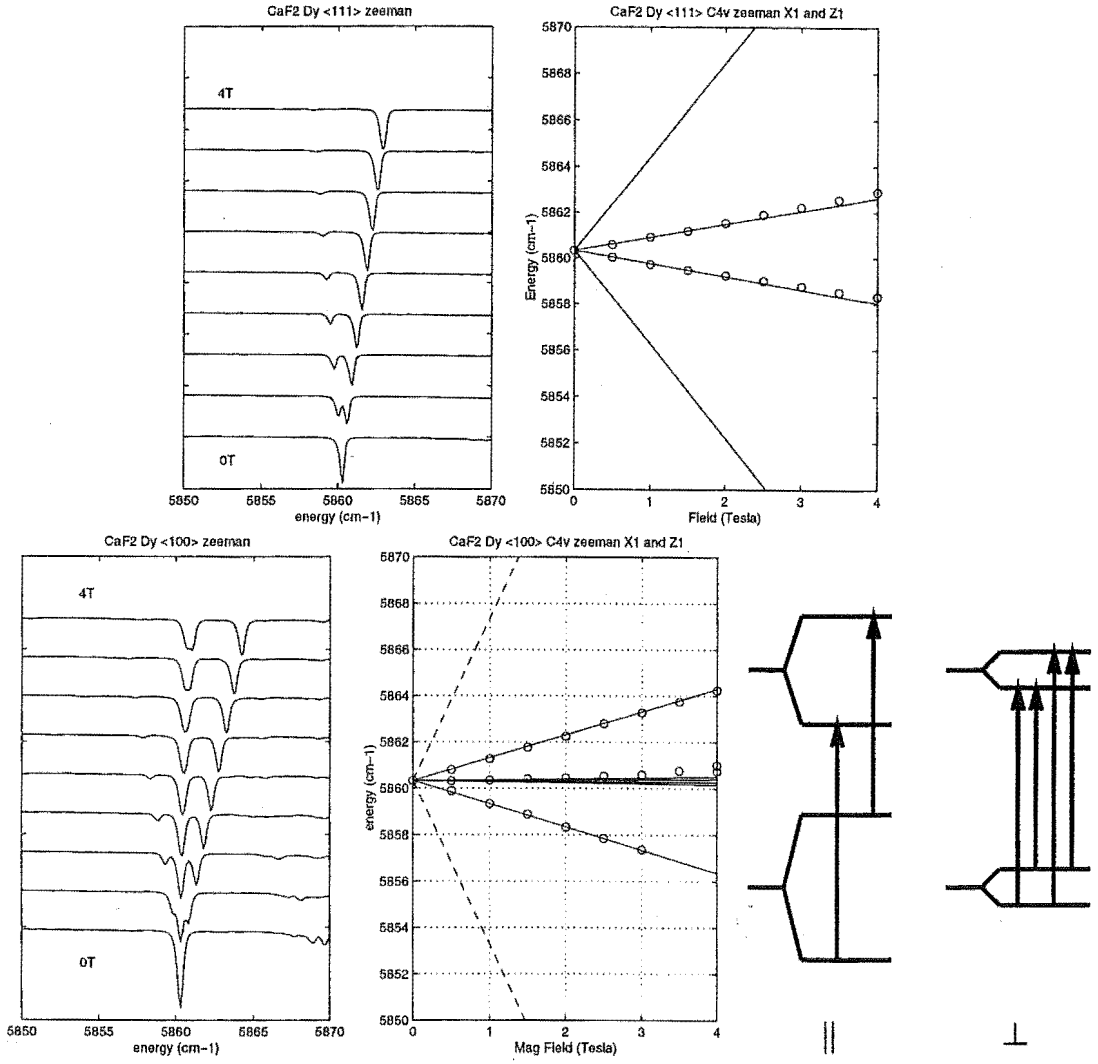

Figure 5.20: The Zeeman splittings of the CaF_2:Dy^{3+} C_{4v} X_1 absorption transition, for the magnetic field configurations of $\boldsymbol{B}\|\langle 100\rangle$ and $\boldsymbol{B}\|\langle 111\rangle$.

enable a comparison of the calculated and experiment splitting values for the X_1 state the previously determined $S_{\langle 111\rangle}(Z_1)$ value is employed in evaluating the experimental splitting value $S_{\langle 111\rangle}(X_1)$.

For the $\boldsymbol{B}\|\langle 100\rangle$ geometry, the (group theory) forbidden transitions of the parallel centers are shown by a dashed line in the splitting diagram of Figure 5.20. The allowed parallel center transitions enable determination of the experimental parallel splitting value for X_1 with the aid of the previously determined value of $S_{\|}(Z_1)$. Only an upper bound on the perpendicular splitting values can be extracted from the data as these splittings are not resolved in the Zeeman spectra.

The experimental and calculated splitting values for the X_1 state are

$$S_{\parallel}(X_1)_{\text{expt.}} = 13.4 \pm 0.1 \qquad S_{\parallel}(X_1)_{\text{calc.}} = 13.0$$

$$S_{\langle 111\rangle}(X_1)_{\text{expt.}} = 7.7 \pm 0.1 \qquad S_{\langle 111\rangle}(X_1)_{\text{calc.}} = 7.5$$

$$S_{\perp}(X_1)_{\text{expt.}} < 0.2 \qquad S_{\perp}(X_1)_{\text{calc.}} = 0.06$$

Once again the good agreement between theory and experiment confirms the accuracy of the C_{4v} wavefunctions.

Zeeman absorption of the C_{4v} Y_1 state.

The consequences of a pure J_z composition of both the ground and excited states are again present in the Zeeman absorption transitions to the Y_1 state (Figure 5.21). The calculated wavefunctions of these states are both dominated by the $J_z = \pm\frac{13}{2}$ components, with 99% and 91% purity for Z_1 and Y_1 respectively. Together with the similar landé g-factors for these two multiplets ($g_L(^6H_{15/2}) = \frac{68}{51}$, $g_L(^6H_{13/2}) = \frac{50}{39}$), this leads to the expectation that both Kramers doublets will split by similar energies for a given applied field, and that the resulting separation of the transition frequencies will be quite small. Indeed, it is found that for the $\boldsymbol{B}\|\langle 100\rangle$ geometry the splittings of the $Z_1 \rightarrow Y_1$ transition cannot be resolved for magnetic fields up to 4 Tesla. For the alternative experimental arrangement with $\boldsymbol{B}\|\langle 111\rangle$ a small splitting is observed, amounting to $1.6\,\text{cm}^{-1}$ at 4 Tesla. For the same reasons discussed in the context of the X_1 Zeeman absorption, namely the pure J_z composition, only two of the four allowed transitions will be expected to have appreciable intensity which is consistent with the observation of only two absorption transitions. The splitting diagram and Zeeman spectra for the Y_1 absorption, for the case in which a resolved splitting is observed, is shown in Figure 5.21. For a numerical comparison between theory and experiment use of the experimental $S_{\langle 111\rangle}(Z_1)$ value enables an experimental splitting value for Y_1 to be obtained. The experimental and calculated splitting factors are found to be

$$S_{\langle 111\rangle}(Y_1)_{\text{expt.}} = 9.2 \pm 0.1 \qquad S_{\langle 111\rangle}(Y_1)_{\text{calc.}} = 9.1$$

$$S_{\perp}(Y_1)_{\text{expt.}} = ?? \qquad S_{\perp}(Y_1)_{\text{calc.}} = 0.27$$

$$S_{\parallel}(Y_1)_{\text{expt.}} = ?? \qquad S_{\parallel}(Y_1)_{\text{calc.}} = 15.71$$

Summarising the Zeeman results for the CaF_2:Dy^{3+} C_{4v} center, the good agreement between theory and experiment adds confidence to the accuracy of the crystal-field calculation, which was based on the laser-selective spectroscopy. The Zeeman splittings of transitions to the X_4 state confirm the assignment of the X_3 level despite the X_3 level not being directly observed in absorption.

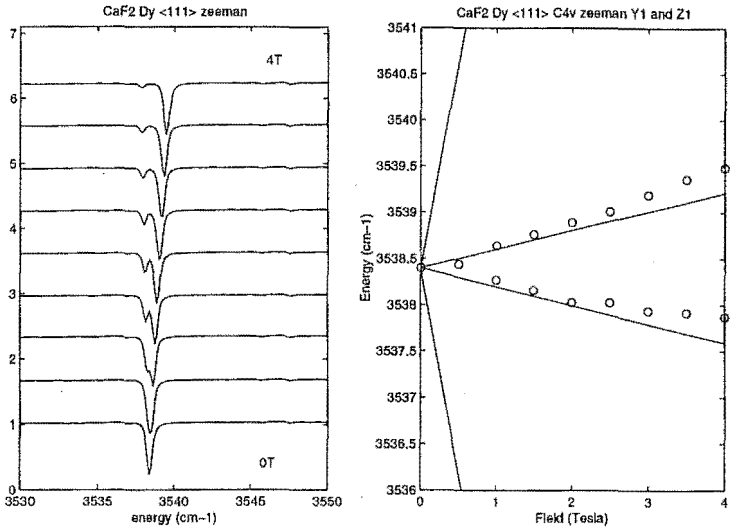

Figure 5.21: The Zeeman splittings of the CaF_2:Dy^{3+} C_{4v} Y_1 absorption transition for the magnetic field configuration of $B\|\langle 111\rangle$.

Table 5.21: CaF_2:Dy^{3+} C_{4v} wavefunctions used in the discussions and Zeeman calculations of this section.

level	energy	irrep	wavefunction
Z_1	0	γ_7	$0.9928\|\frac{\mp 13}{2}\rangle + 0.0971\|\frac{\mp 5}{2}\rangle - 0.0484\|\frac{\pm 3}{2}\rangle + 0.0133\|\frac{\pm 11}{2}\rangle$
Y_1	3539	γ_7	$\mp 0.9514\|\frac{\mp 13}{2}\rangle \pm 0.2962\|\frac{\mp 5}{2}\rangle \mp 0.0298\|\frac{\pm 11}{2}\rangle$
X_1	5859	γ_7	$0.9861\|\frac{\mp 11}{2}\rangle - 0.1114\|\frac{\mp 3}{2}\rangle - 0.0494\|\frac{\pm 5}{2}\rangle$
X_2	5987	γ_6	$-0.9660\|\frac{\mp 9}{2}\rangle - 0.1817\|\frac{\mp 1}{2}\rangle - 0.0918\|\frac{\pm 7}{2}\rangle$
X_3	6021	γ_6	$-0.1343\|\frac{\mp 9}{2}\rangle + 0.2042\|\frac{\mp 1}{2}\rangle + 0.9576\|\frac{\pm 7}{2}\rangle$
X_4	6031	γ_7	$0.1001\|\frac{\mp 11}{2}\rangle + 0.4897\|\frac{\mp 3}{2}\rangle + 0.8524\|\frac{\mp 5}{2}\rangle$
X_5	6113	γ_7	$0.0710\|\frac{\mp 11}{2}\rangle + 0.8506\|\frac{\mp 3}{2}\rangle - 0.4969\|\frac{\mp 5}{2}\rangle$
X_6	6131	γ_6	$\mp 0.1698\|\frac{\mp 9}{2}\rangle \pm 0.9473\|\frac{\mp 1}{2}\rangle \mp 0.2273\|\frac{\pm 7}{2}\rangle$
W_2	7700	γ_7	$-0.4812\|^6H_{9/2}, \frac{\mp 5}{2}\rangle - 0.6721\|^6H_{9/2}, \frac{\pm 3}{2}\rangle$ $\mp 0.2800\|^6F_{11/2}, \frac{\pm 11}{2}\rangle \mp 0.4636\|^6F_{11/2}, \frac{\pm 3}{2}\rangle \pm 0.1053\|^6F_{11/2}, \frac{\mp 5}{2}\rangle$

5.6 Summary of the CaF_2:Dy^{3+} spectroscopy.

Despite a reasonable amount of previous work on the defect centers in CaF_2:Dy^{3+}, an adequate description of the spectroscopy remained elusive. Much disagreement on the energy level scheme for the tetragonal fluorine compensated center is present in the literature. Through a laser selective excitation and fluorescence investigation this situation has been clarified with a new energy level scheme for the C_{4v} centers that encompasses eight multiplets or manifolds. This scheme is of a much greater scope than reported in the previous literature, and is also significantly different from any of the earlier work – although some energy levels are in agreement with previous assignments. Through consideration of the polarisation properties of the observed fluorescence additional information on the irrep assignments has been obtained for the majority of C_{4v} energy levels reported here.

A crystal-field least-squares calculation based on the energy level scheme and irrep assignments is in good agreement with the experimental data. The C_{4v} crystal-field parameters obtained are also consistent with C_{4v} centers reported for other lanthanide ions in the CaF_2 host.

Zeeman infrared absorption experiments have been performed for transitions to a number of states of the $^6H_{13/2}$, $^6H_{11/2}$ and ($^6H_{9/2}$, $^6F_{11/2}$) manifolds. The comparison between experimental Zeeman splittings and those predicted on the basis of the C_{4v} wavefunctions determined from the crystal-field analysis provides good evidence for the accuracy of wavefunctions obtained for this center. In the infrared absorption of the $^6H_{11/2}$ and ($^6H_{9/2}$, $^6F_{11/2}$) manifolds, only a subset of upper-state energy levels are observed, contrary to expectations from the Kramers ion selection rules. It has been shown that this cannot be explained simply through the (almost) pure J_z composition of the ground state. The Zeeman splitting of the X_4 state has been shown to offer good evidence for the correct assignment of at least one of the states (X_3) that was unobserved in absorption.

The spectroscopy of a secondary center, which has not previously been discussed in the literature, has been investigated through laser-selective excitation. The fluorescence information has enabled the determination of 31 levels from eight manifolds with energies below $\approx 21000\,cm^{-1}$. Through a crystal-field analysis and comparison with centers reported for other CaF_2:RE^{3+}systems, this center has been assigned as a trigonal B center, such as that found in CaF_2:Er^{3+}. Because of the weak absorption of this center, and the complications involved with the $1.5\,cm^{-1}$ ground state splitting, the trigonal symmetry has not been confirmed through Zeeman experiments.

Chapter 6

CaF_2:RE^{3+}clustering.

6.1 Introduction

CaF_2:RE^{3+}defects are known to undergo preferential (as opposed to statistical) clustering in which multi-rare earth defects are formed at concentrations as low as 0.05 mol% RE^{3+}. This clustering behaviour varies through the rare-earth series: simple dimers and trimers dominating for the larger (lighter) ions [37, 18, 19], and much more complex clustering, such as hexamers, for the smaller (heavier) ions [98, 97, 70, 18]. An issue arising when discussing multi-rare earth centers in CaF_2 is that of correlating the various centers observed for different rare-earths. This correlation is obviously crucial to any understanding of trends in cluster formation across the rare-earth series. The approach taken here is that of Wells [103], in which double-doped systems are investigated through absorption and laser selective excitation, with the intention of drawing conclusions on the nature of the defect centers present in the singly-doped crystals. In certain cases energy transfer enables a direct correlation of centers present in crystals doped with different rare earths.

In considering double doped systems the clustering present will not necessarily be the same as that which occurs for a system containing any one dopant alone. That is, when considering the clustering due to double doping of a large ion and a small ion it is not clear which ion, if any in particular, to attribute the clustering behaviour to. Hamers et.al. [37] have classified several clusters observed in CaF_2:Eu^{3+}. Those labelled the R- and Q- centers are of interest for the work presented here. The R-center has been assigned as an asymmetric dimer. The Q-center was initially assigned as a dimer but this assignment was later amended to that of a symmetric trimer [18]. Through the observation of energy transfer Wells [103] has shown that Sm^{3+} ions in double doped CaF_2:Sm^{3+}:Eu^{3+} form analogous R- and Q-centers, and that these centers are present in CaF_2:Sm^{3+}:RE^{3+} for rare-earths larger than Dy^{3+}. For co-doping Sm^{3+} with the rare-earths Dy^{3+} through Yb^{3+} the R- and Q- centers are absent in Sm^{3+} broadband excitation, being replaced by a center labelled the S-center.

6.2 CaF_2:Dy^{3+}cluster centers.

In CaF_2:0.05%Dy^{3+} the observation of $^4F_{9/2}$ absorption transitions with no corresponding excitation transitions reveals the presence of centers which decay non-radiatively.

The energy transfer probability between ions is related to the overlap of the emission and absorption profiles [25]. The free-ion energy level diagram of Figure 6.1 highlights the large number of $^4F_{9/2}$ emission and $^6H_{15/2}$ absorption transitions with approximate overlap. Therefore a large number of energy transfer/cross-relaxation pathways are possible from the $^4F_{9/2}$ multiplet. Such cross-relaxation processes are considered responsible for non-radiative decay of the extra centers observed in absorption. These decay processes effectively limit the possibility of a direct investigation into the CaF_2:Dy^{3+}cluster centers.

To reveal some information on the cluster centers several double-doped CaF_2 crystals have been investigated, namely CaF_2:Dy^{3+}:Gd^{3+}, CaF_2:Dy^{3+}:Eu^{3+} and CaF_2:Dy^{3+}:Tb^{3+}. The centers observed in the double-doped systems will not be spectroscopically identical to those in the single-doped Dy^{3+} crystals, however close similarity can be expected when the additional RE^{3+} dopant is from a similar position within the lanthanide series, and therefore of similar ionic size.

The $^4F_{9/2}$ absorption spectra of the various CaF_2:Dy^{3+}:RE^{3+} systems are shown in Fig. 6.2. The centers marked C_{4v} and C_{3v} for the single-doped crystal are the only centers observed in the broadband excitation spectra of singly doped CaF_2:0.05%Dy^{3+} samples.

The cluster centers of the double doped systems are radiative, and are therefore observed in the excitation spectra of the Dy^{3+} $^4F_{9/2}$ multiplet. The fluorescence of these centers in the CaF_2:Dy^{3+}:Gd^{3+} systems enables identification of lower lying levels of the ^6H_J and ^6F_J multiplets. Efficient energy transfer from the Dy^{3+} ion to both Eu^{3+} and Tb^{3+} co-dopants is also observed. In the case of $Dy^{3+}\rightarrow Eu^{3+}$ energy transfer the cluster involved can be correlated with the centers reported for CaF_2:Eu^{3+}.

6.3 CaF_2:Dy^{3+}:Gd^{3+}.

Gd^{3+} has no excited states between 0-32000 cm^{-1}, and is therefore an ideal candidate for double-doping and suppression of the cross-relaxation processes occurring in Dy^{3+} clusters. When double-doping there remains the possibility of maintaining two or more Dy^{3+} ions within the cluster, especially for trimers and higher order clusters. It

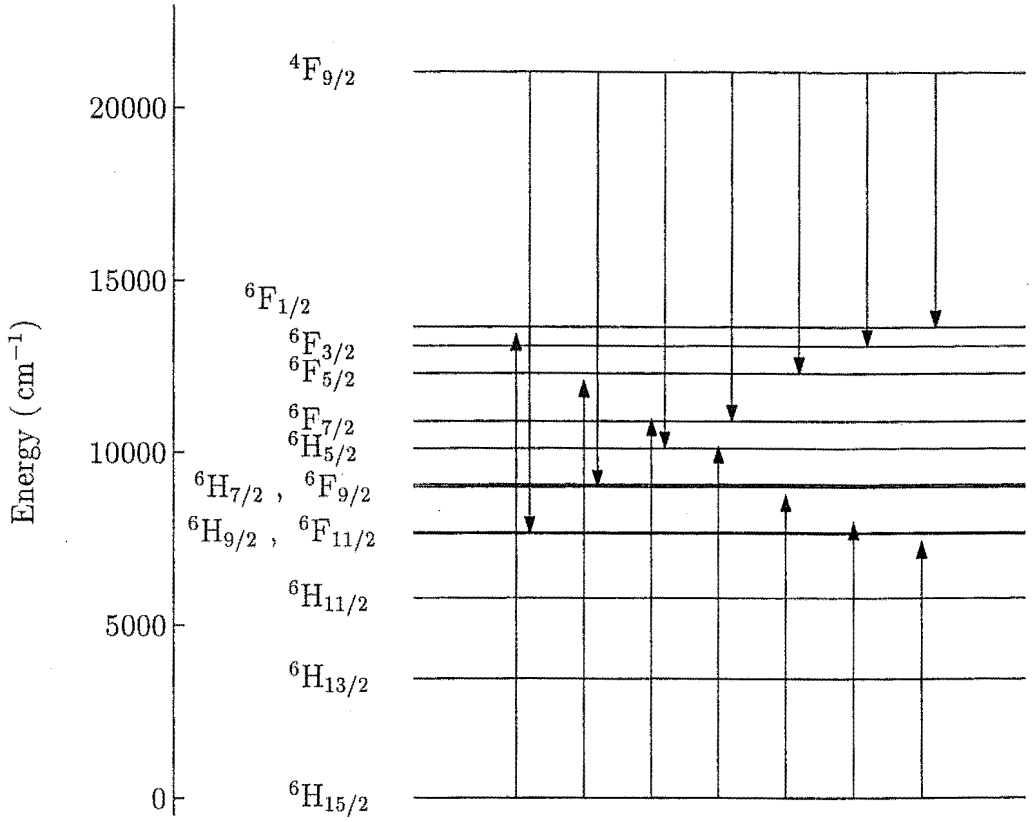

Figure 6.1: Energy level diagram for Dy^{3+}multiplets, showing possible cross-relaxation pathways. The downward and upward transitions are considered to occur on nearby ions.

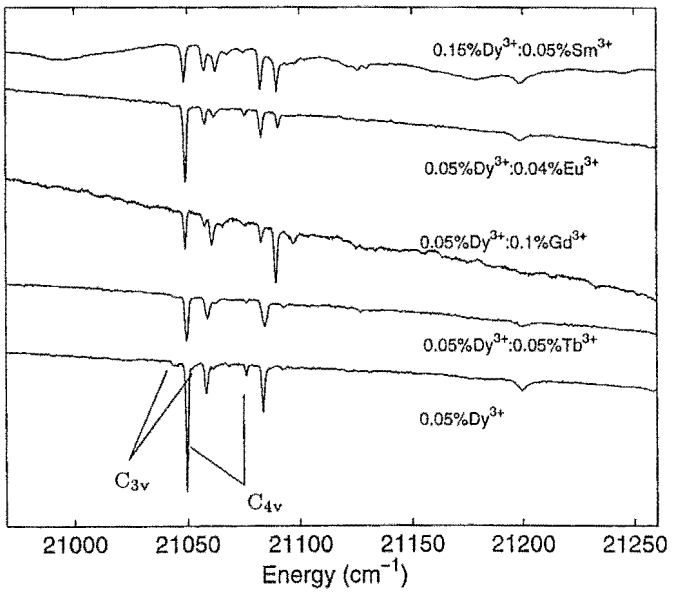

Figure 6.2: 15 K $^4F_{9/2}$ absorption spectra for various CaF_2:Dy^{3+}:RE^{3+}systems.

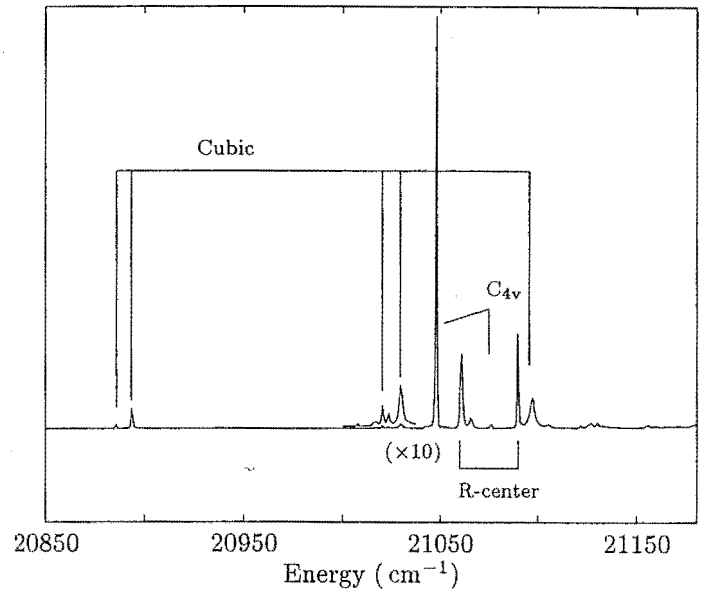

Figure 6.3: 15K broadband excitation spectra for the $^4F_{9/2}$ multiplet of CaF_2:0.05%Dy^{3+}:0.1%Gd^{3+}.

is likely that such centers would then decay non-radiatively. To partially avoid the issues arising from possible cross-relaxation in any center with more than one Dy^{3+} ion it is advantageous to more heavily dope with Gd^{3+} than with Dy^{3+}.

The broadband excitation spectrum of CaF_2:0.05%Dy^{3+}:0.1%$Gd^{3+}$is presented in Figure 6.3. The two main centers in this sample that were not observed in the excitation spectra of a CaF_2:0.05%Dy^{3+} crystal have been characterised. One of these is assigned as a heterogeneous version of the $CaF_2:RE^{3+}$ R-center. From the similarity of the absorption spectra it is inferred that such a center is also present in the singly doped CaF_2:0.05%Dy^{3+} crystal. The assignment as an R-center is made through comparison with $CaF_2:Dy^{3+}:Eu^{3+}$ excitation and fluorescence, as will be discussed in the following section. The second center will be shown to be a single Dy^{3+} ion cubic center, in which there is non-local charge compensation (Section 6.6).

The excitation frequencies of the $CaF_2:Dy^{3+}:Gd^{3+}$ system are given in Table 6.1, along with the transition assignments. The cubic center excitation features include a number of transitions that are associated with vibronics. These vibronics take on the form of transitions with a quite narrow line-width, and with a frequency offset from the parent electron transition that does not coincide with any peaks in the CaF_2 phonon density of states. Such issues will be addressed in the discussion of the cubic centers.

Transition frequency	Assignment		
	R-center	cubic	C_{4v}
21092±2		$Z_{1,2}\rightarrow F_2$	
21083	$Z_1\rightarrow F_2$		
21070			$Z_1\rightarrow F_2$
21059	—	—	—
21055	$Z_1\rightarrow F_1$		
21043			$Z_1\rightarrow F_1$
21027		$Z_1\rightarrow F_1$ + v	
21018		$Z_2\rightarrow F_1$ + v	
20889		$Z_1\rightarrow F_1$	
20880		$Z_2\rightarrow F_1$	

Table 6.1: The excitation transition frequencies for CaF_2:0.05%Dy^{3+}:0.1%Gd^{3+}, and the corresponding center assignments. Frequencies are given in vacuum cm^{-1}, with an absolute uncertainty of $\pm 1\,cm^{-1}$ unless otherwise stated.

CaF_2:Dy^{3+}:Gd^{3+} R-center

The R-center has been proposed as an asymmetric dimer by Hamers et.al. [37] and subsequent studies of the defect kinetics support the assignment of a dimer [18, 19]. Therefore with the Dy^{3+}:Gd^{3+} co-doping it is expected that the formation of R-centers will result in four distinct dysprosium sites: Dy^{3+}-Dy^{3+}, Gd^{3+}-Dy^{3+}, Dy^{3+}-Gd^{3+}. Notationally, the ordering of the rare-earth pair is used to indicate the distinction in the two possible rare-earth sites in the asymmetric dimer. Hence the Dy^{3+} ions in the centers labelled as Gd^{3+}-Dy^{3+} and Dy^{3+}-Gd^{3+} should be considered as distinct and with different environments.

The fluorescence spectra obtained for the CaF_2:Dy^{3+}:Gd^{3+} R-center, with $Z_1\rightarrow F_1$ excitation at $21055\,cm^{-1}$, are presented in Figure 6.4. Although two distinct Dy^{3+} sites are expected (Dy^{3+}–Gd^{3+} and Gd^{3+}–Dy^{3+}, with the Dy^{3+}–Dy^{3+} sites non-radiative), the excitation and fluorescence spectra do not resolve these two sites. This suggests that the asymmetry of the R-center is a minor perturbation of the crystal-field splittings. Such a conclusion is also supported by the infrared absorption as will be discussed below. For determining assignments for the observed excitation and fluorescence transitions, the two Dy^{3+} sites are therefore treated as indistinguishable. In the excitation spectrum of CaF_2:0.05%Dy^{3+}:0.1%Gd^{3+} the two R-center transitions to the $^4F_{9/2}$ multiplet that are observed at $21055\,cm^{-1}$ and $21083\,cm^{-1}$ are assigned as $Z_1\rightarrow F_1$ and $Z_1\rightarrow F_2$ respectively. In the fluorescence spectra both the excited states of F_1 and F_2 are observed as emitting levels, as is expected for the sample temperature of 15 K.

The fluorescence transition frequencies and assignments are tabulated in Table 6.3, and the energy levels of the lower ^6L_J multiplets that have been determined from the fluorescence data are given in Table 6.2.

It is noted that of the tabulated Dy^{3+}–Gd^{3+} R-center fluorescence frequencies, several occur within $5\,cm^{-1}$ of the weak transitions observed in the 2 K $CaF_2:Dy^{3+}$ C_{4v} and C_{3v} fluorescence , described in the previous chapters. This indicates that those additional weak transitions are associated with $CaF_2:Dy^{3+}$ R-center fluorescence, and were correctly considered as extraneous to the tetragonal and trigonal center fluorescence.

Multiplet	Level	Energy (cm^{-1})
$^6H_{15/2}$	Z_1	0
	Z_2	42
	Z_3	93
	Z_4	99
	Z_5	105
$^6H_{13/2}$	Y_1	3534
	Y_2	3548
	Y_3	3581

Multiplet	Level	Energy (cm^{-1})
$^6H_{11/2}$	X_1	5872
	X_2	5896
	X_3	5912
$^6H_{9/2}$, $^6F_{11/2}$	W_1	7630
	W_2	7636
$^6H_{7/2}$, $^6F_{9/2}$	A_1	8986
	A_2	9019
$^4F_{9/2}$	F_1	21055
	F_2	21083

Table 6.2: Energy levels determined for the $CaF_2:Dy^{3+}:Gd^{3+}$ heterogeneous R-center. Energies are in vacuum cm^{-1}.

Multiplet	Trans.	Frequency	Assignment
$^6H_{15/2}$	1	21043	$F_2 \rightarrow Z_2$
	2	21013	$F_1 \rightarrow Z_2$
	3	20990	$F_2 \rightarrow Z_3$
	4(a)	20983	$F_2 \rightarrow Z_4$
	4(b)	20979	$F_2 \rightarrow Z_5$
	5	20956	$F_1 \rightarrow Z_4$
	6	20950	$F_1 \rightarrow Z_5$
	7	20927	
	8	20913	
$^6H_{13/2}$	1	17550	$F_2 \rightarrow Y_1$
	2	17535	$F_2 \rightarrow Y_2$
	3	17521	$F_1 \rightarrow Y_1$
	4	17507	$F_1 \rightarrow Y_2$
	5	17474	$F_1 \rightarrow Y_3$
	6	17455	
	7	17442	
	8	17436	
	9	17378	
$^6H_{11/2}$	1	15212	$F_2 \rightarrow X_1$
	2	15183	$F_1 \rightarrow X_1$
	3	15171	$F_2 \rightarrow X_3$
	4	15159	$F_1 \rightarrow X_2$
	5	15143	$F_1 \rightarrow X_3$
	6	15121	
	7	15112	
	8	15079	
	9	15046	

Multiplet	Trans.	Frequency	Assignment
$^6H_{9/2}$,	1	13453	$F_2 \rightarrow W_1$
$^6F_{11/2}$	2	13448	$F_2 \rightarrow W_2$
	3	13425	$F_1 \rightarrow W_1$
	4	13419	$F_1 \rightarrow W_2$
	5	13361	
	6	13347	
	7	13317	
	8	13295	
	9	13249	
$^6H_{7/2}$,	1	12098	$F_2 \rightarrow A_1$
$^6F_{9/2}$	2	12069	$F_1 \rightarrow A_1$
	3	12065	$F_2 \rightarrow A_2$
	4	12036	$F_1 \rightarrow A_2$
	5	12008	
	6	12002	

Table 6.3: CaF_2:Dy^{3+}:Gd^{3+} R-center fluorescence transition frequencies at 15 K. Line labels are as shown in Figure 6.4. All transition frequencies are in vacuum cm^{-1}, with an absolute uncertainty of $\pm 1\,cm^{-1}$.

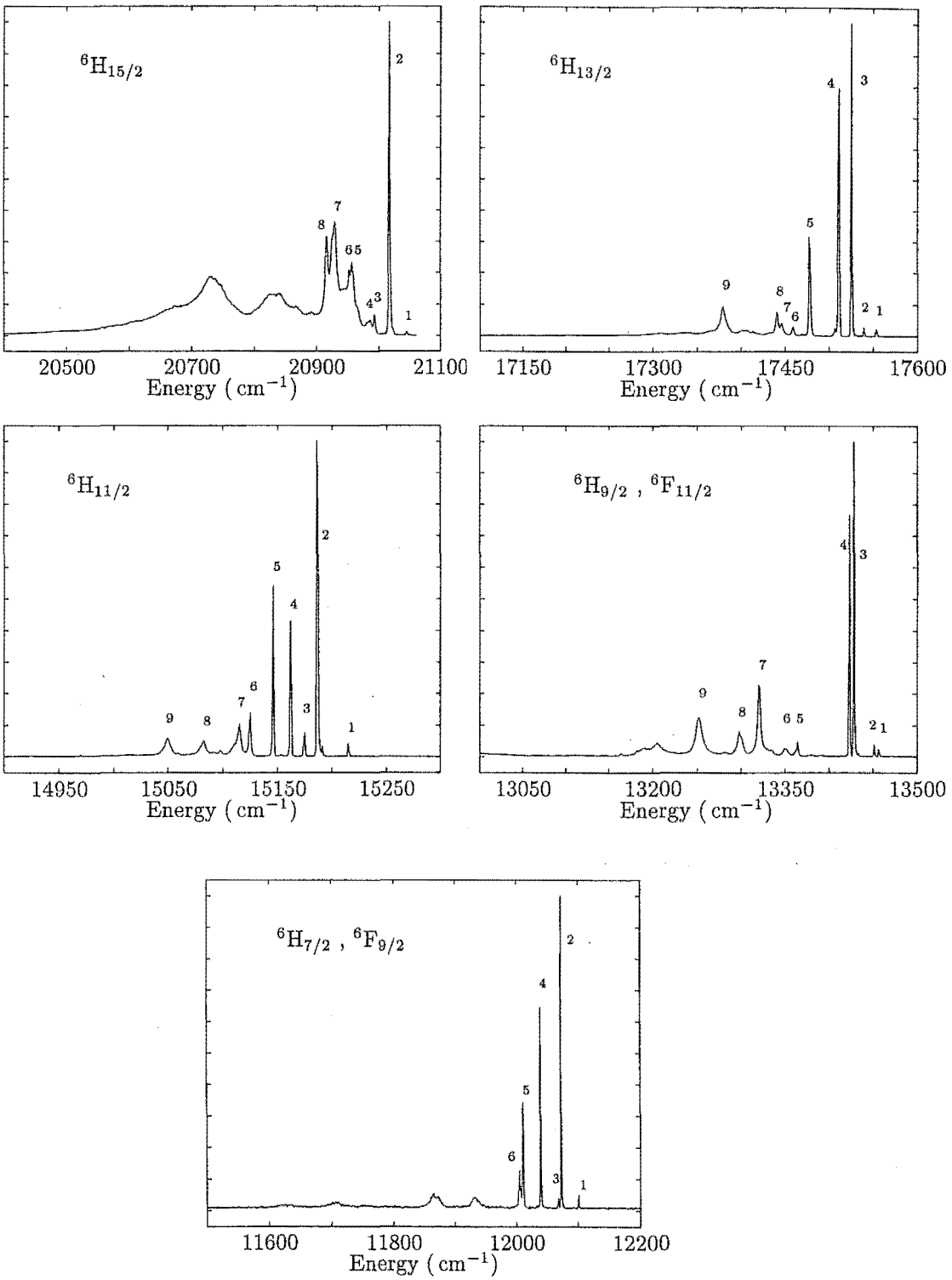

Figure 6.4: 15 K $^4F_{9/2} \rightarrow {}^6H_J$, ^6F_J fluorescence of the CaF_2:Dy^{3+}:Gd^{3+} heterogeneous R-center. Excitation was via the $Z_1 \rightarrow F_1$ transition at 21055 cm^{-1}.

The infrared absorption of CaF_2:0.05%Dy^{3+} and CaF_2:0.05%Dy^{3+}:0.1%Gd^{3+} in the region of the X_1 state is presented in Figure 6.5. For the singly doped Dy^{3+} sample a $0.8\,cm^{-1}$ splitting is observed, which is interpreted as the consequence of site asymmetry. Consistent with this is the absorption for the double doped Dy^{3+}:Gd^{3+} sample, in which two new absorption transitions are observed, shifted by a few wavenumbers and with a splitting of $2.2\,cm^{-1}$. These new absorption transitions are attributed to Dy^{3+}–Gd^{3+} and Gd–Dy^{3+} centers.

Similar results are obtained for absorption transitions to the the X_2 and X_3 states. For the X_2 absorption at $\approx 5897\,cm^{-1}$, the singly doped sample reveals a $0.8\,cm^{-1}$ splitting, while the double doped sample reveals no new features, with only a blurring of the otherwise resolved structure. For the transition at $\approx 5912\,cm^{-1}$(Fig. 6.5), which corresponds to the X_3 absorption, there is a $0.8\,cm^{-1}$ splitting present in the CaF_2:Dy^{3+} sample and an indication of a similar splitting in the CaF_2:Dy^{3+}:Gd^{3+} sample. The changed relative absorption strengths in the pair of absorption features indicates that additional absorptions are present in the double doped sample, as expected from the additional Dy^{3+}–Gd^{3+} and Gd^{3+}–Dy^{3+} sites. The small shifts in the infrared absorption frequencies upon introduction of Gd^{3+} as a co-dopant, and the small splitting between pairs of transitions, are taken as evidence of only a small distinction between the Dy^{3+} sites of the heterogeneous Dy^{3+}–Gd^{3+} R-center.

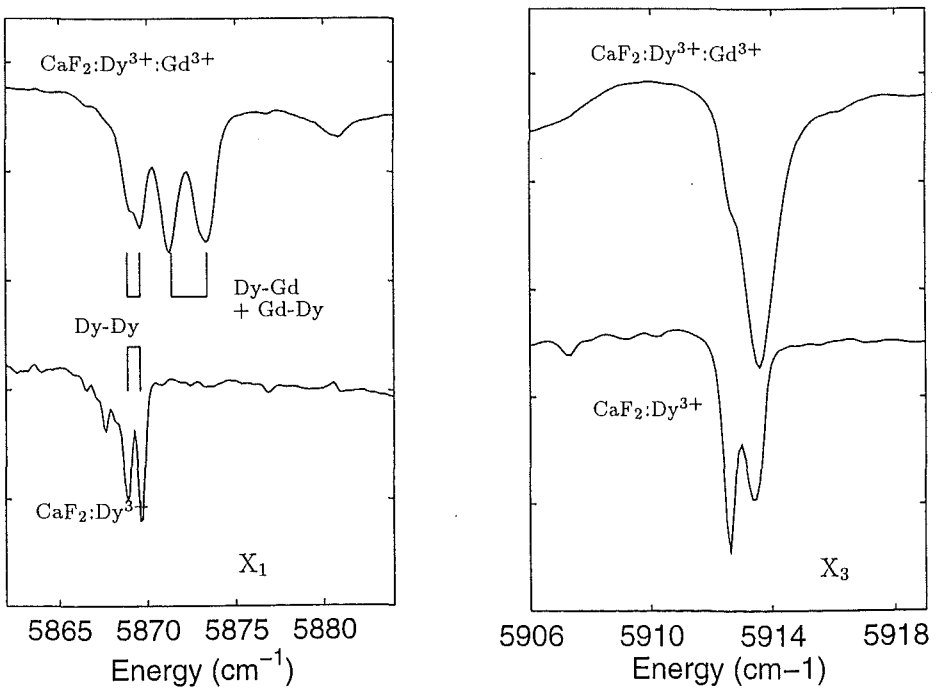

Figure 6.5: Absorption transitions to the X_1 and X_3 states of the R-center in CaF_2:0.05%Dy^{3+} and CaF_2:0.05%Dy^{3+}:0.1%Gd^{3+}.

6.4 $CaF_2:Dy^{3+}:Eu^{3+}$.

Investigation of the $CaF_2:Dy^{3+}:Eu^{3+}$ system has enabled a comparison of the Dy^{3+} cluster centers with those reported to be present in $CaF_2:Eu^{3+}$ [37].

The 15 K broadband excitation spectrum of CaF_2:0.05%Dy^{3+}:0.04%Eu^{3+} is presented in Figure 6.6, with the corresponding transition frequencies listed in Table 6.4.

For excitation into the Dy^{3+} $^4F_{9/2}$ multiplet at 21055 cm^{-1} and 21084 cm^{-1}, the dominant fluorescence corresponds to emission from the Eu^{3+} $^5D_0$ multiplet. These two excitation transitions belong to the same center, as demonstrated by the narrowband spectrum of Figure 6.6. This excitation spectrum was obtained while monitoring the $^5D_0 \rightarrow {}^7F_1$ emission at 16925 cm^{-1}.

The observed fluorescence for excitation into the higher energy of these two transitions, at 21084 cm^{-1}, is presented in Figure 6.7. The transition frequencies for this Eu^{3+} emission are tabulated in Table 6.5, along with the transition frequencies of the $CaF_2:Eu^{3+}$ R-center emission, as reported by Hamers, Wietfeldt and Wright [37]. The similarity of the spectra with those of the R-center fluorescence spectra presented by Hamers et.al., as demonstrated by the close agreement of the transition frequencies in Table 6.5, is the basis of assigning the $CaF_2:Dy^{3+}:Eu^{3+}$ center reported here to be a heterogeneous version of the R-center. The similarity of the excitation frequencies seen in $CaF_2:Dy^{3+}:Eu^{3+}$, $CaF_2:Dy^{3+}:Gd^{3+}$ then forms the basis for assigning the R-center to be present in both of these systems. In addition, the absorption spectra of a pure $CaF_2:Dy^{3+}$crystal, in which the clusters do not fluorescence, indicates that the same center exists in the singly doped samples.

For the emission spectrum in the region of 15200 cm^{-1}, as well as the $^5D_0 \rightarrow {}^7F_3$ Eu^{3+} fluorescence, much weaker features corresponding to Dy^{3+} $^4F_{9/2} \rightarrow {}^6H_{11/2}$ fluorescence are also observed. The Dy^{3+} emission is similar in appearance to that of the Dy^{3+}–Gd^{3+} R-center fluorescence reported in the previous section. It can therefore be concluded that while the dysprosium to europium energy transfer is efficient, it is not so rapid as to completely quench the excited states of dysprosium.

In the $\approx$13200 cm^{-1} region, the Dy^{3+} cubic center fluorescence overlaps the Eu^{3+} $^5D_0 \rightarrow {}^7F_5$ heterogeneous R-center fluorescence, and is due to the small overlap in the excitation frequency of the R-center and the broad cubic center transition centered at 21090 cm^{-1}.

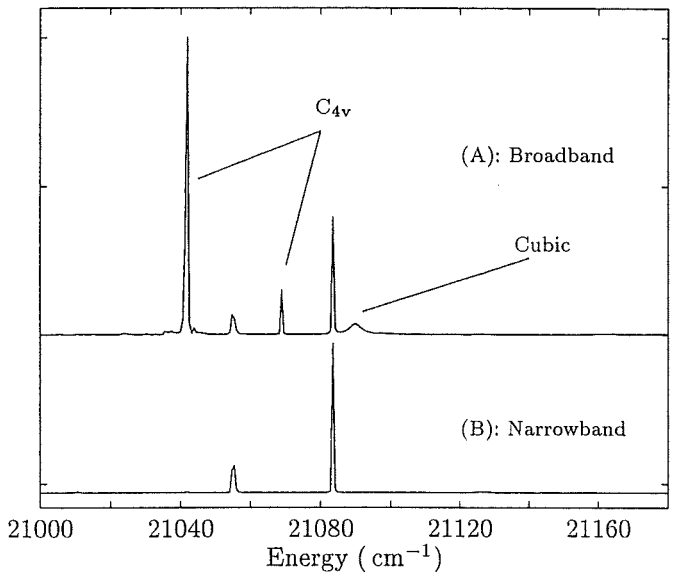

Figure 6.6: 15K broadband and Narrowband excitation spectra for the $^4F_{9/2}$ multiplet of CaF_2:0.05%Dy^{3+}:0.04%Eu^{3+}. (A) Monitoring at 675 nm, (B) monitoring the R-center Eu^{3+} fluorescence at 16925 cm^{-1}.

Transition	Assignment		
frequency	R-center	cubic	C_{4v}
21090±2		$Z_{1,2}\rightarrow F_2$	
21084	$Z_1\rightarrow F_2$		
21069			$Z_1\rightarrow F_2$
21055	$Z_1\rightarrow F_1$		
21042			$Z_1\rightarrow F_1$

Table 6.4: CaF_2:0.05%Dy^{3+}:0.04%Eu^{3+} excitation frequencies at 15K, in vacuum cm^{-1} with an absolute uncertainty of ±1 cm^{-1} unless otherwise stated.

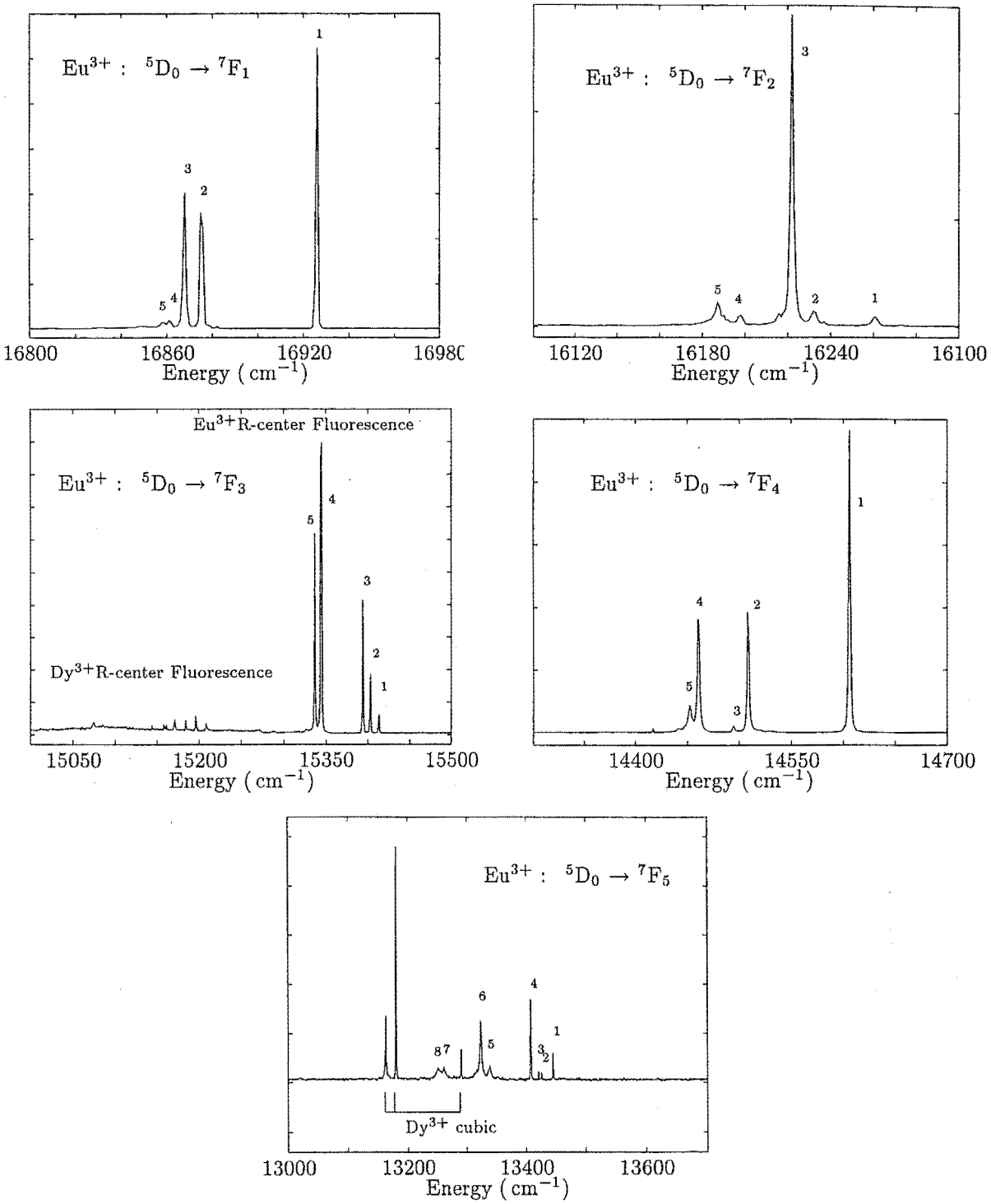

Figure 6.7: 15 K Eu^{3+} fluorescence of the CaF_2:Dy^{3+}:Eu^{3+} R-center, on excitation into the Dy^{3+} $^4F_{9/2}$ multiplet at 21084 cm^{-1}.

Eu^{3+}terminating Multiplet	Transition label (Fig. 6.7)	Frequency (cm^{-1}) CaF_2:Dy^{3+}:Eu^{3+}	Frequency (cm^{-1}) CaF_2:Eu^{3+}[37]
$^7F_1$	1	16925	16933.8
	2	16874	16872.7
	3	16867	16865.0
	4	16860	16859.2
	5	16857	
$^7F_2$	1	16260	16262.8
			16260.9
	2	16231	16233.6
	3	16221	16220.7
	4	16197	16196.1
	5	16186	16184.5
			16178.3
			16154.0
$^7F_3$	1	15412	15410.2
	2	15407	15401.5
	3	15393	15390.9
	4	15344	15341.9
	5	15336	15337.9
$^7F_4$	1	14601	14603.9
			14536.4
	2	14507	14507.5
	3	14494	14493.9
	4	14459	14474.8
	5	14451	14453.4
			14410.4
			14379.6
$^7F_5$	1	13444	13447.3
	2	13424	13440.8
	3	13420	
	4	13406	13411.2
	5	13337	13336.7
	6	13322	13324.0
	7	13259	13257.7
	8	13249	13245.3

Table 6.5: Comparison of the Eu^{3+} fluorescence of the CaF_2:Dy^{3+}:Eu^{3+} R-center and that for the CaF_2:Eu^{3+} R-center reported by Hammers et.al. [37]. All transition frequencies in vacuum cm^{-1}. The frequencies tabulated for CaF_2:Dy^{3+}:Eu^{3+} have an uncertainty of $\pm 1\,cm^{-1}$.

6.5 $CaF_2:Dy^{3+}:Tb^{3+}$.

In the above $CaF_2:Dy^{3+}:RE^{3+}$ systems, the co-doping has served two purposes. First, the addition of Gd^{3+} has enabled the determination of the dysprosium cluster center fluorescence, and also several corresponding energy levels of the lower multiplets. With a co-dopant of Eu^{3+} the dominant cluster center has been identified as an R-center dimer.

$Dy^{3+}:Tb^{3+}$ co-doping has also been investigated, with the intention of bridging the co-dopant investigations across the rare-earths series from Eu^{3+} to Dy^{3+}.

The $Dy^{3+}\rightarrow Dy^{3+}$cross-relaxation is suppressed in the $Dy^{3+}:Tb^{3+}$ clusters, as revealed in the broadband excitation spectra of Figure 6.8. However, it is found that the fluorescence of the clusters, at least for the R-center, is not characteristic of the Dy^{3+} ion in the center, but rather of Tb^{3+} emission following energy transfer from $Dy^{3+}\rightarrow Tb^{3+}$. This emission is visibly green, as opposed to the more usual red observed for dysprosium emission.

Broadband excitation spectra of CaF_2:0.05%Dy^{3+}:0.04%Tb^{3+} obtained for fluorescence monitored in two separated bands are presented in Figure 6.8. The fluorescence bandpass is $\approx$10 nm for both spectra. In the lower spectrum, for fluorescence monitored at 665 nm ($\approx$15000 cm^{-1}), similar features to those present with the previously discussed co-dopants are observed, corresponding to the single ion C_{4v} , C_{3v} and cubic centers, and the heterogeneous R-center. A number of weaker transitions are also observed. In the upper spectrum of Figure 6.8 the fluorescence was monitored at 575 nm ($\approx$17400 cm^{-1}), coinciding with both Tb^{3+} emission [74] and the Dy^{3+} emission of the R-centers and the single ion C_{4v} center.

However, with this monitoring wavelength the broad excitation peak at $\approx$21090 cm^{-1} has been suppressed, while maintaining the broadband nature of the excitation spectrum, revealing a multitude of transitions that were otherwise obscured. The greatly increased complexity of the dysprosium $^4F_{9/2}$ excitation spectrum for Tb^{3+} co-doping provides evidence for the onset of of higher order clustering behaviour, such as that proposed for $CaF_2:Er^{3+}$ [18].

The Tb^{3+} emission that was observed upon excitation of the Dy^{3+} ion at 21054 cm^{-1} is presented in Figure 6.9. Because of the complicated nature of this fluorescence, together with only the spectroscopy of the C_{4v} defect centers in $CaF_2:Tb^{3+}$ being present in the literature [74], the spectroscopy of the $CaF_2:Dy^{3+}:Tb^{3+}$ system has not been pursued further.

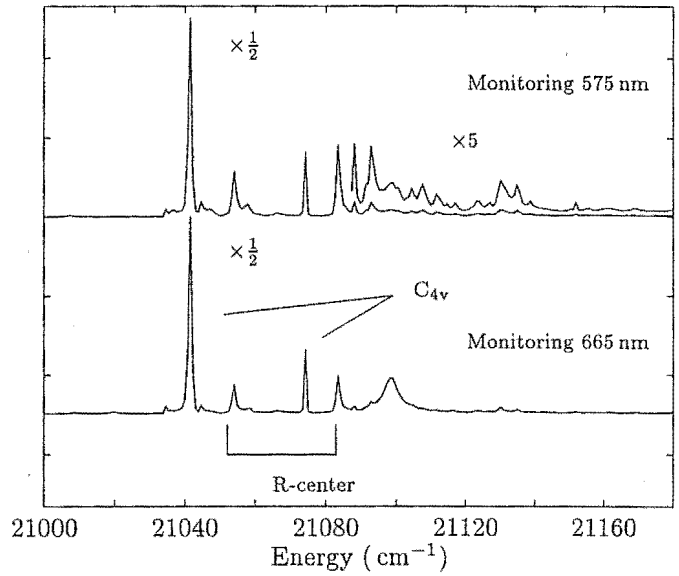

Figure 6.8: 15 K broadband excitation spectra for the Dy^{3+} $^4F_{9/2}$ multiplet of CaF_2:0.05%Dy^{3+}:0.05%Tb^{3+}. Top: Monitoring at 575 nm and suppressing the Dy^{3+} cubic center excitation signal. Bottom: monitoring at 665 nm. The peak intensity of the main C_{4v} transition has been truncated to give a clearer view of the minor features.

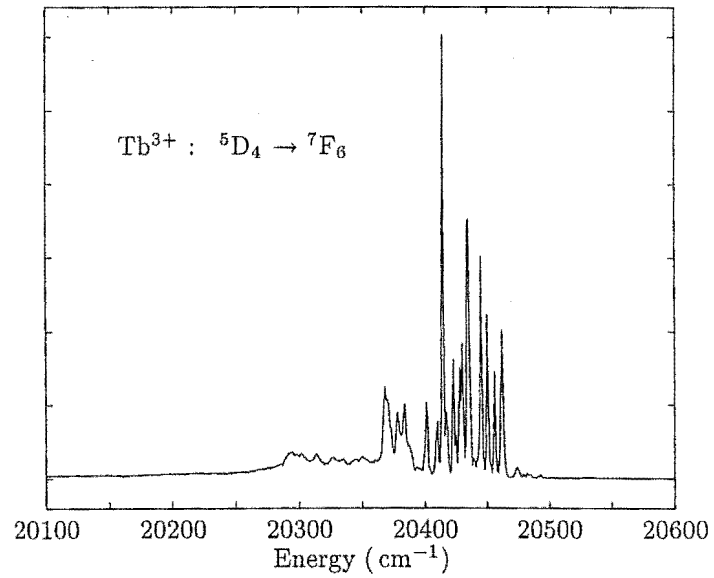

Figure 6.9: 15 K Tb^{3+} emission observed upon Dy^{3+} excitation of the R-center excitation transition at 21054 cm^{-1}.

6.6 CaF_2:Dy^{3+} cubic center

The $^4F_{9/2}$ excitation spectra of CaF_2:0.05%Dy^{3+}:0.1%Gd^{3+} exhibits transitions associated with a cubic symmetry center. Such transitions are absent in the excitation spectra for CaF_2:0.05%Dy^{3+}. The presence of the cubic center in the more highly doped sample is consistent with the scavenging of fluorines by rare-earth clusters [70]. The cubic center has also been confirmed to be present in a more heavily doped CaF_2:0.15%Dy^{3+} sample. The optical quality of the CaF_2:0.05%Dy^{3+}:0.1%Gd^{3+} sample is however superior, and therefore the cubic center investigations have been primarily concerned with this double doped sample.

The simplicity of the fluorescence spectra of this center is the first indication of the cubic symmetry. A crystal-field calculation for the $^4F_{9/2}$ multiplet has been performed to determine the irrep label of the emitting state, and therefore infer the number of allowed fluorescence transitions to each multiplet. In evaluating matrix elements of the cubic crystal-field Hamiltonian the LS mixing of the free-ion $^4F_{9/2}$ multiplet has been taken into account. The free-ion wavefunction of this multiplet is composed of many different LS components, and an expansion has been determined by means of a free-ion calculation using the *f-shell empirical* programs of Dr. M.F. Reid with parameters found for the CaF_2:Dy^{3+} C_{4v} center. This expanded wavefunction is, up to terms of greater than 5% contribution,

$$|^4F_{9/2}) \equiv -0.2929[^6F_{9/2}\rangle - 0.3171[^4F(1)_{9/2}\rangle + 0.6702[^4F(3)_{9/2}\rangle +$$

$$0.2936[^4F(4)_{9/2}\rangle - 0.2179[^4G(1)_{9/2}\rangle - 0.3165[^4G(4)_{9/2}\rangle \qquad (6.1)$$

where the $|^4F_{9/2})$ notation is taken to represent this expansion. For Dy^{3+} there exists more than one $^4F_{9/2}$ and $^4G_{9/2}$ multiplet, and this distinction is indicated by the number in parentheses.

Following Lea, Leask and Wolf [61], the cubic crystal-field Hamiltonian (page 12) is expressed in a form that encompasses all possible ratios of the parameters B_c^4 and B_c^6:

$$\begin{aligned} H &= B_c^4\left(C_0^4 + \sqrt{5/14}(C_4^4 + C_{-4}^4)\right) + B_c^6\left(C_0^6 - \sqrt{7/2}(C_4^6 + C_{-4}^6)\right) \\ &\equiv B_c^4 C_c^4 + B_c^6 C_c^6 \\ &= W\left(xC_c^4 + (1-|x|)C_c^6\right), \end{aligned} \qquad (6.2)$$

The parameters x and W are defined from the following relations:

$$B_c^4 = Wx, \qquad B_c^6 = W(1-|x|) \qquad \text{and} \qquad -1 \le x \le 1$$

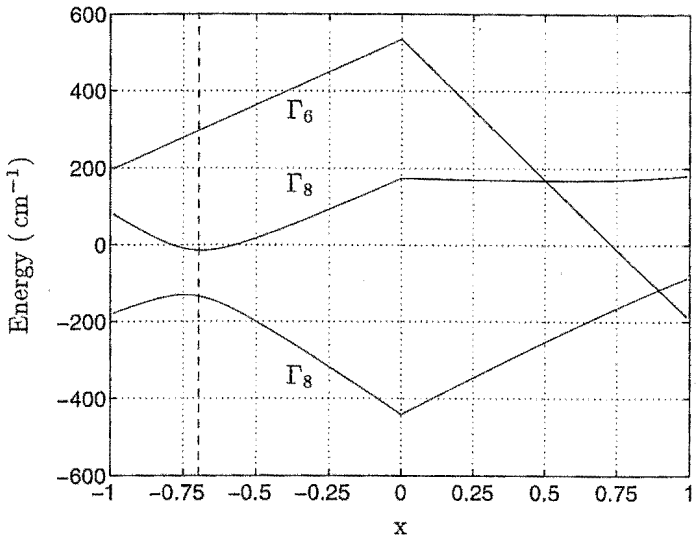

Figure 6.10: Cubic crystal-field splitting for $^4F_{9/2}$ multiplet of CaF_2:Dy^{3+}. The ordinate scale is given for a parameter value of W=1950 cm^{-1}.

From such a parametrisation, the ratio of the two crystal-field parameters is expressed in terms of the variable x as

$$B_c^4/B_c^6 = x/(1-|x|)$$

The crystal-field calculation for the $^4F_{9/2}$ multiplet has been performed in terms of the Hamiltonian 6.2, with the matrix elements of C_q^k calculated for the free-ion decomposition of equation 6.1. The calculated crystal-field energy levels are shown in Figure 6.10 as a function of the parameter x. The remaining parameter W, which simply scales the ordinate of Fig. 6.10, is set at $W = 1950\,\mathrm{cm}^{-1}$ from consideration of the C_{4v} cubic parameters. The values of the cubic parameters found for the C_{4v} center in CaF_2:Dy^{3+} are taken to provide a first approximation to the cubic center. The values of $B_c^6 = 590\,\mathrm{cm}^{-1}$and $B_c^4 = -1360\,\mathrm{cm}^{-1}$ correspond to $x = -0.697$ and $W = 1950\,\mathrm{cm}^{-1}$. From this calculation it is seen that for all reasonable crystal-field parameters the lowest state of $^4F_{9/2}$ will transform as the Γ_8 irrep.

Having determined the irrep of the lowest level of the $^4F_{9/2}$ multiplet for a cubic center, conclusions on the number of allowed fluorescence transitions to a given multiplet can be drawn. For Kramers ions in cubic symmetry the energy levels will transform as one of the irreps $\Gamma_6, \Gamma_7, \Gamma_8$, and the allowed transitions between states are given by

$$\Gamma_8 \rightarrow \Gamma_6, \Gamma_7, \Gamma_8 \qquad \Gamma_7 \rightarrow \Gamma_7, \Gamma_8 \qquad \Gamma_6 \rightarrow \Gamma_6, \Gamma_8$$

Therefore, with the Γ_8 lower level of $^4F_{9/2}$, all transitions to the lower multiplets are allowed. The irrep decompositions of the free-ion multiplets presented in Table 6.6 determines the number of terminating energy levels of each multiplet.

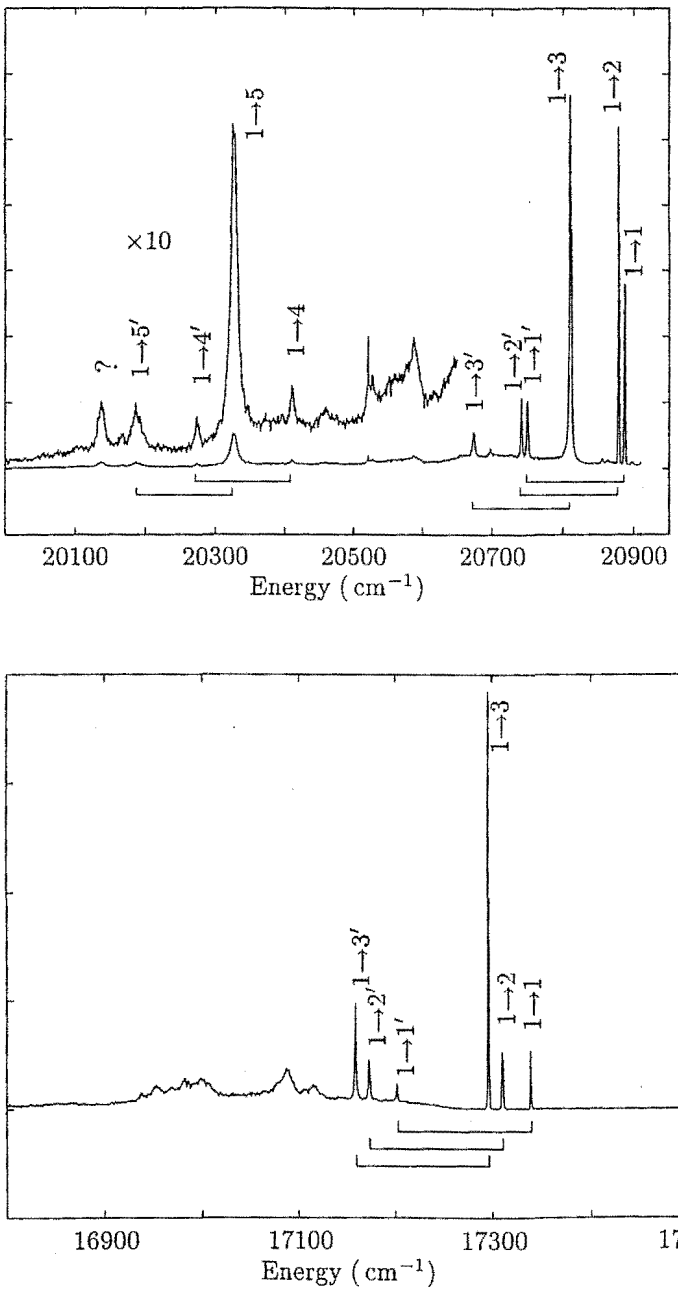

Figure 6.11: 15 K CaF_2:Dy^{3+} cubic center fluorescence spectra, $^4F_{9/2} \rightarrow {}^6H_{15/2}$, $^6H_{13/2}$ multiplets. Vibronic transition are indicated by a prime on the terminating state labels, and by the connecting lines under the spectra. The vibronic interval is $\approx$138 cm^{-1}.

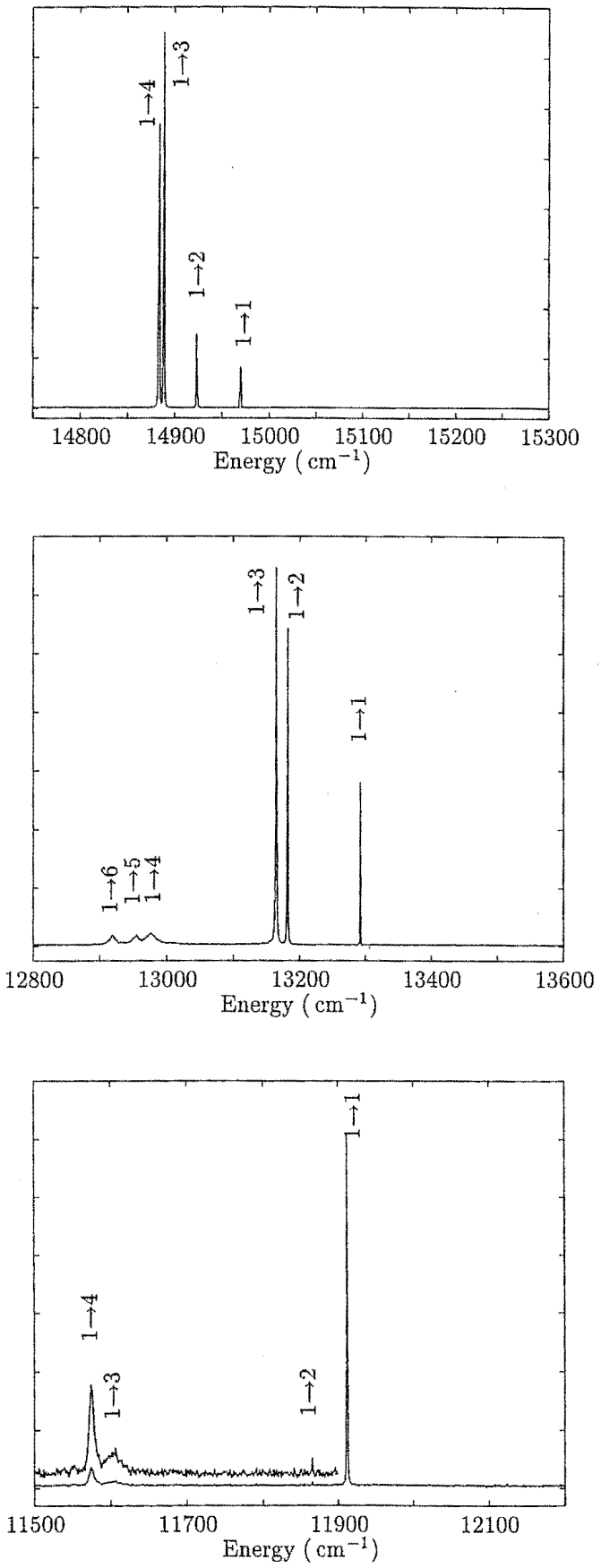

Figure 6.12: 15 K CaF_2:Dy^{3+} cubic center fluorescence spectra, $^4F_{9/2} \rightarrow {}^6H_{11/2}$, W and A manifolds.

Multiplet	Fluor. Energy	Transition	phonon energy
$^6H_{15/2}$	20889	$F_1 \rightarrow Z_1$	–
	20881	$F_1 \rightarrow Z_2$	–
	20813	$F_1 \rightarrow Z_3$	–
	20752	$F_1 \rightarrow Z_1$'	137
	20743	$F_1 \rightarrow Z_2$'	138
	20675	$F_1 \rightarrow Z_3$'	138
	20412	$F_1 \rightarrow Z_4$	–
	20328	$F_1 \rightarrow Z_5$	–
	20275	$F_1 \rightarrow Z_4$'	137
	20188	$F_1 \rightarrow Z_5$'	140
	20138	(?) $F_1 \rightarrow Z_4$'+ 137	137
$^6H_{13/2}$	17335	$F_1 \rightarrow Y_1$	–
	17307	$F_1 \rightarrow Y_2$	–
	17292	$F_1 \rightarrow Y_3$	–
	17198	$F_1 \rightarrow Y_1$'	137
	17169	$F_1 \rightarrow Y_2$'	138
	17155	$F_1 \rightarrow Y_3$'	137
$^6H_{11/2}$	14967	$F_1 \rightarrow X_1$	
	14920	$F_1 \rightarrow X_2$	
	14886	$F_1 \rightarrow X_3$	
	14881	$F_1 \rightarrow X_4$	
$^6H_{9/2}$,	13290	$F_1 \rightarrow W_1$	
$^6F_{11/2}$	13179	$F_1 \rightarrow W_2$	
	13162	$F_1 \rightarrow W_3$	
	12973	$F_1 \rightarrow W_4$	
	12952±2	$F_1 \rightarrow W_5$	
	12917±2	$F_1 \rightarrow W_6$	
$^6H_{7/2}$,	11910	$F_1 \rightarrow A_1$	
$^6F_{9/2}$	11863	$F_1 \rightarrow A_2$	
	11602±2	$F_1 \rightarrow A_3$	
	11571±2	$F_1 \rightarrow A_4$	

Table 6.7: CaF_2:Dy^{3+} cubic center fluorescence transition frequencies and assignments, as shown in the spectra of Figures 6.11, 6.12. All frequencies are given with an uncertainty of $\pm 1\,cm^{-1}$, and are calibrated to vacuum cm^{-1}.

The fluorescence spectra to the $^6H_{15/2}$, $^6H_{13/2}$, $^6H_{11/2}$,W($^6H_{9/2}$, $^6F_{11/2}$) and A($^6H_{7/2}$, $^6F_{9/2}$) multiplets are presented in Figures 6.11, 6.12. The fluorescence to each of the two lowest multiplets, $^6H_{15/2}$ and $^6H_{13/2}$, is expected to consist of only five electronic transitions, associated with the five terminating states. An excess number of transitions are observed which is attributed to the presence of vibronic transitions.

J	irreps
15/2	$\Gamma_6 + \Gamma_7 + 3\Gamma_8$
13/2	$\Gamma_6 + 2\Gamma_7 + 2\Gamma_8$
11/2	$\Gamma_6 + \Gamma_7 + 2\Gamma_8$
9/2	$\Gamma_6 + 2\Gamma_8$
7/2	$\Gamma_6 + \Gamma_7 + \Gamma_8$
5/2	$\Gamma_7 + \Gamma_8$
3/2	Γ_8
1/2	Γ_6

Table 6.6: Irrep decomposition for Dy^{3+} in cubic symmetry.

These vibronics are unusual in their narrow linewidth, which is more in line with that expected for electronic transitions. Further, these vibronics occur with a well defined frequency separation from the electronic transitions that cannot be attributed to the CaF_2 phonon density of states. A fuller discussion of the anomalous characteristics of these vibronics is given later in this chapter.

The vibronic transitions are a feature of both the excitation and emission spectra of this center. In excitation the Z_1,$Z_2 \rightarrow F_1$ transitions occur at 20889 cm^{-1} and 20880 cm^{-1} respectively, with the two Z_1,$Z_2 \rightarrow F_1'$ vibronic transitions at 21027 cm^{-1} and 21018 cm^{-1}. The vibronic shifts are therefore 138 cm^{-1}. Repeating patterns in the fluorescence spectra also reveal this vibronic offset. This is most clearly observed in the $F_1 \rightarrow$ $^6H_{13/2}$ emission, where three narrow electronic transitions all possess associated vibronics separated by 138 cm^{-1}. The $F_1 \rightarrow$ $^6H_{15/2}$ emission also displays sharp vibronic emission offset at 138 cm^{-1} from the electronic transitions. In considering the narrow line-width and large relative intensity of the above mentioned vibronic transitions, it is noted that for a cubic symmetry all electronic electric-dipole transitions are forbidden due to the inversion symmetry of the center. For $^4F_{9/2} \rightarrow$ $^6H_{15/2}$, $^6H_{13/2}$ emission, magnetic dipole (electronic) transitions are only allowed through J-mixing of the multiplets which brings in components that satisfy $\Delta J = 0, \pm 1$, and this is expected to be quite small. Hence the electronic transitions for $^4F_{9/2} \rightarrow$ $^6H_{15/2}$, $^6H_{13/2}$ are expected to be weak. However the vibronics may proceed via an electric-dipole mechanism as the phonons can effectively remove the inversion symmetry of the defect center.

No anomalous vibronics were observed in the emission to the $^6H_{11/2}$ multiplet and the W and A manifolds. It is noted that the two terminating multiplets that display vibronic transitions are the same as those that display strong vibronics in the SrF_2:Dy^{3+} C_{3v} center. In Table 6.7 the transition frequencies and assignments are

listed, with particular reference to the interval between the electronic and associated vibronic transitions. Together with the $^4F_{9/2}$ excitation frequencies tabulated in Table 6.1 on page 170, 22 energy levels been determined out of a total of 27 states for these lower multiplets in cubic symmetry. Two of the $^4F_{9/2}$ energy levels have also been determined from the excitation spectra.

Using the programs of Dr. Mike Reid (Section 4.3.3), a crystal-field least-squares calculation has been performed for CaF_2:Dy^{3+} cubic center, based on 21 of the experimental energy levels. The cubic parameters of the C_{4v} center were used as starting parameters. In table 6.8 the calculated and experimental cubic levels are listed, along with irreps assigned by the crystal field calculation.

Investigations of the CaF_2:Dy^{3+} cubic center have been previously reported in the literature. In particular, a Z_1–Z_2 ground state splitting of $\approx 8\,cm^{-1}$ has been established from EPR data by Bierig and Weber [8] and also by Salva and Tovar [92], in agreement with the ground state splitting observed here. Partial energy levels diagrams of the lower two or three multiplets have been presented by Luks et.al. [66], Al'tshuler et.al. [3] and Nara and Schlesinger [75]. Agreement with many of the cubic center energy levels reported by these authors has been obtained, and this work has expanded the number of energy level assignments for the cubic center.

Cubic center vibronics in CaF_2.

The vibronic transitions assigned in the above section display characteristics not usually associated with vibronics, particularly the narrow line-width. Sharp vibronic features associated with cubic centers in CaF_2:RE^{3+}crystals have been reported previously, but with little discussion on their apparently anomalous nature. Aizenberg et.al. [2] have reported vibronics for the CaF_2:Er^{3+} cubic center, including an offset of 133-136 cm^{-1} from the zero-phonon transitions. Moore [69] also presents a fluorescence spectrum for the $^4S_{3/2} \rightarrow {}^4I_{15/2}$ transitions of the cubic (LL) center in CaF_2:Er^{3+} which reveals a number of vibronic transitions. Four of the zero-phonon transitions have associated vibronics at an offset of $\approx 134\,cm^{-1}$. The line-widths of these vibronics is comparable to the purely electronic transitions. In a paper dealing specifically with vibronics in CaF_2:Er^{3+} Ward and Whippey [101] note numerous vibronics, most of which can be attributed to peaks in the pure CaF_2 density of states [29]. A notable exception is that of a phonon at ≈ 90 cm^{-1}, below any features in the CaF_2 phonon spectrum. No mention is made of a vibronic associated with a $\approx 134\,cm^{-1}$ phonon. However this absence could be explained by their use of non-selective X-ray excitation. The lower intensity cubic center transitions would then be expected to be swamped by the emission from other centers. Al'tshuler et.al. [3] have also reported the presence of

Table 6.8: Calculated and experimental energy levels of the Dy^{3+} cubic center in CaF_2:0.05%Dy^{3+}:0.1%Gd^{3+}. Energies are given in vacuum cm^{-1}. ‡Level not included in the parameter refinement.

Multiplet	level	irrep	measured energy (cm^{-1})	calculated energy (cm^{-1})	measured -calculated
	Z_1	Γ_8	0	0	0
$^6H_{15/2}$	Z_2	Γ_7	8	5	3
	Z_3	Γ_8	76	83	-7
	Z_4	Γ_6	477‡	434	
	Z_5	Γ_8	561‡	516	
	Y_1	Γ_6	3554	3557	-3
$^6H_{13/2}$	Y_2	Γ_8	3582	3586	-4
	Y_3	Γ_7	3597	3594	3
	Y_4	Γ_7		3749	
	Y_5	Γ_8		3795	
	X_1	Γ_7	5922	5919	3
$^6H_{11/2}$	X_2	Γ_8	5969	5961	8
	X_3	Γ_8	6003	6017	-14
	X_4	Γ_6	6008	6024	-16
	W_1	Γ_8	7599	7595	4
$^6H_{9/2}$,	W_2	Γ_6	7710	7719	-9
$^6F_{11/2}$	W_3	Γ_8	7727	7735	-8
	W_4	Γ_8	7916	7919	-3
	W_5	Γ_7	7937	7933	4
	W_6	Γ_6	7972	7967	5
	W_7	Γ_8		8257	
	A_1	Γ_8	8979	8969	10
$^6H_{7/2}$,	A_2	Γ_6	9026	9028	-2
$^6F_{9/2}$	A_3	Γ_8	9287	9280	7
	A_4	Γ_7	9318	9309	9
	A_5	Γ_8		9348	
	A_6	Γ_6		9721	
	F_1	Γ_8	20889	20891	-2
$^4F_{9/2}$	F_2	Γ_8	21092‡	21057	
	F_3	Γ_6		21570	

number of data points	21		
number of parameters	6		
standard deviation	8.5 cm^{-1}		
B_c^4	−2014 cm^{-1}	$B_c^4(C_{4v})$	−1360 cm^{-1}
B_c^6	737 cm^{-1}	$B_c^6(C_{4v})$	590 cm^{-1}

RE^{3+}	vibronic offset (cm^{-1})	comments
Pr^{3+}	142	Pavlichuk [80]
Nd^{3+}	141	Reeves [84]
Sm^{3+}	140	This work, following Wells [103]
Eu^{3+}	139	Reeves [84]
Dy^{3+}	138	This work, Al'tshuler [3]
Er^{3+}	134	Aizenberg [2], Moore [69]

Table 6.9: Progression of the vibronic offset seen in the cubic centers in CaF_2:RE^{3+}.

$\approx$137 cm^{-1} vibronics of the CaF_2:Dy^{3+} cubic centers. In the spectroscopy reported here, vibronic transitions additional to those of Al'tshuler et.al. have been identified.

In light of the very sharp vibronics observed in the CaF_2:Dy^{3+} cubic center spectra, and the above mentioned literature, Reeves [84] and Pavlichuk [80] of this department have searched for similar vibronics in other rare-earth cubic centers. Similar vibronics have indeed been observed, and the vibronic offsets that have been found, or previously reported, are summarised in Table 6.9. Comparable vibronic transitions in the Sm^{3+} cubic centers were not reported in the CaF_2:Sm^{3+} investigations of Wells [103], although a number of transitions assigned as electronic display a $\approx$140 cm^{-1} separation. With the trends in vibronic offset apparent in Table 6.9 indicating that the comparable vibronic in Sm^{3+} cubic centers should involve a phonon of energy $\approx$140 cm^{-1}, it was considered appropriate to revisit the transition assignments of Wells.

6.7 CaF_2:Sm^{3+} cubic centers.

As noted by Wells, the emitting $^4G_{5/2}$ level of the CaF_2:Sm^{3+} cubic center is expected to be a Γ_7 irrep. This conclusion is based on crystal-field calculations in which the cubic crystal-field parameters are approximated by the cubic parameters of the C_{4v} center. With a Γ_7 emitting state only transitions terminating on Γ_7 and Γ_8 states are allowed within the cubic point group selection rules. For fluorescence to many multiplets an excess number of transitions, over that allowed by the cubic selection rules, are observed. Wells has attributed this not only to the occurrence of vibronic transitions, but also to a perturbation from cubic symmetry for the non-locally charge compensated centers, and a subsequent breakdown in the $\Gamma_7 \not\rightarrow \Gamma_6$ selection rule. The need to invoke a breakdown of this selection rule is partially removed if the occurrence of vibronic transitions associated with a $\sim$140 cm^{-1} phonon is acknowledged. Assigning

some transitions as associated with such vibronics also alters the transition and energy level assignments given by Wells for the cubic CaF_2:Sm^{3+} center.

With this in mind, and because several features in the fluorescence spectra have not had the transition frequencies tabulated by Wells, the $^4G_{5/2} \rightarrow {}^6H_{5/2}$, $^6H_{7/2}$, $^6H_{9/2}$, $^6H_{11/2}$ and $^6H_{13/2}$, fluorescence of the CaF_2:Sm^{3+} cubic center has been have re-measured. A CaF_2:0.07%Sm^{3+}:1%Na^+ sample, grown by Dr. G.D. Jones of this department, was used for this investigation. The addition of NaF to the crystal melt is a well known method of promoting cubic center formation in CaF_2:RE^{3+} crystals. The re-measured fluorescence spectra of the CaF_2:Sm^{3+} cubic center are presented in Figures 6.13, 6.14. Excitation was provided by the $Z_1 \rightarrow {}^4F_{3/2}$ transition at 18842 cm^{-1}, and all emission is from the $^4G_{5/2}$ $A_1(\Gamma_7)$ state at 17653 cm^{-1}. The sample was at a temperature of 15 K.

In emission to the $^6H_{5/2}$ multiplet, which consists of two states transforming as Γ_7 and Γ_8, three transitions are observed. Wells has only discussed the most intense $1 \rightarrow 1$ transition. One of the other weak fluorescence peaks is here assigned as the $1 \rightarrow 2$ transition. The remaining feature in the emission spectrum occurs with a 139 cm^{-1} offset from the $1 \rightarrow 1$ transition, and is assigned as a cubic center vibronic transition.

The fluorescence spectrum for $^4G_{5/2} \rightarrow {}^6H_{7/2}$ is more difficult to assign. With the terminating multiplet composed of Γ_6, Γ_7 and Γ_8 states, only two electronic transitions are expected. Wells has assigned transitions to all three $^6H_{7/2}$ states, with the emission to the assigned Γ_6 state being quite weak. Two transitions were left unassigned, and several other features were associated with vibronics (other than the 140 cm^{-1} offset vibronics discussed here). The complexities of the emission spectra to this multiplet have inhibited a more definitive assignment of the observed transitions. A number of transitions occur with a $\sim$140 cm^{-1} separation, possibly indicating an electronic-vibronic pair. Such transitions pairs are indicated in the spectra of Figure 6.13.

The $^6H_{9/2}$ multiplet is composed of two Γ_8 and one Γ_6 states. For the fluorescence spectrum to this multiplet a very weak fluorescence peak is associated with the disallowed $\Gamma_7 \rightarrow \Gamma_6$ transition, in agreement with Wells. However, contrary to Wells, the transition at 15351 cm^{-1} is assigned as the vibronic associated with this Γ_6 terminating electronic state. The vibronic interval is 139 cm^{-1}. The next lowest energy fluorescence feature at 16525 cm^{-1} is assigned as an allowed electronic transition, as opposed to Wells who assigned this as a vibronic transition. The transition at 15157 cm^{-1} is also assigned as a vibronic of the $1 \rightarrow 1$ electronic transition, associated with phonons of frequency $\sim$330 cm^{-1}. Such a frequency is consistent with the resonance in the far-infrared properties of CaF_2 reported by Kaiser [53] and the optical phonon branch of CaF_2 [29]. The final electronic transition assigned for this multiplet is at 15130 cm^{-1}, which also

has an associated vibronic, offset by $140\,cm^{-1}$. One remaining transition is assigned to a combined vibronic of $1\rightarrow1$ $+140\,cm^{-1}+330\,cm^{-1}$. Such combinations of lattice and cubic center phonons have also been observed in the CaF_2:Pr^{3+} cubic centers [80].

In the fluorescence spectrum to the $^6H_{11/2}$ multiplet (Fig. 6.14), two narrow line-width peaks, and two much broader features, are observed. With the $^6H_{11/2}$ multiplet consisting of Γ_6, Γ_7 and two Γ_8 states, only three transitions are allowed. Wells has assigned the two sharp transitions as electronic, and the remaining broad features as vibronics. This requires assigning a phonon of $\sim220\,cm^{-1}$ to be associated with such centers in CaF_2, however this frequency does not correspond to any peaks in the phonon density of states for CaF_2, and such a vibronic interval is not observed in the same consistent manner as the $140\,cm^{-1}$ interval discussed here. The two sharp transitions are here assigned as an electronic/vibronic pair, as suggested by the $139\,cm^{-1}$ separation of these transitions. Likewise the two broader transitions are also assigned as an electronic-vibronic pair.

In the $^4G_{5/2} \rightarrow {}^6H_{13/2}$ fluorescence (Fig. 6.14), a total of four transitions are allowed ($2\Gamma_7 + 2\Gamma_8$) with one transition to the terminating Γ_6 state forbidden. Of the six transitions observed, Wells has assigned five as electronic, and one as vibronic. One of these previously assigned electronic transitions is here reassigned as a vibronic associated with a $140\,cm^{-1}$ phonon of the cubic center. This is an interesting example in that of the two observed transition at $12686\,cm^{-1}$ and $12664\,cm^{-1}$, the lower frequency transition has a considerably narrower lineshape. This is in contrast to what would be expected if both of these transitions were purely electronic, as this implies that the third level of $^6H_{13/2}$ has a narrower width than the second, lower energy, state. The situation becomes much clearer with the reassignment of the $12664\,cm^{-1}$ transition as a vibronic associated with the $1\rightarrow1$ transition, and this coincides with a phonon frequency of $140\,cm^{-1}$. This then leaves the forbidden $\Gamma_7\rightarrow\Gamma_6$ transition still to be observed.

The transition frequencies and assignments for the CaF_2:Sm^{3+} cubic center fluorescence just discussed are presented in Table 6.10. Wells has also detailed the near infrared fluorescence to three other manifolds. This fluorescence has not been re-investigated here as the transition frequencies tabulated by Wells do not display the same $140\,cm^{-1}$ pairing of the transitions which was apparent for much of the above fluorescence.

In summary, it is found that many features in the fluorescence spectra of the CaF_2:Sm^{3+} cubic center can be associated with vibronic transitions, and in particular with a phonon of frequency $140\,cm^{-1}$. This is consistent with the cubic center vibronics that have been observed in the other CaF_2:RE^{3+} systems. The very narrow line-widths of such vibronic transitions are also consistent with that observed in CaF_2:Dy^{3+} cubic

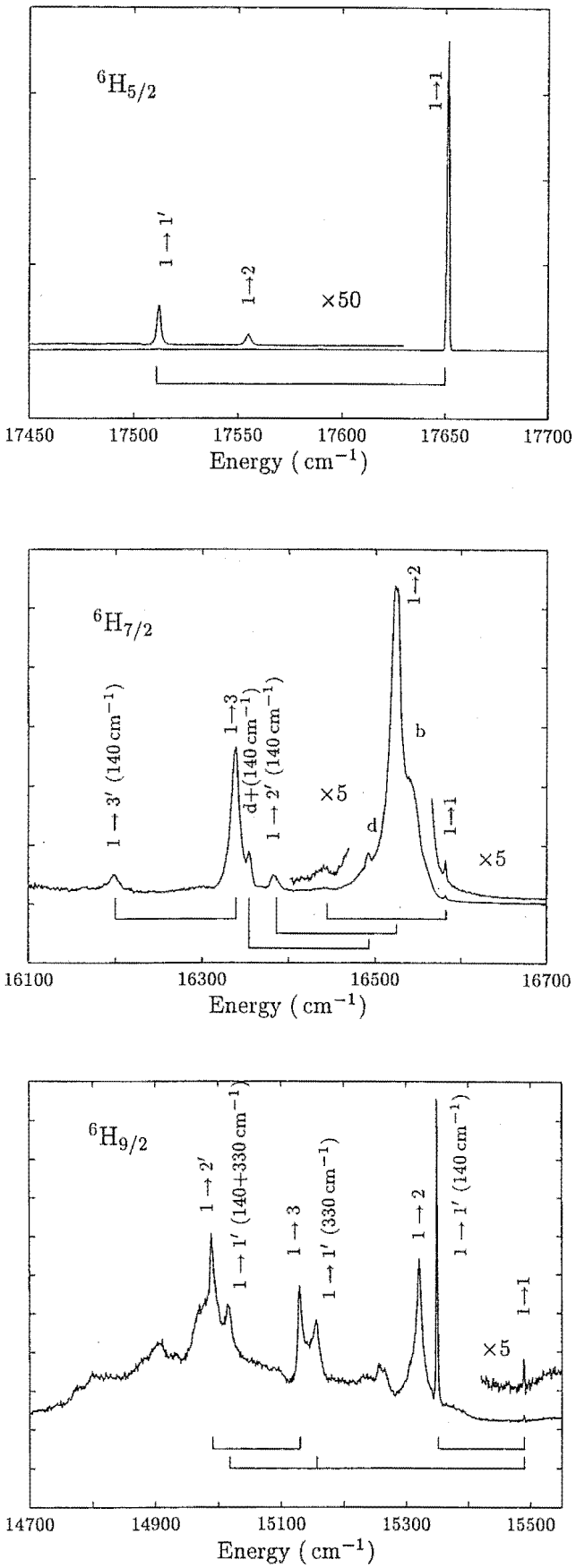

Figure 6.13: 15 K fluorescence spectra of the cubic center in CaF_2:Sm^{3+}. Excitation is into the $^4F_{3/2}$ multiplet, with emission originating from $^4G_{5/2}$. Vibronic transitions are indicated by the prime on the terminating state label.

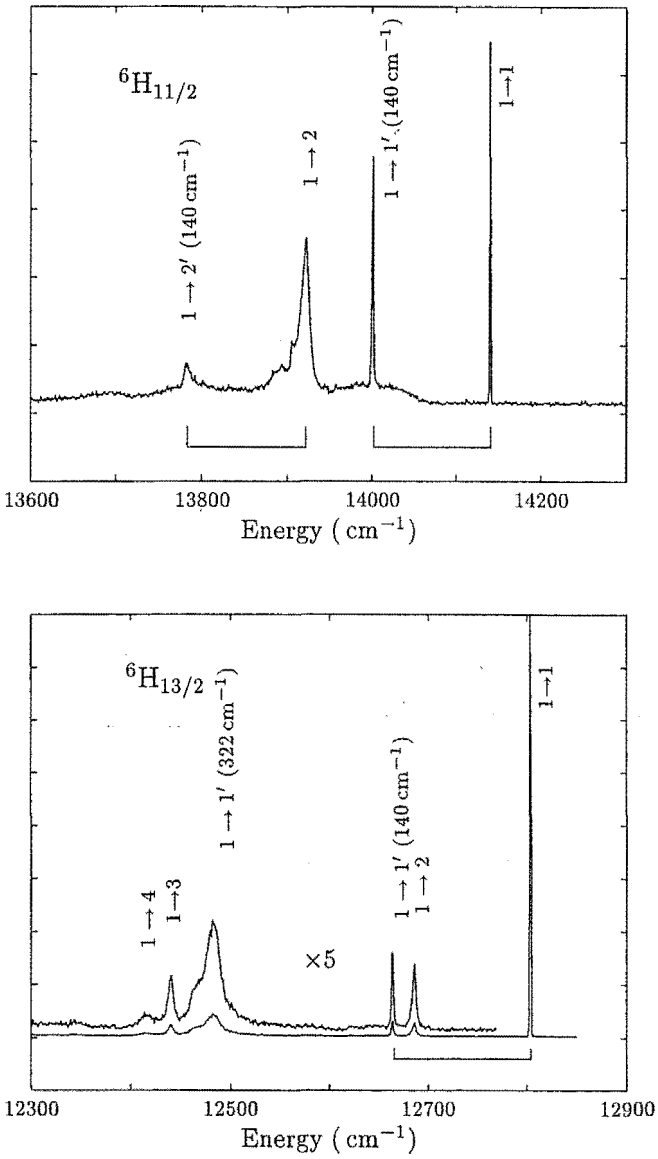

Figure 6.14: 15 K fluorescence spectra of the cubic center in CaF_2:Sm^{3+}. Excitation is into the $^4F_{3/2}$ multiplet, with emission originating from $^4G_{5/2}$. Vibronic transitions are indicated by the prime on the terminating state label.

Multiplet	Transition	Frequency (cm^{-1})	offset (cm^{-1})
	1→1	17653	
$^6H_{5/2}$	1→2	17557	
	1→1 + v_1	17514	139
	1→1	16583	
$^6H_{7/2}$	b	16542	
	1→2	16525	
	d	16493	
	1→2 + v_1	16383	142
	d + v_1	16355	138
	1→3	16339	
	1→3 + v_1	16199	140
	1→1	15490	
$^6H_{9/2}$	1→1 + v_1	15351	139
	1→2	15322	
	1→1 + v_2	15157	333
	1→3	15130	
	1→1 + v_1 +v_2	15017	139 + 334
	1→3 + v_1	14990	140
	1→1	14141	
$^6H_{11/2}$	1→+v_1	14002	139
	1→2	13922	
	1→2 + v_1	13783	139
	1→1	12804	
$^6H_{13/2}$	1→2	12686	
	1→1 + v_1	12664	140
	1→1 + v_2	12482	322
	1→3	12440	
	1→4	12416	

Table 6.10: Transition frequencies and assignments for the cubic center fluorescence in CaF_2:Sm^{3+} presented in Figures 6.13, 6.14. Fluorescence originates from the $^4G_{5/2}$ multiplet. Frequencies are in vacuum cm^{-1}, with an uncertainty of $\pm 1\,cm^{-1}$.

centers.

6.8 Resonance modes

When a substitutional defect is placed in an otherwise ideal crystal the phonon density of states and the nature of the atomic displacements will be changed. In general the normal modes of the ideal lattice will be perturbed in frequency and in some cases a quite distinct new mode, or modes, will be created which may exist outside the continuum of lattice modes. For the case of a light ion substitutional defect, a distinct mode from the continuum will be separated and moved to a higher energy than the cutoff for propagation in the lattice. H^- ions substituting for F^- ions in CaF_2 provide a good example of this behaviour, with new modes appearing at $\approx$1000 cm^{-1} [32], well above the cutoff frequency of $\approx$450 cm^{-1} for CaF_2. Because these modes are unable to propagate through the lattice they are termed local modes. For a heavy mass defect, such as RE ions ($M_u \approx$ 160-170) substituting for Ca (M_u = 40), local modes above the cutoff frequency are not produced. However, modes within the propagation bands may have a considerably changed character in the motion of the ions. Under certain conditions a pseudo-localised mode may result, in which the amplitude of the atomic displacements is enhanced in the region near the defect. Such modes, first suggested by Brout and Visscher in 1962 [9], are known as resonant modes. In general, the resonant mode frequency will decrease as the mass of the defect increases [7].

The vibronics of CaF_2:Dy^{3+} and CaF_2:Sm^{3+}, and also those that have been observed for other rare-earth cubic centers (Table 6.9), show a decreasing vibronic offset with increasing lanthanide mass. In addition, the vibronic transitions occur with an offset from the electronic parent transitions that cannot be described by the CaF_2 lattice modes. This leads to the assignment of the $\approx$140 cm^{-1} vibronic offset observed in the CaF_2:RE^{3+} cubic center to be due to resonant modes induced by the rare-earth impurity.

A considerable amount of literature exists regarding resonant modes of point defects [7, 67, and references therein], including some discussion of the RE^{3+} impurities in CaF_2 [82, 40, 39, 15]. The majority of the CaF_2:RE^{3+} investigations have focused on the far infrared absorption properties, with attempts to describe the absorption from Greens function calculations for impurity induced resonant modes.

In one of the earlier papers dealing with resonant modes of rare-earth defects in CaF_2, Hayes, Wiltshire, Berman and Hudson [39] have measured the far infrared absorption of CaF_2:RE^{3+}, for which the results and discussion of CaF_2:Tm^{3+} are relevant

here. For this system a broad absorption at $\approx 90\,cm^{-1}$ was observed. A theoretical absorption spectrum was also calculated based on the Green function formalism. They found that as well as the mass change ($^{40}Ca^{2+} \rightarrow {}^{169}Tm^{3+}$) a 5% reduction in nearest neighbour force constants was required to account for the frequency of this absorption. Catlow, Hayes and Wiltshire [15] have reevaluated the CaF_2:Tm^{3+} calculations of Hayes et.al. [39] with the inclusion of changes in both the nearest-neighbour (NN) and next-nearest-neighbour (NNN) force constants. For the $Ca^{2+} \rightarrow Tm^{3+}$ substitution they calculated that the NN force constants increase by 100% and that the NNN force constants decrease by 130% .

All the literature that has addressed the resonance modes in CaF_2:RE^{3+} has assumed that the cubic center gives rise to a resonant mode at $\approx 90\,cm^{-1}$. However, in light of the work here that has shown a clear association of the $\approx 140\,cm^{-1}$ vibronics with the cubic center this would appear to be an incorrect assumption. Therefore the calculation of the resonance modes needs to be re-addressed. In calculations that have been performed here, and presented in Appendix B, it has been shown that the change in mass for Dy^{3+} replacing Ca^{2+} leads to a predicted resonant mode at $96\,cm^{-1}$. To obtain a higher frequency mode in agreement with experiment would require an increase in the repulsive force constants associated with the nearest-neighbour rare-earth–fluorine interactions. Such an increase in force constants can be loosely justified from consideration of the increase in charge at the calcium ion site caused by the substitution of Ca^{2+} with RE^{3+}, with an increase in the repulsive force constants counteracting the increased attractive forces between the rare-earth and the surrounding fluorine ions. Such considerations of the excess charge at the rare-earth site have not been addressed by Hayes et.al. [39], who apply a model involving the rare-earth surrounded by a cube of fluorine ions.

In Appendix B it is noted that inclusion of long-range effects of the charged impurity would appear to diminish the applicability, or at least the utility, of the Greens function approach, as it can then no longer be assumed that the defect subspace involves just a small number of ions. It is perhaps also worth noting that the absorption coefficient expression utilised by Hayes et.al. [39] and Catlow et.al. [15] is based on a derivation due to Klien [59] which explicitly makes the assumption that the defect ion is of the same charge as that which it is replacing.

6.9 Summary

The preferential clustering behaviour of Dy^{3+} in CaF_2 has been investigated for moderate dopant concentrations of $RE^{3+} \leq 0.15\%$. Due to efficient non-radiative cross-relaxation of the Dy^{3+} $^4F_{9/2}$ excitation in centers with closely coupled Dy^{3+} ions, this

investigation has turned to the use of double doped CaF_2:Dy^{3+}:RE^{3+} systems.

For CaF_2:0.05%Dy^{3+}:0.04%Eu^{3+} samples only one dominant cluster center has been observed. The presence of a europium ion in this cluster inhibits any non-radiative cross-relaxation of the excited dysprosium $^4F_{9/2}$ multiplet, rendering this center observable through fluorescence detected absorption. It has been shown that this center undergoes efficient energy transfer from the excited states of Dy^{3+} at $\approx$21000 cm^{-1} to the excited states of Eu^{3+}. The observed emission, after Dy^{3+} excitation, is almost exclusively attributed to Eu^{3+} fluorescence from the $^5D_0$ multiplet at $\approx$17000 cm^{-1}. The spectroscopy of this europium emission has revealed the Dy^{3+}–Eu^{3+} cluster center to be closely related to an asymmetric dimer, labelled as the R-center, that has been previously reported for CaF_2:Eu^{3+}. It is therefore concluded that in double doped CaF_2:Dy^{3+}:Eu^{3+} a heterogeneous version of the R-center is present at the quite low concentrations of total rare-earth content $\approx$0.1%.

For the double doped system of CaF_2:0.05%Dy^{3+}:0.1%Gd^{3+} the presence of a Gd^{3+} ion in a Dy^{3+}:Gd^{3+} cluster eliminates the possibility of non-radiative cross-relaxation of the excited Dy^{3+} ion, and enables the cluster center to be observed in laser excitation of the Dy^{3+} $^4F_{9/2}$ multiplet. The similarity of the excitation spectra of the Dy^{3+}:Eu^{3+} and Dy^{3+}:Gd^{3+} samples leads to the conclusion that the R-center dimer is also present for the Gd^{3+} co-dopant. Unlike the case with europium, with gadolinium possessing no excited states below $\approx$32000 cm^{-1} energy transfer between the two rare-earth ions is also eliminated. This has enabled the Dy^{3+} fluorescence of the heterogeneous Dy^{3+}:Gd^{3+} R-center to be observed.

From the fluorescence data of the Dy^{3+}:Gd^{3+} R-center a number of energy levels of the low lying multiplets have been inferred. Observation of absorption transitions to these infrared levels, and comparison with the corresponding absorption in singly doped Dy^{3+} samples, suggests that the asymmetry between the two rare-earth sites of this dimer is a quite small perturbation on the overall crystal-field states. The comparison of the infrared and optical absorption for CaF_2:Dy^{3+}:RE^{3+} and CaF_2:Dy^{3+} samples leads to the conclusion that the R-center is present in the Dy^{3+}–only doped system, despite being unobservable through laser excitation.

The CaF_2:0.05%Dy^{3+}:0.05%Tb^{3+} system has been briefly considered, with the intention of forming a link across the lanthanide series from CaF_2:Dy^{3+}:Eu^{3+} through to the Dy^{3+}–only doped samples. The excitation spectrum of CaF_2:Dy^{3+}:Tb^{3+} is indicative of the presence of an R-center. However there are also quite clear indications of the onset of more complex cluster formation. Efficient energy transfer from Dy^{3+} to Tb^{3+} is also observed, and the resulting Tb^{3+} emission is quite complex. Due to the complexities apparent for the Dy^{3+}:Tb^{3+} clustering, and the scarcity of published data on Tb^{3+}

cluster centers, a more in-depth investigation of this system has not been undertaken here.

The CaF_2:Dy^{3+} cubic center has also been characterised. The formation of cubic centers concurrently with the cluster centers is consistent with the now well established concept of interstitial scavenging by the cluster centers. From the spectroscopy of the Dy^{3+} cubic center an energy level scheme including 24 states from six manifolds has been determined. A crystal-field calculation utilising this information has been performed, and reasonable agreement between experiment and theory obtained. A recurring feature of the cubic center fluorescence is the presence of narrow and intense vibronic transitions, with a vibronic interval of $138\,cm^{-1}$. Recent investigations in this department have shown these vibronics to be a common feature for cubic RE^{3+} centers in the CaF_2 host. The recognition of very sharp vibronic transitions in the region of 130–$145\,cm^{-1}$ has lead to a re-investigation of previous work on the cubic centers in CaF_2:Sm^{3+}. The presence of a $140\,cm^{-1}$ vibronic interval in the Sm^{3+} cubic center fluorescence is established, and this has lead to a number of reassignments of the previously reported fluorescence for this center.

Vibronics with frequency offset of $\approx 140\,cm^{-1}$ cannot be explained in terms of the CaF_2 lattice modes. Together with the observation of a decreasing vibronic offset with increasing rare-earth mass, this leads to the conclusion that these vibronics are associated with a resonant mode induced by the rare-earth ion.

Chapter 7

Interstitial reorientation and optical depolarisation.

7.1 Introduction

In fluorite-type crystals doped with trivalent rare-earth ions, a multitude of different centers can be formed and a considerable body of work concerning the nature of defect formation in the fluorites is represented in the literature [98, 97, 70, 18, 22, 14]. An integral part of any attempt to understand the defect formation process is the nature of the barriers to ionic motion. Techniques such as Ionic Thermal Current (ITC), (sometimes referred to as Thermally Stimulated Depolarisation, TSD), dielectric loss, and EPR line-broadening have all been applied to this problem [57, 56, 27, 24, 68].

This chapter discusses investigations into the properties of ionic motion associated with particular centers in CaF_2:RE^{3+} and SrF_2:RE^{3+}, namely the fluorine compensated C_{4v} centers. The dipoles associated with fluorine compensated C_{4v} centers are randomly oriented in any of the six structurally equivalent directions with the interstitial fluorine situated along any one of the $\langle 100 \rangle$ axes. At temperatures around room temperature the dipoles undergo rapid reorientation, with the interstitial fluorine ions moving between differently oriented interstitial positions. Such reorientation occurs on sub-microsecond time scales at temperatures of 300 K [100].

In ITC experiments an electric field is applied to the sample at these elevated temperatures, creating an excess of dipoles oriented along the field. This applied field is maintained while the sample is cooled sufficiently to freeze in this non-equilibrium distribution of dipole orientations. The field is then removed and the sample slowly heated while monitoring the current across the sample. At the temperature at which the dipoles become mobile, the distribution returns to equilibrium, with an associated current produced by the dipole motion. In dielectric relaxation, the dielectric constant is measured as a function of frequency, for a series of temperatures. The dielectric constant is dependent on the mobility of dipoles at the applied frequency, and hence on the temperature. From such measurements the dipole mobility can therefore be determined.

While both of these techniques determine the barrier energy for dipole reorientation they suffer from being a measurement on the bulk sample, and hence are not site-selective. Correlations to specific centers have generally been made through concentration dependence studies and by comparison with EPR line-broadening work.

The work discussed here involves measurements of the optical polarisation of specific RE^{3+}–F^- C_{4v} transitions, as a function of temperature. The use of tuned laser excitation enables the height of the energy barrier for dipole reorientation to be determined in a site-selective manner, removing much of the ambiguity associated with assigning the barrier to a particular process. The technique of optical depolarisation only measures ionic reorientation that occurs within the fluorescence lifetime of the emitting state, and is therefore not dependent on the thermal history of the sample. Similar optical depolarisation measurements have previously been performed by Voron'ko et.al. [100]. This work extends their results, and obtains some barrier energies that are in disagreement with their results. However, the results presented here are in general agreement with earlier ITC, dielectric loss, and EPR line-broadening work.

An additional effect in the temperature dependence of the polarisation behaviour, which occurs in Pr^{3+} centers but not in Eu^{3+} centers, has also been observed. While this effect makes its appearance as an apparent extra reorientation mechanism, it is interpreted to be a consequence of energy transfer between C_{4v} centers. This is of interest in its own right as a method of determining properties of resonant energy migration, the observation of which is generally hampered by the need to spectroscopically distinguish between donor and acceptor ions.

7.2 Theory of Optical Depolarisation

The fluorine compensated RE^{3+} C_{4v} center has an interstitial fluorine residing in any one of six structurally equivalent nearest neighbour positions, thereby defining a tetragonal axis along any of the six ⟨100⟩ directions. The six orientations will form three inequivalent pairs of centers when interaction with polarized laser light is considered. Electric and magnetic dipole transitions will excite only centers with an axis belonging to a subset of these three inequivalent orientations. Similarly, fluorescence transitions will only be observed for a distinct (different) subset of C_{4v} centers. This leads to polarised fluorescence as the number of centers that can contribute to the observed emission is a function of the orientation of the centers (c.f. Section 3.6, page 25).

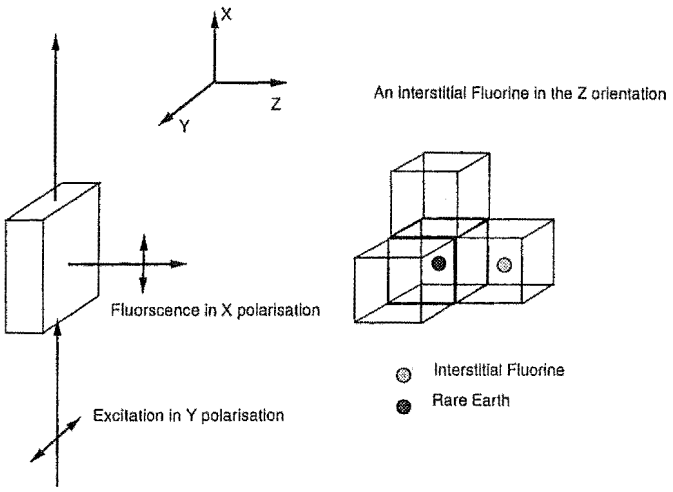

Figure 7.1: orientation of excitation/fluorescence and of interstitials.

In Figure 7.1 the co-ordinate system that will be referred to in the following discussions is presented. For all experiments discussed here the propagation direction of the laser is taken to define the x-axis, while fluorescence is monitored in an orthogonal direction which likewise defines the z-axis. Samples are oriented in such a manner that the crystallographic $\langle 100 \rangle$, $\langle 010 \rangle$ and $\langle 001 \rangle$ directions are parallel to the x,y,z axes so defined. Recalling Section 3.6, a particular combination of excitation and fluorescence polarisations will be signified by two letters, for example YX. The first letter signifies the polarisation of the laser, while the second letter indicates the monitored fluorescence polarisation.

A specific example will be used to highlight the principles involved in the optical depolarisation experiments. Selective excitation of a σ-polarised electric dipole transition allows two of the three center orientations to be placed in an excited state. For a π-polarised fluorescence transition, monitoring the fluorescence of these sites in an appropriate orthogonal direction, will result in observed fluorescence from only one of the excited orientations, and hence in only one polarisation. At temperatures of approximately 200 K or greater the interstitial ion, which defines the principal axis of the C_{4v} center, may undergo reorientation in the interval between absorption and emission of a photon. That is, the ion may follow the path of *excitation, reorientation, then fluorescence.* This leads to a removal of the fluorescence polarisation. Therefore, observing the temperature dependence of the polarised fluorescence enables movement of the interstitial ions to be detected in a simple and direct manner. An example of the temperature dependent polarised spectra is given in Figure 7.2.

A rate equation model describing the absorption, emission and reorientation processes enables the expected optical depolarisation effects to be quantified, and the barrier energies associated with dipole reorientation to be determined. For the specific example of a σ-polarised absorption transition excited with a CW laser polarised in the Y direction, the differential equations that govern the dynamics of the excited interstitial ions can be written as

$$\begin{aligned}
\frac{dN_x}{dt} &= -(W+1/\tau)N_x + \frac{W}{2}N_y + \frac{W}{2}N_z + \sigma_{ed} \\
\frac{dN_y}{dt} &= \frac{W}{2}N_x - (W+1/\tau)N_y + \frac{W}{2}N_z \\
\frac{dN_z}{dt} &= \frac{W}{2}N_x + \frac{W}{2}N_y - (W+1/\tau)N_z + \sigma_{ed}
\end{aligned} \tag{7.1}$$

where N_x is the excited state population of the centers with an orientation defined by an x oriented interstitial, and similarly for N_y and N_z. The source term, σ_{ed}, represents the absorption by two of the three C_{4v} center orientations, W is the probability of interstitial movement past the effective barrier, and τ is the lifetime of the excited state which may itself be temperature dependent. Although any depletion of the ground state would have an effect on absolute intensities, the relative intensities involved in the optical depolarisation measurements will be independent of such considerations. Depletion of the ground state can therefore be neglected.

The polarisation anisotropy is defined in terms of the observed intensity of emission in two different polarisation configurations:

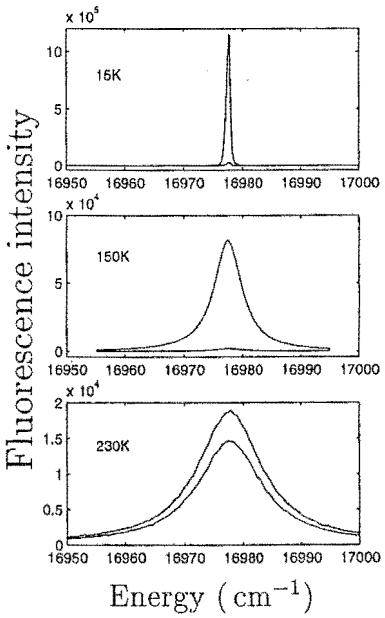

Figure 7.2: An example of the polarised fluorescence observed in SrF_2 :Eu^{3+} at 15 K, 150 K and 230 K. In each figure the most intense spectrum is that for YY polarisation, with the weaker spectrum that of YX polarisation.

$$P = \frac{|I_{yx} - I_{yy}|}{I_{yx} + I_{yy}}. \tag{7.2}$$

The steady state solution to the rate equations 7.1, along with the identification of fluorescent intensity with the excited state population of the differently oriented centers, gives rise to a polarisation anisotropy of

$$P_{\sigma\pi}(T) = \frac{1/\tau}{2W + 1/\tau} \tag{7.3}$$

where the subscript refers to σ-polarised absorption and π-polarised fluorescence.

By a similar analysis, for different excitation and fluorescence transition moments it is found that $P_{\sigma\pi}(T) = P_{\pi\sigma}(T) = P_{\pi\sigma'}(T)$ and that

$$P_{\sigma\sigma}(T) = \frac{1/\tau}{4W + 3/\tau} \tag{7.4}$$

$$P_{\pi\pi}(T) = \frac{1/\tau}{W + 1/\tau} \tag{7.5}$$

Worthy of note is that so far no assumptions have been made as to the nature of the reorientation mechanism, except that the reorientation rate is taken to be independent of the population of ions. This merely states that the dipole reorientation is not a co-operative phenomenon.

Initially it will be assumed that the Arrhenius equation is appropriate to describe the interstitial reorientation rate. Hence the reorientation rate is given by $W = \nu_a \exp(-E/k_B T)$, where E is the barrier energy and ν_a will be referred to as the attempt frequency.

7.3 Experiment and Analysis.

Samples were oriented in their {100} planes, and cooled by a CTI Cryogenics closed cycle helium refrigerator. Temperature control was provided by a heating unit attached to the cold head. The excitation wavevector and polarization were respectively in the [100] and [010] directions. Fluorescence was monitored in the mutually perpendicular [001] direction.

The requirement of well defined polarisation effectively limits the experiments to consideration of non-Kramers ions. At low temperatures the Kramers ions display polarisation ratios of either YX:YY=2:1 or a ratio that is dependent on specific transition moments rather then purely on the geometry of the situation. This is covered in more depth in the earlier chapters on the spectroscopy of Dy^{3+}. In contrast, non-Kramers ions can (theoretically) display polarisation ratios of YX:YY=1:0 or 2:1, for electric dipole processes. In practice, ratios of the order of 30:1 can be obtained for transitions between appropriate states. This results in much more favourable signal to noise characteristics when considering the temperature dependent variation of polarisation ratios of 30:1→ 1:1 compared to the range of 2:1→ 1:1 that may be obtained for Kramers ions.

The chosen transitions are further required to have a sufficient intensity at temperatures up to approximately 250 K, and to be reasonably well isolated spectrally in order to limit the complications arising from overlap of transitions that occurs with the thermal broadening of energy levels.

Pr^{3+} and Eu^{3+} fluorine compensated tetragonal centers in CaF_2 and SrF_2 possess transitions that satisfy the above requirements. Experiments were therefore carried out on all four C_{4v} centers of these systems to determine the characteristics of dipole reorientation in the C_{4v} centers.

Spectra over the relevant transitions were recorded at temperatures from 15 K to 260 K, and in the case of the Pr^{3+} data, line shapes were fitted to these spectra to remove any effects due to broadening of nearby fluorescence transitions. Due to the spectral isolation of the Eu^{3+} transitions, line fitting was not required. The temperature dependent polarisation anisotropy was determined in accordance with the definition of equation 7.2. A weighted least-squares fitting between the experimental and theoretical polarisation anisotropy was performed to obtain the interstitial reorientation barrier energies.

The imperfect polarisation anisotropy obtained at low temperatures leads to an added complication in the least-squares fitting procedure. Two causes for the imperfect polarisation anisotropy were investigated, and have been catered for in the theory and experimental analysis.

The first mechanism considered is that of the imperfect physical orientation of the crystals, and the subsequent degradation of the measured polarisation anisotropy. With careful alignment, ratios of the order of 30:1 could be obtained for the transitions considered here, which corresponds to a polarisation anisotropy of $P = 0.94$. The imperfect ratios cause the experimental polarisation anisotropy to be inconsistent with the low temperature theoretical value of unity. To remove this inconsistency an additional variable was introduced to the function that was being fitted to the data, namely a scaling factor. That is, $P_{\sigma\pi} \rightarrow \alpha P_{\sigma\pi}$, where α is the new variable with a value close to unity. This apparently *ad hoc* approach is justified by a solution to the appropriate differential equations that have been altered to include some misalignment in the crystal. If it is assumed that the crystal is misaligned so that the excitation beam is not perfectly parallel to the [100] direction then it is found that the scaling factor is a trigonometric function of the misalignment angles. This result for misalignment of the pump beam will also hold for the misalignment of the collected fluorescence. This is easiest seen by considering the symmetry of the system associated with interchange of the pump and fluorescent beams. With misalignment of the collected emission leading only to a scaling factor in the polarisation anisotropy, it can also be deduced that the same effect will be introduced by the collection of fluorescence from a finite solid angle. The total of this solid angle consists of contributions of slightly "misaligned" fluorescence paths. The integral of the misalignment factor over the solid angle will again be ≈ 1, as the integrand is itself always ≈ 1. Hence the simple scaling factor introduced above also serves to account for the finite solid angle of the collection optics.

There remains a second possible mechanism for degrading the polarisation anisotropy, namely that the assumption of purely electric-dipole transitions (or pure magnetic-dipole) is invalid. Therefore the inclusion of a small magnetic dipole transition mo-

ment in the excitation transition has been considered. For at least one of the chosen excitation pathways in Pr^{3+} , which involves a $\Gamma_5 \rightarrow \Gamma_1$ transition, both electric dipole and magnetic dipole processes are allowed in σ- or σ'-polarisation. With the inclusion of a magnetic dipole σ'-polarised absorption cross-section in the rate equations a functionally equivalent polarisability is obtained, but with the addition of the above mentioned scaling parameter. From the steady state solution of the rate equations, the polarisation anisotropy is found to be

$$P_{(\sigma\sigma')\pi}(T) = \alpha \frac{1/\tau}{2W + 1/\tau}, \quad \text{where} \quad \alpha = \frac{\sigma/\sigma' - 1}{\sigma/\sigma' + 1}. \tag{7.6}$$

In the definition of the scaling parameter, σ/σ' is taken to signify the ratio of the electric dipole and magnetic dipole transition moments. To include the magnetic dipole absorption explicitly in the analysis would require an accurate knowledge of the relative intensities of electric and magnetic dipole transition moments. As this ratio is not known, these effects are subsumed into the fitted scaling parameter.

To recap, a scaling parameter has been included in the analysis of the polarisation anisotropy in order to account for the imperfect polarisation properties at low temperature. This scaling factor can be justified in two ways. First, as a consequence of mis-oriented crystals and the finite solid angle of the fluorescence collection optics, and second from the inclusion of both electric and magnetic dipole absorption processes.

Parameter fitting

Parameter values have been obtained from a least-squares fitting of the polarisation anisotropy data to the appropriate theoretical functions expressed in equations 7.3–7.5. An Arrhenius reorientation rate was initially assumed. The scaling factor discussed in the preceding section was included as a parameter to be determined from the least-squares fitting. What becomes apparent in such a procedure is that the attempt frequency ν_a of the Arrhenius rate is not well determined by the data when included as a parameter. This problem is not readily overcome as the uncertainties associated with the frequency factor are essentially intrinsic to the functional form of the Arrhenius equation, as is discussed in reference [20]. The badly determined parameters are also associated with a high degree of correlation between the attempt frequency and the barrier energy that will be determined from the fitting. The converse side to this issue is that the hopping probability $W = \nu_a \exp(-E/k_B T)$, and hence the polarisation anisotropy, is less sensitive to the frequency factor than to the barrier energy. This relative insensitivity of the polarisation anisotropy to the attempt frequency allows some leeway in applying the assumption that lattice phonons are essentially what drives the attempt frequency and the interstitial reorientation process, and setting the

frequency factor to a fixed value. The correlation between parameters and the relative sensitivity of the polarisation anisotropy to these parameters will be discussed more fully in the context of uncertainties in the parameters. To avoid presupposing the experimental results such a discussion is postponed until Section 7.5 (page 223).

Through consideration of the phonon density of states of CaF_2 and SrF_2 [29][28], the attempt frequency has been set at $\nu_a = 10^{13}\,s^{-1} \approx 330\ cm^{-1}$. This assumed frequency is within the bounds of the various values reported for ITC measurements [57]. A further *a-posteri* justification of this assumption is also able to be obtained from the measurements on SrF_2:Pr^{3+}, and will be discussed in the context of those measurements. With the frequency factor held at this fixed value, the fitting procedure includes two free parameters, the barrier energy and the scaling factor. It is found that with the frequency factor held at the above value, the barrier energy can be consistently determined by the least squares fitting procedure when applied to different data sets.

It has also been found that for the Pr^{3+} C_{4v} centers a hopping probability involving two effective Arrhenius barriers is required to adequately describe the data. In such cases four parameters have been included in the fitting routines, the two barrier energies, one frequency factor and the scaling parameter. It was found that constraining only one frequency factor was sufficient to provide consistent parameter fits to different data sets.

7.4 Results

7.4.1 Lifetimes

To analyse the polarisation anisotropy in terms of the energy barriers for interstitial reorientation the excited state lifetime, τ, is required. This lifetime will in general be temperature dependent. The fluorescent lifetime enters in an intuitively obvious way, as the longer the lifetime, the more time is available in which an excited C_{4v} center may reorient before emission of fluorescence.

Before discussing the depolarisation experiments, the lifetimes of the states used in the subsequent experimental analysis will be addressed. The lifetimes of interest are those for $^5D_0$ of CaF_2:Eu^{3+} and SrF_2:Eu^{3+}, $^1D_2$ of CaF_2:Pr^{3+} and SrF_2:Pr^{3+}, and $^3P_0$ of SrF_2:Pr^{3+}.

$^5D_0$ multiplet of CaF_2:Eu^{3+} and SrF_2:Eu^{3+}

For Eu^{3+} the $^5D_0$ multiplet is positioned at $\approx$17000 cm^{-1} and is separated by a large energy gap of $\approx$12000 cm^{-1} to the next lowest multiplet of $^7F_6$. Such a large spacing below the emitting multiplet, coupled with the reasonably low phonon cutoff energies in both hosts (480 cm^{-1} in CaF_2 and 400 cm^{-1} in SrF_2) leads to the expectation of temperature independent lifetimes for this multiplet. Wells and Reeves [104] have measured the lifetime of $^5D_0$ as a function of temperature for both hosts considered here and have found that the lifetimes of 11.8 ms for CaF_2 and 13.4 ms for SrF_2 are indeed independent of temperature between 15 K and 300 K.

$^1D_2$ multiplet of CaF_2:Pr^{3+} and SrF_2:Pr^{3+}

The low temperature lifetimes of the $^1D_2$ multiplet in the CaF_2 and SrF_2 C_{4v} centers have been reported by Reeves, Jones and Syme [87], but the temperature dependence is not present in the literature and has been measured here from 15 K to 250 K.

For determining the fluorescence decay times of the CaF_2:Pr^{3+} C_{4v} center the $Z_1 \rightarrow D_1$ transition at 16828 cm^{-1} was excited, and the $D_1 \rightarrow Y_2$ fluorescence transition at 14617 cm^{-1} was monitored. For the same center in SrF_2:Pr^{3+} the excitation transition was $Z_1 \rightarrow D_2$ at 16872 cm^{-1} and the monitored emission was the $D_2 \rightarrow Y_2$ transition at 14652 cm^{-1}. The experimental procedure for determining the lifetimes was discussed in Section 3.7 (page 30). For these measurements a specific transition was monitored, rather than the fluorescence within a broad bandwidth, ensuring that the determined lifetimes are appropriate for the C_{4v} centers. This eliminates possible artifacts due to energy transfer from the C_{4v} centers to other centers present in the samples.

The temperature dependence of the $^1D_2$ lifetimes of the C_{4v} centers in CaF_2 and SrF_2 are presented in Figure 7.3, along with examples of the observed fluorescence transients. For CaF_2 the low temperature lifetime was determined to be 500 μs, which compares with the values of 420 μs reported by Reeves et.al. [87], and 510 μs found by Murdoch [73].

The temperature dependence of this lifetime is unexpected, in that it increases with temperature, with a value of 870 μs measured at a temperature of 220 K. While a satisfactory explanation for this anomalous temperature dependence has not been found, it is noted that processes such as (non-resonant) energy transfer and radiation trapping could possibly lead to such a lengthening of the lifetime [47][46].

For SrF_2 the 15 K lifetime of the $^1D_2$ multiplet was measured to be 1.7 ms, which compares to the values of 2.0 ms measured by Reeves [87] and 1.3 ms reported by

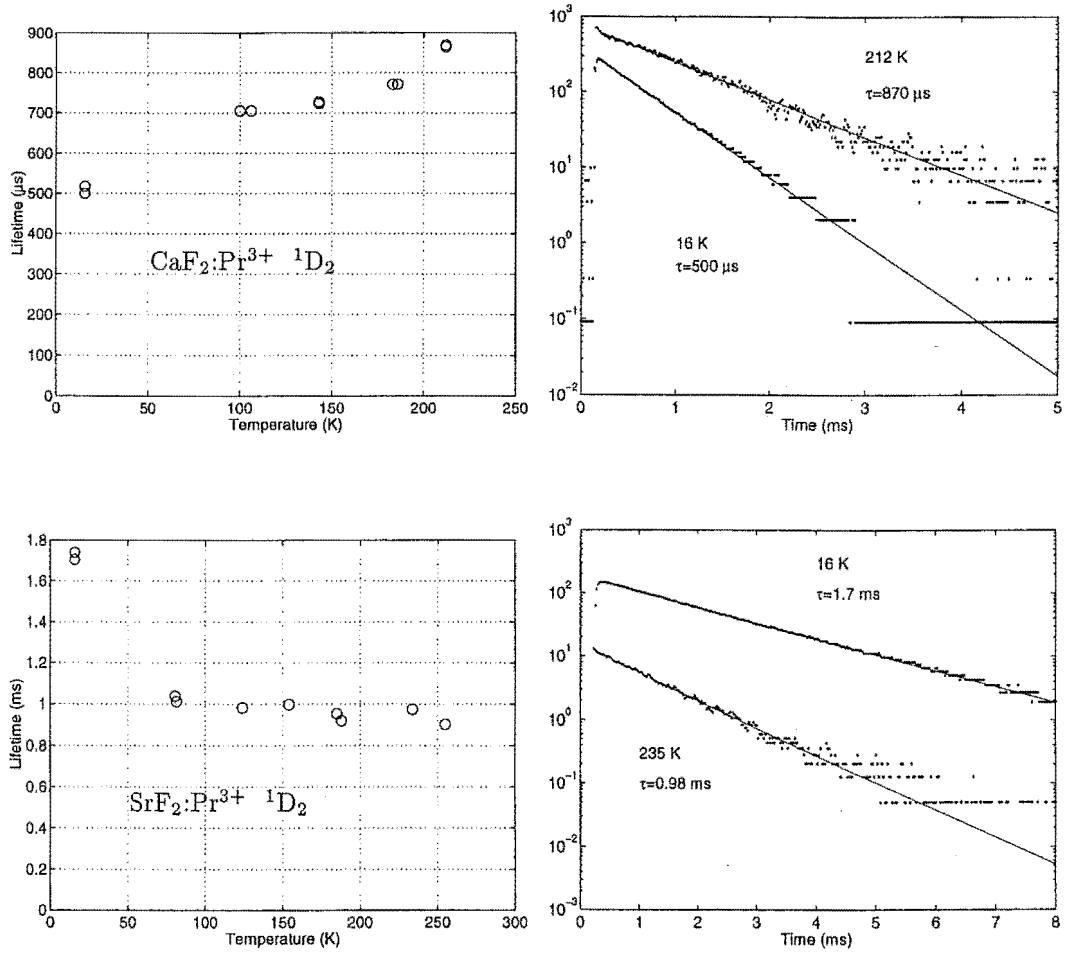

Figure 7.3: $^1D_2$ lifetimes of the C_{4v} centers in (Top) CaF_2, and (Bottom) SrF_2. The intensities of the displayed transients have been scaled to enable clear presentation.

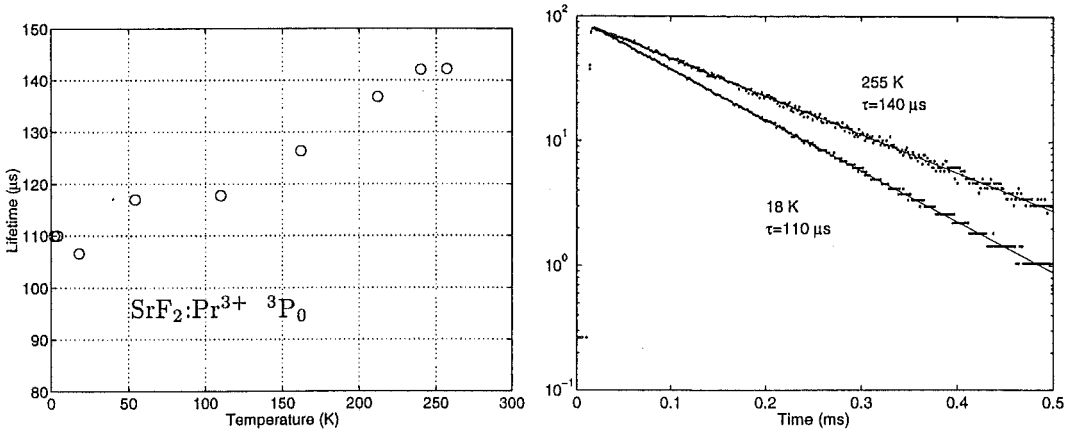

Figure 7.4: The temperature dependence of the $^3P_0$ lifetime for the C_{4v} F^- center in SrF_2.

Murdoch [73]. As discussed by Murdoch, various cross-relaxation and upconversion processes involving $^1D_2$ may impact on the measured fluorescence transients, and therefore explain the apparent disparity in the reported lifetimes for this center. Such processes would be expected to depend on the rare-earth dopant concentration and sample preparation and history, as the annealing and growth conditions can affect the relative defect concentrations in the crystal. The SrF_2 $^1D_2$ lifetime is observed to decrease with increasing with temperature, as would normally be expected. The lifetime decreases to a value of approximately 1.0 ms and maintains this value throughout the temperature region of 100 K to 250 K.

$^3P_0$ multiplet of SrF_2:Pr^{3+}

While the low temperature lifetime of the $^3P_0$ can be obtained from the literature [87], the temperature dependence has not been reported and was therefore measured here, in the same manner as described above.

The fluorescence monitored for the lifetime measurements was the intense $^3P_0 \rightarrow W_3$ transition at 15672 cm^{-1}, while excitation was provided by the pulsed dye laser into the single level of $^3P_0$ at 20986 cm^{-1}. The measured lifetimes are presented in Figure 7.4 along with representative transients. At all temperatures the fluorescence decay was able to be described by a single exponential, however an anomalous temperature dependence, with the lifetime increasing with temperature, is again observed.

7.4.2 Optical depolarisation of CaF_2 :Eu^{3+} and SrF_2:Eu^{3+} .

The spectroscopy of the dominant fluorine compensated C_{4v} center in CaF_2:Eu^{3+} and SrF_2:Eu^{3+} has been reported by Hamers et.al. [37] and Jouart et.al. [50] respectively, and extended by Wells [103]. For depolarisation measurements on the C_{4v} :F^- Eu^{3+} centers in both CaF_2 and SrF_2 , the chosen excitation transitions were $^7F_0(\Gamma_1) \rightarrow {}^5D_0(\Gamma_1)$ at 17283 cm^{-1} and 17293 cm^{-1} respectively. As this excitation transition is between states transforming as Γ_1 irreps of the C_{4v} point group only the π-polarised electric-dipole transition moments will be non-zero. The monitored fluorescence transition was also the same in both hosts, namely $^5D_0(\Gamma_1) \rightarrow {}^7F_1(Y_1\Gamma_5)$, at frequencies of 16975 cm^{-1} in CaF_2 and 16969 cm^{-1} in SrF_2. As the fluorescence transition is between states transforming as the Γ_1 and Γ_5 irreps, both electric-dipole and magnetic dipole processes are allowed. However, from the low temperature polarisation behaviour Wells [103] has shown that this transition proceeds almost exclusively via the σ'-polarised magnetic-dipole moment. Therefore, for this particular combination of transitions the polarisation anisotropy is $P_{\pi\sigma'}$ and will be given by equation 7.3.

Polarised fluorescence spectra were recorded in the temperature region of 15-250 K. Due to the spectral isolation of the fluorescence transitions, there was no need to take account of any line-broadening and overlap effects, and the intensities could be obtained directly from the spectra. Examples of the temperature dependent polarised spectra of SrF_2:Eu^{3+} are shown in Figure 7.2 (page 202).

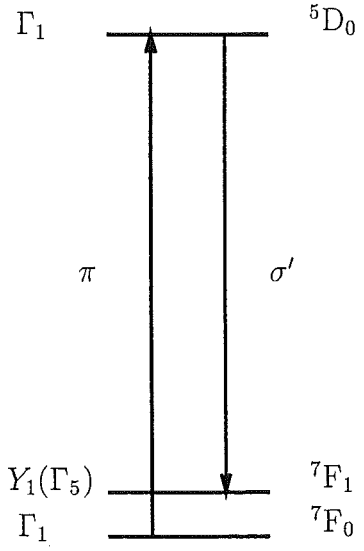

Figure 7.5: The excitation and fluorescence transitions employed in the CaF_2:Eu^{3+} and SrF_2:Eu^{3+} C_{4v} center depolarisation experiments.

In comparing theory and experiment to obtain the barrier energy associated with dipole reorientation, a theoretical curve of $P_{\pi\sigma'}$ was fitted to the polarisation anisotropy data by a least-squares procedure. The hopping rate was taken to be expressed by the Arrhenius equation $W = \nu_a \exp(E/k_B T)$. The calculated polarisation anisotropy involved two parameters, the barrier height E and the scaling parameter α which accounts for misalignment and the collection of fluorescence from a finite solid angle. The attempt frequency was held fixed at the value of $\nu_a = 10^{13}\,s^{-1}$, as described on page 205.

The experimental data for CaF_2 :0.05%Eu^{3+} and SrF_2 :0.05%Eu^{3+} is presented in Figure 7.6, along with the calculated polarisation

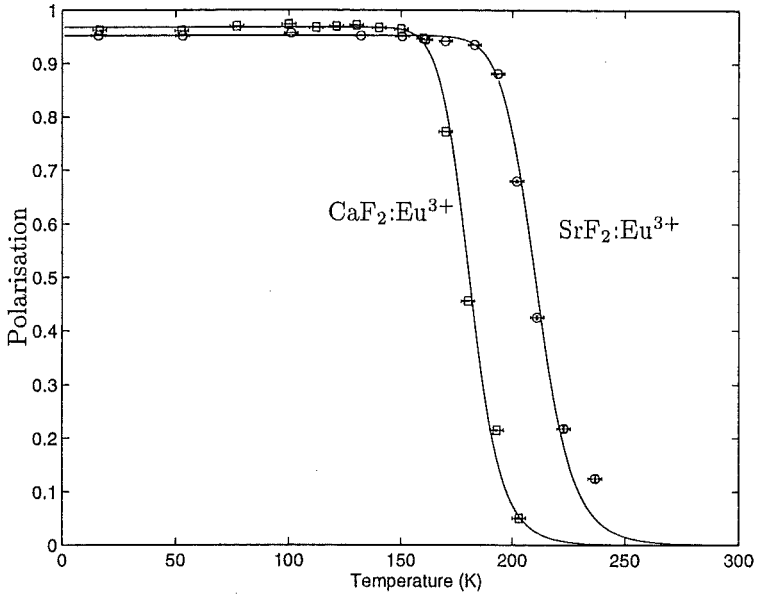

Figure 7.6: Depolarization of CaF_2:Eu^{3+} and SrF_2:Eu^{3+} with excitation of $^7F_0(\gamma_1) \rightarrow {}^5D_0(\gamma_1)$ and monitoring $^5D_0(\gamma_1) \rightarrow {}^7F_1(Y_1, \gamma_5)$ fluorescence. Solid lines are that obtained from fitting the data to a single barrier.

anisotropy.

For both hosts the experimental polarisation behaviour is well described by the model with Arrhenius-type hopping between the different possible orientations of the interstitial fluorine. From the weighted least-squares calculation, barrier energies of E=0.41±0.01 eV for CaF_2:Eu^{3+} and E=0.48±0.01 eV in SrF_2:Eu^{3+} were obtained.

The barrier energy for the CaF_2:Eu^{3+} C_{4v} center has been obtained by Voron'ko et.al. [100] by the same technique as presented here. They have reported a significantly different barrier energy, with E=0.32±0.03 eV. In the same paper, Voron'ko et.al. have also given the barrier energy as E=0.37±0.05 eV, as obtained from the fluorescence transients that were measured as a function of temperature. [1]

The disparity between the result presented here and that of Voron'ko et.al. should be seen in the light of the large uncertainties in their results. However, the barriers determined here and by Voron'ko et.al. using the same CW technique do not agree within the stated uncertainties. Further comparison of the barrier energies presented

[1]Time-resolved measurements such as those of Voron'ko et.al. were unable to be performed here due to limitations in the available pulsed laser and detection system. However, it is noted that the analysis of Voron'ko et.al. employs an incorrect expression for the decay transients. Solutions to the rate equations for time resolved experiments yield a time constant of $(\frac{1}{\tau} + \frac{3}{2}W)^{-1}$ associated with the reorientation processes, as opposed to the time constant given by Voron'ko et.al. of $(\frac{1}{\tau} + 2W)^{-1}$.

here can be made with the ITC measurements present in the literature. While many of the ITC experiments have focused on Gd^{3+} centers, Kitts and Crawford [56] have presented ITC results for CaF_2:RE^{3+}, in which a value of E=0.426 eV is given for CaF_2:Eu^{3+}. In an earlier paper of Kitts, Ikeya and Crawford [57] a comparison of the barrier energies for different hosts is given, for Gd^{3+} centers. This shows an increase in the barrier height going from CaF_2:Gd^{3+} to SrF_2:Gd^{3+}, with values of 0.42 eV and 0.45 eV respectively. Both the magnitudes of the barrier energies and the increased barrier energy for SrF_2 are consistent with the optical depolarisation results presented here.

7.4.3 Optical depolarisation of SrF_2:Pr^{3+}, $^3P_0$

The spectroscopy of the fluorine compensated C_{4v} centers in SrF_2:Pr^{3+} and CaF_2:Pr^{3+} has been reported by Reeves, Jones and Syme [87], where they note that the energy of the $^3P_0$ state for the Pr^{3+} C_{4v} center coincides with the frequency of the 476.5 nm argon laser line. This fortuitous overlap has been exploited to perform depolarisation measurements on this center with the $Z_1(\Gamma_5) \rightarrow {}^3P_0$ (Γ_1) excitation provided by the 476.5 nm (20986 cm^{-1}) argon laser line. This $\Gamma_5 \rightarrow \Gamma_1$ transition is both electric and magnetic dipole allowed, however the low temperature polarisation behaviour of the fluorescence clearly indicates that the $Z_1 \rightarrow {}^3P_0$ absorption is a σ-polarised electric dipole process. The emission from the $^3P_0$ state of this center displays quite large intensities in fluorescence to the $^3F_2$ multiplet, and specifically to the W_2 and W_3 states of this multiplet.[2] The $^3P_0 \rightarrow W_2(\Gamma_1)$ transition at 15705 cm^{-1} and $^3P_0 \rightarrow W_3(\Gamma_5)$ at 15672 cm^{-1} were chosen for determining the depolarisation behaviour of the SrF_2:Pr^{3+} C_{4v} centers. The transitions to W_2 and W_3 are both electric dipole processes, and are respectively π-polarised and σ-polarised. The polarisation anisotropy will therefore be given by $P_{\sigma\pi}$ of equation 7.3 for the $^3P_0 \rightarrow W_2$ fluorescence, and $P_{\sigma\sigma}$ of equation 7.4 for the $^3P_0 \rightarrow W_3$ emission.

The 15 K polarised spectra of these particular fluorescence transitions are depicted in Figure 7.8. The polarisation behaviour of the transition terminating on the W_2 state is more pronounced, with the YX:YY intensities varying from ~1:0 through to ~1:1, as opposed to the $^3P_0 \rightarrow W_3$ emission which has a corresponding variation in polarised intensity ratios of ~1:2 through to ~1:1. For this reason the emission to W_2 is expected to provide more accurate polarisation anisotropy data.

Polarised fluorescence spectra of the $^3P_0 \rightarrow W_2, W_3$ transitions have been recorded for

[2] For brevity of notation the $^3F_2$ multiplet will often be referred to by the common alphabetical label of W. The ground state multiplet of $^3H_4$ will be referred to as 'Z'.

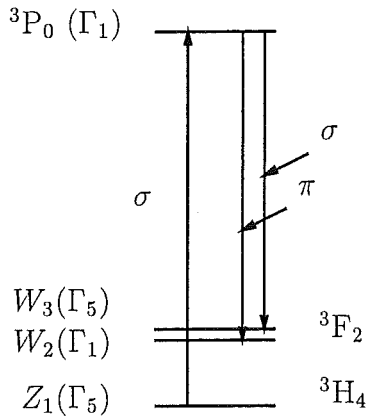

Figure 7.7: The $^3P_0 \rightarrow {}^3F_2$ transitions observed in SrF_2:Pr^{3+} for the optical depolarisation measurements.

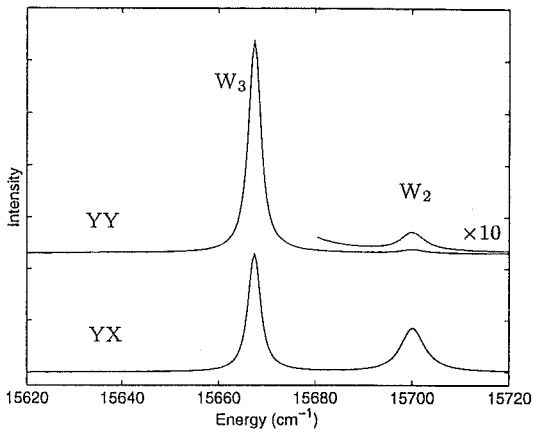

Figure 7.8: The $^3P_0 \rightarrow {}^3F_2$ polarised fluorescence observed in SrF_2:Pr^{3+} at 15 K.

temperatures between 15 K and 260 K. In analysing the polarised intensities of these transitions an additional complication is encountered that was not present for the Eu^{3+} investigations, namely the issue of line-broadening and spectral overlap. In particular the spectral overlap of the high frequency wings of the $^3P_0 \rightarrow W_3$ transitions with the weak $^3P_0 \rightarrow W_2$ transition can give a spurious contribution to the fluorescence intensity. Therefore, lineshape fitting to the recorded spectra has been performed to accurately determine relative intensities of the transitions between different polarisations. This accounts for the overlap of the neighbouring transitions and gives a true intensity for each transition in a given polarisation.

The fluorescence spectra were fitted to the combination of two Lorentzian lineshapes. The lineshape fitting was performed via a weighted least-squares procedure, where the weighting was taken as the inverse of the intensity. The spectral positions of the transitions were fixed manually, with the width and intensity treated as free parameters. Because of weak intensities, it was found necessary to explicitly fix the width of the $^3P_0 \rightarrow W_2$ transition in the YY polarised spectra to be the same as that obtained from the fit to the YX polarised spectra. Spectra obtained at various temperatures are shown in Figure 7.9 along with the fitted lineshapes. The experimental spectra are clearly well represented by the calculated lineshapes.

Figure 7.10 presents the experimental polarisation anisotropy obtained from the analysis of the $^3P_0 \rightarrow W_2, W_3$ fluorescence as described above. The dashed line of Figure 7.10 shows the theoretical polarisation anisotropy obtained by a least-squares fit to the experimental data. For this theoretical curve an Arrhenius hopping rate for interstitial reorientation was employed. Two parameters were varied to obtain the theoretical curve, the barrier energy E and the scaling parameter α. The attempt frequency was held at

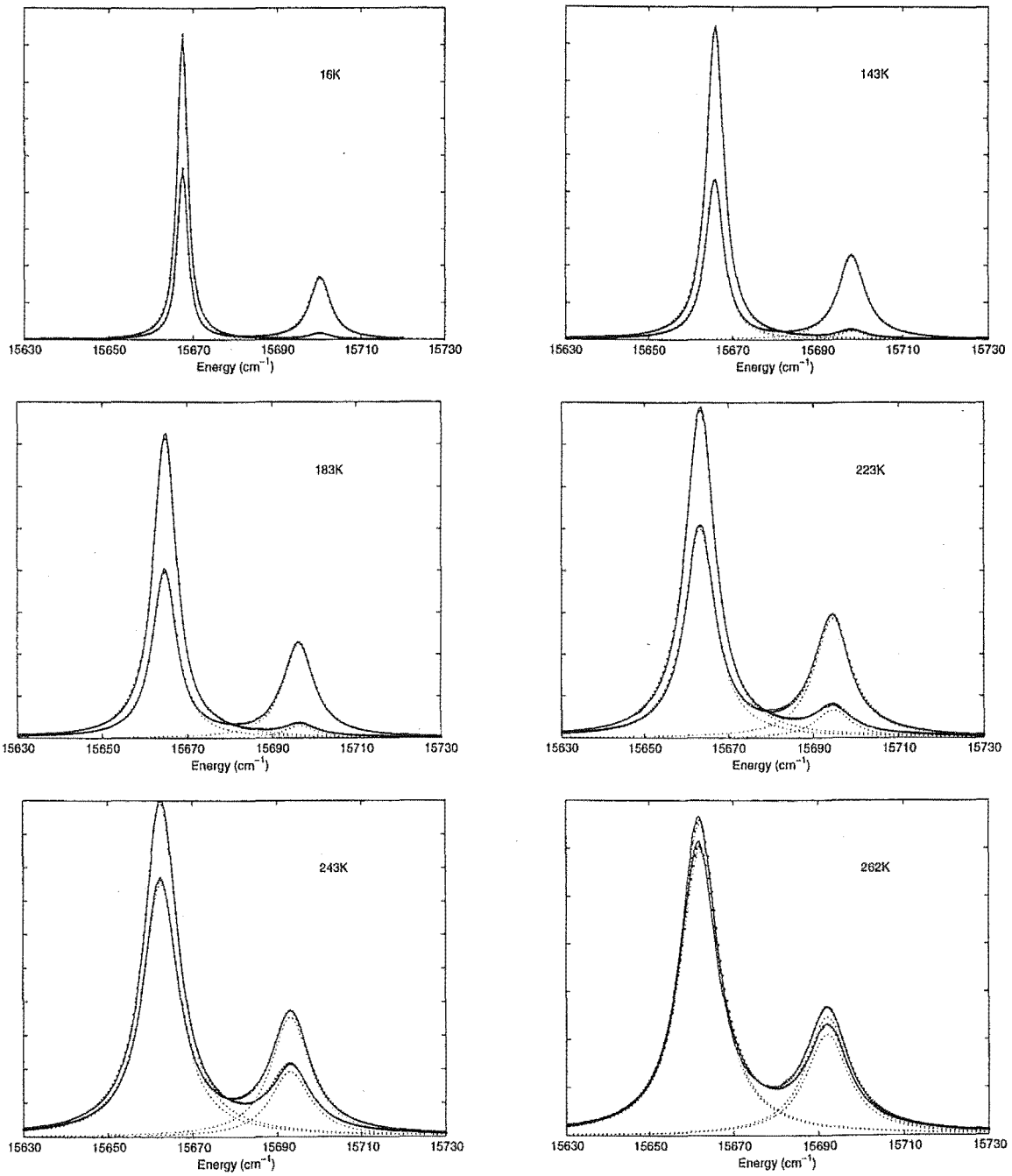

Figure 7.9: Measured and fitted spectra for the $^3P_0 \rightarrow {}^3F_2$ (W_2,W_3) transitions in SrF_2:Pr^{3+} for different temperatures and the YX, YY polarisation configurations. The experimental spectra are shown as a solid line, while the fitted spectra are given by the heavy dotted line. The lighter dotted lines display the contributions from the individual transitions.

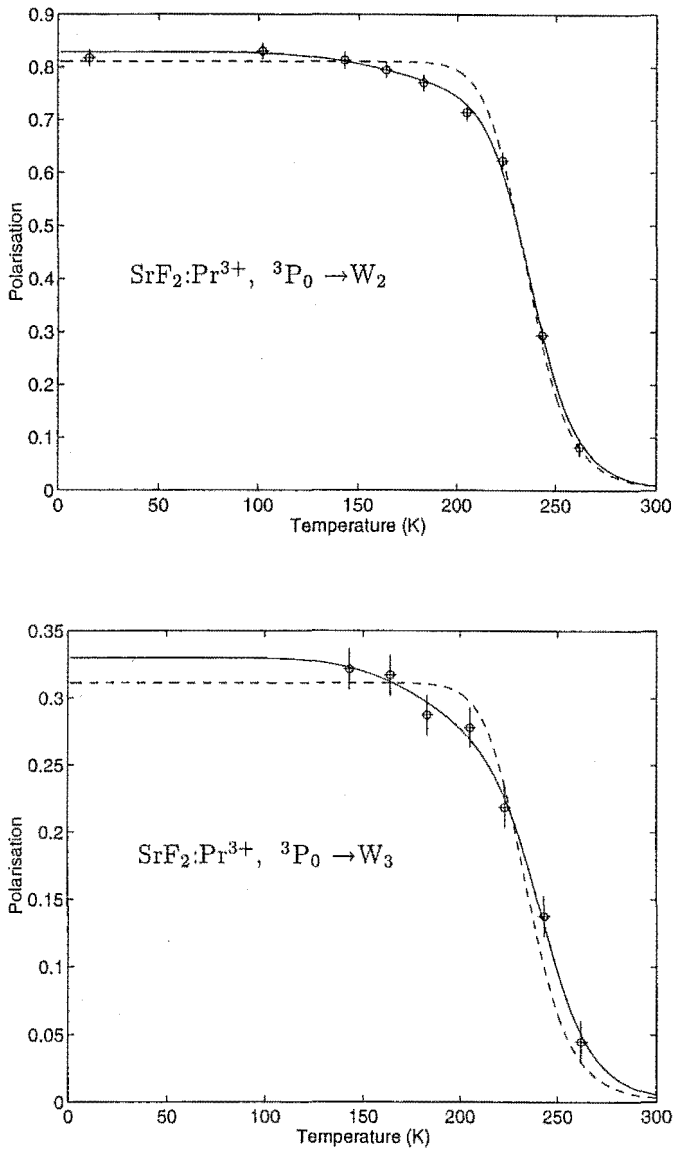

Figure 7.10: The $SrF_2:Pr^{3+}$ polarisation anisotropy obtained by exciting $^3H_4(Z_1, \Gamma_5) \rightarrow {}^3P_0(\Gamma_1)$ and monitoring the $^3P_0(\Gamma_1) \rightarrow {}^3F_2(W_2, \Gamma_1)$ fluorescence. The solid curve is that obtained from the model with two reorientation processes, while the dashed curve is that for only one process. Also shown is the polarisation anisotropy for the $^3P_0(\Gamma_1) \rightarrow {}^3F_2(W_3, \Gamma_5)$ transition.

the assumed value of $\nu_a = 10^{13}\,s^{-1}$. The polarisation anisotropy will be relatively insensitive to the excited state lifetime, compared to the barrier energy, for the same reasons discussed with respect to the attempt frequency (page 205). This can be clearly seen from expressing the polarisation anisotropy in the form $P_{\sigma\pi} = 1/(2\tau\nu\exp(E/k_BT)+1)$. Because of this relative insensitivity, and the fact that most of the effect of reorientation is observed in a narrow temperature region, a fixed effective lifetime was used in the experimental analysis. The depolarisation temperature T_d will be defined to be that at which the polarisation anisotropy falls to half of its maximum value, which for the $^3P_0$ emission is approximately $T_d = 235\,K$. A lifetime of $\tau = 140\,\mu s$, which corresponds to the lifetime in the region of this depolarisation temperature, was used in the experimental analysis.

When the polarisation anisotropy is fitted to the depolarisation data in this manner an unsatisfactory result in the temperature region of the first turning point (150 K to 210 K) is obtained. It is found that the simple Arrhenius hopping rate model is unable to explain this slow onset of depolarisation which precedes the rapid change that occurs in the region of the depolarisation temperature.

One explanation that has been considered for this anomaly is that it may be due to an inhomogeneous distribution of barrier heights, so that a proportion of the interstitial ions will undergo reorientation at lower temperatures. For such a situation an effective hopping probability W can be obtained from the convolution of the Arrhenius equation with a Gaussian distribution of barrier energies centred at E with standard deviation σ. This effective hopping probability is given by

$$W = \nu_a\sigma\sqrt{\pi}\exp\{-E_o/k_BT + \sigma^2/4k_B^2T^2\}. \tag{7.7}$$

Such a broadening of activation energies has been applied by den Hartog and Langevoort [24] for the ITC conductivity of highly doped SrF_2:LaF_3 and BaF_2 :LaF_3. Attempts to describe the polarisation anisotropy in terms of such a hopping probability have been unsuccessful, from which it is concluded that a simple distribution of barrier energies cannot describe the observed polarisation behaviour.

A somewhat more successful explanation has been found in assuming that there exists two possible reorientation pathways, with different barrier energies and attempt frequencies. For such a model the hopping probability is expressed as

$$W = \nu_1\exp(-E_1/k_BT) + \nu_2\exp(-E_2/k_BT). \tag{7.8}$$

When the polarisation anisotropy of equation 7.3 or 7.4, with the hopping probability of equation 7.8 is fitted to the appropriate data, a considerably better agreement between the theoretical curve and the experimental data is obtained. The results of the improved

calculation are shown as a solid line in Figure 7.10. The improvement in describing the slow onset of depolarisation is quite clear, although it must be acknowledged that this may be partly due to an increase in the number of adjustable parameters. Four parameters have been varied for the double barrier polarisation anisotropy calculation, namely both barrier energies, the scaling parameter, and one of the attempt frequencies. The remaining attempt frequency associated with the dominant reorientation process, was held fixed at the value of $\nu_a = 10^{13}\,s^{-1}$.

The double barrier model is also found to be appropriate for analysis of the experiments involving $^1D_2$ emission, as will be discussed in the following section.

For the model with a single hopping mechanism a barrier energy of 0.44 eV is obtained (with a fixed attempt frequency of $\nu_a = 10^{13}\,s^{-1}$), while for the double barrier model the results obtained are E_1=0.45±0.01 eV, $\nu_1 = 10^{13}\,s^{-1}$ and E_2=0.04±0.02 eV, $\nu_2 = 10^3\,s^{-1}$±50%. Henceforth the principal and secondary barriers will be taken to refer to E_1, ν_1 and E_2, ν_2 respectively. The very small magnitude of both the barrier energy and attempt frequency of the secondary barrier appear somewhat unphysical if they are interpreted in terms of a reorientation process induced by lattice phonons. While this secondary barrier will be discussed more fully in a later section, it is mentioned here that this secondary depolarisation process is considered to be due to energy migration amongst the C_{4v} centers, rather than a physical reorientation of the center.

Subsequent to publication of the optical depolarisation results presented here [48], the SrF_2:Pr^{3+} $^3P_0$ experiments were repeated by Charnock et.al. [16] and they have confirmed the anomalous depolarisation associated with the secondary barrier. However there is some disagreement in the value of the principal barrier energy, with the results of Charnock et.al. suggesting a barrier energy of $E = 0.42$ eV. The origin of this discrepancy is not currently known, although possible inaccuracies of the temperature measurements may partially explain this anomaly. It is also noted that the measurements of Charnock et.al. were performed with a higher concentration sample, with 0.1%Pr^{3+} compared to the 0.05%Pr^{3+} employed here.

7.4.4 Optical depolarisation of CaF_2:Pr^{3+} and SrF_2:Pr^{3+}, $^1D_2$

For CaF_2:Pr^{3+} and SrF_2:Pr^{3+} fluorine compensated C_{4v} centers the temperature dependent polarisation anisotropy for excitation into, and fluorescence from, the $^1D_2$ multiplet has been measured. For the $^1D_2$ multiplet the two lowest states, D_1 and D_2, are separated by 19 cm^{-1} in SrF_2 and 17 cm^{-1} in CaF_2.[3] The low temperature

[3]The common alphabetic labelling of 'D' will be used to refer to the $^1D_2$ multiplet. The $^3H_4$ and $^3H_5$ multiplets will often be referred to as Z and Y respectively.

polarisation properties of the fluorescence from these two levels also identifies a different irrep ordering for D_1 and D_2 in the two hosts, such that for SrF_2 the states are $D_1(\Gamma_3)$, $D_2(\Gamma_1)$ while in CaF_2 the irrep labelling of the states is $D_1(\Gamma_1)$, $D_2(\Gamma_3)$. In both hosts the ground state of the C_{4v} center transforms as the Γ_5 irrep. The absorption transitions to both D_1 and D_2 of both hosts are electric-dipole σ-polarised processes.

Because it is desirable to measure the polarisation anisotropy for the combination of σ- and π-polarised transitions, rather than two σ-polarised transitions, the measurements presented here have focused on fluorescence transitions to the $Y_2(\Gamma_1)$ state. As transitions between two Γ_1 states are only allowed via π-polarised electric-dipole moments, the analysed fluorescence transitions were $D_2(\Gamma_1)\rightarrow Y_2(\Gamma_1)$ at $14652\,cm^{-1}$ for $SrF_2:Pr^{3+}$, and $D_1(\Gamma_1)\rightarrow Y_2(\Gamma_1)$ at $14617\,cm^{-1}$ for $CaF_2:Pr^{3+}$. The excitation was provided directly to the emitting states of the chosen fluorescence transitions. Hence the excitation transitions employed were $Z_1(\Gamma_5)\rightarrow D_2(\Gamma_1)$ at $16872\,cm^{-1}$ for $SrF_2:Pr^{3+}$ and $Z_1(\Gamma_5)\rightarrow D_1(\Gamma_1)$ at $16828\,cm^{-1}$ for $CaF_2:Pr^{3+}$. The excitation and fluorescence scheme for the two hosts is summarised in Figure 7.11. [4]

Polarised fluorescence spectra of the appropriate spectral regions were recorded for temperatures between 15 K and 250 K. Examples of these spectra for $SrF_2:Pr^{3+}$ are presented in Figure 7.11. Lineshape fitting of the $^1D_2 \rightarrow {}^6H_5$ fluorescence spectra was required to determine the true intensity of the particular fluorescence transitions of interest. This lineshape fitting was performed in the same manner as described in the previous section.

The temperature dependence of the polarisation anisotropy in $SrF_2:Pr^{3+}$ and $CaF_2:Pr^{3+}$ for $^1D_2$ emission is presented in Figure 7.12. As with the SrF_2 $^3P_0$ data, a small but significant decrease in the polarisation anisotropy is observed in the region before the depolarisation temperature. It is again found that the single barrier model is unable to adequately describe the experimentally determined polarisation anisotropy over the measured temperature range. Therefore the $^1D_2$ data of both hosts has also been analysed in terms of the double barrier model discussed earlier.

For the purposes of calculations of the reorientation barrier energies from the depolarisation data of CaF_2, the $^1D_2$ lifetime of $850\,\mu s$ is used, corresponding to the lifetime in the vicinity of the depolarisation temperature of T_d=207 K. For $SrF_2:Pr^{3+}$ the depolarisation temperature is T_d=215 K, and an effective fluorescence lifetime of $\tau = 1.0$ ms was employed for the theoretical calculations. Two parameters were varied in calculations for the single barrier model (the energy E, and the scaling parameter α), while for the double barrier model four parameters (E_1, E_2, ν_2 and α) were varied.

[4]The irreps of the particular states used for the depolarisation experiments were given incorrectly by Jamison and Reeves [48], with the Γ_1 and Γ_3 assignments transposed.

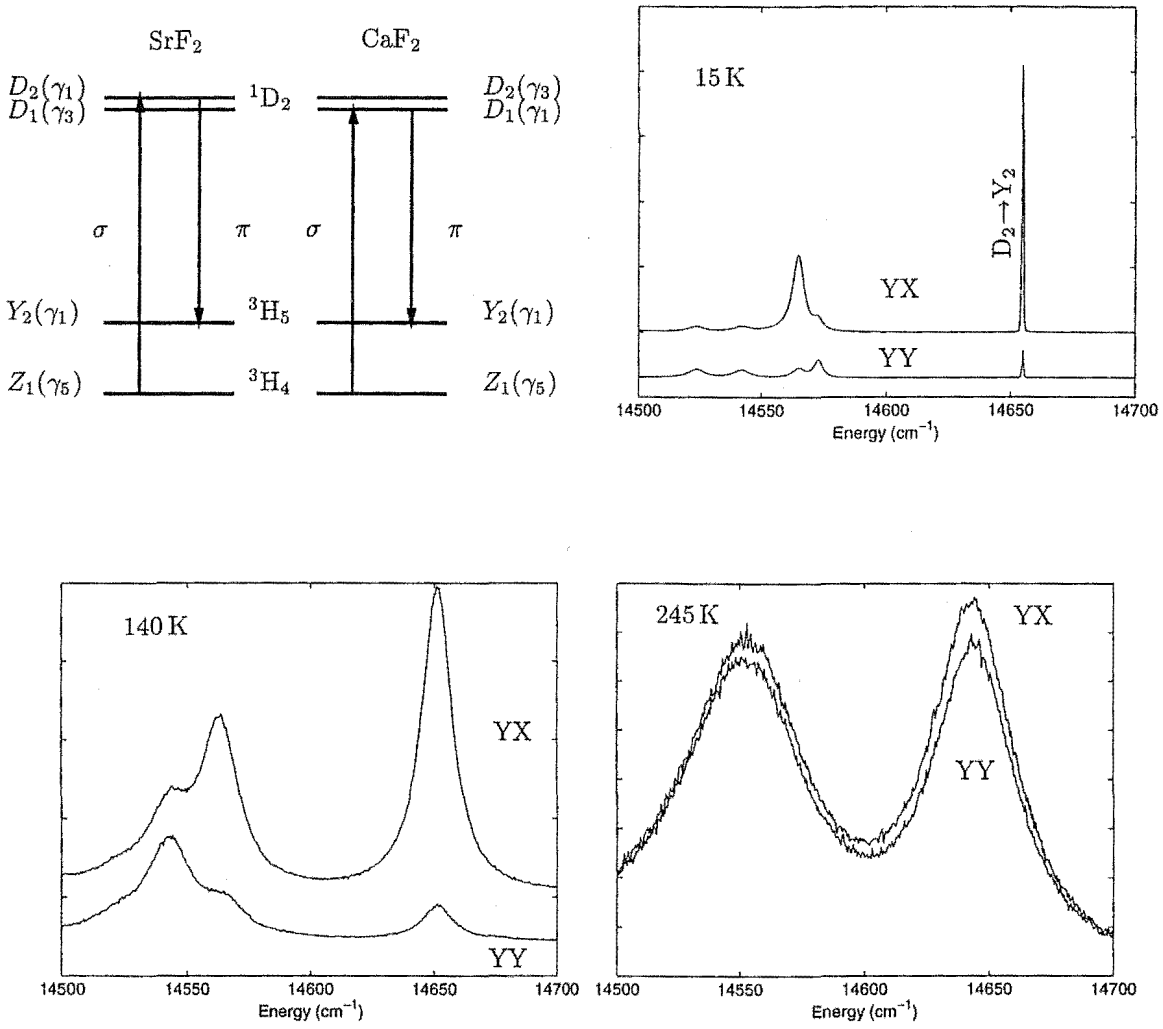

Figure 7.11: The excitation and fluorescence transitions employed for the CaF_2 and SrF_2 Pr^{3+} C_{4v} :F^- center depolarisation experiments, and representative fluorescence spectra obtained for SrF_2:Pr^{3+} at 15 K, 140 K and 245 K. The 15 K and 140 K spectra have been offset for clarity. No offset is present in the 245 K spectra.

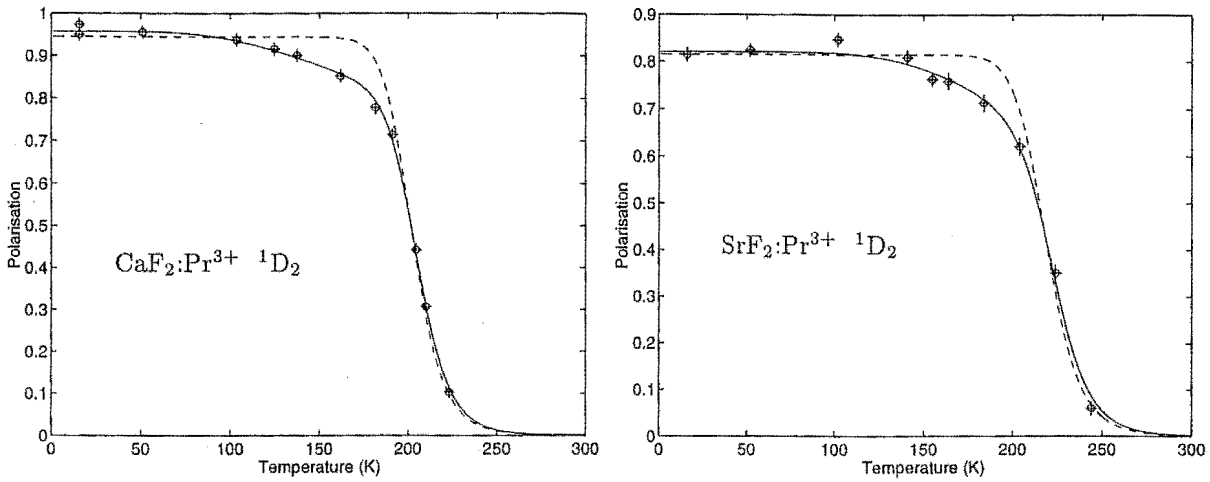

Figure 7.12: The temperature dependence of the polarisation anisotropy for SrF_2:Pr^{3+} and CaF_2:Pr^{3+} obtained with $^1D_2$ excitation and emission. The solid line is that obtained from calculation with the double barrier model, while the dashed line is that obtained from the single barrier model.

The attempt frequency of the principal barrier was held fixed at $\nu_1 = 10^{13}\,\mathrm{s}^{-1}$.

The principal barrier energies obtained from the double barrier model are 0.46±0.01 eV for SrF_2 and 0.43±0.01 eV for CaF_2. Similar barrier energies are also obtained from the single barrier model. The slightly larger barrier energy obtained for SrF_2 is in agreement with the Eu^{3+} results and with reported ITC experiments [57]. It is also worth mentioning that the barrier energy obtained for SrF_2:Pr^{3+} is the same, within uncertainties, for measurements involving the two different excited states of $^1D_2$ and $^3P_0$.

The results for the four centers investigated here are summarised in Table 7.1. The barrier energies are found to be in general agreement with the trends reported for ITC experiments, with SrF_2 having slightly higher barriers. The numerical values for the barrier energies are also in broad agreement with ITC results which place the C_{4v} barrier energies in the region of 0.4–0.5 eV, although such a comparison is difficult given the large range of energies that have been reported [56]. The CaF_2:Eu^{3+} barrier energy of E=0.41±0.01 eV obtained here is in disagreement with that found by Voron'ko et.al. who have applied the same technique of optical depolarisation to obtain E=0.32±0.03 eV [100]. The value of E=0.43±0.01 eV obtained for the CaF_2:Pr^{3+} barrier energy agrees within uncertainties with the value of E=0.40±0.03 eV that was reported by Voron'ko et.al.

7.4.5 Justification of the ν_a approximation.

The polarisation anisotropy in SrF_2:Pr^{3+} has been obtained from two independent experiments, namely emission from the $^3P_0$ and $^1D_2$ multiplets. This enables the attempt frequency to be estimated directly from experiments, and so check the validity of the assumed value of $\nu = 10^{13}\,s^{-1}$ for the principal barrier. Note that for both of the SrF_2:Pr^{3+} experiments, the polarisation anisotropy is given by $P_{\sigma\pi}$ of equation 7.3. At the depolarisation temperature T_d, defined as the temperature at which the anisotropy falls to half of the maximum value ($P_{\sigma\pi} = 1/2$), the relationship between the barrier energy and attempt frequency is given by $E/k_B T_d = \ln(2\tau\nu)$. In obtaining this relation it is assumed that there is only one reorientation pathway, and that the second barrier observed for the Pr^{3+} centers has a negligible effect on the depolarisation temperature. Using the lifetimes τ_1 and τ_2 for the $^3P_0$ and $^1D_2$ levels respectively, along with the appropriate depolarisation temperatures T_{d1} and T_{d2}, the attempt frequency ν can be eliminated, to obtain the barrier energy as

$$E = \frac{T_{d1}T_{d2}}{T_{d2} - T_{d1}} k_B \ln(\tau_1/\tau_2). \tag{7.9}$$

In this manner, using lifetimes and depolarization temperatures summarised in Table 7.1, a barrier energy of E=0.43 eV is obtained, independent of any assumption regarding the attempt frequency, and in reasonable agreement with the results presented in Table 7.1.

Substituting this value of the barrier energy back into the expression relating the barrier energy to attempt frequency (at the depolarisation temperature), along with the lifetimes and depolarisation temperature of the $^3P_0$ multiplet, gives a value for the attempt frequency of $\nu = 6 \times 10^{12} s^{-1}$. The close agreement of this calculated attack frequency and the assumed value is considered to support the initial estimation of $\nu = 10^{13} s^{-1}$.

Sample & Excited Multiplet	Depolarisation Temperature (K)	Lifetime	Single Barrier model		Double Barrier model	
			Barrier Energy (eV)	Attack Frequency (s^{-1})	Barrier Energy (eV)	Attack Frequency (s^{-1})
CaF_2:Eu^{3+} $^5D_0$	175	11.8 ms	0.41±0.01	1×10^{13}	N/A	N/A
SrF_2:Eu^{3+} $^5D_0$	212	13.4 ms	0.48±0.01	1×10^{13}	N/A	N/A
CaF_2:Pr^{3+} $^1D_2$	207	850 μs	0.42	1×10^{13}	0.43±0.01 0.04±0.02	1×10^{13} $9\times10^2 \pm 50\%$
SrF_2:Pr^{3+} $^1D_2$	215	1.0 ms	0.45	1×10^{13}	0.46±0.01 0.07±0.02	1×10^{13} $7\times10^3 \pm 50\%$
SrF_2:Pr^{3+} $^3P_0$	235	140 μs	0.44	1×10^{13}	0.45±0.01 0.06±0.02	1×10^{13} $12\times10^3 \pm 50\%$

Table 7.1: Barrier energies for dipole reorientation of the $C_{4v}(F^-)$ centers. The principal barriers have been constrained to have an attempt frequency of $\nu = 10^{13}s^{-1}$. Uncertainties in the barrier energies have been estimated from consideration of the χ^2 surface. No uncertainties are given for the single barrier model of the Pr^{3+} centers as such a model does not well describe the observed data.

7.5 Uncertainties.

To enable an estimation of the uncertainties in the parameters obtained from the least-squares refinement, the χ^2 surface has been mapped in the vicinity of the χ^2 minimum.

Figure 7.13 presents an example χ^2 contour plot for the two variables associated with the principal barrier, (E_1 and ν_1). The narrow valley displayed in this plot demonstrates the high degree of correlation that exists between the attempt frequency and the barrier energy. It is this correlation that gives rise to unreliable parameter refinement when both parameters are simultaneously varied. Also apparent from the logarithmic scale of the ordinate and the linear scale of the abscissa is that the attempt frequency will be less well determined from the data than the barrier energy, and conversely that fixing the attempt frequency to within ≈50% of its true value will introduce little error to the barrier energy.

An example of the χ^2 contours corresponding to the secondary barrier is shown in Figure 7.14. The minimum of the χ^2 surface is more clearly defined than for the principal barrier, enabling the attempt frequency and barrier energy to be obtained simultaneously from the least-squares refinement.

Similar χ^2 surfaces are obtained from different data sets, including those involving different excitation and fluorescence pathways.

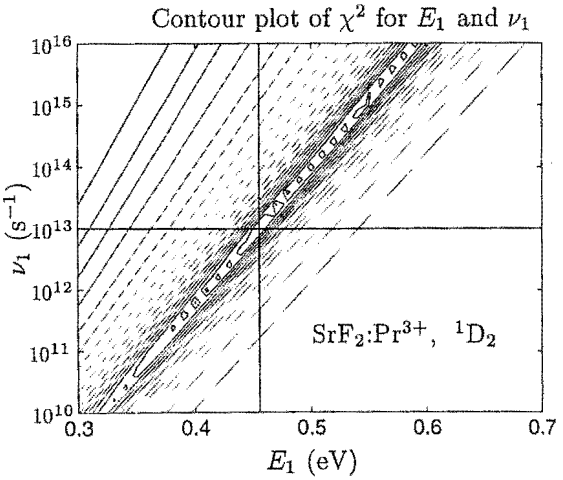

Figure 7.13: The χ^2 contour plot for the attempt frequency and barrier energy of the principal barrier. An approximate doubling of χ^2 is represented by successive contours. The vertical line indicates the parameter value obtained from the least-squares refinement, with the fixed attempt frequency of $\nu_1 = 10^{13}\,s^{-1}$.

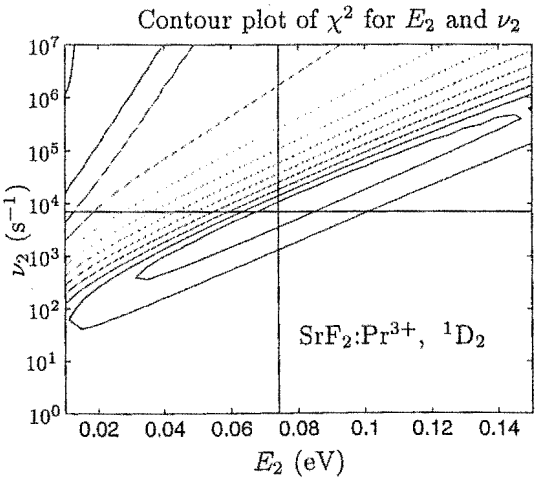

Figure 7.14: The χ^2 contour plot for the attempt frequency and barrier energy of the secondary barrier. A 150% increase in χ^2 is represented by successive contours. The horizontal and vertical lines indicate the parameter values obtained from the least-squares refinement.

The standard approach of calculating parameter uncertainties, involving the co-variance matrix [20], is rendered invalid by the correlation in the parameters demonstrated in the χ^2 surfaces. Indeed it is found that the co-variance matrix approach produces uncertainties that are significantly smaller than the variance in results obtained from analysis of different data sets. Therefore, the uncertainties that will be associated with the parameters have been estimated from consideration of the χ^2 surfaces. The somewhat arbitrary distinction is made that the uncertainties correspond to an approximate doubling of χ^2, providing uncertainty estimates of $\Delta E_2 = \pm 0.02\,\mathrm{eV}$ and $\Delta\nu_2 = \pm 50\%$ for the secondary barrier. For the principal barrier the uncertainty in the barrier energy is estimated to be $\Delta E_2 = \pm 0.01\,\mathrm{eV}$, although this must be seen in the light of the constrained value for the attempt frequency, and is only considered valid if the approximated attempt frequency is correct to within 50%. These estimates of the uncertainties are also consistent with the spread in the parameter values obtained from analysis of different sets of data.

7.6 Discussion of the secondary energy barrier.

A number of possible explanations for the origins of the secondary barrier have been considered. Some of these mechanisms, and the reasons for rejecting them as the origin of the secondary barrier, will first be discussed. Resonant energy transfer, which is considered to be the likely mechanism behind the secondary barrier, will then be addressed.

Catlow [13] has discussed two possible mechanisms for re-orientation. The first, the concerted or interstitialcy mechanism, involves a two step process with a lattice fluorine moving into an interstitial position and the original interstitial replacing this now vacant lattice position. The second process, the direct interstitial mechanism, has the interstitial distorting the lattice while moving directly to another interstitial position. It may therefore be possible that both processes are occurring, which would be consistent with a double barrier model of the reorientation processes. However, invoking the combination of concerted and direct motions in reorientation to describe the barriers observed in the optical depolarisation measurements requires ascribing a considerable disparity between the barrier heights for the two mechanisms. More dramatically, approximately ten orders of magnitude difference in the attempt frequencies of the two mechanisms would also need to be accepted. It is considered that this dramatic disparity of the numerical values of the attack frequency and barrier energy is unphysical. The interpretation of the second barrier as being due to the combination of concerted and direct reorientation mechanisms is therefore rejected. It is worth noting that conclusions cannot be drawn from the optical depolarisation data as to which of these two

mechanisms is involved in the reorientation process.

Charnock et.al. [17] have discussed the possibility of dipole reorientation involving both the tetragonal C_{4v} sites and the trigonal C_{3v} sites. The concept of this interchange has its basis in the common saddle point in the dynamics of the two different symmetry sites, as discussed by Catlow [13]. Therefore the $C_{4v} \rightleftharpoons C_{4v}$ barriers must be considered along with the $C_{4v} \rightleftharpoons C_{3v}$ and $C_{3v} \rightleftharpoons C_{3v}$ barriers. Charnock et.al. have investigated these processes through temperature dependent EPR of SrF_2:Gd^{3+}, and concluded that the C_{4v} and C_{3v} centers are indeed interchangeable. However there is an absence of C_{3v} centers in CaF_2:Pr^{3+}, and this has the associated implication that a significant barrier exists between the C_{3v} and C_{4v} configurations. There is also no indication of double barrier effects in the Eu^{3+} systems. For these reasons the $C_{4v} \rightleftharpoons C_{3v}$ dynamics are also rejected as the mechanism underlying the secondary reorientation process.

Energy Transfer.

Another mechanism for achieving depolarisation of the observed fluorescence involves energy transfer. If a C_{4v} center with a particular orientation undergoes energy transfer to another remote C_{4v} center of a different orientation, a reduced polarisation anisotropy will be observed. In the particular case of the Pr^{3+} experiments, to invoke energy transfer to account for the secondary "barrier", the transfer must proceed via a resonant process. This requirement follows from the experimental conditions, where fluorescence was monitored from the same state as was excited. Such resonant energy transfer processes include multipole-multipole transfer [44], radiation trapping or reabsorption [46], and phonon assisted transfer [79].

There exists independent evidence that the single-ion C_{4v} centers in CaF_2:Pr^{3+} may undergo energy transfer. Upconversion fluorescence from the $^3P_0$ multiplet has been observed following excitation of the $^1D_2$ multiplet by Lezama et.al. [63] and Reeves et.al. [87], and from the time-resolved properties of this fluorescence was attributed by Reeves to energy transfer processes between remote C_{4v} centers.

Resonant non-radiative (multipole-multipole) transfer between identical centers will in general have no effect on the observed excited state lifetime of a center [41]. This conclusion is based on the indistinguishibility of donor and acceptor ions involved in the transfer process. However, through polarised excitation and fluorescence measurements, a distinction between donor and acceptor may be possible in some systems. The decay transients will then exhibit features that are dependent on the characteristics of the energy transfer. Richter, Wannemacher and Heber [90] have employed polarisation measurements of the excited state decay transients in YAG:Tb^{3+} to investigate the res-

onant transfer processes occurring in this system. While the technique of time resolved polarised fluorescence is not one used here, the results of Richter et.al. provide insights into resonant transfer processes which are applicable to a description of the CW investigations. From their time resolved measurements Richter et.al. have determined resonant energy transfer rates, and the temperature dependence of those rates. They have found that the temperature dependence can be described by an energy transfer rate of the form $W = \nu \exp(E/k_B T)$, which coincides with the additional rate included in the phenomenological double barrier model of the polarisation anisotropy. Such a temperature dependence is indicative of a two-phonon Orbach process [81] involved in the energy transfer.

For such a process to be responsible for the secondary "barrier" encountered in the Pr^{3+} optical depolarisation experiments , the barrier energy must be interpreted as the separation between particular energy levels which can be bridged by lattice phonons. The pairs of energy levels are to be associated with either the ground state ($^6H_4$) or the excited state ($^3P_0$ or $^1D_2$). From the optical depolarisation experiments the second energy barrier was estimated to be $E \approx 0.05\,\text{eV}$=$400\,\text{cm}^{-1}$. Such an energy is consistent with the above interpretation of a two phonon process, with phonons of this energy being present in the density of states for both CaF_2 and SrF_2 hosts. Because the secondary barrier energy has been determined with a relatively large uncertainty it is not possible to assign the particular energy levels to be associated with such an Orbach process. However, it is noted that there exists states separated from the ground state by an appropriate energy. In particular, the Z_1-Z_3 splitting in CaF_2:Pr^{3+} C_{4v} centers has been reported as $447\pm10\,\text{cm}^{-1}$, while for SrF_2:Pr^{3+} the Z_1-Z_3 splitting is $373\,\text{cm}^{-1}$[87]. For experiments involving the $^1D_2$ multiplet it is also possible that the undetermined D_1-D_3 splitting may be involved in such Orbach processes. It is also noted that the approximate frequency factor associated with the secondary barrier, with $\nu = 10^3 - 10^4\,\text{s}^{-1}$, is not unreasonable for such an energy transfer process.

From the above discussion it is concluded that the secondary barrier observed in the optical depolarisation experiments is to be interpreted as due to resonant energy transfer between C_{4v} :Pr^{3+} centers with different orientations, rather than a physical reorientation process. Such a conclusion is consistent with energy transfer involving a two-phonon Orbach process. It is also worth noting that because of the limited temperature range over which such "secondary barrier" effects can be observed, two phonon Raman processes cannot be ruled out as possibly contributing to the resonant energy transfer.

7.7 Summary

The properties of ionic motion associated with fluorine compensated C_{4v} centers in CaF_2 and SrF_2 have been investigated. The method employed, that of monitoring the temperature dependence of the fluorescence polarisation anisotropy, enables the ionic motion to be determined in a site-selective manner. Because of this site-selectivity of the experimental procedure, the ambiguity in assignment of barrier energies to a specific reorientation process, which accompanies experiments such as ITC, can be largely removed. The particular process investigated was that involving the reorientation of an interstitial fluorine ion to a structurally equivalent, but differently oriented, interstitial position.

It has been found that for the Eu^{3+} C_{4v} centers in both CaF_2 and SrF_2 the temperature dependence of the polarisation anisotropy is well described by a model in which the interstitial ion has a probability of reorientation given by the Arrhenius equation. The barrier energies associated with these reorientation processes have been determined from an analysis of the polarisation anisotropy, and found to be in general agreement with reported energies obtained from ITC experiments. Specifically, it is found that the barrier energy in CaF_2:Eu^{3+} is lower than that in SrF_2:Eu^{3+}, with energies of 0.41 ± 0.01 eV and 0.48 ± 0.01 eV respectively. For CaF_2:Eu^{3+} the barrier energy obtained is significantly larger that that reported by Voron'ko et.al. [100], who have performed similar optical depolarisation experiments on the CaF_2:Eu^{3+} C_{4v} centers.

The polarisation anisotropy data obtained for the Pr^{3+} C_{4v} centers has been shown to be inconsistent with a single Arrhenius reorientation rate, but well described by an effective rate involving the combination of two Arrhenius type barriers. Several possible mechanisms for this secondary reorientation rate have been considered. It was concluded that the secondary "barrier" is not associated with a physical reorientation, but rather should be interpreted as a consequence of resonant energy transfer processes, in which an excited C_{4v} center transfers this excitation to another C_{4v} center with different orientation. These experiments have therefore shown the applicability of CW polarisation experiments in determining information regarding resonant energy transfer processes. Such processes are difficult to investigate by traditional means due to the spectroscopic indistinguishibility of the donor and acceptor ions. As for the Eu^{3+} data, the barrier energies obtained for the physical reorientation of an interstitial ion in the Pr^{3+} centers are consistent with reported ITC results. The barrier energies associated with the physical reorientation have been determined to be 0.45 ± 0.01 eV for SrF_2:Pr^{3+} and 0.43 ± 0.01 eV for CaF_2:Pr^{3+}.

It has also been shown that the observation of the polarisation anisotropy associated

with emission from states with different lifetimes enables a determination of barrier energies independent of any consideration of the attempt frequency, a parameter that is not well determined by experiment.

Chapter 8

Conclusions and summary.

Laser site-selective excitation techniques have been applied to the spectroscopic investigation of Dy^{3+} defect centers in CaF_2 and SrF_2, and also to the study of ionic motion of interstitials in the Pr^{3+} and Eu^{3+} C_{4v} centers of these hosts.

The spectroscopy of SrF_2:Dy^{3+} has characterised the two main centers, which have been shown to correspond to the C_{4v} and C_{3v} symmetry symmetry centers reported in other SrF_2:RE^{3+} systems. Absorption transitions of these centers occur with approximately equal absorption strength, leading to the conclusion of approximately equal concentrations of the C_{4v} and C_{3v} centers. The presence of both the C_{4v} and C_{3v} centers establishes Dy^{3+} as the lanthanide ion for which the preferred defect center changes from C_{4v} to C_{3v} .

The spectroscopy of the SrF_2:Dy^{3+} C_{4v} center, which has not previously been addressed in the literature, has identified a total of 33 energy levels from eight multiplets or manifolds. The polarisation properties of the fluorescence from the $^4F_{9/2}$ multiplet is degraded through the combination of electric and magnetic dipole transition moments. It has been shown that an experimental determination of the pure electric (or magnetic) dipole nature of the absorption transition in these centers is possible despite the combination of dipole moments in the fluorescence transitions. This method, which revolves around the identity of intensities in two polarisation configurations, is amenable to phase-sensitive techniques involving a photoelastic modulator. From such experiments it has been clearly established that the excitation transitions are purely electric dipole processes. This in turn has allowed constraints to be placed on the polarised fluorescence - without assuming a pure electric dipole (or magnetic dipole) fluorescence transition moment. These constraints have enabled an experimental determination of the irreducible representation labels of many of the C_{4v} center energy levels. A least-squares fitting of the experimental energy levels to those of a crystal-field calculation has provided a satisfactory crystal-field parametrisation of the C_{4v} center, where the parameters are in general agreement with those reported for other SrF_2:RE^{3+} C_{4v} centers.

The spectroscopy of the SrF_2:Dy^{3+} C_{3v} center has identified 45 of the 59 energy levels below $\approx$22000 cm^{-1}. A stronger coupling of this center to the lattice vibrations has been observed, with the identification of vibronics associated with an unassigned 135 cm^{-1} phonon, and also with the 217 cm^{-1} transverse optical phonon. Crystal-field parameters for the C_{3v} center have been determined via a least-squares fitting to the experimental energy levels. These parameters display general agreement with those reported for the SrF_2:Eu^{3+} [103] and SrF_2:Er^{3+} J-centers [21], and a disparity with the SrF_2:Ho^{3+} trigonal B-center parameters [72]. The anomalous nature of the Ho^{3+} C_{3v} center is therefore confirmed by the spectroscopy and analysis of the Dy^{3+} centers.

Zeeman infrared absorption measurements involving states from several of the Dy^{3+} multiplets below 8000 cm^{-1} have been employed to test the SrF_2:Dy^{3+} C_{4v} and C_{3v} wavefunctions that are obtained from the crystal-field analyses. The calculated and experimental Zeeman splittings of the C_{4v} states are in very good agreement, thereby supporting not only the crystal-field calculation, but also confirming the accuracy of energy level assignments obtained from the site-selective fluorescence measurements. While a smaller number of absorption transitions have been investigated for the C_{3v} center, these results also tend to support the crystal-field analysis. Of interest is the presence of additional small splittings in the high field C_{3v} center Zeeman spectra. Such anomalous splittings have previously been observed for the SrF_2:Er^{3+} trigonal center [23], and the possibility of a small non-C_{3v} distortion was raised. Through consideration of the expected Zeeman splittings for a slightly misaligned sample, and the observation of such splittings in both the C_{4v} and C_{3v} centers, it has been concluded that these anomalous splittings can be attributed to sample misalignment. Because of the relatively large splitting factors of the Dy^{3+} and Er^{3+} centers it is likely that such experimental artifacts would not be observable with the other rare-earth C_{3v} centers.

In performing the Zeeman splitting calculations discussed above, an often overlooked ambiguity in the crystal-field coordinate basis has been addressed. This ambiguity stems from the non-unique form of the crystal-field Hamiltonian, in that a C_{nv} center has two bases, rotated by π/n about the principal axis, each with a Hamiltonian of the same functional form. Although different signs will be determined for parameters associated with particular crystal-field operators (B_4^4, B_4^6 and B_3^4, B_3^6 for C_{4v} and C_{3v} respectively), the use of parameter fitting alone in the crystal-field analysis leaves the coordinate basis undetermined. The corresponding ambiguity in the crystal-field wavefunctions can be determined from ab-initio calculations if the structure of the center is known. In this thesis it was attempted to determine the appropriate basis from the consideration of the Zeeman splittings, where the symmetry reduction imposed by the magnetic field can in principal resolve the basis ambiguity. It has been shown that for Kramers ions the basis can only be distinguished through the Zeeman interaction

if two (or more) states transforming as different irreps undergo significant mixing. For isolated Kramers doublets no basis dependent effects will be observed in the Zeeman splittings. The experimental determination of the C_{4v} basis was hampered by the complexity of the accessible Zeeman transitions, which included an overlapping C_{3v} absorption along with transitions to three C_{4v} states. The C_{3v} basis was more clearly determined from the Zeeman splittings. While an effective charge model calculation for the C_{3v} center is present in the literature, the particular basis was not reported. Therefore, a point-charge model calculation has been performed here, and the resulting implied basis is in agreement with that determined experimentally.

Site-selective spectroscopy of the CaF_2:Dy^{3+} system has characterised the C_{4v} and C_{3v} centers, along with the cubic center. The C_{4v} center has previously been addressed in the literature, although much disagreement is present between various authors. This earlier work is also inconsistent with superposition-model calculations of the energy level scheme [88]. The spectroscopy presented in this thesis has considerably extended and revised the C_{4v} center energy level scheme. The irreducible representations of many of the C_{4v} states have also been determined through consideration of the polarised fluorescence from the $^4F_{9/2}$ multiplet. A crystal-field analysis based on these energy levels and irrep assignments has produced crystal-field parameters that are in reasonable agreement with the reported trends across the lanthanide series. With these CaF_2:Dy^{3+} parameters, the C_{4v} center has now been characterised for all ions of the lanthanide series with the sole exceptions of Pm^{3+} (radioactive) and Gd^{3+} and Yb^{3+} (states at unfavourable energies for site-selective spectroscopy).

The infrared absorption of the $^6H_{11/2}$ and ($^6H_{9/2}$, $^6F_{11/2}$) manifolds reveals that a number of CaF_2:Dy^{3+} C_{4v} transitions are absent, despite all transitions being allowed for Kramers ions in C_{4v} symmetry. The possibility that the absence of these transitions is due to the almost pure J_z composition has been discussed, although it is concluded that this J_z composition alone cannot describe the apparently anomalous spectra. The good agreement obtained between experimental and calculated Zeeman infrared absorption spectra confirms the accuracy of the C_{4v} crystal-field wavefunctions. The Zeeman spectra of the X_4 state are well described only with the inclusion of the mixing with the X_3 state, thus confirming the assignment of X_3 despite this level remaining unobserved in absorption.

The CaF_2:Dy^{3+} C_{3v} center that has been characterised here has not previously been discussed in the literature. A total of 31 energy levels from eight multiplets or manifolds have been determined for this minority center from site-selective laser spectroscopy. A crystal-field analysis forms the basis of the C_{3v} symmetry assignment, and the crystal-field parameters are consistent with the B-centers of CaF_2:Ho^{3+} and CaF_2:Er^{3+}.

The CaF_2:Dy^{3+} cubic center is observed in higher concentration single and double doped samples, with $\approx$0.1%RE^{3+}. This is consistent with the concept of fluorine scavenging by RE^{3+} cluster centers, which also occur at these higher concentrations. A total of 24 energy levels from six manifolds have been characterised from the laser spectroscopy, significantly extending previous energy level schemes for this center. Reasonable agreement is obtained between these experimental energy level assignments and a crystal-field analysis. A distinctive feature of the Dy^{3+} cubic center fluorescence is the observation of vibronic transitions with a very narrow linewidth. The 138 cm^{-1} energy separation between the vibronic and electronic transitions does not correspond to any distinctive features in the CaF_2 phonon density of states. In light of the Dy^{3+} vibronics, the spectroscopy of CaF_2:Sm^{3+} cubic centers has here been re-evaluated, and shown to possess similar vibronic transitions with an electronic-vibronic separation of 140 cm^{-1}. This has led to a number of changed assignments in the fluorescence transitions of the CaF_2:Sm^{3+} cubic center. Subsequent to observation of these Dy^{3+} vibronics, other members of this department have looked for, and observed, similar vibronics in other CaF_2:RE^{3+} cubic centers. A trend of decreasing vibronic offset with increasing lanthanide mass leads to the association of these vibronics with pseudo-localised resonance modes, which are caused by the mass and force constant changes accompanying the substitution of the Ca^{2+} ion with the much heavier rare-earth.

The optical absorption of the $^4F_{9/2}$ multiplet of CaF_2:Dy^{3+} reveals a number of transitions which are not present in the broadband excitation spectrum. These transitions are due to centers containing closely coupled Dy^{3+} ions, which enables efficient non-radiative cross-relaxation from the excited multiplet at $\approx$21000 cm^{-1}. To investigate these clusters centers the double doped CaF_2:Dy^{3+}:RE^{3+} (RE=Eu, Gd, Tb) systems have been considered. The broadband excitation spectrum of CaF_2:Dy^{3+}:Eu^{3+} reveals one dominant cluster center, for which excitation into the Dy^{3+} $^4F_{9/2}$ multiplet is efficiently transferred to the Eu^{3+} ion. The resulting Eu^{3+} fluorescence from the $^5D_0$ multiplet enables correlation of this cluster with the R-center asymmetric dimer reported for CaF_2:Eu^{3+} [37]. With the analogous center in double doped CaF_2:Dy^{3+}:Gd^{3+}, the Dy^{3+} R-center fluorescence was able to be observed, as the presence of a Gd^{3+} in the dimer center removes the cross-relaxation pathways. A number of approximate energy levels of the Dy^{3+} R-center were thus able to be determined. The narrowband excitation spectra and optical and infrared absorption spectra of the double doped systems, along with the absorption spectra of singly doped CaF_2:Dy^{3+}, indicates that the proposed asymmetry of the R-center is a minor perturbation on the crystal-field interactions. In the double doped CaF_2:Dy^{3+}:Tb^{3+} system, the broadband excitation spectra indicate a large number of cluster centers. Efficient $Dy^{3+}\rightarrow Tb^{3+}$ energy transfer was also observed. Due to the limited literature on the CaF_2:Tb^{3+} centers and the apparent complexities of the Tb^{3+} spectroscopy, further investigation of the multitude

of centers in CaF_2:Dy^{3+}:Tb^{3+} has not been pursued here.

The motion of C_{4v} interstitial fluorine ions has been investigated through the temperature dependence of fluorescence polarisation. This work constitutes only the second such study, following that of Voron'ko et.al. [100]. The results of this earlier study have been extended to include both the CaF_2 and SrF_2 hosts, with barrier energies for interstitial reorientation obtained for the C_{4v} centers in CaF_2:RE^{3+} and SrF_2:RE^{3+} (RE=Pr, Eu) C_{4v} centers. While the results presented here are in general agreement with reported ITC experiments, some disagreement with Voron'ko et.al. is obtained for the CaF_2:Eu^{3+} barrier energies. For the praseodymium centers an additional slow onset of fluorescence depolarisation has been interpreted as the consequence of resonant energy transfer between C_{4v} centers with different orientations. This in itself establishes the feasibility of such CW experiments for the investigation of resonant energy transfer processes. Investigations of these transfer processes are generally hampered by the indistinguishability of the donor and acceptor ions. It has also been shown how application of this technique to a number of excited states with differing lifetimes can lead to a determination of the reorientation barrier energies independent of any consideration of the attempt frequency, a parameter that is usually not well determined.

Suggestions for further work.

The resonance modes of the CaF_2:RE^{3+} cubic center could form the basis of future studies, with a quantitative explanation of these modes presenting a significant challenge in itself, not least because of the excess charge associated with the center. It is also possible that the temperature dependent properties of the cubic center vibronic transitions could prove fruitful for investigation of the electron-phonon coupling of the lanthanides. Because such vibronics possess a well defined frequency, and are relatively intense, such an investigation would overcome the approximations required in previous studies, such as an assumed Debye phonon distribution [30][31].

Perhaps the most promising area of research following from this thesis involves the optical depolarisation technique for monitoring ionic motion. Such a technique could possibly be applied to determining the barrier energies associated with hydrogenic compensated rare-earth centers. Such centers are known to undergo photo-induced interstitial reorientation [86, 73], and optical depolarisation experiments could further clarify the underlying dynamics and mechanisms. It may also be possible to apply this technique to provide direct experimental confirmation of the predicted interchangeability of C_{3v} and C_{4v} fluorine compensated centers [13]. The presence of both C_{3v} and C_{4v} centers in SrF_2:Dy^{3+} make this a candidate system for such an investigation. It

is noted that preliminary investigations by the author, while not reported here, have shown that both of the above optical depolarisation experiments present significant experimental challenges, largely associated with detection sensitivity of CW fluorescence and lifetime measurements.

Appendix A

Crystal-field Parameter Transformations.

C_{3v} parameters.

The following are the transformations between the $\sum B_k^q V_k^q$ parametrisation of Eremin, Luks and Stolov [34] and the $\sum B_q^k C_q^k$ parametrisation of of Wybourne [105] for the parameters relevant to the C_{3v} Hamiltonian.

$$B_2^0 = \frac{1}{2}B_0^2$$

$$B_4^0 = \frac{1}{8}B_0^4$$

$$B_4^3 = -\frac{\sqrt{35}}{2}B_3^4$$

$$B_6^0 = \frac{1}{16}B_0^6$$

$$B_6^3 = -\frac{\sqrt{105}}{8}B_3^6$$

$$B_6^6(\mathrm{Erm}) = \frac{\sqrt{231}}{16}B_6^6(\mathrm{Wyb}).$$

The transformations from the Wybourne parameters to those used in this thesis, which will be termed the Butler parameters, are as follows:

$$B_A^2 = B_0^2$$

$$B_A^4 = \frac{20}{27}B_0^4 - \frac{2\sqrt{70}}{27}B_3^4$$

$$B_c^4 = \frac{7}{27}B_0^4 + \frac{2\sqrt{70}}{27}B_3^4$$

$$B_c^6 = \frac{32}{81}B_0^6 - \frac{8\sqrt{2}\sqrt{105}}{243}B_3^6 + \frac{8\sqrt{231}}{243}B_6^6$$

$$B_A^6 = \frac{\sqrt{2}\sqrt{231}}{21} B_3^6 + \frac{2\sqrt{105}}{21} B_6^6$$

$$B_A^{6\prime} = \frac{49}{81} B_0^6 + \frac{8\sqrt{2}\sqrt{105}}{243} B_3^6 - \frac{8\sqrt{231}}{243} B_6^6$$

The reverse transformation, from the Butler parameters to the Wybourne parameters is given by:

$$B_0^2 = B_A^2$$

$$B_0^4 = B_A^4 + B_c^4$$

$$B_3^4 = -\frac{1}{2}\sqrt{\frac{7}{10}} B_A^4 + \sqrt{\frac{10}{7}} B_c^4$$

$$B_0^6 = B_A^{6\prime} + B_c^6$$

$$B_3^6 = \sqrt{\frac{11}{42}} B_A^6 + \frac{4}{7}\sqrt{\frac{10}{21}} B_A^{6\prime} - \sqrt{\frac{35}{96}} B_c^6$$

$$B_6^6 = \sqrt{\frac{5}{21}} B_A^6 - \frac{4}{7}\sqrt{\frac{11}{21}} B_A^{6\prime} + \frac{1}{8}\sqrt{\frac{77}{3}} B_c^6.$$

C_{4v} parameters.

The following relations give the transformation of the C_{4v} crystal-field parameters between the simple form of the Hamiltonian

$$H = B_0^2 C_0^2 + B_0^4 C_0^4 + B_0^6 C_0^6 + B_4^4 (C_4^4 + C_{-4}^4) + B_4^6 (C_4^6 + C_{-4}^6)$$

and the Hamiltonian that is used in this thesis (equation 2.6, page 12). Such transformations between forms of the Hamiltonian are useful in that for the two possible C_{4v} bases, the B_4^4 and B_4^6 parameters of the above Hamiltonian simply undergo a sign change.

The transformations from the Wybourne parameters to the Butler parameters are:

$$B_A^2 = B_0^2$$

$$B_A^4 = \frac{5}{12} B_0^4 - \frac{\sqrt{70}}{12} B_4^4$$

$$B_C^4 = \frac{7}{10} B_0^4 + \frac{\sqrt{70}}{12} B_4^4$$

$$B_A^6 = \frac{7}{8}B_0^6 + \frac{\sqrt{14}}{8}B_4^6$$
$$B_C^6 = \frac{1}{8}B_0^6 - \frac{\sqrt{14}}{8}B_4^6$$

The transformations from the Butler parameters to the Wybourne parameters are:

$$B_A^2 = B_0^2$$
$$B_0^4 = B_A^4 + B_C^4$$
$$B_4^4 = -\sqrt{\frac{7}{10}}B_A^4 + \sqrt{\frac{5}{14}}B_C^4$$
$$B_0^6 = B_A^6 + B_C^6$$
$$B_4^4 = \sqrt{\frac{1}{14}}B_A^4 - \sqrt{\frac{7}{2}}B_C^4$$

Appendix B

Resonant Modes in CaF_2:RE^{3+}.

This appendix describes attempts to calculate the expected resonant mode frequencies for the RE^{3+} cubic center in CaF_2, and hence show the feasibility of attributing the observed vibronic transitions to such a resonance mode.

While similar calculations have been reported previously [39][15] they have attempted to describe a far-infrared absorption feature at $\approx 90\,cm^{-1}$, although it appears that this absorption has not been explicitly associated with the cubic center, in contrast to the $\approx 135\,cm^{-1}$ vibronics observed here. While the calculations performed here have not been particularly successful in extending those present in the literature, it is considered worthwhile reporting them here for two reasons. First, the published literature does not contain a unified formalism for such a calculation, with a number of different sign and normalisation conventions encountered when piecing together such a calculation from different sources. Secondly, a number of errors have been found in various papers that address such a calculation. While these appear to be merely publication errors, they are not immediately obvious. It is also not clear that a number of approximations employed in the literature for calculating the CaF_2 resonance modes are necessarily valid for the cubic centers. A number of points that are not explicitly mentioned in the literature, such as Brillouin zone grid choice for density of states and normal mode calculation, are also addressed.

To calculate the resonant mode frequency, a succession of separate calculations need to be performed, and these are each addressed in turn. The formulation of the problem of calculating the phonon normal modes, the first step to be encountered, follows that given by Kellerman [54].

Following the formulation of the problem, the calculation of the Coulomb and short-range repulsive interactions is addressed. Srinivasan [95] has given general expressions, based on Ewalds method [54], for the Coulomb interactions for the specific case of crystals of the fluorite structure. The evaluation of these Coulomb terms is discussed in Section B.2. The short-range forces for UO_2 (with the same structure as CaF_2) have been discussed by Dolling et.al. [26], while Elcombe and Pryor [29] have also given

such expressions for CaF_2, including particular parameter values that are required here. Both of these papers contain what appear to be publication errors. A sign convention is also different than that employed here and by Srinivasan.

In Section B.4 the actual evaluation of the normal modes of CaF_2 is discussed.

Finally, in Section B.5 the Greens function method for calculating the resonant mode frequency is described, following the presentation by Maradudin et.al. [67]. Such a calculation requires knowledge of the normal modes of the pure crystal, which have been calculated according to the above description. The Greens function is then employed for a simple mass defect calculation of the Dy^{3+} cubic center resonant mode frequency. A discussion of difficulties in the approximations required for extension of these calculations is also given.

B.1 Calculation of the normal modes in CaF_2

The formulation of the normal mode problem is due to Kellerman [54], and this section draws on that original presentation.

The lattice energy Ψ, is expressed as a Taylors expansion in small ionic displacements from equilibrium positions of the ions,

$$\Psi = \Psi_0 + \Psi_1 + \Psi_2 + \cdots$$

$$\text{where } \Psi_2 = -\frac{1}{2}\sum_{\kappa\kappa'}\sum_{ll'}\sum_{xy'}\left[\frac{\partial^2}{\partial x \partial y}\psi^{l-l'}_{\kappa\kappa'}\right]_{r=r^l_{\kappa\kappa'}} u^l_{\kappa x}u^{l'}_{\kappa' y}.$$

Here κ refers to the type of ion (Ca, F(1), F(2)) of the unit cell, l to the particular unit cell of the lattice, and x, y, z to the Cartesian coordinates. $u^l_{\kappa x}$ is a small displacement from equilibrium of the κ ion, in the lth cell, in the x direction. $\psi^{l-l'}_{\kappa\kappa'}$ is the potential experienced by ion κ in cell l due to ion κ' in cell l'. The term Ψ_0 is a constant and of no further interest here. At equilibrium the gradient of the lattice potential vanishes, so that $\Psi_1 = 0$. Therefore only the motion of the system of ions under the influence of the harmonic potential Ψ_2 need be considered. Further, because of the translational symmetry of the pure crystal only solutions for the motion of ions within any given primitive cell need to be found. With this in mind the general ionic displacements are given in terms of the unit cell displacements, $(u^l_{\kappa x}, u^l_{\kappa y}, u^l_{\kappa z}) = (U_{\kappa x}, U_{\kappa y}, U_{\kappa z})\exp(-i\omega t)\exp(-2\pi i \boldsymbol{k}\cdot\boldsymbol{r}^l_\kappa)$. The equations of motion for the ions in the primitive cell can then be written as

$$\omega^2 m_\kappa U_{\kappa x} + \sum_{\kappa'}\sum_{y}\begin{bmatrix}\kappa & \kappa' \\ x & y\end{bmatrix} U_{\kappa' y} = 0$$

$$\text{where} \qquad \begin{bmatrix} \kappa & \kappa' \\ x & y \end{bmatrix} = \sum_l \left[\frac{\partial^2}{\partial x \partial y} \psi^l_{\kappa\kappa'} \right]_{r=r^l_{\kappa\kappa'}} \exp(-2\pi i \boldsymbol{k} \cdot \boldsymbol{r}^l_\kappa)$$

This can be expressed in matrix form as a set of nine coupled equations for the CaF_2 lattice;

$$\omega^2 \boldsymbol{m}\boldsymbol{U} + \boldsymbol{A}\boldsymbol{U} = 0$$

where the elements of the matrix $\boldsymbol{A}$ are given by $\begin{bmatrix} \kappa & \kappa' \\ x & y \end{bmatrix}$.

With the definition $\boldsymbol{v} = \boldsymbol{m}^{1/2}\boldsymbol{U}$, left multiplication of the above matrix equation by $\boldsymbol{m}^{-1/2}$ leads to the eigenvector equation

$$\{\boldsymbol{m}^{-1/2}\boldsymbol{A}\boldsymbol{m}^{-1/2} + \omega^2 \boldsymbol{I}\}\boldsymbol{v} = 0$$

Hence the square of the normal mode frequencies are the eigenvalues of the dynamical matrix $\boldsymbol{D} = -\boldsymbol{m}^{-1/2}\boldsymbol{A}\boldsymbol{m}^{-1/2}$. The elements of $\boldsymbol{A}$ are separated into additive Coulomb (electrostatic) and short-range components, $\begin{bmatrix} \kappa & \kappa' \\ x & y \end{bmatrix} = C \begin{bmatrix} \kappa & \kappa' \\ x & y \end{bmatrix} + R \begin{bmatrix} \kappa & \kappa' \\ x & y \end{bmatrix}$, which will be discussed separately.

B.2 Matrix elements for the Coulomb potential.

These matrix elements are essentially the lattice summation of the second derivatives of the Coulomb $1/r$ potential. However, convergence of the direct summation is conditional and as such the truncation of the infinite lattice sum becomes an issue. The Ewald method overcomes this problem of convergence by converting the conditional sum into two rapidly convergent summations, one over real space and the second over reciprocal (Fourier) space. Following Srinivasan[95], and including a change to SI units, the Coulomb terms are

$$C \begin{bmatrix} \kappa & \kappa \\ x & y \end{bmatrix} = \left(-G^{\kappa\kappa}_{xy} + \overset{(l)}{H}_{xy} + \frac{8}{3}\frac{\epsilon^3}{\pi^{1/2}}\delta_{xy} \right) \frac{Z^2_\kappa}{v_a 4\pi\epsilon_0}$$

$$C \begin{bmatrix} \mathrm{Ca} & \mathrm{F(1)} \\ x & y \end{bmatrix} = \left(-G^{\mathrm{CaF(1)}}_{xy} + \overset{(n)}{H}_{xy} \right) \frac{Z_{\mathrm{Ca}} Z_{\mathrm{F}}}{v_a 4\pi\epsilon_0}$$

$$C \begin{bmatrix} \mathrm{F(1)} & \mathrm{F(2)} \\ x & y \end{bmatrix} = \left(-G^{\mathrm{F(1)F(2)}}_{xy} + \overset{(m)}{H}_{xy} \right) \frac{Z^2_{\mathrm{F}}}{v_a 4\pi\epsilon_0}$$

$$G^{\kappa\kappa}_{xy} = 4\pi \sum_h \frac{(h_x + q_x)(h_y + q_y)}{(\boldsymbol{h} + \boldsymbol{q})^2} \exp\left(\frac{-\pi^2}{4\epsilon^2}(\boldsymbol{h} + \boldsymbol{q})^2\right)$$

$$G_{xy}^{CaF(1)} = 4\pi \sum_{h} \frac{(h_x + q_x)(h_y + q_y)}{(\boldsymbol{h}+\boldsymbol{q})^2} \exp(\frac{-\pi^2}{4\epsilon^2}(\boldsymbol{h}+\boldsymbol{q})^2) \exp(-\frac{i\pi}{2}(h_x + h_y + h_z))$$

$$G_{xy}^{F(1)F(2)} = 4\pi \sum_{h} \frac{(h_x + q_x)(h_y + q_y)}{(\boldsymbol{h}+\boldsymbol{q})^2} \exp(\frac{-\pi^2}{4\epsilon^2}(\boldsymbol{h}+\boldsymbol{q})^2) \cos(\pi(h_x + h_y + h_z))$$

$$\overset{(l)}{H}_{xy} = 2 \sum_{l} \left(-f(l)\delta_{xy} + g(l)\frac{l_x l_y}{l^2} \right) \cos(\pi \boldsymbol{q} \cdot \boldsymbol{l})$$

$$\overset{(n)}{H}_{xy} = 2 \sum_{n} \left(-f(n)\delta_{xy} + g(n)\frac{n_x n_y}{n^2} \right) \exp(i\pi \boldsymbol{q} \cdot \boldsymbol{n})$$

$$\overset{(m)}{H}_{xy} = 2 \sum_{m} \left(-f(m)\delta_{xy} + g(m)\frac{m_x m_y}{m^2} \right) \cos(\pi \boldsymbol{q} \cdot \boldsymbol{m})$$

$$f(l) = -\frac{2\epsilon}{\sqrt{\pi}|l|^2} \exp(-\epsilon^2|l|^2) + \frac{\operatorname{erfc}(\epsilon|l|)}{|l|^3}$$

$$g(l) = 3f(l) + \frac{4\epsilon^3}{\sqrt{\pi}} \exp(-\epsilon^2|l|^2)$$

The definition given for $f(l)$ and $g(l)$ also applies for $f(n)$, $f(m)$, $g(n)$, $g(m)$. For calculations performed here, the value of $\epsilon = 1$ has been used.

The summations present in the above expressions will now be clarified. For the reciprocal space summation, the sum is over all $\{\boldsymbol{h}\} = (h_x, h_y, h_z)$ such that h_x, h_y, h_z are all even or all odd. Truncation of the series is accomplished by the additional constraint $|h_x|, |h_y|, |h_z| \leq h_{\max}$. It has been found that $h_{\max} = 3$ provides rapid convergence. For the real space summations, $\boldsymbol{l}$ is the set of lattice vectors, and therefore corresponds to the separation of all like ions in the lattice. For the FCC lattice of CaF_2 the summation is therefore over all $\boldsymbol{l} = (l_x, l_y, l_z)$ such that $\sum_x l_x$ is even. For the calculations performed here truncation is given by $|l_x|, |l_y|, |l_z| \leq l_{\max}$, and $l_{\max} = 3$ provides good convergence without undue computation time. The set of Ca-F(1) vectors can be given by $\boldsymbol{n} = (n_x, n_y, n_z) = (l_x + \frac{1}{2}, l_y + \frac{1}{2}, l_z + \frac{1}{2})$ where l_x, l_y, l_z satisfy the above restrictions. Likewise, the F(1)-F(2) vectors are given by $\boldsymbol{m} = (m_x, m_y, m_z)$ such that $\sum_x m_x$ is odd. The truncation employed here is given by $|m_x|, |m_y|, |m_z| \leq l_{\max}$ where $l_{\max}$ is taken as above. Further, it is noted that the $\boldsymbol{l} = (0, 0, 0)$ term is excluded from the summation for like ions, $\overset{(l)}{H}_{xy}$, but is included when evaluating the allowed set of $\{\boldsymbol{n}\}$ from the set of $\{\boldsymbol{l}\}$.

B.3 Matrix elements for the repulsive potential.

These matrix elements are much more straight forward to calculate, as the potential is of a short range nature and hence only acts on a subset of near ions. The expressions

given here are are essentially those given by Dolling et.al. [26] and Elcombe and Pryor [29], who include up to next-nearest-neighbour interactions. [1]

$$R\begin{bmatrix} Ca & Ca \\ x & x \end{bmatrix} = -\frac{8}{3}(A_1+2B_1) - 2(A_3+2B_3)(2-C_x(C_y+C_z)) - 4B_3(1-C_yC_z)$$

$$R\begin{bmatrix} Ca & Ca \\ x & y \end{bmatrix} = -2(A_3-B_3)S_xS_y$$

$$R\begin{bmatrix} F(1) & F(1) \\ x & x \end{bmatrix} = R\begin{bmatrix} F(2) & F(2) \\ x & x \end{bmatrix} =$$

$$-\frac{4}{3}(A_1+2B_1) - 2A_2 - 4B_2 - 2(A_4+B_4)(2-C_x(C_y+C_z)) - 4B_4(1-C_yC_z)$$

$$R\begin{bmatrix} F(1) & F(1) \\ x & y \end{bmatrix} = R\begin{bmatrix} F(2) & F(2) \\ x & y \end{bmatrix} = -2(A_4-B_4)S_xS_y$$

$$R\begin{bmatrix} Ca & F(1) \\ x & x \end{bmatrix} = R\begin{bmatrix} Ca & F(2) \\ x & x \end{bmatrix}^* = \frac{4}{3}(A_1+2B_1)(C_{2x}C_{2y}C_{2z} - iS_{2x}S_{2y}S_{2z})$$

$$R\begin{bmatrix} Ca & F(1) \\ x & y \end{bmatrix} = R\begin{bmatrix} Ca & F(2) \\ x & y \end{bmatrix}^* = -\frac{4}{3}(A_1-B_1)(S_{2x}S_{2y}C_{2z} - iC_{2x}C_{2y}S_{2z})$$

$$R\begin{bmatrix} F(1) & F(2) \\ x & x \end{bmatrix} = 2A_2C_x + 2B_2(C_y+C_z)$$

$$R\begin{bmatrix} F(1) & F(2) \\ x & y \end{bmatrix} = 0$$

with

$$C_x = \cos(\pi q_x) \quad , \quad S_x = \sin(\pi q_x)$$
$$C_{2x} = \cos(\pi q_x/2) \quad , \quad S_{2x} = \sin(\pi q_x/2)$$

and $A_1, A_2, A_3, A_4, B_1, B_2, B_3, B_4$ parameters. For consistency in units, the numerical values for A_i, B_i taken from Elcombe must be multiplied by $e^2/v_a 4\pi\epsilon_0$.

[1] The negative of the coefficients given by Dolling and Elcombe is given here in order to be consistent with the earlier definition of the equation of motion and the electrostatic coefficients. Note also that both Elcombe et.al. and Dolling et.al. have errors in the published expressions for the repulsive terms. These errors can lead to negative eigenvalues which imply an unstable crystal. Their expressions do not satisfy the $\sum_{\kappa'} R\begin{bmatrix} \kappa & \kappa' \\ x & y \end{bmatrix} = 0$ constraint. However it appears these are only publication errors and do not imply their results are incorrect.

B.4 Evaluation of the normal modes in CaF_2.

For a particular set of phonon wave-vectors $\boldsymbol{q}$, the above matrix elements of $\boldsymbol{A}$ have been calculated for each chosen value of the phonon wave-vector $\boldsymbol{q}$, the dynamical matrix $\boldsymbol{D} = -\boldsymbol{m}^{-1/2}\boldsymbol{A}\boldsymbol{m}^{-1/2}$ constructed, and the eigenvalues determined. These eigenvalues are the square of the normal mode frequencies, ω^2. The eigenvectors have also been calculated. In these calculations only the first Brillouin zone, and of that only 1/48 of the volume that is irreducible, need be explicitly calculated. The reciprocity of the crystal, that is, the equivalence of forward and reverse directions, reduces the calculation to considering 1/8 of the first zone $[(abc) \simeq (ab\bar{c}) \simeq (a\bar{b}\bar{c})\cdots]$. The cubic nature of the CaF_2 crystal gives rise to a further 1/6 reduction in the irreducible volume $[[(abc) \simeq (bac) \simeq (bca)\cdots]$. The irreducible part of the Brillouin zone can be described by the relations

$$q_x \leq 1/2, \quad q_x \geq q_y \geq q_z \geq 0, \quad q_x + q_y + q_z \leq 3/4$$

Both the full and irreducible part of the first Brillouin zone are shown in the Figure B.1.

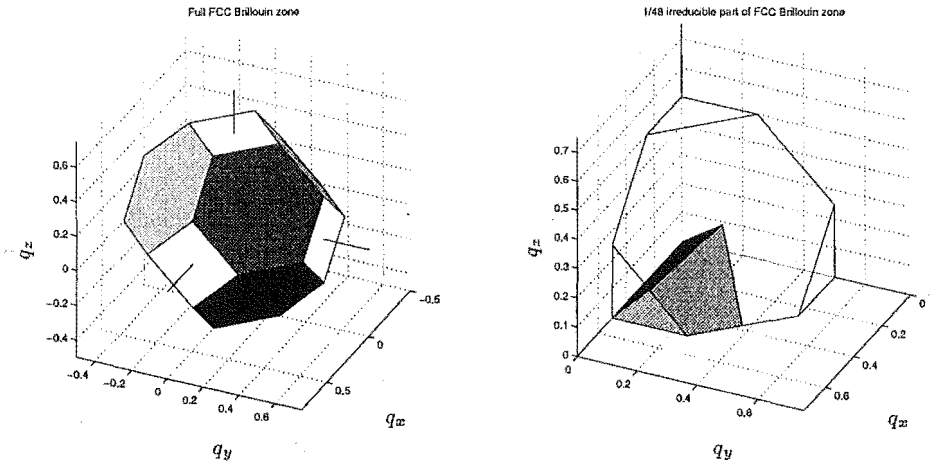

Figure B.1: Full, and 1/48 irreducible part, of the the first Brillouin zone.

The above calculations have been performed for a sampling of 1638 $\boldsymbol{q}$ vectors chosen from a uniform grid within the irreducible zone, giving rise to 14742 calculated frequencies and eigenvectors. The dispersion curves along the [100], [110], and [111] directions have also been calculated. For both calculations the rigid-ion model parameters of Elcombe [29] have been used. These parameters were obtained by a fitting of the calculated dispersion curves to points obtained from neutron scattering experiments, the elastic constants, and the high and low frequency dielectric constants. It has been noted in the literature that the eigenvalues so obtained are not very sensitive to the particular microscopic model chosen, and that a good interpolation of the density of

states can be achieved. However, whether the eigenvectors are likewise insensitive to the model is debatable. The eigenvectors obtained for the dynamical matrix should posses orthogonality properties. Tests of whether the obtained eigenvectors satisfy the orthogonality relations have been performed. These relations have been found to be satisfied for all 14742 eigenvectors except for 13 eigenvectors corresponding to $\boldsymbol{q}$ vectors those along the [111] direction. It was found, for example, that $\boldsymbol{q} = (0.4, 0.4, 0.4)$ gives rise to non-orthogonal eigenvectors, but that with $\boldsymbol{q} = (0.4, 0.4, 0.40001)$ orthogonality is restored. However, in both cases the same normal mode frequencies are obtained.

A note on applying calculations in the 1/48 irreducible zone to the full zone is considered necessary. As some points in $\boldsymbol{q}$-space will lie on symmetry points or boundaries of the irreducible zone, it cannot be said in general that each $\boldsymbol{q}$-point has a multiplicity of 48. In fact it can easily be seen that the multiplicity must be one of 1, 6, 8, 12, 24 or 48. The occurrences of these multiplicities for two different grid sizes, and with the grid including the origin point $\boldsymbol{q}$=(0,0,0), are shown in Figure B.2. Of note is that with even a reasonably fine grid approximately 20% of the $\boldsymbol{q}$-vectors have a reduced multiplicity of 24. These particular points fall into two categories, those that can be given as $(q_x, q_y, 0)$ for $q_x \neq q_y$, and secondly those with two identical components (q_x, q_x, q_z) or (q_x, q_y, q_y). Each category contributes approximately half of the $\boldsymbol{q}$ points with multiplicity of 24. Note that the chosen grid is uniform in reciprocal space and is positioned to include the origin. It is possible to reduce the number of multiplicity 24 points by approximately half simply by shifting the grid off the origin. All reduced multiplicity points can be eliminated by shifting the grid by different amounts in the q_x, q_y and q_z directions. That is, by centering the grid at (a, b, c) rather than $(0, 0, 0)$. The multiplicities for such a situation are also shown in Fig B.2. At first it may appear that shifting the origin of the grid would therefore be the easiest method for dealing with the problem of multiplicities. However additional difficulties are encountered in shifting the grid from the origin. While retaining a uniform sampling in the irreducible zone, there will no longer be a uniform sampling in the full zone. This is most easily seen for points near a boundary of the irreducible zone. The two grid points that are at, or near, a boundary $(q_x, q_y, 0)$ and(q_x, q_y, Δ), where Δ is the grid spacing, will serve to demonstrate this problem. These points are first shifted by a uniform translation of the grid by $(0, 0, \delta)$, to give the new grid points (q_x, q_y, δ) and $(q_x, q_y, \Delta + \delta)$. Turning our attention to the full zone in each case, the following points are obtained. For the unshifted grid, the operation $z \rightarrow -z$ gives one new corresponding point, $(q_x, q_y, -\Delta)$. For the offset grid the same operation gives rise to two new points, $(q_x, q_y, -\delta)$ and $(q_x, q_y, -\Delta - \delta)$. While the separation of adjacent points in the unshifted grid is a uniform Δ, the separation of the adjacent points in the offset grid varies, being either 2δ or Δ. Hence a non-uniform grid spacing in the full zone is created by shifting the grid origin. Note that simply choosing $\delta = \Delta/2$ will make the full zone uniform in

density in the q_z direction, but the density will not be simultaneously uniform in all directions, as the translation is required to be of the form (a, b, c) where $a \neq b \neq c$, $a \neq c$.

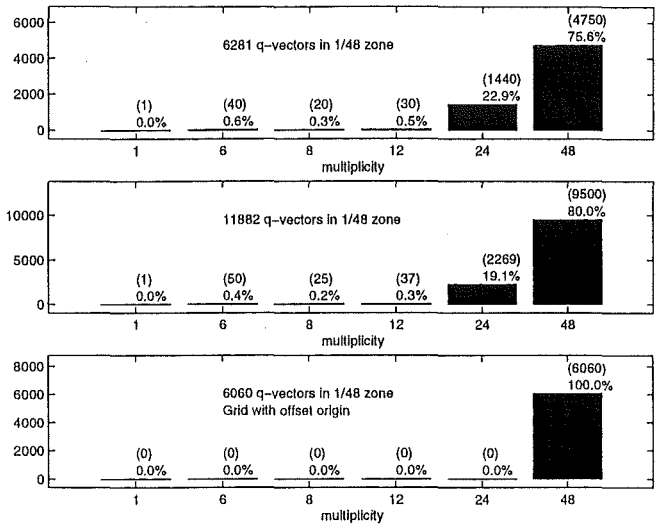

Figure B.2: Multiplicity of q-vectors in the 1/48 zone for different grid sizes. The upper two two histograms show the multiplicities for two different grid sizes, where the grid includes the origin. The bottom histogram if for the same grid spacing at the top figure, but with a displaced origin.

To reinforce this point, and to gain some indication of the magnitude of error introduced by the non-uniform density of grid points, the total number of points in the full zone have been calculated when using a grid spacing of $\Delta = 1/40\zeta$, centered on the origin and also when translated by $(0.05, 0.10, 0.15)\Delta$. For the first case the multiplicity depends on the particular $\boldsymbol{q}$-point, while in the second it is always 48. Numerically, it is found that positioning of a grid on the origin gives 6281 $\boldsymbol{q}$-vectors in the irreducible zone, corresponding to 263321 uniformly spaced $\boldsymbol{q}$-vectors in the full zone. For the offset grid 6060 vectors are found in the irreducible zone, and an increased number of 290880 vectors in the full zone. This represents a 10% increase in the number of $\boldsymbol{q}$-vectors of the full zone. This increase is simply due to the non-uniform nature of the grid in the full zone for the translated grid. For these reasons, in all calculations involving sampling of $\boldsymbol{q}$-space a uniform grid in the 1/48 irreducible zone that is centered on the origin has been chosen. The multiplicity of each sampled point is calculated and this multiplicity is taken into account in calculations where a sampling of the full zone is required.

It is also noted that the reduced multiplicity points occur on the boundaries and vertices of the irreducible zone. From the diagram of this 1/48 zone in Fig. B.1, it is clear that for a given grid size these points will become proportionatly greater in number in the region near the origin of the brilluion zone. It is precisely these $\boldsymbol{q}\approx\mathbf{0}$ phonons which are of interest for the optical properties in the perturbed crystal.

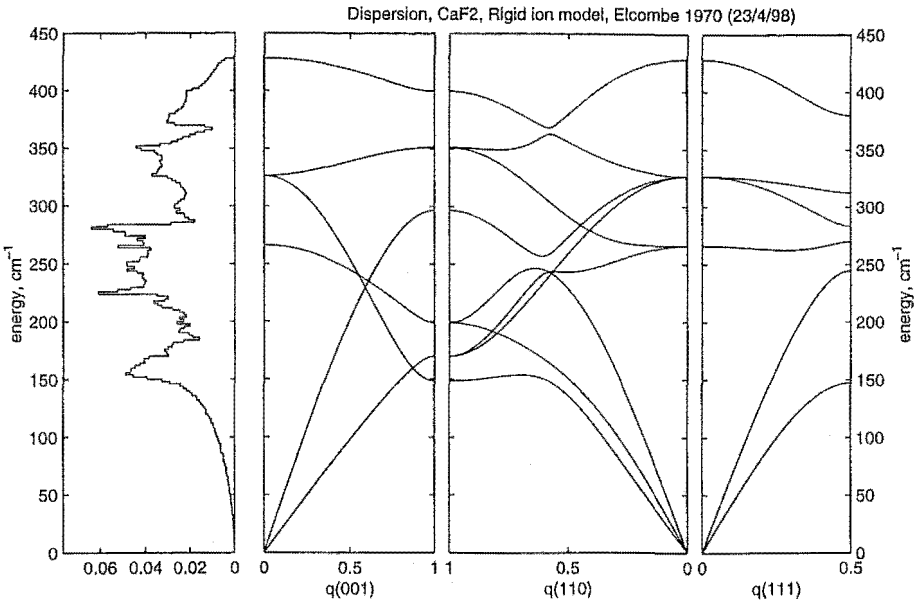

Figure B.3: Density of states and dispersion curves along symmetry directions for CaF_2 calculated from the rigid-ion model parameters of Elcombe et.al. [29].

B.5 Greens functions and the resonant mode frequency.

The formulation of the Greens function method for calculating the resonant mode frequency that is presented here follows closely that given by Maradudin et.al. [67]. The use of the 1/48 Brillouin zone normal-mode results for calculating the Greens functions is also adressed here.

The equations of motion for the ions in the crystal are first rewritten without reducing the problem by refering to the translational symmetry of the crystal. This is in anticipation of introducing a defect into the crystal calulations.

$$\sum_{l'\kappa'\beta} \left[M_{l\kappa}\omega^2 \delta_{l'l}\delta_{\kappa'\kappa}\delta_{\alpha\beta} - \Phi_{\alpha\beta}(l\kappa; l'\kappa') \right] u_\beta(l'\kappa') = 0. \tag{B.1}$$

This can be summarised as

$$(\boldsymbol{L} - \delta\boldsymbol{L})\,\boldsymbol{u} = 0 \tag{B.2}$$

where $\boldsymbol{L}$ is the equivalent of the left hand side of equation B.1 for the perfect crystal, and $\delta\boldsymbol{L}$ is given by the difference from the perfect crystal and the crystal containing an impurity at the site labelled by $l\kappa$.

$$\delta L_{\alpha\beta}(l\kappa; l'\kappa', \omega^2) = -\omega^2(M_{l\kappa} - M_\kappa)\delta_{l'l}\delta_{\kappa'\kappa}\delta_{\alpha\beta} + \Phi_{\alpha\beta}(l\kappa; l'\kappa') - \Phi^{(0)}_{\alpha\beta}(l\kappa; l'\kappa')$$

$$= \omega^2 M_\kappa \epsilon \delta_{l'l}\delta_{\kappa'\kappa}\delta_{\alpha\beta} + \Delta\Phi_{\alpha\beta}(l\kappa; l'\kappa')$$

where $\epsilon = (M_\kappa - M_{l\kappa})/M_{l\kappa}$ and M_κ is the mass of the ion designated by κ in the perfect crystal (hence there is no need for the subscript l), and $M_{l\kappa}$ is the new mass for the impurity (which as already stated is taken to be at site $l\kappa$).

The Greens function matrix for the perfect crystal is defined by

$$\boldsymbol{GL} = \boldsymbol{I}.$$

Taking the equation of motion given by equation B.2 and left multiplying by the Greens function for the perfect crystal

$$\boldsymbol{G}(\boldsymbol{L} - \delta\boldsymbol{L})\boldsymbol{u} = 0$$

results in the equation

$$\boldsymbol{u} = \boldsymbol{G}\delta\boldsymbol{L}\boldsymbol{u}.$$

Partitioning the matrices $\delta\boldsymbol{L}$, $\boldsymbol{G}$ and $\boldsymbol{u}$ in such a way as to group those ions that are directly affected by the introduction of the impurity,

$$\delta\boldsymbol{L} = \left(\begin{array}{c|c} \delta\boldsymbol{l} & 0 \\ \hline 0 & 0 \end{array}\right) \qquad \boldsymbol{G} = \left(\begin{array}{c|c} \boldsymbol{g} & \boldsymbol{G}_{12} \\ \hline \boldsymbol{G}_{21} & \boldsymbol{G}_{22} \end{array}\right) \qquad \boldsymbol{u} = \left(\begin{array}{c} \boldsymbol{u}_1 \\ \hline \boldsymbol{u}_2 \end{array}\right) \tag{B.3}$$

enables the following equations for motion of the ions in the perturbed crystal to be obtained

$$\boldsymbol{u}_1 = \boldsymbol{g}\delta\boldsymbol{l}\boldsymbol{u}_1 \tag{B.4}$$

$$\boldsymbol{u}_2 = \boldsymbol{G}_{21}\delta\boldsymbol{l}\boldsymbol{u}_1 \tag{B.5}$$

The solubility condition for the perturbed modes is therefore $|\boldsymbol{I} - \boldsymbol{g}\delta\boldsymbol{l}| = 0$. It is at this point that the advantages of assuming the direct influence of the defect on a small number of ions can lead to significant simplification. Because the introduction of a defect with excess charge will not necessarily satisfy this assumption of a local influence, it is unclear how applicable this procedure will be for calculating the resonance modes of a charged defect.

The elements of the Greens function can be shown to be [67]

$$G_{\alpha\beta}(l\kappa; l'\kappa', \omega^2) = \frac{1}{N\sqrt{M_\kappa M_{\kappa'}}} \sum_{\boldsymbol{k}j} \frac{W_\alpha(\kappa|\boldsymbol{k}j) W^*_\beta(\kappa'|\boldsymbol{k}j)}{\omega^2 - \omega^2_{\boldsymbol{k}j}} \exp\left(i\boldsymbol{k}\cdot(\boldsymbol{x}_{l\kappa} - \boldsymbol{x}_{l'\kappa'})\right)$$

In these expressions for the Greens functions, it should be emphasised that the summation is over the $\boldsymbol{k}$ vectors of the first Brillouin zone, and the nine different branches labelled by j. However, as noted earlier, the calculation of the eigenvalues and eigenvectors of the first zone can be reduced to those of the 1/48 irreducible zone. The

problem at hand then becomes one of expressing the above Greens function into one expressed in terms of a summation over this reduced volume of the Brillouin zone. First it is noted that the eigen-frequencies (actually the squared frequencies) are unchanged by any operation $\boldsymbol{S}$ on $\boldsymbol{k}$ that is an operation of the crystal symmetry. That is $w^2(\boldsymbol{k},j) = w^2(\boldsymbol{Sk},j)$. Considering a permutation of the components of the wavevector, for example $(k_x,k_y,k_z) \rightarrow (k_y,k_z,k_x)$, then this results in an effective relabelling of the Cartesian co-ordinates (x,y,z), and the appropriate eigenvector components can be found by an appropriate rearrangement $(W_x,W_y,W_z) \rightarrow (W_y,W_z,W_x)$. For a change in sign of a component of the eigenvector $(k_x,k_y,k_z) \rightarrow (\overline{k_x},k_y,k_z)$ there is a corresponding change in the eigenvector $(W_x,W_y,W_z) \rightarrow (\overline{W_x},W_y,W_z)$. Considering the specific Greens function $G_{xx}(l\kappa,l\kappa;\omega)$, then the specific permutations in components in $\boldsymbol{k}$ can be accounted for by introducing the equivalence $\sum_{\boldsymbol{kj}} W_x W_x^* = \frac{1}{3}\sum_{\boldsymbol{kj}} \boldsymbol{W}\cdot\boldsymbol{W}^*$. Denoting the multiplicity of $\boldsymbol{k}$ by $M(\boldsymbol{k})$, then

$$\frac{1}{N}\sum_{\boldsymbol{kj}} W_x(\boldsymbol{kj})W_x^*(\boldsymbol{kj}) = \frac{1}{3N}\sum_{\boldsymbol{kj}} \boldsymbol{W}(\boldsymbol{kj})\cdot\boldsymbol{W}^*(\boldsymbol{kj}) = \frac{1}{3N}\sum_{(\boldsymbol{kj})} \boldsymbol{W}(\boldsymbol{kj})\cdot\boldsymbol{W}^*(\boldsymbol{kj})M(\boldsymbol{k}).$$

A summation in the full zone has been denoted by $\sum_{\boldsymbol{kj}}$, and a sum in the irreducible zone by $\sum_{(\boldsymbol{kj})}$. N is the number of $\boldsymbol{k}$-vectors in the full zone, and can be given in terms of a summation in the irreducible zone by $N = \sum_{(\boldsymbol{k})} M(\boldsymbol{k})$. Hence the Greens function can be expressed in terms of the irreducible zone as

$$G_{\alpha\alpha}(l\kappa;l\kappa,\omega^2) = \frac{1}{3NM_\kappa}\sum_{(\boldsymbol{kj})} \frac{\boldsymbol{W}(\boldsymbol{kj})\cdot\boldsymbol{W}^*(\boldsymbol{kj})}{\omega^2-\omega_{\boldsymbol{kj}}^2}M(\boldsymbol{k})$$

For an isotopic impurity the only change in the equations of motion relates to a mass change. That is, $\Delta\Phi_{\alpha\beta}(l\kappa;l'\kappa')$ is taken to be zero. Further, only the ion substituted is directly involved in the perturbation, and hence the matrix $\boldsymbol{\delta l}$ is simply a diagonal matrix representing the mass change on ion $l\kappa$ for the three equations in the (x,y,z) directions.

$$\boldsymbol{\delta l}_{\alpha\beta} = \omega^2 M_\kappa \epsilon \delta_{\alpha\beta}$$

$$\boldsymbol{g}_{\alpha\beta} = \frac{1}{NM_\kappa}\sum_{\boldsymbol{kj}} \frac{W_\alpha(\kappa|\boldsymbol{kj})W_\beta^*(\kappa'|\boldsymbol{kj})}{\omega^2-\omega_{\boldsymbol{kj}}^2}$$

From the condition for solubility three identical equations for the eigen-frequencies of the perturbed modes are obtained, namely

$$\frac{M_\kappa}{\omega^2(M_\kappa - M'_\kappa)} = \frac{1}{N}\sum_{\boldsymbol{kj}} \frac{W_\alpha(\kappa|\boldsymbol{kj})W_\alpha^*(\kappa'|\boldsymbol{kj})}{\omega^2-\omega_{\boldsymbol{kj}}^2} \tag{B.6}$$

For an isotopic defect, in which the ion κ is substituted by another ion of different mass and which possesses the same force constants as the original ion, the resonant modes therefore satisfy equation B.6

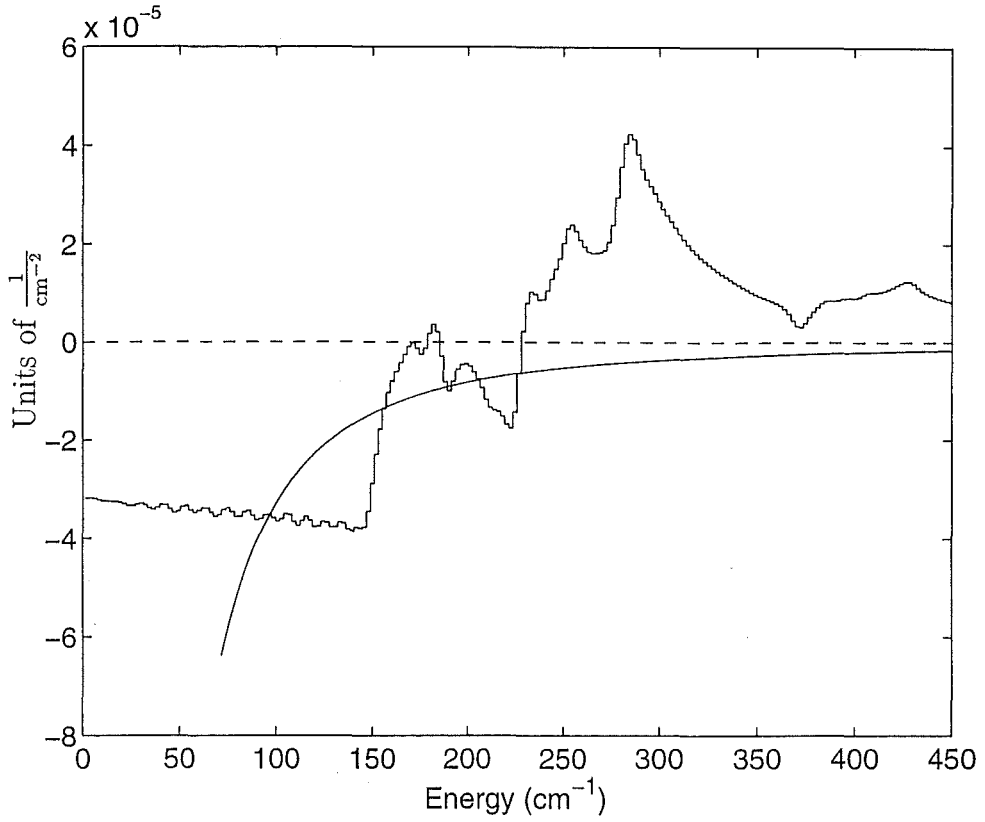

Figure B.4: The Greens function for CaF_2 calculated from the eigenvectors obtained with the rigid-ion model parameters of Elcombe et.al. [29] and the mass defect function for $^{40}Ca \rightarrow ^{162}Dy$ substitution. The intersection occurs at $96\,cm^{-1}$ and represents the resonant mode frequency predicted for an isotopic impurity.

The Greens function for the Ca^{2+} site in CaF_2 has been calculated from the above formalism with the eigenvectors evaluated as described in the earlier sections. The obtained Greens function is presented in Figure B.4. The mass defect function, defined as the left hand side of equation B.6 is superimposed on this Greens function, and the intersection graphically displays the solution to the resonant mode conditions. The defect mass has been taken to correspond to ^{162}Dy

The intersection occurs at $96\,cm^{-1}$, and therefore a resonant mode is predicted at this frequency, for dysprosium ions replacing calcium ions in a cubic center, where it has been assumed that there are no force constant changes associated with this substitution. To provide a more realistic calculation, changes in the force constants associated with the nearest neighbour ions can be considered. This is the approach taken by Hayes et.al. [39], where the force constants are reduced to give a lower resonant mode frequency more in line with the lower frequency peak in the far-infrared absorption. However in a subsequent paper Catlow et.al. [15] considered changes in both the nearest-neighbour

(NN) and next-nearest-neighbour (NNN) force constants and concluded that the NN force constants should be increased. This highlights one of the problems with extending these calculations, namely how to treat changes in the force constants.

Note that to include force constant changes a larger number of ions are included in the defect sub-space as defined by the partition of equation B.3. This leads to what is here considered a more fundamental obstacle to calculating the cubic center modes from the Greens function method. Because of the excess charge of the substitutional RE^{3+} ion, it is not clear that the defect space can be treated as a small region around the ion. The electrostatic force is essentially long range, and as demonstrated by the lengthy calculation required to evaluate the Ewald summation in Section B.2, simple truncation of the defect space is not necessarily valid. To include a large defect space would however lead to a removal of the simplifications that come from the partitioning of equation B.3. Therefore, it is not clear that the Greens function formalism is appropriate for calculating the resonant mode frequency of the CaF_2:RE^{3+} cubic centers, as the excess charge of this center cannot be treated in a satisfactory manner.

References

[1] Abragam A., Bleaney B.: *Electron paramagnetic resonance of transition ions*. Dover, New York (1970).

[2] Aizenberg I.B., Malkin B.Z., Stolov A.L.: *Cubic centers of the Er^{3+} ion in crystals of the fluorite type*. Sov. Phys. Solid State, **13**, 2155 (1971).

[3] Al'tshuler N.S., Eremin M.V., Luks R.K., Stolov A.L.: *Analysis of MeF_2:Dy^{3+} cubic centers from luminescence spectra*. Sov. Phys. Solid State, **11**, 2921 (1970).

[4] Al'tshuler N.S., Kozyrev B.M.: *Electron Paramagnetic Resonance*. Academic Press, New York (1964), Translation from the Russian of *Elektronniy Paramagnitniy Rezonans*.

[5] Antipin A.A., Davydova M.P., Eremin M.V., Luks R.K., Stolov A.L.: *Crystalline field in anisotropic activator Dy^{3+} centers in fluorite single crystals*. Optics and Spectroscopy, **33**, 372 (1972).

[6] Ashcroft N.W., Mermin N.D.: *Solid state physics*. Holt, Rinehart and Winston, New York (1976).

[7] Barker A.S., Sievers A.J.: *Optical studies of the vibrational properties of disordered solids*. Rev. Modern Phys., **47**, Supplement 1 (1975).

[8] Bierig R.W., Weber M.J.: *Paramagnetic resonance of Dysprosium in cubic axial fields in CaF_2*. J Chem Phys, **91**, 627 (1963).

[9] Brout R., Visscher W.: *Suggested experiment on approximate localised modes in crystals*. Phys. Rev. Lett., **9**, 54 (1962).

[10] Brown M.R., Roots K.G., Williams J.M., Shand W.A., Groter C., Kay H.F.: *Experiments on Er^{3+} in SrF_2. II. Concentration dependence of site symmetry*. J. Chem. Phys., **50**, 69 (1969).

[11] Butler P.H.: *Point group symmetry applications*. Plenum Press, New York (1981).

[12] Carnell W.T., Crosswhite H., Crosswhite H.M.: *Energy level structure and transition probabilities of the trivalent lanthanides in LaF_3*. Argonne National Laboratory, Argonne, Illinois, USA (1978).

[13] Catlow C.R.A.: *The defect properties of anion-excess alkaline-earth fluorides:I. Low defect concentrations*. J. Phys. C: Solid State Phys., **9**, 1845–1857 (1976).

[14] Catlow C.R.A.: *The defect properties of anion-excess alkaline-earth fluorides:II. intermediate and high dopant concentration*. J. Phys. C: Solid State Phys., **9**, 1859–1869 (1976).

[15] Catlow C.R.A., Hayes W., Wiltshire M.C.K.: *Changes of force constants near rare-earth impurity sites in CaF_2*. J. Phys. C: Solid State Phys., **10**, L243 (1977).

[16] Charnock F., H, Matthews G.E.J., Williams R.T., Pieslak B.: *Dielectric and Fluorescence studies of SrF_2:Pr^{3+}* (1998), Presentation at APS March meeting, Los Angeles, and private communication.

[17] Charnock F., Tackett A., Sheilds H., Matthews G.E.J.: *Relaxation modes of fluoride interstitials in gadolinium-doped SrF_2*. Phys. Rev B, **51**, 1 (1995).

[18] Cirillo-Penn K.M., Wright J.C.: *Laser spectroscopic measurement of point-defect dynamics in Eu^{3+}:CaF_2*. Phys. Rev. B, **41**, 10799 (1990).

[19] Cirillo-Penn K.M., Wright J.C.: *Identification of defect structure in Eu^{3+}:CaF_2 by site selective spectroscopy of relaxation dynamics*. J. Lumin., **48 & 49**, 505 (1991).

[20] Clifford A.A.: *Multivariate error analysis : a handbook of error propagation and calculation in many-parameter systems.*. Wiley / Halsted Press, New York (1973).

[21] Cockroft N.J.: *Laser selective excitation or erbium ions in crystalline soilds*. Ph.D. thesis, University of Canterbury (1987).

[22] Corish J., Catlow C.R.A., Jacobs P.W.M., Ong S.H.: *Defect agregation in anion-excess fluorites. Dopant monomers and dimers*. Phys. Rev B, **25**, 6425 (1982).

[23] Dean T.: *Infrared spectroscopy of the principal Er^{3+} centre in BaF_2 and SrF_2 crystals*. 4th year project report. (1996).

[24] den Hartog H.W., Langevoort J.C.: *Ionic thermal current of concentrated cubic solid solutions of SrF_2:LaF_3 and BaF_2:LaF_3*. Phys. Rev. B, **24**, 3547 (1981).

[25] Dexter D.L.: *Theory of sensitised luminescence in solids*. J. Chem. Phys., **21**, 836 (1953).

[26] Dolling G., Cowley R.A., Woods A.D.B.: *The crystal dynamics of uranium dioxide*. Can. J. Phys., **43**, 1397 (1965).

[27] Edgar A., Welsh H.K.: *Dielectric loss and EPR studies of CaF_2:Gd^{3+}*. J. Phys. C: Solid State Phys., 8, L336–L340 (1975).

[28] Elcombe M.M.: *The lattice dynamics of strontium fluoride*. J. Phys. C: Solid State, **5**, 2702 (1972).

[29] Elcombe M.M., Pryor A.W.: *The lattice dynamics of calcium fluoride*. J. Phys. C: Solid State, **3**, 492 (1970).

[30] Ellens A., Andres H., Meijerink A., Blasse G.: *Spectral-line-broadening study of the trivalent lanthanide-ion series. I. Line broadening as a probe of the electron-phonon coupling strength*. Phys. Rev. B, **55**, 173 (1997).

[31] Ellens A., Andres H., ter Heerdt M.L.H., Wegh R.T., Meijerink A., Blasse G.: *Spectral-line-broadening study of the trivalent lanthanide-ion series. II. The variation of the electron-phonon coupling strength through the series*. Phys. Rev. B, **55**, 180 (1997).

[32] Elliot R.J., Hayes W., Jones G.D., Macdonald H.F., Sennett C.T.: *Localised vibrations of H^- and D^- ions in the alkaline earth fluorides*. Proc. Royal Soc. (London), **289 A**, 1 (1965).

[33] Eremin M.V., Leushin A.M.: *Ambiguity in the signs of field parameters in crystals*. Sov. Phys. Solid State, **12**, 1003 (1970).

[34] Eremin M.V., Luks R.K., Stolov A.L.: *Crystal field parameters of trigonal Dy^{3+} ion centers in fluorite-type single crystals.*. Sov. Phys. Solid State, **12**, 2820 (1971).

[35] Freeth C.A.: *Solid state spectroscopy: The transverse Zeeman effect in CaF_2:Er^{3+}*. Ph.D. thesis, University of Canterbury (1980).

[36] Görller-Walrand C., Binnemans K.: *Rationalization of crystal-field parametrization*. In Gschneidner K.A., Eyring L., editors, *Handbook on the physics and chemistry of rare earths*, volume 23, Elsiever Science, Amsterdam (1996).

[37] Hamers R.J., Wietfeldt J.R., Wright J.C.: *Defect chemistry in CaF_2:Eu^{3+}*. J. Chem Phys., **77**, 683 (1982).

[38] Han T.P.J.: *Solid state spectroscopy: Laser selective excitation studies of neodymium*. Ph.D. thesis, University of Canterbury (1988).

[39] Hayes W., Wiltshire M.C.K., Berman R., Hudson P.R.W.: *Infrared absorption and thermal conductivity of CaF_2 containing heavy metal impurities*. J. Phys. C: Solid State, **6**, 1157 (1973).

[40] Hayes W., Wiltshire M.C.K., Manthey W.J., McClure D.S.: *Localised vibrational modes induced in CaF_2 by rare-earth impurites*. J. Phys. C: Solid State, **6**, L273 (1973).

[41] Heber J.: *Energy transfer and rate equations - application to ruby*. Phys. Stat. sol., **42**, 497 (1970).

[42] Hecht E.: *Optics*. Addison-Wesley, Massachusetts (1975).

[43] Hilerbrand F.: *Advanced Calculus for Applications*. Prentice-Hall, New Jersey (1976).

[44] Huber D.L.: *Dynamics of incoherent transfer*. In Yen W.M., Selzer P.M., editors, *Laser spectroscopy of solids*, Springer-Verlag, New York (1986).

[45] Hüfner S.: *Optical spectra of transparent rare earth compounds*. Academic Press, New York (1978).

[46] Imbusch G.F.: *Energy transfer in ruby*. Phys. Rev., **153**, 326 (1967).

[47] Jamison S.P., Imbusch G.F.: *Temperature dependence of the luminescence from heavily doped ruby*. J. Lumin., **75**, 143 (1997).

[48] Jamison S.P., Reeves R.J.: *Optical depolarization in CaF_2:RE^{3+} and SrF_2:RE^{3+} C_{4v} centers due to dipole reorientation*. J. Lumin., **66&67**, 169 (1996).

[49] Jasperson S., Schnatterly S.: *An improved method for high reflectivity ellipsometry based on a new polarization modulation technique*. Rev. Sci. Inst., **40**, 761 (1969).

[50] Jouart J.P., Bissieux C., Mary G., Egee M.: *A spectroscopic study of Eu^{3+} centers in SrF_2 using a site-selective excitation technique*. J. Phys. C: Solid State, **18**, 1539 (1985).

[51] Judd B.: *Operator techniques in Atomic Spectroscopy*. McGraw-Hill, New York (1963).

[52] Judd B.R.: *Optical absorption intensities of rare-earth ions*. Phys. Rev., **127**, 750 (1962).

[53] Kaiser W., Spitzer W.G., Kaiser R.H., Howarth L.E.: *Infrared properties of CaF_2, SrF_2, and BaF_2*. Phys. Rev., **127**, 1950 (1962).

[54] Kellerman E.W.: *Theory of the vibrations of the sodium chloride lattice*. Phil. Trans. Roy Soc. A, **A238**, 513–548 (1940).

[55] Kemp J.: *Piezo-optical birefringence modulators: New use for a long-known effect*. J. Opt. Soc. Am., **59**, 950 (1969), Note that in the given fourier decomposition of the intensity, all the oscillating terms should be negative of that stated. Also, the term $\sin(\phi_0 \sin\omega t)$ should actually read $\sin(\frac{\phi_0}{2}\sin\omega t)$.

[56] Kitts E.L., Crawford J.H.: *Relaxation of type-I dipolar complexes in calcium fluoride containing trivalent rare-earth impurities*. Phys. Rev. B, **9**, 5264 (1974).

[57] Kitts E.L., Ikeya M., Crawford J.H.: *Reorientation kinetic of dipolar complexes in Gadolinium-doped alkaline-earth fluorides*. Phys. Rev. B, **8**, 5840 (1973).

[58] Klein M.J.: *On a degeneracy theorem of Kramers*. Am. J. Phys., **20**, 65 (1951).

[59] Klein M.V.: *Localised modes and resonance states*. In Fowler W.B., editor, *Physics of color centers*, Academic Press, NY (1968).

[60] Koster G.F., Dimmock J.O., Wheeler R.G., Statz H.: *Properties of thirty-two point groups*. MIT Press, Massachusetts (1963).

[61] Lea K.R., Leask M.J.M., Wolf W.P.: *The raising of angular momentum degeneracy of the f-electron terms by cubic crystal fields*. J. Chem. Phys. Solids, **23**, 1381 (1962).

[62] Lesniak K., Richardson F.S.: *Crystal fields and microscopic local structures of some trigonal symmetry centers in fluorite crystals doped with trivalent rare-earth ions*. J. Phys. Condens. Matter, **4**, 1743 (1992).

[63] Lezama A., Oria M., de Araujo C.B.: *Site-selective spectroscopy via energy up-conversion in CaF_2:Pr^{3+}*. Phys. Rev B, **33**, 4493 (1986).

[64] Lide D.R., editor: *Handbook of chemistry and physics*. CRC Press, Boston (1990-1991).

[65] Luks R.K., Livanova L.D., Stolov A.L.: *Oxygen centers in the CaF_2:Dy^{3+} and SrF_2:Dy^{3+} systems*. Sov. Phys. Solid State, **11**, 1810 (1970).

[66] Luks R.K., Saitkulov I.G., Stolov A.L.: *Optical spectra of CaF_2 single crystals activated by Dy^{3+}.*. Sov. Phys. Solid State, **11**, 210 (1969).

[67] Maradudin A.A., Montrol E.W., Weiss G.H., Ipatova I.P.: *Theory of lattice dynamics in the harmonic approximation*. In *Solid State Physics, Supplement 3*, Academic Press, New York (1971).

[68] Meuldijk J., Mulder H.H., den Hartog H.W.: *Depolarization experiments on space charges in concentrated solutions of NdF_3 in SrF_2*. Phys. Rev. B, **25**, 5204 (1982).

[69] Moore D.S.: *Laser spectroscopic and EPR studies of defect equilibria in rare-earth doped fluorite structure crystals*. Ph.D. thesis, University of Wisconsin-Madison (1980).

[70] Moore D.S., Wright J.C.: *Evidence for cluster control of the defect equilibria in fluorite structure crystals*. Chem. Phys. Lett., **66**, 173 (1979).

[71] Mujaji M.: *Solid state spectroscopy: Laser selective excitation of Holmium ions in crystalline solids*. Ph.D. thesis, University of Canterbury (1992).

[72] Mujaji M., Jones G.D., Syme R.W.G.: *Polarization study and crystal-field analysis of the laser-selective excitation spectra of Ho^{3+} ions in CaF_2 and SrF_2 crystals*. Phys. Rev. B, **46**, 14398 (1992).

[73] Murdoch K.M.: *Laser excitation, Energy-transfer and bleaching processes in crystalline rare-earth centers*. Ph.D. thesis, University of Canterbury (1993).

[74] Murdoch K.M., Jones G.D., Syme R.W.G.: *Site-selective spectroscopy of Tb^{3+} centers in SrF_2 and CaF_2*. Phys. Rev. B, **56**, 1254 (1997).

[75] Nara H., Schlesinger M.: *Optical studies of Dy^{3+}-doped calcium fluoride. Cubic sites*. Sol. State Comm., **9**, 1247 (1971).

[76] Nara H., Schlesinger M.: *Analysis of the optical spectra of Dy^{3+} doped calcium fluoride*. J. Phys. C., **5**, 606 (1972).

[77] Nielson C.W., Koster G.F.: *Spectroscopic coefficients for the p^n, d^n and f^n configurations*. MIT Press (1963).

[78] Ofelt G.S.: *Intensities of crystal spectra of rare-earth ions*. J. Chem. Phys., **37**, 511 (1962).

[79] Orbach R.: *Phonon sidebands and energy transfer*. In Crosswhite H.M., E M.H., editors, *Optical properties of Ions in crystals*, Interscience, New York (1967).

[80] Pavlichuk P.: Private communication.

[81] Powell R.C.: *Physics of solid-state laser materials*. AIP Press, New York (1998).

[82] Pukhov K.K., Sakun V.P.: *The effect of quasilocalisable oscillations on the spin-lattice relaxation of some rare-earth ions in a CaF_2 lattice*. Sov. Phys. Solid state, **10**, 1148 (1968).

[83] Rabbiner N.: *Fluorescence of Dy^{3+} in CaF_2.*. Phys. Rev., **132**, 224 (1963).

[84] Reeves R.J.: Private communication.

[85] Reeves R.J.: *Laser selective spectroscopy of praseodymium ions in hydrogenated fluorite crystals*. Ph.D. thesis, University of Canterbury (1987).

[86] Reeves R.J., Jones G.D., Syme R.W.G.: *Spectroscopy of reversible bleaching centers in hydrogenated CaF_2:Pr^{3+} and SrF_2:Pr^{3+} crystals*. Phys. Rev. B, **40**, 6475 (1987).

[87] Reeves R.J., Jones G.D., Syme R.W.G.: *Site-selective laser spectroscopy of Pr^{3+} C_{4v} symmetry centers in hydrogenated CaF_2:Pr^{3+} and SrF_2:Pr^{3+} crystals*. Phys. Rev. B, **46**, 5939 (1992).

[88] Reid M.F., Butler P.H.: *The point group crystal field and the superposition model for RE^{3+} ions in CaF_2 and SrF_2*. J. Phys. C, **15**, 4103 (1982).

[89] Richman I.: *Vibronic spectra of SrF_2:Sm^{2+} and BaF_2:Sm^{2+}.*. Phys. Rev., **133**, A1364 (1964).

[90] Richter K., wannemacher R., Heber J.: *Direct observation of migration of optical excitation energy in TAG:Tb^{3+}*. J. Lumin., **47**, 169 (1991).

[91] Rotenburg M., Bivens R., Metropolis N., Wooten J.K.: *The 3j and 6j symbols*. MIT Press, Massachusetts (1959).

[92] Salva H., Tova M.: *The crystal field splitting between the $\Gamma_8 - \Gamma_7$ levels of the Dy^{3+} in CaF_2: an indirect EPR measurement.*. Solid State Comm., **16**, 1251 (1975).

[93] Schlesinger M., Kwan C.T.: *Optical studies of Dy^{3+}-doped calcium fluoride*. Phys. Rev. B, **3**, 2852 (1970).

[94] Sivaram A., Jagannath H., Ramachandra Rao D., Venkateswarlu P.: *Steady state and transient fluorescence studies of CaF_2:Dy^{3+} single crystals*. Phys. Chem. Solids, **40**, 1007 (1979).

[95] Srinivasan R.: *Elastic Constants of Calcium Fluoride*. Proc. Phys. Soc. (Lond), **72**, 566 (1958).

[96] Strickland N.M.: *Laser excitation and infrared absorption spectroscopy of rare-earth ion centres in fluorite crystals*. Ph.D. thesis, University of Canterbury (1996).

[97] Tallant D.R., Moore D.S., Wright J.C.: *Defect equilibra in fluorite structure crystals*. J Chem Phys, **67**, 2897 (1977).

[98] Tallant D.R., Wright J.C.: *Selective laser excitation of charge compensated sites in CaF_2:Er^{3+}*. J Chem Phys, **63**, 2074 (1975).

[99] Voron'ko Y.K., Osiko V.V., Udovenchik V.T., Fursikov M.M.: *Optical properties of CaF_2-Dy^{3+} crystals*. Sov. Phys. Solid State, **7**), 204 (1965).

[100] Voron'ko Y.K., Oskio A.V., Oskio V.V., Sobol' A.A., Ushakov S.N., Tsymbal L.I.: *Mobility of interstitial fluorine bound in activator centers of TR^{3+} ions in the fluorite structure*. Phys. Solid State, **36**, 410 (1994).

[101] Ward R.W., Whippey P.W.: *Vibronic sideband of Er^{3+} in CaF_2*. Can. J. Phys., **52**, 1185 (1974).

[102] Weissbluth M.: *Atoms and molecules*. Academic Press, New York (1978).

[103] Wells J.P.R.: *Laser spectroscopy of alkaline earth fluoride crystals doped with trivalent samarium and europium ions*. Ph.D. thesis, University of Canterbury (1997).

[104] Wells J.P.W., Reeves R.J.: *Up-conversion fluorescence of Eu^{3+} doped alkaline earth fluoride crystals*. J. Lumin., **66&67**, 219 (1996).

[105] Wybourne B.G.: *Spectroscopic properties of rare earths*. John Wiley and Sons Inc, New York (1965).